University of Nottingham

Ph.D. Thesis

Physical and numerical modelling of ground-borne vibrations in sand

Authors:
Ge Cui

Supervisor:
Dr. Charles Heron
Dr. Alec Marshall



Nottingham centre for Geomechnics
Department of Civil Engineering

October 2020

Declaration of Authorship

I, Ge Cui, declare that this report titled, 'Physical and numerical modelling of ground-borne vibrations in sand' and the work presented in it are my own. I confirm that:

- This work was done wholly or mainly while in candidature for a research degree at this University.
- Where any part of this thesis has previously been submitted for a degree or any other qualification at this University or any other institution, this has been clearly stated.
- Where I have consulted the published work of others, this is always clearly attributed.
- Where I have quoted from the work of others, the source is always given. With the exception of such quotations, this thesis is entirely my own work.
- I have acknowledged all main sources of help.
- Where the thesis is based on work done by myself jointly with others, I have made clear exactly what was done by others and what I have contributed myself.

Signed: Ge Cui

Date: October 2020

"To my parents"

Acknowledgements

The research work described in this thesis was carried out at the University of Nottingham. The project was suggested by Dr Charles Heron and Dr Alec Marshall, who also acted as my main and secondary supervisors, respectively. I would like to sincerely thank them for their support, suggestions, and most importantly, for their encouragement.

A special note of recognition and appreciation goes to all the technicians in the Nottingham Centre for Geomechanics research group. I want to thank Dr Solomon Idinyang and Mr Luke Bedford, who provided the enthusiastic technical contributions in geotechnical centrifuge modelling. I would like to thank Mr Lee Hickling, Mr Andrew Maddison, Mr Steven Lawton and Mr Jim Meakin for their professional help and support. My thanks also go to the post-doctoral researchers for their help and inspirations, in particular Dr Mir Hashemi Afrapoli, who lately became a technician in our research group.

I want to thank all of my fellow researchers in the Nottingham Centre for Geomechanics research group. Many thanks also go to Dr Andrea Franza, Mr Jingmin Xu, Mr KunKun Chen and Mr Geyang Song for their help and friendship.

For financial support, I would like to thank my supervisors for their great effort in securing funding for my PhD study.

Finally, my special thanks go to my parents and my family. In particular, I would like to thank my mum and aunt for their endless and wonderful love and encouragement in my life.

Abstract

The problems caused by urban congestion and population growth result in a growing need to construct railway networks in urban areas due to the advantages of safety, efficiency and reliability over alternative mass transportation options. However, railway systems can cause environmental issues due to the transit of vehicles, including railway noise and vibration. The problem of ground-borne vibration has gained increasing attention because people are becoming less likely to tolerate environmental disturbance and sensitive buildings and equipment could be significantly affected by nearby ground-borne vibrations. Therefore, it is necessary to investigate those effects and provide a better understanding of ground-borne vibrations from railways. This research work was primarily concerned with the transmission of vibration from railways via a single friction pile through the soil-pile interface and the ground.

In this study, dynamic centrifuge tests were conducted to study the dynamic pile behaviour, the soil-pile interaction and ground-borne vibration propagation characteristics generated from the vertical oscillation of a single pile in sand. The use of the centrifuge is attributed to its great advantage of reproducing the full scale stress field within a small scale model, thus correctly modelling soil behaviour and soil-pile interface characteristics. However, the boundary effects in centrifuge models on vibration propagation have not been fully understood. In addition to the boundary effects, centrifuge and shaker induced vibrations and the embedded piezoelectric accelerometors can also affect the measured vibration results in a centrifuge test; these were also considered in this research project.

The main aims of this study were to provide insights into the soil-pile interaction and ground-borne vibrations in sand from the vertical oscillation of a single pile and to examine the use of centrifuge modelling as a tool for investigating this problem. To achieve these aims, centrifuge tests were performed to simulate the ground-borne vibration by applying small vertical harmonic loads to the top of a single rough pile (with sand stuck to the pile surface) embedded in sand. The effects of vibration absorbing material used in the centrifuge tests, Duxseal, on the soil stress field and soil stiffness were investigated experimentally by measuring the shear wave velocity of the soil using centrifuge based air hammer tests and triaxial based bender elememt tests. A series of numerical models were developed in FLAC3D to further the understanding of soil-pile interaction under vertical harmonic loads and to examine the effects of Duxseal and piezoelectric accelerometers on the centrifuge measurements.

A series of combinations of dead loads and dynamic loads were used to investigate their effects on pile and soil behaviours. Three dead loads with a safety factor (ratio=ultimate

bearing capacity of the pile/dead load) of approximately 8, 4 and 2 were employed in this study to investigate the effect of the static load amplitude on the dynamic pile and soil behaviour. The dynamic loads with two different amplitudes were applied by an electromagnetic shaker for each dead load. Centrifuge test results demonstrated that both dynamic pile and soil behaviour were in the linear range when the safety factor was greater than 2. Under all the combined forces applied in this study, the soil and the pile experienced the same displacement at the interface and the dynamic load applied to the pile top did not result in accumulated pile displacement. Therefore, the soil-pile interface can be treated as a perfectly bonded interface for the setup used in this study. Under the three dead loads (safety factor>2), the pile top response amplitude indicated the pile top response decreased with the increasing dead load.

It was also found that the pile was compressible and the displacement of the pile element under vertical harmonic loading was purely caused by the axial elastic deformation. The axial load within the pile decreased with depth, thus resulting in a decreasing axial elastic deformation of the pile and soil particle displacement along depth at the soil-pile interface. It was found that the vibration level at the same horizontal distance from the pile center decreased almost linearly with depth.

The damping ratio of soil along depth was calculated by an empirical equation and the logarithmic decrement method using data measured by the accelerometers. It was found that within very small shear strain (less than 1.0×10^{-6}), the material damping had a slight effect on the vibration attenuation at three depths. The vibration attenuation along radial distance from the pile center was evaluated by comparing the ratio of vibration responses measured by two accelerometers with the same embedded depth. It was found that test results agreed well with the theoretical estimation at most frequencies. The vibration attenuation curves at three depths (3.36 m, 10 m and 16.8 m at prototype scale) were calculated. It was found that within the radial distance of 15 m (prototype scale), the vibration attenuates very quickly. The curves tend to be flat when the radial distance from the pile is greater than 27 m (prototype scale).

The original purpose of the use of Duxseal was to absorb vibrations and reduce reflections from the rigid boundaries of the centrifuge container so that more accurate model response can be measured in the centrifuge. However, it was found that Duxseal can change the lateral stress in the soil and the soil stiffness due to soil behaviour being stress dependent. It is suggested that side Duxseal should not be used to investigate the ground-borne vibration because the soil-pile interaction and measured ground-borne vibrations were affected and the Duxseal was not able to eliminate reflections.

The effects of piezoelectric accelerometers embedded in the soil were examined by comparing the results from two FLAC3D models: one with piezoelectric accelerometers

embedded in the soil and one without piezoelectric accelerometers. It was observed that calculated results with and without the piezoelectric accelerometers were close to each other at most frequencies. This indicated that the presence of piezoelectric accelerometers did not significantly change the model response.

Contents

Declaration of Authorship i

Acknowledgements iii

Abstract iv

Contents vii

List of Figures xii

List of Tables xvi

1 Introduction 1
- 1.1 Background . . . 1
- 1.2 Research aims and objectives . . . 4
- 1.3 Thesis structure . . . 4

2 Literature Review 6
- 2.1 Problem of ground-borne vibration . . . 6
  - 2.1.1 Properties of railway induced ground-borne vibration . . . 7
    - 2.1.1.1 Introduction . . . 7
    - 2.1.1.2 Excitation mechanisms . . . 7
    - 2.1.1.3 Wave propagation . . . 7
    - 2.1.1.4 Vibration attenuation . . . 8
    - 2.1.1.5 Frequency range and vibration levels from railways . . . 11
  - 2.1.2 Methods of reducing ground-borne vibration from railways . . . 13
- 2.2 Dynamic soil behaviour . . . 14
  - 2.2.1 Overview . . . 14
  - 2.2.2 Shear modulus . . . 14
    - 2.2.2.1 Shear modulus under different strain levels . . . 14
    - 2.2.2.2 Experiments to measure G_{max} . . . 17
    - 2.2.2.3 Empirical equations to determine G_{max} . . . 17
  - 2.2.3 Soil material damping . . . 18
    - 2.2.3.1 Vibration damping . . . 18
    - 2.2.3.2 Soil damping and factors affecting soil damping ratio . . . 20
  - 2.2.4 Soil non-homogeneity . . . 21

2.3 Soil-pile interaction and ground borne vibration . . . 23
2.3.1 Overview . . . 23
2.3.2 Soil-pile-interaction . . . 24
2.3.2.1 Modelling of soil-pile interface . . . 24
2.3.2.2 Behaviour of pile and soil under cyclic loading . . . 26
2.3.2.3 Railway-induced vibration transmitted to or from piles . 27
2.3.3 Modelling vibration from surface and underground railways . . . 29
2.3.3.1 Analytical and numerical methods . . . 30
2.3.3.2 Physical modelling of vibration from railways . . . 33
2.4 Concluding remarks . . . 37

3 Research Methodology 39
3.1 Introduction . . . 39
3.2 Centrifuge modelling and model development . . . 39
3.2.1 Scaling factors for centrifuge modelling . . . 40
3.2.2 Stress error . . . 41
3.2.3 Soil material and sample preparation . . . 42
3.2.4 Scaling considerations for piles in sand and pile preparation . . . 44
3.2.5 Model container and boundary effects . . . 45
3.2.6 Excitation method . . . 45
3.2.7 Instrumentation and equipment specifications . . . 47
3.2.7.1 Loading system and transducers . . . 47
3.2.7.2 Model layout . . . 48
3.2.8 Data acquisition system and signal processing . . . 49
3.2.9 Model preparation . . . 51
3.2.10 Test procedure . . . 52
3.2.11 Model development: centrifuge and shaker induced interference . . . 53
3.2.11.1 Isolation from the vibration sources with rubber mat . . . 53
3.2.11.2 Centrifuge induced vibration properties during spin-up . 55
3.2.11.3 Wind effect from centrifuge . . . 60
3.2.11.4 Supporting systems and noise and vibration from shaker 60
3.2.12 Model development: input signal for shaker . . . 66
3.2.12.1 Input signal . . . 66
3.2.12.2 Selection of input signal . . . 69
3.2.12.3 Test results and determination of input signal . . . 70
3.2.13 Summary of ground-borne vibration tests . . . 73
3.3 Shear wave velocity measurement using air-hammer and bender elements 74
3.3.1 Introduction . . . 74
3.3.2 Air hammer test in the centrifuge . . . 74
3.3.3 Bender element test in the triaxial cell . . . 76
3.3.3.1 Operating principle of a bender element system . . . 76
3.3.3.2 GDS Bender Element System . . . 77
3.3.3.3 Factors affecting the accuracy of bender element testing . 78
3.3.3.4 Preparation and deformation measurement of soil specimen 80
3.3.3.5 Stress state on the specimen: isotropic versus anisotropic 81

4 Estimation of soil stiffness and Duxseal effect in the centrifuge 84

4.1 Introduction . . . 84
4.2 Signal processing method . . . 85
4.2.1 Typical data from air hammer and bender element tests . . . 85
4.2.2 Methods to determine travel time . . . 86
4.2.2.1 Direct time methods . . . 87
4.2.2.2 Indirect time methods . . . 87
4.2.2.3 Changing wave period effect on all methods . . . 89
4.3 Shear wave velocity: air-hammer and bender element test results . . . 91
4.3.1 Bender element data versus empirical curves . . . 91
4.3.2 BE data versus air-hammer data . . . 93
4.3.3 Bender element: isotropic versus anisotropic . . . 95
4.4 Shear modulus and elastic modulus . . . 96
4.4.1 Pressure wave velocity . . . 96
4.4.2 Soil moduli . . . 97
4.5 Effect of Duxseal on horizontal stress in the centrifuge . . . 99
4.5.1 Procedure to back-calculate K in the centrifuge . . . 99
4.5.1.1 Empirical equation to calculate v_s at depth h_m . . . 99
4.5.1.2 Empirical equation to calculate v_s of a soil layer . . . 100
4.5.1.3 Step-by-step procedure to calculate K of a soil layer . . . 100
4.5.2 K in the centrifuge: with and without side Duxseal . . . 102
4.5.2.1 Without side Duxseal . . . 102
4.5.2.2 With side Duxseal . . . 102
4.5.2.3 Duxseal effect on soil stiffness . . . 103
4.6 Chapter summary . . . 104

5 Centrifuge Test Results and Analysis 107
5.1 Introduction . . . 107
5.2 Linearity of model . . . 107
5.2.1 Introduction . . . 107
5.2.2 Loading stages in the centrifuge tests . . . 108
5.2.2.1 Stage 1: Static loading . . . 108
5.2.2.2 Stage 2: Dynamic loading . . . 110
5.2.3 Frequency response function and coherence function . . . 111
5.2.3.1 Frequency response function . . . 111
5.2.3.2 Coherence function . . . 113
5.2.4 Linearity of pile behaviour . . . 114
5.2.5 Linearity of soil behaviour . . . 118
5.3 Dead weight effect on pile and soil response amplitude . . . 120
5.3.1 Pile and soil responses . . . 121
5.3.2 Result discussion . . . 124
5.3.2.1 Pile top behaviour under axially dynamic loading . . . 124
5.3.2.2 Soil-pile interaction under axially dynamic loading . . . 128
5.4 Soil damping along depth and vibration propagation . . . 135
5.4.1 Soil damping ratio . . . 135
5.4.1.1 Logarithmic decrement method . . . 136
5.4.1.2 Shear strain of soil in the centrifuge model . . . 136
5.4.1.3 Damping ratio of soil along depth . . . 139

5.4.2 Vibration attenuation with radial distance . . . 142
5.4.2.1 Theoretical estimation . . . 142
5.4.2.2 Centrifuge test results versus theory . . . 143
5.4.2.3 Vibration propagation . . . 145
5.5 Chapter summary . . . 147

6 Numerical Modelling in FLAC3D and Comparison with Centrifuge Test Results 150
6.1 Introduction . . . 150
6.2 FLAC3D modelling . . . 151
6.2.1 Overview of FLAC3D . . . 151
6.2.2 Numerical analysis with FLAC3D . . . 152
6.2.2.1 Finite difference grid . . . 153
6.2.2.2 Constitutive models and material properties . . . 153
6.2.2.3 Boundary condition . . . 153
6.2.2.4 Dynamic excitation . . . 154
6.3 Calibration of the FLAC3D model against centrifuge model . . . 155
6.3.1 Description of FLAC3D model . . . 155
6.3.1.1 FLAC3D model mesh . . . 155
6.3.1.2 Material properties . . . 158
6.3.1.3 Boundary conditions . . . 160
6.3.2 Numerical modelling procedure . . . 160
6.3.3 Static calibration . . . 161
6.3.3.1 Soil properties . . . 161
6.3.3.2 Duxseal properties . . . 163
6.3.3.3 Calibration results . . . 164
6.3.4 Dynamic calibration . . . 166
6.3.4.1 Pile response . . . 167
6.3.4.2 Soil response . . . 169
6.3.5 Brief summary . . . 171
6.4 Duxseal effects on soil stress field . . . 171
6.4.1 Description and calibration of FLAC3D models used to investigate the stress field . . . 172
6.4.2 The stress field in the soil . . . 174
6.5 Duxseal effects on dynamic model response . . . 177
6.5.1 FLAC3D models used to examine Duxseal effects . . . 177
6.5.2 Comparison of numerical modelling results . . . 179
6.5.2.1 Stiffness changing effect . . . 179
6.5.2.2 Vibration absorbing . . . 181
6.5.2.3 Flexible boundary versus rigid boundary . . . 182
6.6 Piezoelectric accelerometer effects . . . 183
6.7 Chapter summary . . . 185

7 Conclusions and Recommendations for Future Work 188
7.1 Conclusions . . . 188
7.1.1 Soil-pile interaction and ground-borne vibrations . . . 189
7.1.2 Duxseal effects . . . 190

7.1.3 Piezoelectric accelerometer effects 191
7.2 Recommendations for future work 192

References **195**

Appendix: material, equipment and transducer specifications **207**

List of Figures

1.1 Ground-borne vibration generation, propagation and reception (Lombaert et al., 2015) . . . 2
1.2 Generic vibration criteria (Nugent et al., 2012) . . . 3

2.1 Wave fields generated by impact at the top of a single pile (Kim and Lee, 2000) . . . 9
2.2 Illustration of horizontal distance, scaled-distance, and seismic distance (Cleary and Steward, 2016) . . . 10
2.3 Vertical shear strain amplitude with distance from track (Connolly et al., 2014) . . . 12
2.4 Vibration change rate with distance from track . . . 13
2.5 Soil characteristics and modelling methods for different strain levels (Ishihara, 1996) . . . 15
2.6 Soil stiffness degradation curve (Nanda, 2014) . . . 15
2.7 Hysteresis loop for one cycle of loading showing G_{max}, G, and D (Zhang et al., 2005) . . . 16
2.8 Soils stress-strain behaviour (Nanda, 2014) . . . 16
2.9 Factors affecting damping ratio of sand (Hardin and Drnevich, 1972) . . . 21
2.10 Confining pressure effects on damping ratio of (a) saturated sand and (b) dry sand (Hardin and Drnevich, 1972) . . . 22
2.11 Distribution of (a) wave velocity and (b) damping ratio with depth (Yang, 2012) . . . 23
2.12 Friction piles and end bearing pile . . . 25
2.13 Model of trains moving over an elevated bridge: (a) schematic view (b) simplified model (Wu and Yang, 2004) . . . 29
2.14 Finite element mesh of the multi-span bridge and piled foundations. (Ju, 2007) . . . 30

3.1 Comparison of stress variation with depth in prototype and its corresponding model . . . 42
3.2 Air pluviated soil . . . 43
3.3 Side and bottom Duxseal . . . 45
3.4 Schematic view of model layout in centrifuge testing (all in mm) . . . 48
3.5 A view of devices and transducers used in centrifuge testing . . . 50
3.6 Frequency range and vibrations from centrifuge at 60 g: (a) PCV and (b) VPNP3 . . . 55
3.7 Vibration measurement location . . . 56
3.8 Accelerations on centrifuge platform during spin-up (within 8000 Hz) . . . 57
3.9 Accelerations on centrifuge platform during spin-up (within 1000 Hz) . . . 57

3.10 Accelerations on pile top during spin-up (within 8000 Hz) . . . 58
3.11 Accelerations on pile top during spin-up (within 1000 Hz) . . . 59
3.12 Accelerations within the soil during spin-up (within 1000 Hz) . . . 59
3.13 Wind shield . . . 60
3.14 Wind effect on PCV and PCH: (a) without wind shield and (b) with wind shield . . . 61
3.15 A schematic view of old supporting system and transducers in Test Pre03_T01 62
3.16 A schematic view of new supporting system and transducers in Test Pre04_T01 . . . 62
3.17 Vibrations from centrifuge with old and new supporting system: (a) PCV and (b) VPNP3 . . . 63
3.18 Aluminium angle mounted to the steel beam . . . 64
3.19 Noise levels of dynamic load cell and accelerometers on pile in time domain 64
3.20 Noise levels of vertical and horizontal accelerometers in soil . . . 65
3.21 Frequency range of background noises and vibrations from centrifuge and shaker (data extracted from the whole time history data shown in Figure 3.20) . . . 66
3.22 An example of sine chirp input signal (dynamic load) . . . 68
3.23 An example of single frequency input signal (dynamic load) . . . 69
3.24 Coherence at VPNP1, VPNP3 and PCV . . . 71
3.25 Steady state response of soil (4600 Hz) . . . 72
3.26 Coherence at VPNP1, VPNP3 and PCV (Pre03_T03: old supporting system) . . . 72
3.27 Coherence at VPNP1, VPNP3 and PCV (Pre04_T03: new supporting system) . . . 73
3.28 Air hammer pellet . . . 75
3.29 Air hammer and MEMS accelerometers . . . 75
3.30 Air hammer and bender element test setup . . . 76
3.31 GDS Bender Element System . . . 78
3.32 Pedestal (left) and top cap (right) with bender elements . . . 78
3.33 A schematic view of bender element testing in triaxial cell . . . 79
3.34 Equipment time delay of GDS-BES . . . 80
3.35 Bender element test in triaxial cell . . . 81

4.1 Typical data from a centrifuge based air-hammer test . . . 86
4.2 Typical data from a triaxial based bender element test (depth=3.6 m) . . . 86
4.3 Cross correlation method (an example from BE test) . . . 88
4.4 Shear wave velocity comparison using three approaches to analyse BE data 89
4.5 Error from cross correlation method by changing period . . . 90
4.6 Shear wave velocities from BE and Equation 4.2 . . . 92
4.7 Stress error in this study . . . 95
4.8 Shear wave velocity: isotropic versus anisotropic (BE) . . . 96
4.9 Pressure wave velocity: isotropic VS anisotropic (BE) . . . 97
4.10 Shear wave and pressure wave velocity (BE) . . . 98
4.11 Shear modulus and elastic modulus (BE) . . . 98
4.12 Comparison of shear modulus: theory versus measurements with and without Duxseal in centrifuge . . . 104

5.1 Axially loaded pile and load distribution along pile depth . . . 108
5.2 Typical pile load-displacement curve . . . 109
5.3 Loading stages in the centrifuge test . . . 111
5.4 Dynamic force, pile displacement and FRF (GBV_m1:F_s/P_{ult}=44%) . . . 115
5.5 Dynamic force, pile displacement and FRF (GBV_m2:F_s/P_{ult}=24%) . . . 115
5.6 Dynamic force, pile displacement and FRF (GBV_m3:F_s/P_{ult}=12%) . . . 116
5.7 Static pile and soil displacement during excitation under 500 mV . . . 118
5.8 Static pile and soil displacement without dynamic loading . . . 118
5.9 The FRF and coherence at VPNP3 and VPDP1 (GBV_m1) . . . 119
5.10 The FRF and coherence at VPNP3 and VPDP1 (GBV_m2) . . . 120
5.11 The FRF and coherence at VPNP3 and VPDP1 (GBV_m3) . . . 120
5.12 FRFs (velocity/force) at PCV and VPNP3 (linear scale) . . . 121
5.13 FRFs (velocity/force) at PCV and VPNP3 (logarithmic scale) . . . 122
5.14 Response ratios at PCV under different dead weights . . . 123
5.15 Response ratios at VPNP3 under different dead weights . . . 124
5.16 Simplified MDOF system of above ground system in the centrifuge . . . 125
5.17 Dynamic load, pile top velocity and FRFs for PCV (GBV_m1) . . . 126
5.18 Dynamic load, pile top velocity and FRFs for PCV (GBV_m2) . . . 127
5.19 Dynamic load, pile top velocity and FRFs for PCV (GBV_m3) . . . 127
5.20 FRFs and coherence values of PCV . . . 128
5.21 Travel time difference in the soil for incompressible pile (model scale: in mm) . . . 129
5.22 An example of travel time difference in the soil from GBV_m2_500mV (model scale) . . . 130
5.23 Simplified soil-pile system in the centrifuge . . . 131
5.24 Response ratio (VPNP3/PCV) in linear and log scale . . . 132
5.25 Response ratios and velocity responses at PCV and VNPN3 (GBV_m1) . 134
5.26 Response ratios and velocity responses at PCV and VNPN3 (GBV_m2) . 134
5.27 Response ratios and velocity responses at PCV and VNPN3 (GBV_m3) . 135
5.28 Logarithmic decrement method . . . 136
5.29 shear strain calculation using particle velocity . . . 137
5.30 Shear strain of soil (GBV_m1_800mV) . . . 138
5.31 Shear strain of soil (GBV_m2_800mV) . . . 138
5.32 Shear strain of soil (GBV_m3_800mV) . . . 139
5.33 Soil damping for dry sand (Seed et al., 1986) . . . 139
5.34 Soil damping (an example from GBV_m2) . . . 140
5.35 Soil damping at VPNP3, VPNP2 and VPNP1 . . . 141
5.36 Soil damping ratio with depth in prototype scale . . . 142
5.37 Response ratio: centrifuge versus theory (GBV_m2) . . . 143
5.38 Response ratio: centrifuge versus theory (GBV_m3) . . . 144
5.39 Response ratio distribution (GBV_m2) . . . 145
5.40 Response ratio distribution (GBV_m3) . . . 145
5.41 Ratio of soil response and pile top with distance at three depths . . . 147

6.1 FLAC3D model used to simulate the centrifuge model (FLAC3D-m2) . . 156
6.2 Cross-section of the model FLAC3D-m2 at the ground surface . . . 157
6.3 Soil damping ratio with depth in prototype scale . . . 159

6.4 Air hammer MEMS accelerometers array postion (AHA position) 164
6.5 Duxseal elastic modulus used for numerical modelling calibration 165
6.6 Comparison of the centrifuge results and numerical modelling results from FLAC3D-m2 and FLAC3D-m3 (PCV) 168
6.7 Pile velocity response along depth from FLAC3D-m2 and FLAC3D-m3 . . 169
6.8 Comparison of the centrifuge results and numerical modelling results from FLAC3D-m2 (soil response near pile) 169
6.9 Comparison of the centrifuge results and numerical modelling results from FLAC3D-m2 (soil response distant to pile) 170
6.10 Comparison of the centrifuge results and numerical modelling results from FLAC3D-m3 (soil response near pile) 170
6.11 Comparison of the centrifuge results and numerical modelling results from FLAC3D-m3 (soil response distant to pile) 171
6.12 FLAC3D models used to investigate Duxseal effect (a) FLAC3D-FBM (b) FLAC3D-RBM 173
6.13 Vertical stress field in the soil calculated with and without side Duxseal . 175
6.14 K calculated with and without side Duxseal 175
6.15 Lateral displacement of the soil and the side Duxseal 177
6.16 FLAC3D model used to simulate the centrifuge model without side Duxseal (FLAC3D-m2-RBM) 178
6.17 Pile top and soil response under different boundary conditions (PCV and VPNP3) 179
6.18 Soil response under different boundary conditions (VPNP2 and VPNP1) . 180
6.19 Soil response under different boundary conditions (VPDP3 and VPDP2) . 180
6.20 FLAC3D model used to simulate the centrifuge model without Piezos in the soil 184
6.21 Comparison of numercal modelling results with and without Piezos in the soil (soil response near pile) 185
6.22 Comparison of numercal modelling results with and without Piezos in the soil (soil response distant to pile) 185

List of Tables

2.1 Geometric damping coefficients for various sources (Kim and Lee, 2000) . 10

3.1 Scaling factors for the centrifuge tests (Taylor, 1995) 41
3.2 Physical properties of HST95 Silica Congleton Sand (Lauder, 2010) 43
3.3 Instrumentation and equipment 47
3.4 Surcharge masses on the top of the pile 49
3.5 Transducers and DAQ system in centrifuge tests 51
3.6 Details of preliminary tests 54
3.7 Details of dead loads and input signal in preliminary tests 67
3.8 Details of dead loads and input signal in GBV (model scale) 74
3.9 Equations to calculate $\sigma'_{v,s}$ and $\sigma'_{h,s}$ in two stress state tests 83
3.10 Stresses applied in two types of stress state tests 83

4.1 Details of dead loads and input signal in preliminary tests 85
4.2 Shear wave velocity from air-hammer testing using different data lengths 89
4.3 Mean wave period and v_s from AHA-C1 before and after correction 91
4.4 Shear wave velocities from AHA and BE 95
4.5 v_s and K in the centrifuge with and without Duxseal 103

5.1 Dead load, pile top displacement and safety factor (Test GBV) 110
5.2 Dead load ratios and mean pile top and soil response ratios 124
5.3 Mean FRFs and response ratios 146

6.1 Constitutive model and material properties 159
6.2 Parameters used for parametric study 164
6.3 Lateral earth pressure coefficient obtained from the centrifuge ($K_{\mathrm{exp},i}$) and the FLAC3D modelling ($K_{\mathrm{num},i}$) and the RMS distance (D_{RMS}) . . . 165
6.4 Lateral earth pressure coefficient obtained from the centrifuge ($K_{\mathrm{exp},i}$) and the FLAC3D modelling ($K_{\mathrm{num},i}$) with and without side Duxseal . . . 173
6.5 Boundary conditions applied to the numerical models 178
6.6 RMS distances of the FRFs from two models with the same boundary condition 181
6.7 RMS distances of the FRFs from the same model with different boundary conditions 182
6.8 RMS distances of the FRFs used to evaluate the boundary effects 183

Chapter 1

Introduction

1.1 Background

The public transportation system makes great contributions to the normal running of a major city. Given the advantages of safety, reliability and efficiency, many cities are building new railway systems. In the UK, the £16 billion Crossrail Project is being built to improve transportation links. This huge project includes new twin tunnels passing under the central area of London (Kuo, 2010). In China, underground railways are currently being built in more than 20 major cities, and over 25 cities already have this transport system. In addition, at least 5 major cities already have a light railway system which runs mainly on the ground surface and viaducts. The planned underground railways will pass underneath hundreds of vibration-sensitive buildings, many of which are built on piled foundations. High speed train (HST) networks have been widely developed in Europe and Asia and have led to a significant increase in speed of passenger trains. Moreover, the desired shift of freight transport by road to rail will lead to higher axle loads and an increased number of freight trains. At present, railway systems have been developed in various forms, including trams, light railways, high speed railways, surface railways and underground railways, as shown in Figure 1.1.

The railway system plays an increasingly important role in densely populated cities due to its high transport efficiency. However, with the development of railway systems, there are many issues that need to be considered, such as railway-induced vibrations. Inevitably, railways built in the city pass near a number of buildings. The vibration generated by the railways could propagate through several pathways (see Figure 1.1): the soil-foundation-building pathway (P1), the tunnel-soil-foundation-building pathway (P2) and the piles-soil-foundation-building pathway (P3). Railway-induced vibration

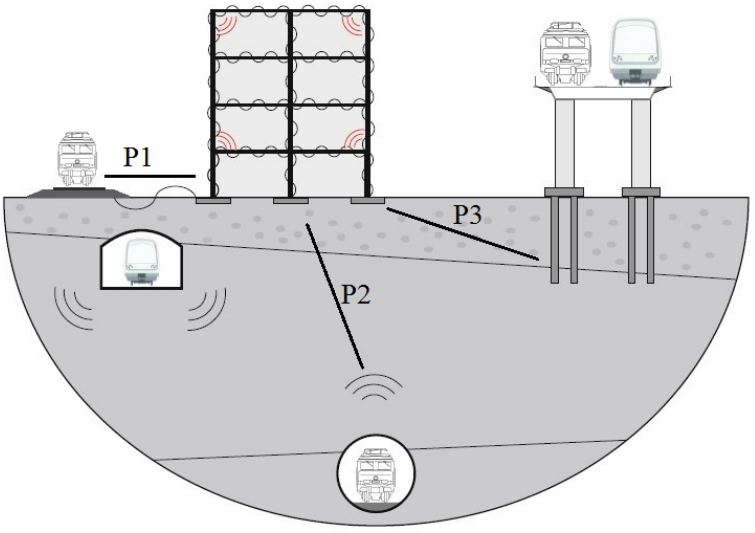


FIGURE 1.1: Ground-borne vibration generation, propagation and reception (Lombaert et al., 2015)

amplitudes are low compared with earthquake ground motions, however the effects of the ground-borne vibration cannot be neglected.

In a densely populated city, homes and offices are closer to sources of ground-borne vibration due to limited space. The train induced vibration frequency is within the range of 2 to 250 Hz (Thompson, 2009). Low frequency vibration (2 to 80 Hz) can be felt and perceived as mechanical vibration to the human body. Higher frequency vibration (16 to 250 Hz) can cause re-radiated or structure-borne noise through vibrating walls, floors and ceilings of a building, thus disturbing the occupants. As the living standard rises, people pay more attention to environmental disturbance and are less likely to tolerate noise and vibration.

In addition to humans, sensitive equipment or devices can also be affected by the low levels of ground-borne vibration generated by railway systems, particularly at universities in busy urban settings (e.g. the laboratories in the University of Nottingham adjacent to trams). In the 1980s, researchers at Bolt Beranek and Newman developed a set of generic vibration criteria (VC) curves to define classes of vibration-sensitive equipment to help the design process early on in a project (Nugent et al., 2012). Figure 1.2 shows the common family of VC curves, in which the vibration criteria are expressed in terms of vibration velocity (μin/s) with a frequency range of 4 Hz to 80 Hz. For this vibration criteria, the whole frequency range is split into several smaller frequency ranges, called the 1/3 Octave Frequency, as shown in Figure 1.2. Sensitive equipment can be impacted by vibrations with a minimum amplitude of about 0.003 mm/s.

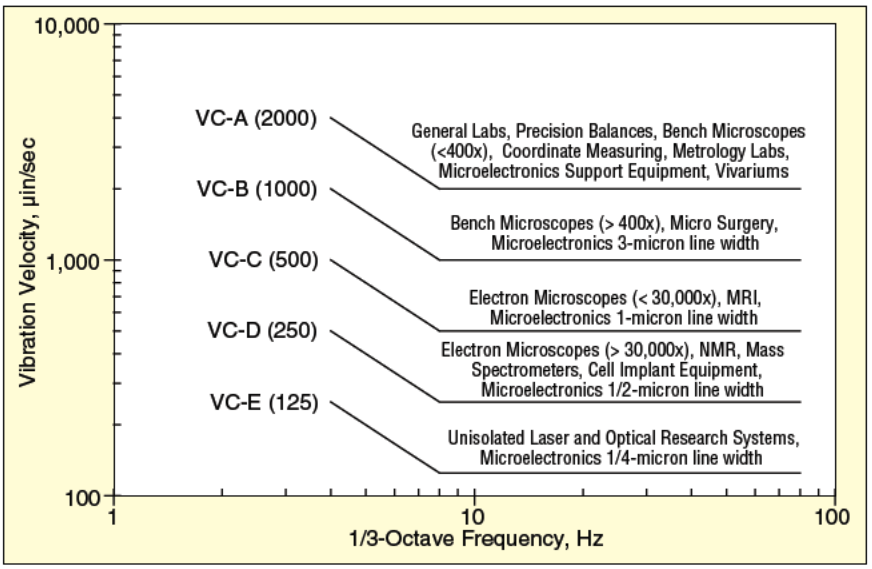


FIGURE 1.2: Generic vibration criteria (Nugent et al., 2012)

In addition, these dynamic forces could have adverse effects on the piles and buildings in the long term. The duration of the vibration is a main influence factor on structural response (BS, 2005), especially for those piles close to vibration sources, for example: piled buildings near underground railways. Guidance on the levels of ground-borne vibration which can cause damage or intrusion can be found in British Standards. BS (1992) recommends a conservative threshold for non-structural damage to residential property: a peak particle velocity (PPV) of 10 mm/s for intermittent vibration.

A lot of research has been conducted to understand the mechanisms of generation and propagation of the ground-borne vibration to design effective engineering approaches to reduce the effects. Of this research work, most are focused on the ground-borne vibration from the surface railways (P1) and underground railways (P2), as reviewed in Chapter 2. In terms of the ground-borne vibration generated from the trains running on a viaduct with piled foundations (P3), the mechanisms of vibration generation and propagation have not been fully understood, as well as the soil-pile interaction under dynamic loads. Therefore, this research work is primarily concerned with the transmission of vibration from the railways via a single friction pile, the soil-pile interface and the ground.

Geotechnical centrifuges have been used by several researchers to investigate small railway induced ground-borne vibration due to its advantage of realistically replicating the full scale stress field within a scaled model, thus correctly modelling the soil behaviour and the soil-structure interaction. However, some effects, such as boundary conditions, reflections and centrifuge induced interference, on the investigation of small vibrations have not been fully examined and understood. A detailed review of this technology is

provided in Chapter 2. Another focus of this project is to investigate these centrifuge modelling related effects.

1.2 Research aims and objectives

There are two aims of this research project. The first aim is to improve the understanding of the soil-pile interaction and ground-borne vibrations from the vertical oscillation of a single pile. The second aim is to provide insights into the use of a geotechnical centrifuge, as an experimental tool to study railway induced ground-borne vibration.

To pursue these aims, the following specific objectives were achieved:

- conduct a series of centrifuge tests to study centrifuge induced interference and implement measures to reduce the effects;
- examine the effect of vibration absorbing material (Duxseal) on stress field distribution in the centrifuge by performing a series of centrifuge based air hammer and triaxial based bender element tests;
- conduct a series of centrifuge tests to study the dead weight effects on the dynamic behaviour of a single pile, the dynamic soil-pile interaction, and dynamic soil response;
- conduct a series of centrifuge tests to study the propagation of vibrations in sand from a single pile;
- verify an empirical equation to evaluate the small strain shear modulus of dry sand with depth to provide parameters for numerical models by performing a series of triaxial based bender element tests;
- build and validate 3D numerical models in FLAC3D to investigate the ground-borne vibration caused by a vertically loaded pile;
- build 3D numerical models in FLAC3D to investigate the effects of piezoelectric accelerators and boundary conditions on the measured ground-borne vibration;

1.3 Thesis structure

Chapter 1 discusses the effects of the ground-borne vibration caused by railways, followed by the research aims this study attempts to achieve and the specific objectives.

Chapter 2 reviews the relevant literature, including the sources of the ground-borne vibration, the effects and properties of railway-induced vibration, the property of soil non-homogeneity, and the soil-pile interaction due to railway induced vibrations. The state of the art is summarized and the research interests of this study are discussed.

The experimental research methodology used to investigate the ground-borne vibration is summarized within Chapter 3. Centrifuge modelling of ground-borne vibration generated from a single pile in dry sand is detailed. The principles, scale factors, and scaling considerations for centrifuge tests are summarized first. All the transducers, devices, wave absorbing material and model soil are detailed. The vibration system, centrifuge model set-up and test procedure are presented. Chapter 3 also discusses several problems encountered in the preliminary tests and corresponding solutions that were developed to improve the tests. In addition, two methods to measure the shear wave velocity in a geotechnical centrifuge and triaxial cell (air hammer test and bender element test) are introduced.

Chapter 4 discusses test results from the air hammer test and bender element test. The methods used to determine the shear wave velocity of each soil layer are discussed and compared. The effects of the vibration absorbing material, Duxseal, on the lateral stress and soil stiffness are presented.

Chapter 5 presents the centrifuge test data. The dynamic pile behaviour, the soil-pile interaction and the ground-borne vibration propagation and attenuation in sand are discussed in detail in this chapter.

Chapter 6 presents the three-dimensional numerical models built in FLAC3D to simulate the centrifuge tests and to provide further insights into the problem of ground-borne vibration from the oscillation of a single pile. The effects of Duxseal and Piezoelectric accelerometers on the centrifuge measurements were examined by the numerical models.

Chapter 7 summarizes the overall conclusions and some recommendations for the future work.

Chapter 2

Literature Review

This chapter provides a review of the previous research relevant to this study. Section 2.1 summarizes the properties of railway induced ground-borne vibrations. Section 2.2 discusses the soil non-homogeneity properties which should be correctly modelled when studying railway induced ground-borne vibrations. Section 2.3 reviews the previous studies of soil-pile interaction and the modelling of railway induced ground-borne vibrations.

2.1 Problem of ground-borne vibration

As discussed in Chapter 1, to solve the problems caused by urban congestion and population growth, there is a growing need to construct railway networks in urban areas. The main reasons relate to advantages of safety, efficiency and reliability over alternative mass transportation options. However, railway systems can cause environmental issues due to the transit of vehicles, including railway noise and vibration. The problem of ground-borne vibration has gained increasing attention because people are becoming less likely to tolerate environmental disturbance and sensitive buildings and equipment could be significantly affected by nearby ground-borne vibrations. Therefore, it is necessary to investigate those effects and provide a better understanding of ground-borne vibrations. This section provides a review of railway induced vibration properties.

2.1.1 Properties of railway induced ground-borne vibration

2.1.1.1 Introduction

Ground-borne vibrations can be generated a variety of ways, including natural disasters, such as earthquakes and volcanic eruptions, and human activities, such as construction activities, the operation of underground railways and heavy trucks. In addition, some activities within the building itself may also generate vibrations, such as air conditioners and machines with rotating out-of-balance masses. In this study, sources of vibration from inside buildings and natural disasters are not taken into consideration. The primary source of ground-borne vibration considered in this study is railway related vibrations.

2.1.1.2 Excitation mechanisms

The railway-induced vibrations are generated by several mechanisms, such as the roughness or unevenness at the wheel-rail interface and impact excitation due to rail joints and wheel flats (Kouroussis et al., 2014). Roughness or unevenness at the wheel-rail interface results in a relative displacement between the wheel and the rail, which can propagate through the rail, sleepers and ballast and into the ground as vibration. The impact excitation due to rail joints and wheel flats can also produce ground-borne vibration. Parametric excitation is another important mechanism, which occurs because the stiffness of the support system of the train varies in space (e.g. the discrete nature of sleeper support, variations in the ballast stiffness and variations in the mechanical properties of the ground).

The dynamic load component, also known as the wheel load, is determined by train-track interaction. The dynamic load amplitude is determined by several factors: the weight of the locomotive or the carriages, the speed of the train and the condition of the rail. A comprehensive review of the wheel load can be found in Zhang et al. (2016) and Wu et al. (2015). Usually, the estimated dynamic load amplitude ranges from 100 kN to 200 kN. This is relatively small compared to the bearing capacity of a pile.

2.1.1.3 Wave propagation

The transmission of railway induced ground-borne vibration from sources through the surrounding medium into the concerned structures is related to wave propagation. Therefore, it is necessary to have a fundamental understanding of the propagation of vibrations through the soil.

A region of soil including the ground surface is a half-space medium in which vibrations propagate, and two major types of waves can be generated in such a half space by railways: body waves and surface waves (Lombaert et al., 2015). Body waves travel within the soil, including compression waves (P-waves) and shear waves (S-waves). Compression waves are longitudinal waves where the soil particles move in the same direction of wave propagation. Shear waves are transverse waves where the particles oscillate perpendicular to the direction of wave propagation. At the free surface of the soil half space, a surface wave, also known as Rayleigh wave, is generated by the interaction between P-waves and S-waves. Rayleigh waves combine both longitudinal and transverse motion to create an elliptic orbit motion in the same plane as the wave propagation. The wave speeds of the three types of waves depend solely on the elastic properties. P-waves travel fastest, followed by S-waves and then Rayleigh waves.

This study focuses on the transmission of vibration from railways via a single pile, the soil-pile interface and the ground. Therefore, wave fields generated by impact at the top of a single pile are detailed in this section and shown in Figure 2.1 (Kim and Lee, 2000). It should be noted that in addition to railways, some methods of installing piles can generate significant vibration: vibratory pile drivers and percussive piling hammers. An impact on the top of a friction pile could generate a P-wave which travels along the pile to the soil-pile interface at the toe of the pile. At this interface, part of the wave transmits into the soil and part is reflected. The incident compression waves propagate from the area of the pile toe, expanding outwards over a spherical wavefront. The vertical shear waves are generated by shaft friction and the shear waves expand around a conical surface. At the free surface of the soil half space, Rayleigh waves are generated by the interaction between reflected P-waves and advancing S-waves. Of those waves, S-waves carry most of the energy and soil particle motions are mostly in the vertical direction. This case could be regarded as a line source generating body waves and the travel distance can be estimated as a horizontal distance from the source.

2.1.1.4 Vibration attenuation

During the planning phases of a project, determining the expected magnitude of ground vibrations at different distances from a vibration source is important to evaluate the potential effects on surrounding structures. Ground vibrations can be quantified using three parameters: displacement, velocity or acceleration. Ground vibrations are typically measured by the maximum velocity at the ground surface (Cleary and Steward, 2016), and this is reported as Peak Particle Velocity (PPV). Vibrations generated from all kinds of sources attenuate during propagation in the ground. Vibration amplitude decreases with the increase in distance from the source. Soil generally has two types

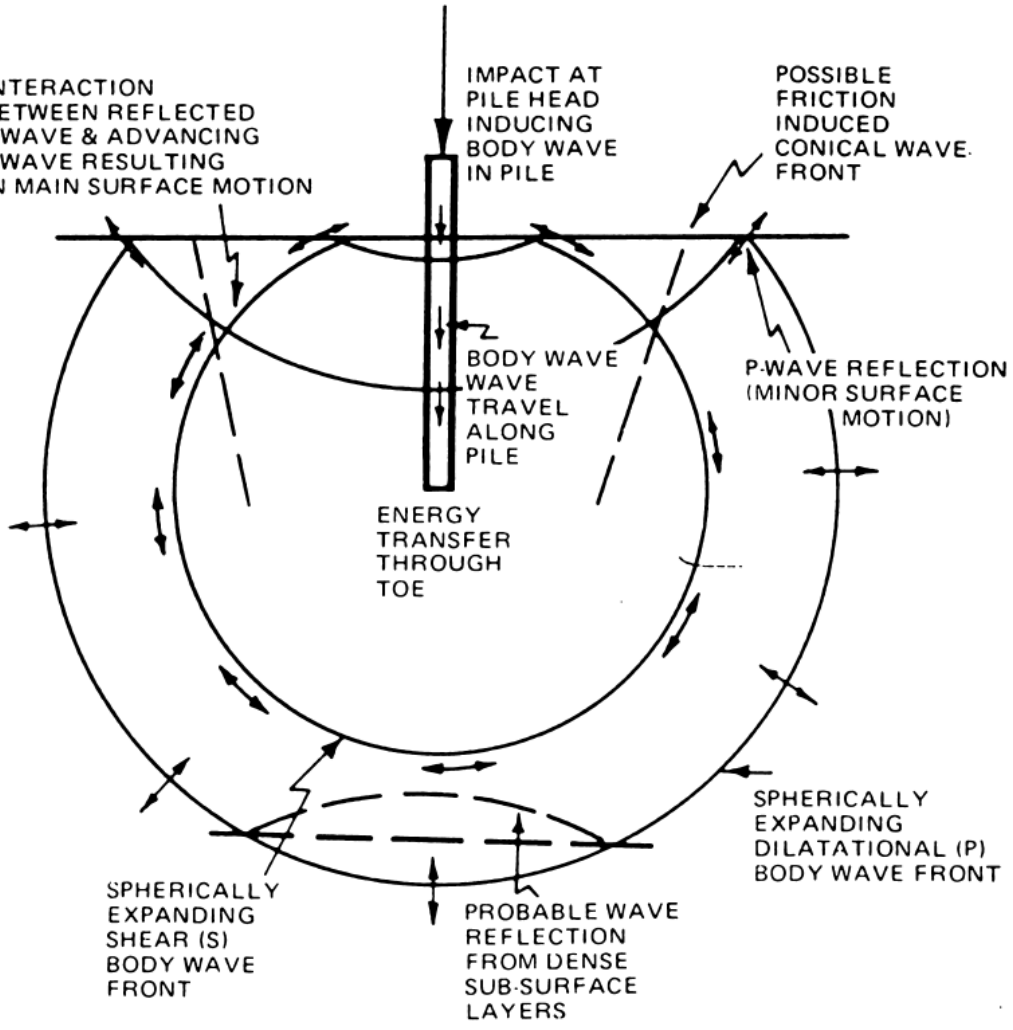


FIGURE 2.1: Wave fields generated by impact at the top of a single pile (Kim and Lee, 2000)

of damping: geometric damping and material damping, detailed in Section 2.2.3. Both geometric damping and material damping lead to the decay of vibration amplitude with distance, also known as vibration attenuation. The mechanism of vibration attenuation involves several factors, and it is difficult to predict. However, several semi-empirical equations have been developed to predict the vibration level at the ground surface at a given distance from a pile. Typically, the vibration prediction equations used to predict ground vibrations from pile driving use three different distances: horizontal distance, scaled-distance, and seismic distance (SD).

As shown in Figure 2.2, the horizontal distance is the distance from the vibration source to the location of interest along the horizontal direction. The scaled-distance is the horizontal distance divided by the square root of the input energy. The seismic distance is the distance from the pile toe to the point of interest.

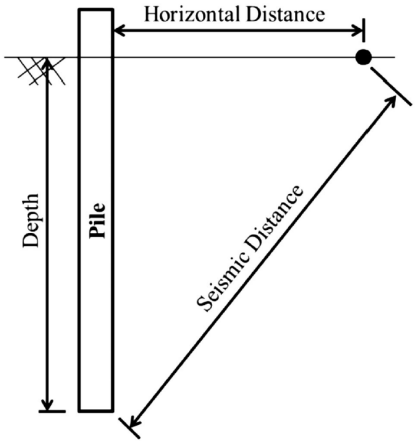


FIGURE 2.2: Illustration of horizontal distance, scaled-distance, and seismic distance (Cleary and Steward, 2016)

One of the early equations used to predict ground vibrations from construction activity is described by the following equation, reported by Kim and Lee (2000):

$$W_2 = W_1 \left(\frac{r_1}{r_2} \right)^n e^{-\alpha(r_2 - r_1)} \tag{2.1}$$

where W_1 and W_2 are vibration amplitudes at horizontal distances r_1 and r_2 from vibration source, n is a geometric damping coefficient and α is the material damping coefficient.

A geometric damping coefficient can be analytically determined through the assessment of source type, propagating wave type, and location, as shown in Table 2.1.

TABLE 2.1: Geometric damping coefficients for various sources (Kim and Lee, 2000)

Vibration sources	Location/ Type of source	Induced wave type	n
Short length and high speed train	Surface/Combination of point and infinite line	Body wave	1
Hydraulic compaction	Surface/Point	Surface wave	0.5
Long length and slow speed train	Surface/Infinite line	Body wave	1.0
In-depth blasting/ friction pile driving	In-depth/Point	Body wave	1.0

The material damping coefficient, α, can be represented by (Kim and Lee, 2000):

$$\alpha = \frac{\pi \eta f}{c} \tag{2.2}$$

where η is a damping loss factor, which is related to the hysteretic damping ratio of the soil and $\eta = 2D$ (D is the damping ratio defined by Equation 2.12 in Section 2.2.3.2), f is wave frequency, and c is wave velocity.

Cleary and Steward (2016) reported a simpler equation that incorporates both geometric and material damping into a single power function.

$$V = V_0 \left(\frac{D_0}{D} \right)^n \tag{2.3}$$

where V is the PPV at horizontal distance D, V_0 is the PPV at reference horizontal distance D_0 and n is a soil attenuation parameter that can be determined experimentally.

Wiss (1981) developed one commonly used equation that incorporates energy:

$$V = p \left(\frac{D}{\sqrt{W_t}} \right)^{-n} \tag{2.4}$$

where W_t is the energy of the source, V is the PPV at distance D, p is the intercept value of the PPV at a scaled distance $(D/(W_t)^{1/2})$ of one and n is a soil attenuation parameter that must be determined experimentally. The energy that is used can be either the rated energy of the hammer or the transferred energy.

2.1.1.5 Frequency range and vibration levels from railways

The frequency range and degree of railway-induced vibration are influenced by several factors: train type, train speed, car weight, ground conditions, rail properties and track conditions (Connolly et al., 2014, Tsuno et al., 2005). Some attempts have been made by field tests to assess the railway-induced vibration levels during the past decades by several researchers (Connolly et al., 2015, 2014, Kim and Lee, 2000, Kouroussis et al., 2014, Nugent et al., 2012, Wilson et al., 1983). Some features of the railway-induced vibration are summarizied as follows:

- The vertical shear strain within the soil tested by Connolly et al. (2014) is about 10^{-6} to 10^{-5}, as shown in Figure 2.3. Within this range, the non-linear behaviour of soil can be neglected. Therefore, linear elastic soil behaviour can be assumed in the investigation of railway-induced ground-borne vibration (Kouroussis et al., 2014).
- The dominant frequency range is more or less train speed dependent and increasing speeds could shift the excitation frequency to a higher spectrum (Kouroussis et al.,

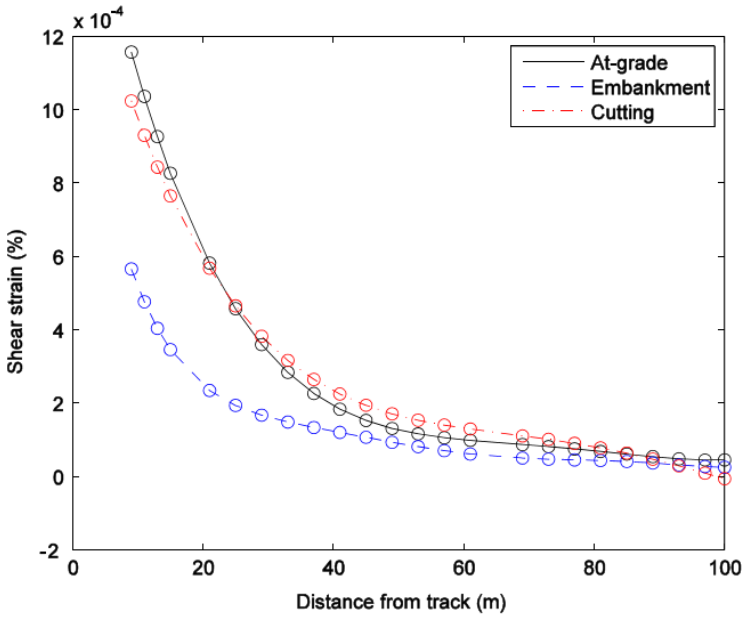


FIGURE 2.3: Vertical shear strain amplitude with distance from track (Connolly et al., 2014)

2014). Heavy freight trains at particular sites can generate low frequency ground-borne vibration between about 2 and 80 Hz. Higher frequency vibration from about 16 and 250 Hz is associated with surface railways and trains in tunnels in urban areas, such as underground railways, (Lombaert et al., 2015, Thompson, 2009). Measurements by Heckl et al. (1996) indicate that dominant frequency range of ground vibration from passenger trains and goods trains is in 40–100 Hz, where the wheel/track resonance lies.

- Acceleration level measured on the ground surface generated by the underground railway is mostly around 0.1 to 1 cm/s^2. The absolute peak values are usually at about 40 to 80 Hz (Tsuno et al., 2005).

- Kim and Lee (2000) measured the particle motions generated by a surface railway (trains travelling at speeds < 200 km/h) in three directions on the ground surface and at depth and observed: the energy generated in all three directions are nearly even which is consistent with the findings of Kouroussis et al. (2014); the vibration amplitude decreases from 10 cm/s on the sleeper to about 2 cm/s on the adjacent ground due to the effect of ballast and 0.2 cm/s at 13 m away from the sleeper; the vibration amplitude usually increases with the increase of the train speed; the frequency measured on the ground is widely distributed from 7 to 70 Hz. Nugent et al. (2012) also measured the ground surface vibrations and concluded that the greatest vibrations occurs between 6.3 and 40 Hz.

- Field measurements of high speed rail vibrations by Connolly et al. (2015, 2014) and Kouroussis et al. (2014) indicate that the vibrations decay rapidly from the track to about 40 m away from the track. The vibration amplitude decreases gradually from 40 m to about 80 m away from the track and then remains almost constant. The velocity amplitude is about 1.5 mm/s to 3.5 mm/s in the near field (distance from the track $<$ 15 m) and 0.5 mm/s to 1 mm/s in the far field (distance from the track $>$ 15 m). It can seen from Figure 2.3 that the vibration reduction rate over distance decreases with the travel distance away from the track. Equation 2.1 is used to calculate the vibration change rate, V_r, by taking the derivative of this vibration attenuation equation with respect to distance. The vibration change rate, see Equation 2.5, over distance from the track is shown in Figure 2.4. The negative values mean the vibration reduces with distance and the magnitude (absolute value) of the change rate means the vibration reduction rate. It can be seen from Figure 2.4 that the vibration change rate decreases quickly from 10 m to 40 m away from the track and then remains almost constant. This is consistent with the results presented in Figure 2.3.

$$V_r = -r_1\left(\frac{1}{r_2} + \frac{1}{r_2^2}\right)e^{-\alpha(r_2-r_1)} \tag{2.5}$$

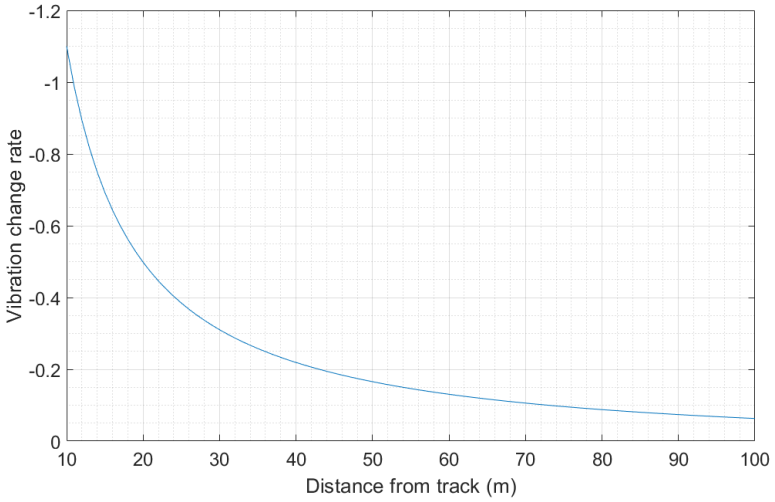


FIGURE 2.4: Vibration change rate with distance from track

2.1.2 Methods of reducing ground-borne vibration from railways

The vibration generated due to the interaction of the train and the track propagates through a variety of paths into the nearby receivers. This process means that there are a number of ways in which a ground-borne vibration problem can be addressed. The first mechanism is the reduction of the vibration sources (railways),

such as reducing rail and wheel surface irregularities by rail welding, rail grinding and wheel truing, the maintenance of the track/slab assembly. Barriers can be built to disrupt the transmission paths, such as open trenches, in-filled trenches, wave-impeding blocks (WIBs), and pile rows (Cai et al., 2009). Several methods can be employed to reduce the vibration levels of pile foundations, buildings and equipment, such as damping treatments, base isolation, or a box-in-box design. A wide range of detailed vibration reduction methods can be found in the thesis written by Kuo (2010).

2.2 Dynamic soil behaviour

2.2.1 Overview

Soil is the main medium in which railway-induced vibrations propagate so it is essential to model the soil properties accurately. Usually, to simplify the problem, researchers treat soil as a homogeneous half space. However, in reality soil properties change with the magnitude of shear strain developed within the soil and depth under the action of increasing confining stress due to gravity. Two of the most important parameters in soil dynamics are the shear modulus and the damping ratio. These features of the two parameters are discussed in this section in detail.

2.2.2 Shear modulus

2.2.2.1 Shear modulus under different strain levels

One feature of soil materials is that the soil properties vary under different shear strain levels. The shear strain levels were classified by Ishihara (1996) into four ranges: small, medium, large, and failure. Soil exhibits different characteristics and different models are used to analyse soil behaviour at different strain levels (shown in Figure 2.5). Nanda (2014) divided the soil stress-strain behaviour into three regions: very small strain, small strain and large strain, as shown in Figure 2.6. The three regions correspond to the first three ranges by Ishihara (1996). Considering that the strain levels in the soil caused by railway-induced vibration are relatively low (10^{-6} to 10^{-5}), small and medium strains are the focus of the following discussion.

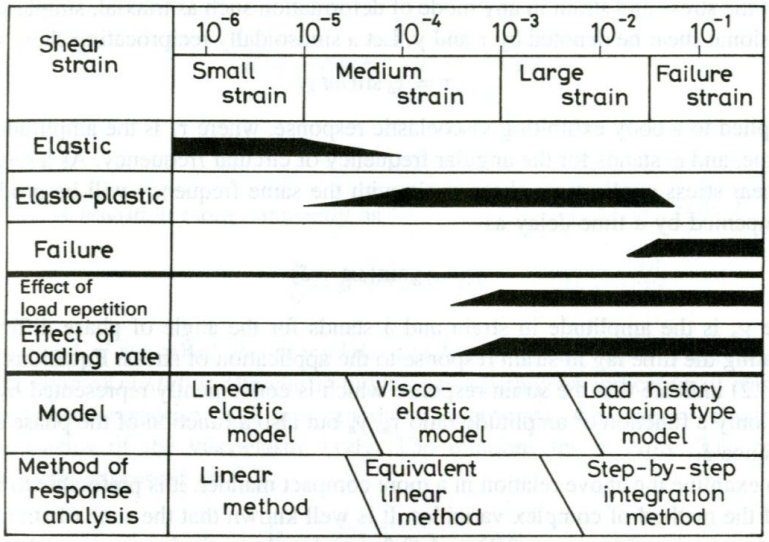


FIGURE 2.5: Soil characteristics and modelling methods for different strain levels (Ishihara, 1996)

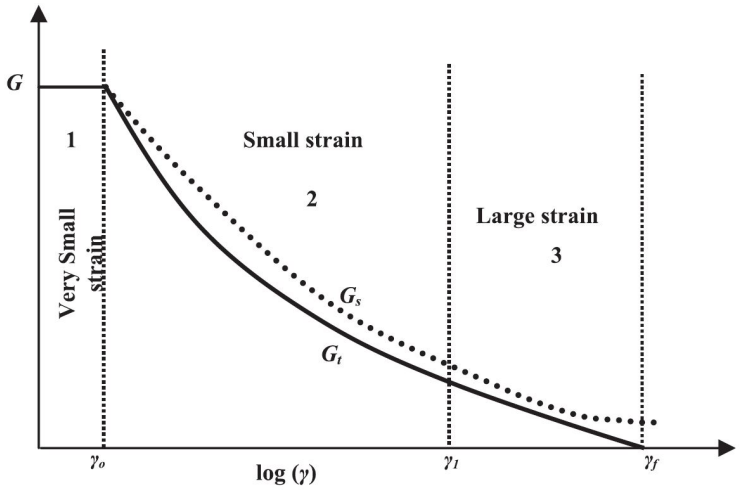


FIGURE 2.6: Soil stiffness degradation curve (Nanda, 2014)

– In terms of small range of strain, 10^{-6} to 10^{-5}, the soil behaviour is within the linear elastic range and the shear modulus is a key parameter to properly model the soil behaviour. Under the very small range of strain levels, shear modulus and damping remain essentially constant, and the shear modulus is at its maximum value (Rollins et al., 1998). The maximum shear modulus G_{max} is also known as the small strain shear modulus or dynamic shear modulus (G_0). A typical stress-strain relationship of soil, also known as a hysteresis loop for one cycle of loading, is shown in Figure 2.7. G_{max} is defined as the initial slope of the curve. Methods to determine G_{max} are discussed in the following sections.

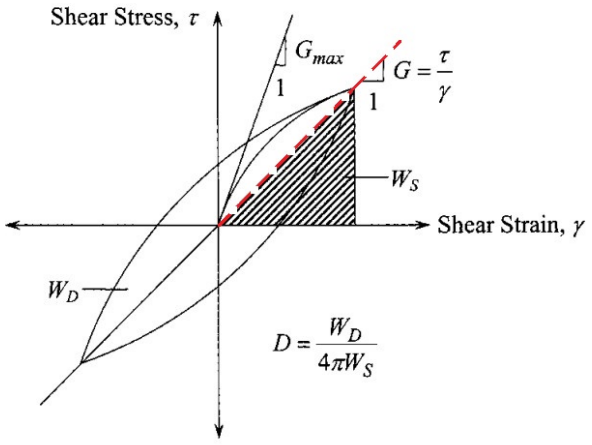


FIGURE 2.7: Hysteresis loop for one cycle of loading showing G_{max}, G, and D (Zhang et al., 2005)

– When the soil behaviour is within the medium range of strain, approximately below the level of 10^{-3}, the stress–strain relationship becomes nonlinear and the shear modulus tends to decrease rapidly as the shear strain increases (shown in Figure 2.6 and Figure 2.8). At medium strains, the secant shear modulus is used to represent the average soil stiffness. The secant shear modulus ($G = \tau/\gamma$) is defined as the slope of a line drawn from the origin of the shear stress-shear strain diagram and intersecting the curve at the point of interest (see the dashed red line in Figure 2.7).

– In the third region, soil stiffness continues decreasing slowly to a smaller value from a strain of γ_1 to the soil failure strain of γ_f. The corresponding failure shear stress is τ_m. The shear stress-strain behaviour is shown in Figure 2.8.

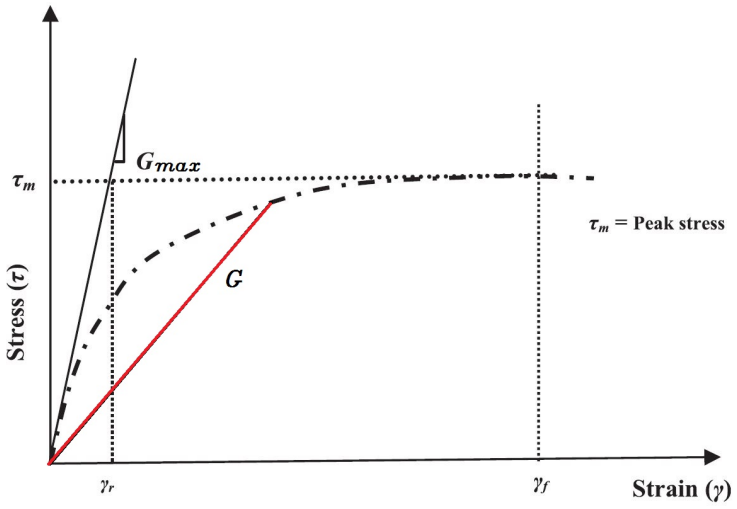


FIGURE 2.8: Soils stress-strain behaviour (Nanda, 2014)

2.2.2.2 Experiments to measure G_{max}

The maximum shear modulus is usually back-calculated from measured shear wave velocity (v_s) using Equation 2.6. Generally, resonance column, torsion and bender element tests are commonly used in the laboratory to determine G_{max}. In addition, several methods have been developed by centrifuge modellers to measure in-flight values of v_s, including bender elements (Brandenberg et al., 2006, Kim and Kim, 2010, Lee et al., 2014, 2012) and air hammers (Arulnathan, 2018, Ghosh, 2002). It should be noted that laboratory tests only measure G_{max} at discrete sample locations, which may not be representative of the entire soil profile (Shantz, 2012).

$$G_{max} = \rho v_s^2 \tag{2.6}$$

where ρ is soil density.

2.2.2.3 Empirical equations to determine G_{max}

In addition to experimental methods, empirical equations have been developed by many researchers to predict G_{max}. Parameters which can influence G_{max} are: mean effective stress (confining stress), void ratio and over consolidation ratio (Dobry and Vucetic, 1987, El-Sekelly et al., 2014). Of these parameters, the confining stress changes significantly with depth, resulting in significant shear modulus variation with depth.

It was found by El-Sekelly et al. (2014), Hardin (1965), Hardin and Drnevich (1972), Hardin and Richart (1963), Lee et al. (2012), Stokoe et al. (1985) that the following general equation can be used to predict G_{max} of normally consolidated dry sands.

$$G_{max} = BF(e)(\sigma_m^{'})^n \tag{2.7}$$

where G_{max} is the dynamic shear modulus (kPa), B is a constant, e is the void ratio of the soil, $F(e)$ is a function of e, $\sigma_m^{'}$ is the mean effective stress (kPa) and n is a constant.

The constant B in Equation 2.7 depends on the grain shape and the grain-size distribution. Hardin and Richart (1963) concluded from the resonant column tests on round grained Ottawa sand that the constants B and n can be taken as 7000 and 0.5, respectively. In addition, it was found by Hardin and Richart (1963) that the following expression for $F(e)$ can be used to calculate G_{max} for round-grained sand particles.

$$F(e) = \frac{(2.17 - e)^2}{1 + e} \tag{2.8}$$

The empirical equation developed by Hardin and Richart (1963) to estimate G_{max} of round-grained particles is presented below. This empirical equation is applicable for the round-grained sand used in this study (this sand is detailed in Chapter 3). This equation has been validated by Fu et al. (2004) in a series of centrifuge tests using the bender elements method .

$$G_{max} = 7000 \frac{(2.17 - e)^2}{1 + e} (\sigma_m^{'})^{0.5} \tag{2.9}$$

Another important parameter is the elastic modulus of soil which can be obtained from bender element tests by measuring the shear wave velocity (v_s) and the pressure wave velocity (v_p). The elastic modulus (E) can be calculated from the following equation:

$$E = 2G_0(1 + \nu) \tag{2.10}$$

where ν is Poisson$^{'}$s ratio. ν can be determined by using the equation below:

$$\nu = \frac{v_p^2 - 2v_s^2}{2(v_p^2 - v_s^2)} \tag{2.11}$$

It should be noted that one of the objectives in this study is to determine an appropriate equation to estimate soil parameters (G and E), which are used within the numerical models. The experimental results are used to the determine the equation to calculate G and E and results are presented in Chapter 4.

2.2.3 Soil material damping

2.2.3.1 Vibration damping

Damping is defined as the energy dissipation property of materials and structures that are subjected to time-variable loading. Many mechanisms have been proposed to explain the energy loss in a dynamic system (De Silva, 2007): geometric (radiation) damping, material (internal) damping, and structural damping (at joints and interfaces). In this study, the vibrations go through a series of media: piled foundations, soil-pile interface, and soil. Therefore all the damping types should be taken into consideration.

- Geometric (radiation) damping

Body waves travel radially outward from an oscillating source through a hemispherical wave front and Rayleigh waves propagate radially outward along a cylindrical wave front, see Figure 2.1. The volume of the medium (in which the waves propagate) increases with distance from the source. Therefore, the energy density of each wave decreases as the wave front propagates away from a source. This phenomenon is called geometric damping or radiation damping and it occurs even in perfectly elastic media. Note that the total amount of energy is neither lost nor converted to another form. It is just the density of the energy decreases due to the increasing volume. Geometric damping has the greatest effect on the Rayleigh waves (Ronald et al., 1994).

– Material (internal) damping

Internal damping of materials is associated with microstructure defects. Those defects include grain boundaries and impurities, thermoelastic effects caused by local temperature gradients because of non-uniform stresses, as in vibrating beams, eddy-current effects in ferromagnetic materials, dislocation motion in metals, and chain motion in polymers (De Silva, 2007). With respect to soil, material damping represents energy dissipation caused by friction between solid particles in the skeleton and by the relative motion between the soil skeleton and the pore fluid. However, these mechanisms are not yet fully understood and no single model can satisfactorily represent the internal damping characteristics of all materials. Nevertheless, there are two major types of internal damping which can be generally used in the modelling of soil-structure interaction: viscoelastic damping and hysteretic damping. It is worth noting that the latter term, hysteretic damping, is actually a misnomer because both damping types have hysteresis-loop effects (De Silva, 2007). A difference between the two types of damping is that stress and the internal damping force of a viscoelastic damping material depends on the strain rate and consequently on the frequency of motion, whereas hysteretic damping is rate independent.

– Structural damping (at joints and interfaces)

Structural damping is a result of rubbing friction due to relative motions between components that have common contact points. Energy dissipation can also be caused by impacting or intermittent contact at the joints in a mechanical system or structure. Energy dissipation caused by rubbing is usually represented by a Coulomb-frictional model. Energy dissipation caused by impacting should be determined from the coefficient of restitution of the two members that are in contact.

Interface damping, an important form of structural damping, is generated at the interfaces of two sliding surfaces. Therefore this form of damping is also called slip damping. Interface damping is governed by a variety of factors, such as contact forces, surface properties, geometry of moving parts and the relative velocity.

2.2.3.2 Soil damping and factors affecting soil damping ratio

Soil generally has two types of damping: geometric damping and material damping. Of them, the geometric damping is a reduction of the energy density due to the increasing volume. Material damping of soil is more complicated and will be discussed in detail in this section.

Similar to the shear modulus, soil damping is also strain dependent. Soil is not a perfectly elastic material even under small shear strain. Therefore, even at very low strain levels, there is some energy dissipation. At the small strain level, soil material damping is mostly frequency independent and of a hysteretic nature. The damping ratio at very low strain levels is referred to as the small-strain damping ratio, D_{min} (Zhang et al., 2005). Within the medium range of strain, the soil behaviour becomes viscoelastic. Soil damping ratio increases with increasing strain amplitude. The damping can be defined as functions of shear strain and the equivalent linear viscoelastic method can effectively model the problem in this strain range.

It was concluded by Hardin and Drnevich (1972) that the damping ratio of sand is influenced strongly by shear strain and effective principal stress ($\sigma_v^{'}$ in this study) while being slightly influenced by lateral earth pressure, K_0, void ratio, e, angle of friction, and degree of saturation. Figure 2.9 shows the effects of various factors on the damping ratio for sand. It can be seen from Figure 2.9 that damping is slightly affected by these factors at small strain ($< 10^{-3}$).

It can be seen from Figure 2.10 that the damping ratio of both saturated and dry sand tends to be significantly affected by $\sigma_v^{'}$ for all strain amplitudes. At the same shear strain, the damping ratio increases with decreasing $\sigma_v^{'}$, which indicates the damping ratio changes with depth like shear modulus.

Another factor which can affect the soil damping is the number of loading cycles. Hardin and Drnevich (1972) concluded that the number of cycles does not significantly affect damping by determining the damping for the first 5 cycles and then the number of cycles from 5 to 30. Bolton and Wilson (1990) conducted many laboratory tests to study the frequency effects on soil material damping. Lo Presti et al. (1997) have also investigated the effect of number of cycles and stress history on soil damping. They concluded that when the soil behaviour is in the

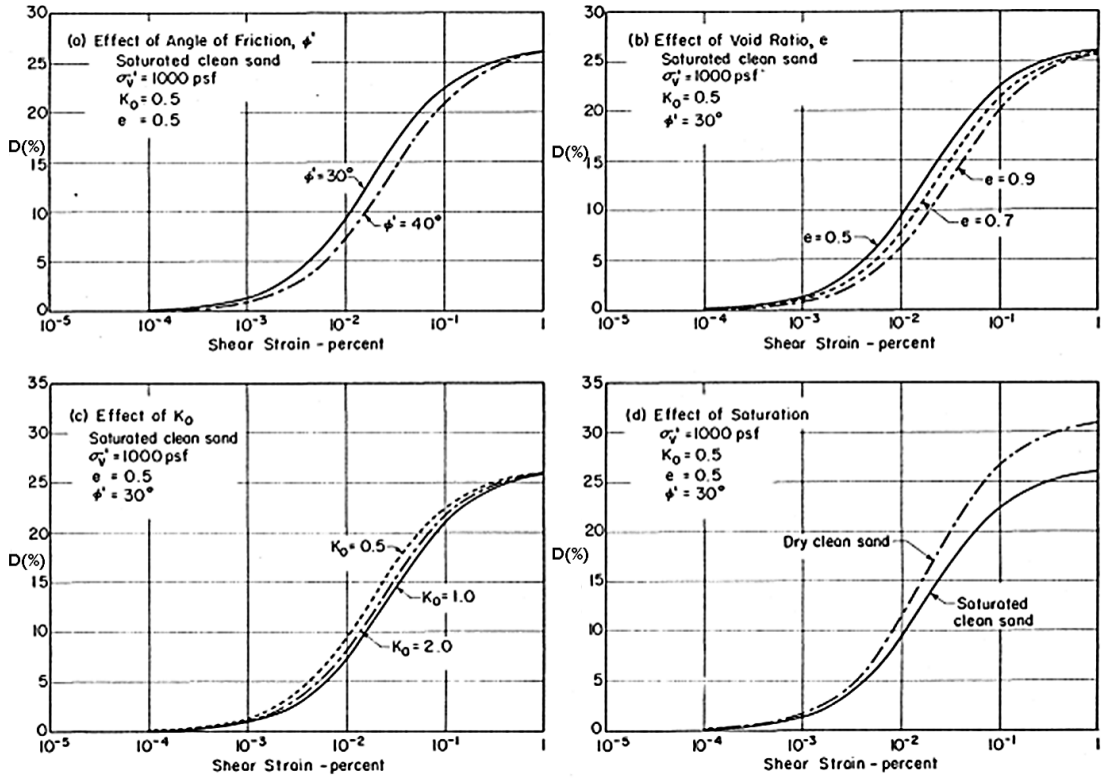


FIGURE 2.9: Factors affecting damping ratio of sand (Hardin and Drnevich, 1972)

small strain level, soil material damping is frequency independent and insensitive to number of loading cycles. Therefore, hysteretic damping can be used to represent soil damping for most ground borne vibration applications. The hysteretic damping ratio of soil can be calculated as (see Figure 2.7):

$$D = \frac{W_D}{4\pi W_S} \tag{2.12}$$

where W_D is energy dissipated in one cycle of loading, which equates to the area enclosed by the hysteresis loop, and W_S is the maximum strain energy stored during the cycle; W_S equals the area of the triangle, see Figure 2.7, bounded by a straight line defining the secant modulus (Ishihara, 1996).

2.2.4 Soil non-homogeneity

An important feature of soil properties (shear modulus and damping) is that they are affected by confining stress: values of soil properties change with depth because of increased stress. This feature is referred to as soil non-homogeneity in this study. Muravskii (1997) studied the surface vibration of a compressible half-space and compared the results from the homogeneous half-space model with the non-homogeneous model, and showed that soil non-homogeneity could significantly

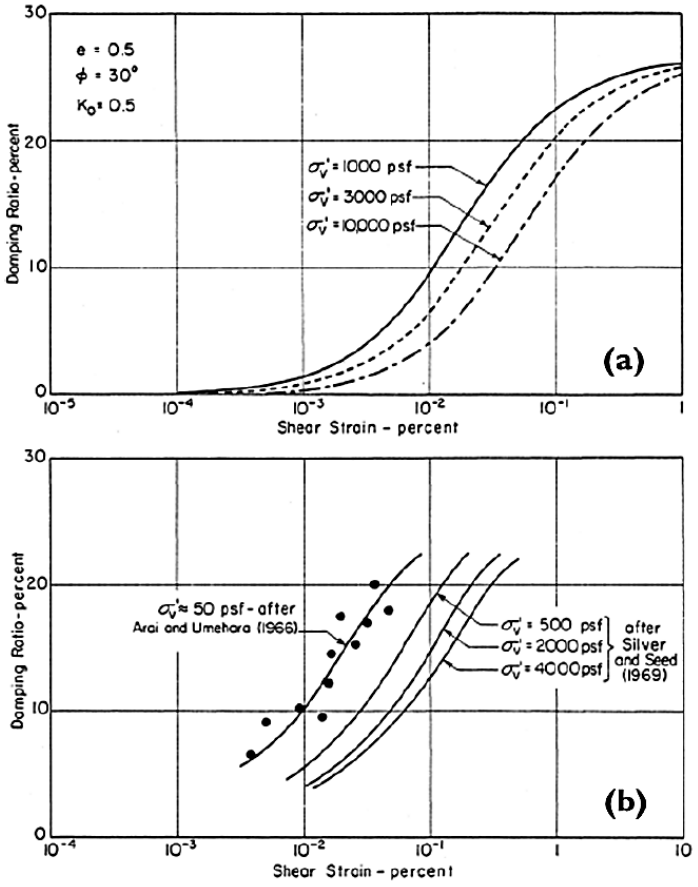


FIGURE 2.10: Confining pressure effects on damping ratio of (a) saturated sand and (b) dry sand (Hardin and Drnevich, 1972)

increase the soil response at large distances from the applied force. Rayhani and El Naggar (2007) used a geotechnical centrifuge to investigate the dynamic response of soft soils and seismic soil–structure interaction. It was found that the stiffness of the soil had a significant effect on the characteristics of the input motions and the overall behaviour of the structure, which implies the importance of correct modelling of soil properties.

More recently, Jones et al. (2012) investigated the effect of soil non-homogeneity on prediction uncertainties and inaccuracies of ground vibration. It was concluded that at least a 5 dB uncertainty range can be obtained when simulating ground vibration using simplified soil models (a homogeneous half-space). A numerical model was developed by Jian-hua et al. (2012) to study the dynamic response of pile groups embedded in layered poroelastic half space under axial harmonic loads. The results show that the soil non-homogeneity has a significant influence on the response of pile groups: for a half space with two soil layers, a thicker upper softer soil layer leads to a smaller real part impedance of the pile group, and the load transfer along the pile shaft is more gradual with the increasing thickness

of the upper softer soil layer. Yang (2012) studied soil non-homogeneity effects due to the changing of soil properties with depth on ground-borne vibration using geotechnical centrifuge modelling and numerical simulations. The wave velocities (corresponding to dynamic shear modulus and elastic modulus) and damping ratio profile of dry sand adopted by Yang (2012) are shown in Figure 2.11. It can be seen that both the elastic modulus and the shear modulus increase with depth in his model. A very high damping ratio of 10% was used throughout the top few meters. This was employed to achieve a good fit between experimental and numerical results. It was suggested by Yang (2012) that the variation of soil properties should be taken into account to obtain good estimates of the soil and structure behaviour. Therefore, this criterion, soil non-homogeneity, should be adopted in this study to get more accurate estimates of the soil and structure responses when studying ground-borne vibrations.

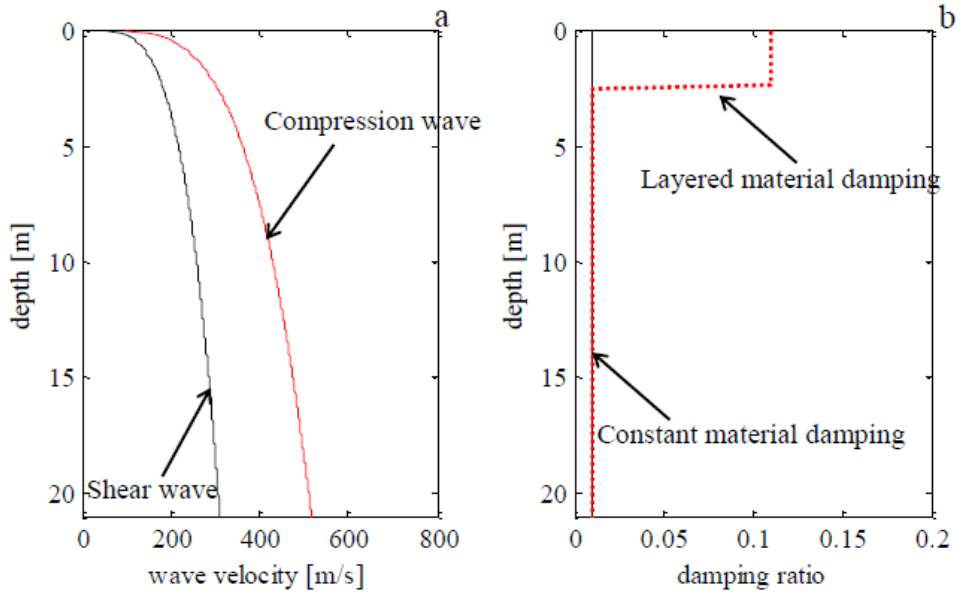


FIGURE 2.11: Distribution of (a) wave velocity and (b) damping ratio with depth (Yang, 2012)

2.3 Soil-pile interaction and ground borne vibration

2.3.1 Overview

This study is focused on the dynamic soil-pile interaction and the ground-borne vibrations induced by railways, which relates to trains running on piled structures (such as a viaduct, shown in Figure 2.12). This section discusses the literature of soil-pile interaction and the relevant modelling techniques applied in this research to investigate railway induced vibrations.

2.3.2 Soil-pile-interaction

Most of the previous studies conducted by researchers (Akgüner and Kirkit, 2012, Coyle and Reese, 1966, Lehane et al., 2005, Lehane and White, 2005, Liu et al., 2004, Nanda, 2014, Poulos and Davis, 1968, Viggiani, 2012, White and Bolton, 2004, Xu et al., 2018, Zhang et al., 2010) mainly focused on the load-displacement behaviour of the pile and the bearing capacity of piles and pile groups under static loading. Even though this study is focused on the dynamic soil-pile interaction, some aspects, such as soil-pile interface, from the previous research related to static soil-pile interaction are helpful to understand the dynamic soil-pile interaction.

A comprehensive review of the research work related to dynamic soil–pile interaction under axial dynamic loading, mainly focusing on load capacity and the cyclic and permanent deformations of the pile, can be found in Ai and Liu (2015), Holmquist and Matlock (1976), Jian-hua et al. (2012), Kim et al. (2004), Maeso et al. (2005), Reddy (1996), Wang et al. (2003), Zhou et al. (2009). It should be noted that the corresponding ground-borne vibration generated by applying harmonic loads onto the pile top was not analysed in these studies. Some of the most relevant literature for this research topic are discussed in this section.

Although there is a lot of research into the train-induced ground vibrations, most of them are aimed at the vibrations caused by trains moving on the ground surface or in underground tunnels, discussed in detail in the following section. To the best of the author's knowledge, only two attempts (Ju, 2007, Wu and Yang, 2004) have been made to analyse ground vibrations induced by trains moving on elevated bridges with piled foundations, which are reviewed herein. In addition, the research work related to the modelling of railway induced vibrations to piled foundations is also discussed to provide a comprehensive review.

2.3.2.1 Modelling of soil-pile interface

To investigate soil-pile interaction, it is necessary to understand how the loads transfer from the pile to the surrounding soil or rock and the interface property between the pile shaft and the surrounding soil. As shown in Figure 2.12, for end bearing piles built on rock or relatively dense sand, they obtain most of the carrying capacity from the resistance of the stratum at the toe of the pile (Viggiani, 2012). Friction piles built in soil derive the greater part of their bearing capacity by skin friction at the soil-pile interface and partly by normal stress at the toe of the pile. This study focuses on the friction piles where the interface friction is the main mechanism to transfer load to the soil. Therefore, the modelling of the

soil-pile interface is a key issue for investigating ground-borne vibrations generated from a pile.

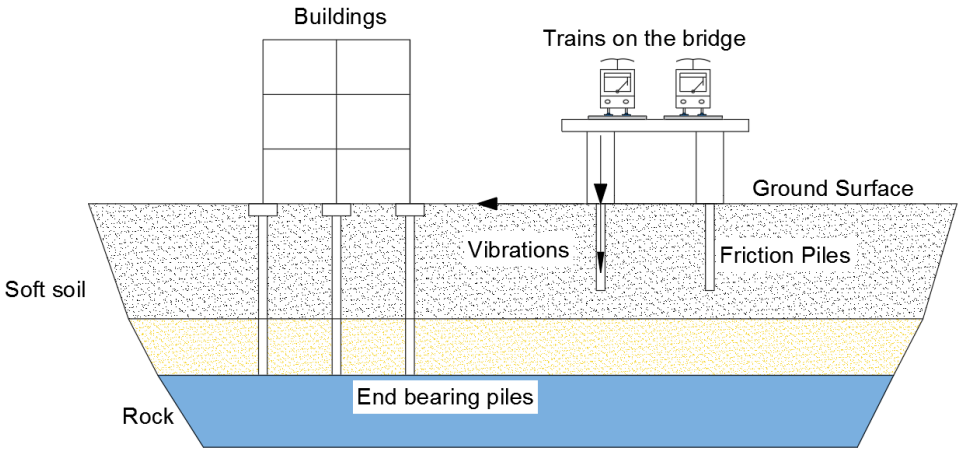


FIGURE 2.12: Friction piles and end bearing pile

In numerical or analytical modelling, two methods are usually used to model the soil-pile interface: a perfectly bonded interface (soil and pile experience same displacement at the interface) or a frictional interface (soil-pile slipping and gapping may occur). In reality, the interface should be modeled to incorporate slipping and gapping. However, if the problem to be analyzed is not dependent on slipping and gapping, researchers would treat the soil-pile interface as perfectly bonded interface to reduce computational time and modeling difficulties in some applications. The relative displacements at any soil-pile element are considered by Kuo (2010), Wang et al. (2008), Xu and Poulos (2001) as zero in elastic response range. Maeso et al. (2005) assumed that piles are fully bonded to the surrounding soil and pile–soil interaction effects are taken into consideration through equilibrium and compatibility conditions at interfaces in the three-dimensional boundary element model. Ai and Liu (2015) also assumed the pile was fully bonded to the surrounding soils in their analytical model to study the dynamic response of a single pile embedded in transversely isotropic multilayered soils under time-harmonic vertical loads.

In addition, Kim et al. (2004) developed a numerical model by coupling the finite element method (FEM) and the boundary element method (BEM) to calculate the pile response in the frequency domain under vertical harmonic loads applied at the pile cap in the layered half plane. The soil-pile interface was modelled using elastic springs, and the model was validated by comparing with a forced vibration test and the known experimental and analytical results. Some conclusions were drawn from this study: bigger spring stiffness increases the natural frequency and decreases the resonant amplitude, but the difference between the perfect bond interface and

biggest spring stiffness used in this numerical model is very small. This indicates perfectly bonded interface can be used to replicate fully rough interface in the numerical modelling and this would not result in significant differences.

In terms of physical modelling, the interface behaviour depends on the soil type, grain size distribution, interface material, surface roughness, normal stresses at the interface, and rate of shear displacement (Giraldo and Rayhani, 2013). Research has been conducted to investigate the soil-pile interface in sands experimentally. A series of constant normal load tests and constant normal stiffness tests carried out by Lehane et al. (2005) using aluminium interface with bonded sand showed that the ultimate interface friction angle is approximately equivalent to the ultimate friction angle of soil, which was also concluded by Dietz (2000). Therefore, for the soil-pile interface, a thin layer of sand can be stuck to the surface of the pile to achieve the soil-soil interface in the physical modelling. This can also eliminate the potential variations in interface friction angles (Lehane et al., 2005).

2.3.2.2 Behaviour of pile and soil under cyclic loading

Studies have been carried out to investigate the soil behaviour and the pile behaviour due to two-way cyclic loading: loading alternating between tension and compression. When a pile is subjected to upward loading, the loads transfer to the soil by surface friction. This could create strains in the soil and change the properties of the soil. Under two-way cyclic loading, the sand undergoes recoverable and irrecoverable displacement depending on the amplitude of cyclic stress. The failure of foundations is generally related to the irrecoverable strains in soils.

In addition, the response of soil may in turn affect the soil-pile interface as well as the behaviour of the pile, such as the shear stress distribution along the pile length and bearing capacity. During cyclic loading, the sand undergoes a reduction in volume with number of cycles until it reaches a maximum density. This leads to a drop in the normal stress applied to the pile shaft (Reddy, 1996). It was found by Holmquist and Matlock (1976) from a series of model tests on piles that considerable loss of skin friction could occur if the load magnitude was approximately 50% of the static pile capacity. Poulos (1981) conducted a further investigation on cyclic degradation of the soil and concluded: the ultimate bearing capacity and cyclic stiffness of the pile decrease with increasing load cycles N and increasing load magnitude; the effect of load cycles becomes more significant when the cyclic load level approaches 50% of the static ultimate load capacity. If the cyclic load magnitude is larger than about 50% of its ultimate pull-out load capacity, the irrecoverable displacement (accumulation of permanent displacement) increases fast and the pile loses its capacity within a limited load cycles. If the

cyclic load magnitude is less than about 30% of its ultimate pull-out load capacity, the irrecoverable displacement is small (Reddy, 1996). Therefore, it can be concluded that the amplitude of the dynamic load can significantly affect the soil-pile interaction.

2.3.2.3 Railway-induced vibration transmitted to or from piles

Some research has been conducted to investigate the railway-induced vibration transmitted to piled foundations. Jones et al. (2012) discussed the effects of six commonly used assumptions in modelling vibration from underground railways on prediction uncertainties and inaccuracies. Of them, piled foundations close to underground railways are often neglected in predictive models to simplify the problem. However, they play an important role in the transmission of ground-borne vibration. It was found by Jones et al. (2012) that the presence of piles can reduce the vertical vibration levels at the same location at most frequencies and increase the vibration levels within a small frequency range, which indicate that piles can reflect or absorb some of the vibrations.

Hussein et al. (2013) presented a 3D numerical model by coupling two sub-models: one for a building on pile foundation (beam elements used to model the building and its pile foundation) and another for a tunnel in an elastic half space (the well-known PiP model which is detailed in Section 2.3.3.1). This model was used to calculate vibration in a building caused by moving trains in a nearby underground tunnel within 1 Hz to 80 Hz. Results show that the vibration level at the pile top is almost the same as the center of the first storey. This study also highlights the importance of accounting for the dynamic effect of the building.

Rees and Gomez-Agustina (2018) predicted and assessed the vibration in a residential development with piled foundations proposed above the Piccadilly Line in London. The PiP model was used to predict the vibrations at the surface and at the bottom of pile foundations. Results showed that the vibration level at the top of the pile, generated by underground railways beneath the pile, is smaller than that at the bottom of the pile at most frequencies. The propagation of vibration into the piles and up through the superstructure was predicted using building transfer functions. It was found that tactile vibration within residential rooms is large enough for levels of structure-borne noise to cause annoyance.

Kuo (2010) developed several computational models to assess the vibration response of two different embedded structures: piled foundations and twin tunnels, subjected to ground-borne vibration generated by the underground railway. The

responses of a single pile and a pile group subjected to underground-railway induced vibration were calculated in the frequency range of interest of 1-80 Hz. The effect of neighbouring tunnels on ground-borne vibration was addressed. It was suggested that the piled-building model may be used to study the dynamic behaviour of a foundation with some form of excitation at the pile heads.

On the other hand, some researchers focused on the train induced vibrations from piled foundations. Wu and Yang (2004) developed a three dimensional semi-analytical model to study the ground vibrations induced by trains moving over an elevated bridge, as shown in Figure 2.13. Some assumptions were made to simplify the model: the train with a speed of v, was simplified as two sets of moving loads of equal intervals; the track system on the bridge was neglected; the superstructure of the elevated bridge was idealized as elastic beams; piers and pile foundations were idealized as rigid bodies; the half space ground is assumed to be a visco-elastic, homogeneous and isotropic soil. The force acting on every pier, which equals the force acting on each pile cap, was determined first, and then the vertical response of ground surface to the excitation of a single pier was calculated. The excitation was treated as a point load applied to the interface between the pile cap of each pier and the underlying soil based on the study by Wolf (1994). Finally, the total response of ground surface can be obtained by superimposing all the ground vibrations from all the piers. The effects of train speed, span length and elastic bearing on vertical vibration levels of the ground surface were examined. However, the proposed numerical model is suitable only for analysis of ground surface vibrations in the far field, responses in the interior of the ground were not investigated.

Multi-span simply supported bridges are usually built in cities for high-speed trains. High-speed trains can produce significant ground vibration, which may transmit through the bridge superstructure, bridge substructure (i.e. piles), half space soil and building foundation into near-by buildings and produce environmental problems. Ju (2007) developed a 3D time-domain finite element model to evaluate the vibration behaviour of buildings with slab foundations induced by high-speed trains passing along this type of bridge, shown in Figure 2.14. The accuracy of the finite element model was validated by comparing the results from the numerical modelling with the field measurements. It was found: the soil surface vibration without buildings is always larger than that on the first floor of the building; the vertical vibration level on each floor of the building is similar to the horizontal vibrations; vibrations in both directions do not always decrease with increasing floor number, sometimes increase with increasing floor number,

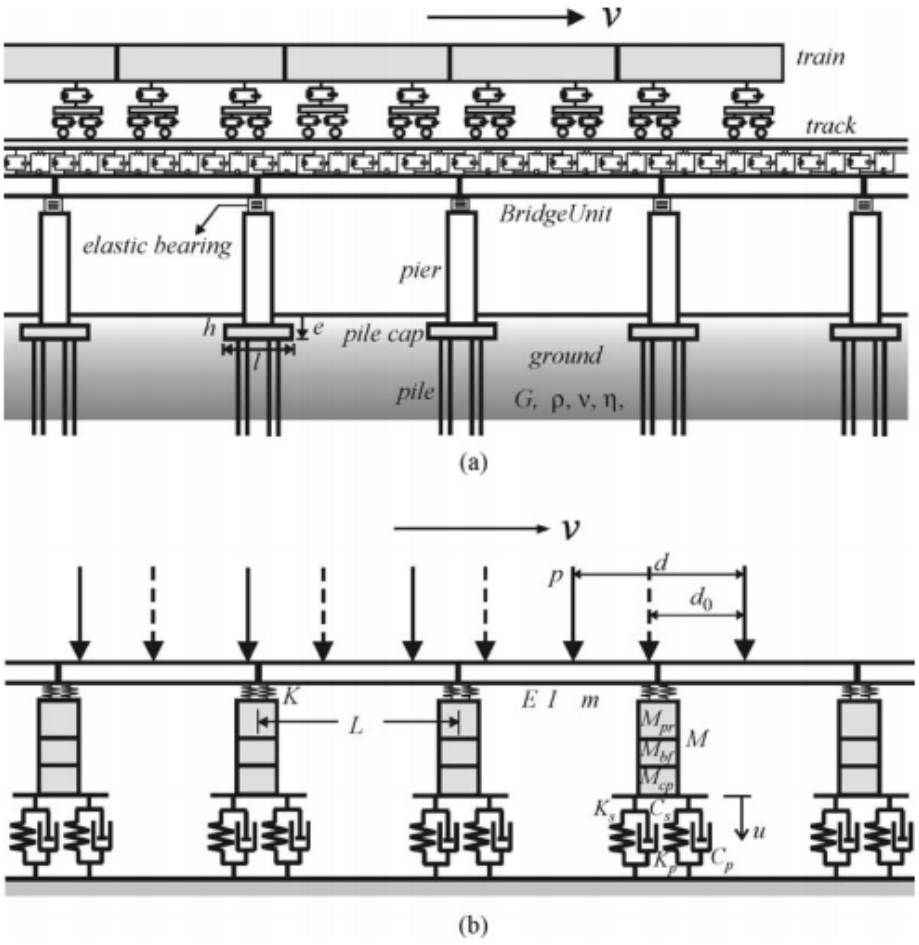


FIGURE 2.13: Model of trains moving over an elevated bridge: (a) schematic view (b) simplified model (Wu and Yang, 2004)

depending on the frequency. The efficiency of vibration isolation methods (retaining walls, pile foundations and soil improvement) were also investigated and it was found: pile foundations can only reduce vertical vibrations; retaining walls are not effective way to reduce vibrations in both directions; soil improvement method can effectively reduce both horizontal and vertical directions.

Therefore, it is found that studies have not been carried out concentrating on the understanding of dynamic soil-pile interaction and ground-borne vibrations due to small dynamic loads using experimental methods.

2.3.3 Modelling vibration from surface and underground railways

Ground-borne vibration transmitted from railways to the surrounding environment is a complicated problem which usually involves the vehicle, the track structure, tunnels, foundations, buildings and the soil. The best way to investigate this problem is to monitor the soil and structure behaviour by field testing. However,

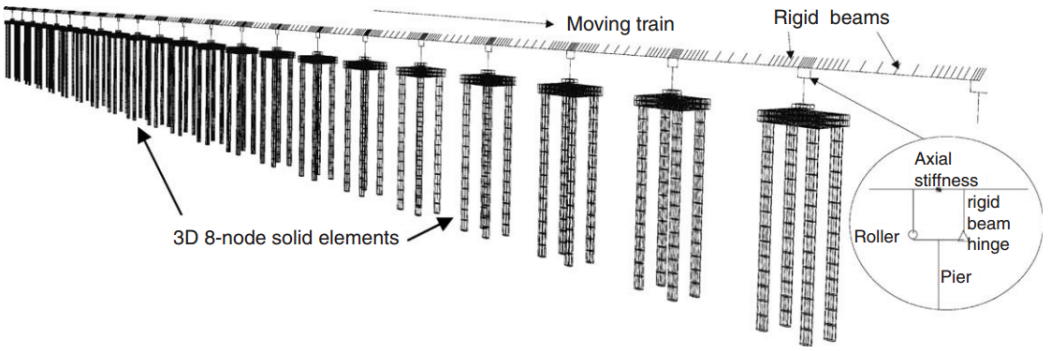


FIGURE 2.14: Finite element mesh of the multi-span bridge and piled foundations. (Ju, 2007)

field trials are difficult to be carried out because of high costs, required time, and safety reasons. Alternatively, analytical, numerical and experimental methods are usually employed by researchers to study this geotechnical problem.

As mentioned above, the modelling methods of vibrations from surface and underground railways are reviewed in this section to provide an overview of research work carried out on railway-induced ground-borne vibrations. Ideally, all of the components involved in the real situation should be accurately modelled to realistically replicate the real situation and obtain reliable results. However, for all the modelling techniques, assumptions and simplifications have to be made to approximate the real scenario. Another purpose of this section is to provide a summary of the advantages and disadvantages of each method.

2.3.3.1 Analytical and numerical methods

Analytical and numerical methods have been widely used to investigate ground-borne vibration from railways. This method can approximately model all the components involved in the problem. However, assumptions are usually made to simplify the problem.

Krylov (1995) was probably the first researcher who developed an analytical model to calculate the soil response led by a point load (with a low frequency range of 1 to 4 Hz) applied at the base of a tunnel. The model assumes that the soil wavelengths are larger than the tunnel diameter so the tunnel diameter effects can be neglected. Jones and Block (1996) developed an analytical model by taking the vehicle design, track structure and propagation characteristics of layered soil into consideration to study vibrations from freight trains in the range of 4 Hz to 30 Hz. It was found that the analytical model agreed well with measurement results within this frequency range.

In analytical models, the track or the tunnel are usually simplified as an infinite beam, and a beam on half-space elastic soil under impulse or moving loads is used to represent this problem. This method was adopted by Gupta and Degrande (2005) to investigate the beam response at different frequencies under an impulse load. In their model, a series of springs and dashpots were used to model the rail-pads between the beam and the soil. Metrikine and Vrouwenvelder (2000), Yuan et al. (2015) built 2D models by considering the tunnel as an embedded Euler beam to study the ground vibrations generated from a moving load inside a tunnel. To develop an analytical model to study the response of the floating slab track system under harmonic moving loads, Hussein and Hunt (2006) employed two infinite beams to model rail and floating slab, respectively. Each beam was supported by a series of springs and dashpots and the whole track was fixed on a rigid bed. Sheng et al. (1999b) also used two infinite beams to model the railway track. Different from the the model by Hussein and Hunt (2006), ballast was modelled by using a continuous layer comprised of a linear spring to support the beams and a number of homogeneous soil layers were involved to model the ground. The ground surface responses were calculated. Based on the earlier work by Sheng et al. (1999b), the ground-borne vibration under harmonic loads and moving non-harmonic loads was calculated by Sheng et al. (1999a). To investigate the effect of variation of moving load speed, speeds lower than, near to and larger than the Rayleigh wave velocity were used to excite the model. It was found by Sheng et al. (1999a) that a constant load with a speed smaller than any of the wave speeds of the ground produces a quasi-static response pattern in the ground surface away from the track. If moving load speeds are higher than the Rayleigh wave speed of the upper ground layer, propagating waves are produced.

The transmission of ground-borne vibration from railways is a 3D problem. Currently, 2D, 2.5D and 3D numerical models have been used to study this problem. Coupled finite element method-boundary element method (FEM-BEM) provides an approach to properly model the semi-infinite soil in numerical modelling. For the tunnel-soil interaction problem, a tunnel can be modelled by the FEM and the semi-infinite soil can be simulated by the BEM. This method was adopted by Jones et al. (2002) to build a 2D model to study the effects of lining in a tunnel on vibration propagation. Both vertical and horizontal responses of lined and unlined tunnels with a circular cross-section under vertical dynamic load were calculated. However, the accuracy of 2D underground railway induced vibration models is usually unacceptable due to a limitation: the longitudinal and circumferential modes can not be taken into account simultaneously (Hunt, 2001). This was confirmed by Andersen and Jones (2006) by comparing the results from FEM-BEM based

2D and 3D models. They concluded that 2D models were only capable of providing qualitative information to assess vibration isolating measures. Even though a 3D model takes much longer computational time, it is needed to obtain vibration transmission predictions and accurate estimates.

In order to reduce the computational time, a FEM-BEM based 2.5D model was proposed by (Sheng et al., 2006). This model assumes that the ground and built structures are homogeneous in the direction of the movement of the train. For example, Sheng et al. (2006) assumed that the cross-section of the tunnel-soil system is invariant along the tunnel axis as a compromise. This assumption allows the use of the discrete wave number method and the discretization is only made over the cross-section of the whole tunnel-soil system. Consequently, the total number of degrees of freedom and required computational time are both reduced compared with the corresponding 3D model. Sheng et al. (2006) employed this method to investigate vibrations from both surface and underground railways. Three engineering cases (surface vibration at a location with an embankment, the reduction of vibration affected by a wave impeding block and vibration from trains running in tunnels) were simulated by this method This method was found to be efficient in computational terms taking a few minutes for the computation of surface vibration cases and about 20 h for a spectrum result of a larger model for the tunnel case on a desktop personal computer. In addition, it was found that in the case of the embankment, the model was shown to be accurate by comparison with measurement data. In the 2.5D model developed by Jin et al. (2018), the tunnel lining and the track were modelled by solid and beam finite elements. A train consisting of several vehicles was represented by multi-body models. The predicted responses on the rail, tunnel and ground surface were compared with the field measurements obtained during train passages and had a good agreement with the measured vibration. In addition, a 2.5D numerical model, Pipe-in-Pipe (PiP) model, developed by Forrest and Hunt (2006b) was used to investigate the tunnel-soil dynamic interaction and wave propagation in soil. This model was based on the cylinder theory: two concentric pipes. The tunnel lining with a circular cross-section (the inner pipe) was surrounded by the full-space soil with an infinitely long cylindrical cavity (the outer pipe). The soil behaviour was described by elastic continuum theory. The tunnel and soil responses were calculated by applying point harmonic loads on the tunnel invert. The PiP model was then improved by Forrest and Hunt (2006a) and Hussein and Hunt (2007) who incorporated a floating slab track of the underground tunnel. Rikse et al. (2007) modified the PiP model by taking the rigid bedrock into account and assuming that the near-field tunnel displacement is not affected by the rigid rock. The PiP model

is very efficient with respect to computational time but it is only applicable to a tunnel with a circular cross-section. Gupta et al. (2007) developed two prediction models for calculating vibration from underground railways: the PiP model and the coupled periodic FEM–BEM model. The PiP model was used to validate the coupled periodic FE–BE model, and the free field responses due to a harmonic load in the tunnel obtained with both models were compared.

The finite difference method (FDM) is another numerical modelling approach which can be used to investigate the dynamic soil-structure interaction problem. An advantage of the finite difference method is it takes less computational time compared with FEM and BEM (Yang, 2012). A commercial finite difference program FLAC2D was employed by Aiello et al. (2008) to conduct a 2D numerical simulation of vibration propagation induced by underground railways. Measured velocity time histories were applied as input excitation to the model. The soil responses obtained from the numerical model were compared with the field testing results. The results indicate that the numerical simulations appear to underestimate the experimental values: the computed peak velocity amplitudes are approximately half the measured values at different locations. Nejati et al. (2012) used finite difference code to develop a numerical model for the underground railway induced vibrations. In this model, a force history was applied on the rail road and vibration of ground surface was obtained. It was concluded that the most important factors affecting the vibration level are axle weight, spacing of wheel axles and speed of train. Wolf (2003) developed a 3D numerical model using a similar finite difference program, FLAC3D, to study the low frequency range ground vibration effects on vibration sensitive research activities at the laboratories of the University of Washington (UW) Physics and Astronomy Building. Displacements were predicted from the 3D finite difference model due to train loads and bus loads near the building.

2.3.3.2 Physical modelling of vibration from railways

Physical modelling provides an alternative approach to investigate vibrations from railways, including scaled geotechnical centrifuge tests and 1 g model tests. Unlike the numerical methods presented in the above section, only a limited number of physical modelling studies have been performed to investigate the ground-borne vibration from railways, especially for the geotechnical centrifuge testing. In addition, the use of geotechnical centrifuge to study the small ground borne vibrations from railways has not been fully examined, as discussed below.

– Dynamic centrifuge modelling

Centrifuge tests have been successfully employed during the past decades concerning soil-structure interaction under both static and dynamic conditions. One disadvantage of the analytical or numerical methods is that the soil behaviour cannot be fully modelled, however this can be achieved by centrifuge modelling. As discussed in Section 2.2, soil behaviour is highly confining stress dependent, with parameters such as stiffness and damping being affected (soil non-homogeneity). The full scale stress field of a corresponding full scale model can be reasonably reproduced in a small scale centrifuge model, thus realistically replicating the soil behaviour. The principle of centrifuge modelling is that by using small scale models subjected to acceleration fields of magnitude many times Earth's gravity, the self-weight stress field of the full scale prototype situation is effectively reproduced. In this way, the behaviour of soils can be modelled effectively. Therefore, the soil-pile interaction can be correctly modelled in the tests. Centrifuge modelling has been used to investigate the ground borne vibration problem from railways, as reviewed in the following.

In reality, the load generated by a moving train is a moving dynamic load. In physical modelling, it is very hard to accurately model this moving dynamic load and it is usually simplified. Two commonly used methods in physical modelling to generate the excitation are the ball dropping system and the electromagnetic shaker. To apply vertical impact forces onto the soil surface in a geotechnical centrifuge, Luong (1994) developed a simple in-flight ball dropping system consisting of an electromagnet motor, a steel guide, a horizontal guide and a vertical guide. A steel ball pushed by the electromagnet motor travels along the horizontal guide until it drops into the vertical guide. The vertical guide can ensure the ball drops vertically, thus providing vertical impacts. Accelerometers were used to measure responses at the surface and interior of the soil. Luong concluded that a consistent vibration generation source can be obtained by this ball dropping system. Itoh et al. (2002) expanded the above single ball dropping system (SBDS) to a multiple ball dropping system (MBDS) to simulate not only an impact point load, but also a quasi-moving load caused by trains running through a viaduct with foundations. It was also concluded that the MBDS can provide a consistent and repeatable source of surface ground vibration.

In addition to the in-flight ball dropping system, the electromagnetic shaker has been used by several researchers to generate the excitation. Itoh et al. (2005) developed a centrifuge vibration testing system to simulate dynamic loading acting on shallow foundations. An exciter with a good control over frequency and force was used to model railway induced vibrations. However, the exciter was supported by two linear bearings and the two linear bearings were connected to the model

container directly. To investigate the attenuation characteristics, physical models with a clear ground condition and known boundary conditions have been employed by Tsuno et al. (2005) to deduce quantitative conclusions. They developed a centrifuge model test system to simulate the subway-induced vibration by applying harmonic loading to the invert of a model tunnel with a vibration shaker. Similarly, the shaker was also connected to the model container. This setup may affect the measured vibrations in the soil due to part of the vibration generated by the exciter can travel through the container into the soil.

Yang (2012) employed the centrifuge to study the soil non-homogeneity effects on the propagation of ground-borne vibration from a surface source and an underground tunnel by the use use of a small shaker to apply dynamic loads. A vibration absorbing material, Duxseal, was adopted to reduce reflections from boundaries. The tunnel and soil responses at different locations were measured by piezoelectric accelerometers. The test results indicate that in order to have accurate estimates of the soil dynamic response, it is important to consider the soil non-homogeneity effects. However, the effects of the piezoelectric accelerometers embedded in the soil have not been investigated. The density of this kind of transducer is quite different from the soil, and the measured dynamic soil response maybe affected by the transducers. In addition, the centrifuge induced noise and vibration was found by Yang (2012) to be significant for investigating ground-borne vibrations from railways within 1200 Hz. However, Yang did not extend the investigation to evaluate shaker induced noise and vibration levels.

Another problem is related to the reflections in a centrifuge model. In the prototype, vibrations (P-waves and S-waves) generated from an impact at the top of a single pile propagate within an infinite soil layer, see Figure 2.1. However, centrifuge models have to be enclosed within a container with finite boundaries, which may lead to more or less boundary effects. One important influence caused by the boundaries is the energy and waves reflection from the end-walls. At some frequencies, the incident waves and the reflection waves are in phase and this can amplify the soil response, which is also known as constructive interference. To the contrary, destructive interference can appear at other frequencies if waves are out of phase, which leads to a decrease of soil response.

To minimise the boundary effects, rigid containers with absorbing boundaries are usually employed (Zeng and Schofield, 1996). Conventional absorbing materials used by centrifuge modellers during the past decades are foam (Ha et al., 2011), sponge rubber (Itoh et al., 2005), and Duxseal (oil based industrial fill material). The effectiveness of the foam and the sponge rubber has not been carefully examined (Yang, 2012). Duxseal is a multi-purpose sealing and caulking rubber

compound with adhesion and shape retention properties. It has a heavy, putty-like consistency and will remain pliable and useable even when exposed to air over a long period of time. Duxseal was previously used by several researchers (Cheney et al., 1990, Cilingir, 2009, Pak and Guzina, 1995, Steedman et al., 1990, Yang, 2011) and it was found by Madabhushi (1991) that it can absorb about 65% of the incident P-waves and 60% of the incident S-waves.

However, Zeng and Schofield (1996) pointed out that the use of Duxseal can cause other problems, as friction and stiffness of Duxseal are difficult to determine in standard laboratory tests. In addition, the consistent numerical model is also difficult to find for such a boundary condition so that theoretical and numerical analysis on the model testing results can be carried out. Moreover, the lateral stiffness of the container should be high enough to maintain zero lateral strain condition (initial K_0 condition) during the spin-up of a centrifuge (Zeng and Schofield, 1996). To the contrary, Duxseal is relatively soft and it may deform laterally under high horizontal stress during the spin-up of a centrifuge. As a consequence, the initial K_0 condition can not be satisfied. Pak and Guzina (1995) mentioned the compressible Duxeal can lead to some undesirable deformations, causing small failure wedges around the side of the soil model. As discussed above, soil properties are highly confining stress dependent. The lateral deformation of Duxseal can lead to the decrease of soil stiffness, thus affecting the accuracy of experimental results.

As discussed above, rigid boundaries can reflect vibrations from the walls of the container and reflections would superimpose with the incident waves, thus affecting the measured vibration level in the soil. However, a 1 g experiment conducted by Thusyanthan and Madabhushi (2003) indicated the reflections off the rigid tub walls was insignificant. Hajialilue-Bonab et al. (2007) developed a centrifuge testing system to perform horizontally impacted piles tests and they found that reflected waves by the sides of the rigid soil container had no evident or quantifiable influence on the response of piles. Therefore, whether rigid boundary or absorbing boundary is more appropriate for investigating small ground-borne vibrations in the centrifuge still remains a problem.

– 1 g scaled model tests

Unlike centrifuge testing, 1 g scaled model tests are not capable of correctly modelling soil-structure interaction since these type of model tests cannot reproduce the same stresses that are experienced in the prototype (Itoh et al., 2005). However, they can still provide some qualitative results. Some 1 g experimental studies are reviewed to provide an overview of the relevant research work.

Thusyanthan and Madabhushi (2003) presented a 1 g experimental study on the vibration absorbing properties of tunnels with different lining materials. Surface vibrations generated by impulsive and vibratory loadings were measured by miniature accelerometers mounted onto two model tunnels made of brass and plastic (PCV). The testing results indicate that the energy transferred into the plastic tunnel is higher than that transferred into the brass one. Conclusion highlights the importance of selecting proper tunnel lining material with the lowest vibration absorbing capability to reduce vibration levels experienced by the tunnels. A 1:100 scaled tunnel-soil model at 1 g was used by Tamura et al. (1975) to study deformation of the model tunnel made of Perspex under dynamic excitation generated by a small shaker placed in the tunnel. Asano and Kumagai (1978) employed a 1 g experiment with a scale factor of 1:19.2 to study the propagation characteristics of ground-borne vibrations generated from a railway tunnel buried in a loam layer. Two excitation mechanisms, a dropping ball system and a small vibration shaker, were used to apply impulse loading and harmonic excitation, respectively. Yang et al. (2018) conducted a series of 1 g scaled model tests to explore the dynamic characteristics of segmental tunnel linings and study the effects of joints between tunnel segments on tunnel and soil responses.

2.4 Concluding remarks

Ground borne vibrations caused by surface railways, underground railways and elevated railways can propagate through tunnels, the soil, and piles into nearby buildings, thus affecting nearby sensitive buildings built on piled foundations and sensitive lab equipment and generate annoyances to nearby residents. The vibration generated by the railways should therefore not be neglected.

Currently, most of the research that has been carried out focuses on the train-induced ground vibration caused by surface or underground railways. Ground vibrations induced by trains moving on elevated bridges with pile foundations has not been fully examined and understood experimentally and numerically. This study will focus on the soil-pile interaction due to railway-induced vibrations taking advantage of the geotechnical centrifuge as the main research method. It should be noted that ground-borne vibrations from the railways on elevated bridges with pile foundations are actually a consequence of dynamic wheel loads with a certain amplitude, typically 100 kN to 200 kN, within a certain frequency range, typically 2 Hz to 100 Hz, as reviewed in Section 2.1.1. The dynamic loads transfer through the bridge-pier-pile pathway into the ground though the soil-pile interaction. It is not realistic to model all the components within a centrifuge test. In this study,

a simplified model which consists of a dead weight (representing all the components above the pile), a single pile and the soil will be used. A single pile is the fundamental unit for understanding the dynamic response of piled foundations. In this study, dynamic centrifuge tests will be conducted to study the dynamic pile behaviour, the soil-pile interaction and ground-borne vibration propagation characteristics generated from the vertical oscillation of a single pile in sand. An electromagnetic shaker is used to generate vertical excitations to the top of a single pile. The electromagnetic shaker can provide dynamic loads within the frequency range of interest of this study to represent the dynamic wheel loads. In addition, some numerical simulations will be performed to investigate this issue.

The employment of the centrifuge is attributed to its great advantage of reproducing the full scale stress field within a small scaled model, thus correctly modelling soil behaviour and soil-pile interface characteristics. However, the boundary effect in a centrifuge model on vibration propagation and measured results in the centrifuge have not been fully understood. In addition to the boundary effect, centrifuge and shaker induced vibrations, embedded piezoelectric accelerometers can also affect the measured vibration results in a centrifuge. These issues are also studied in this research project.

Chapter 3

Research Methodology

3.1 Introduction

In this study, physical modelling and numerical methods have been used to achieve the research objectives. Centrifuge tests were conducted to investigate railway-induced vibrations by applying dynamic loads to the top of a single pile. To obtain required parameters and calibrate the numerical model, centrifuge based air hammer testing and triaxial based bender element testing were carried out to measure the shear modulus and the elastic modulus of the soil. The experimental methodologies for the centrifuge and laboratory testing are detailed in this chapter. A FLAC3D model was built using parameters obtained from the air hammer and bender element tests. The numerical analysis procedure is provided in Chapter 6, along with a comparison of results between numerical and physical model tests.

3.2 Centrifuge modelling and model development

In this research project, physical modelling using a geotechnical centrifuge was carried out using the Nottingham Centre for Geomechanics (NCG) beam centrifuge at the University of Nottingham. This centrifuge is 4 m in diameter and has a payload capacity of 500 kg at 1.7 m nominal radius up to 100 g.

This section outlines the scaling factors for the centrifuge tests, stress field error in the centrifuge, the model soil, devices, transducers, excitation methods and input signals utilized in these tests. It also details the model preparation process and the test specifications. Some model development results are presented in this section. Some preliminary tests (Pre_01, Pre_02, Pre_03 and Pre_04) were conducted to examine the electric noise and physical vibrations (interference) from the operation of the centrifuge and the shaker and several approaches were employed to reduce

the interference. In addition, the determination of appropriate input signal used to apply dynamic loads is investigated by the preliminary tests and discussed in this section. A summary of formal ground borne vibration tests (Test GBV) is presented in the last section.

3.2.1 Scaling factors for centrifuge modelling

The scaling laws are required to convert results from small scale centrifuge tests into prototype scale equivalents. Most of the important scaling laws were derived by Schofield (1980) using a dimensional analysis method by considering the same stress-strain relationship at homologous points.

The principle of centrifuge modelling is that the dimensions (length L) of a prototype model are decreased by a factor of N whilst the gravitational acceleration is increased by the same scale $N_{gravity}$ by taking advantage of the centrifugal acceleration. The following relations for length L between the model and the prototype is obtained:

$$L_{model} = L_{prototype}/N \tag{3.1}$$

where L_{model} is length in model scale, $L_{prototype}$ is length in prototype scale.

At homologous points, the stresses in both prototype and model ($\sigma_{prototype}$ and σ_{model}) are the same, and the following equation can be written for the stress level at a depth $L_{prototype}$ in a soil medium with a density of ρ:

$$\sigma_{model} = \sigma_{prototype} = L_{model}\rho g N_{gravity} = L_{prototype}\rho g \tag{3.2}$$

where g is the gravitational acceleration of the Earth.

The scaling factor for $N_{gravity}$ can be obtained by substituting Equation 3.1 into Equation 3.2:

$$N_{gravity} = N \tag{3.3}$$

In this study, the scaling factors for length and gravitational acceleration (N and $N_{gravity}$) were 60. The fundamental scaling factors for the main parameters are summarised in Table 3.1. More discussion about the centrifuge scale and details on centrifuge modelling can be found in Taylor (1995) and Iai et al. (2005). Model scale data should be divided by the appropriate scaling factor in Table 3.1 to obtain prototype scale equivalents.

TABLE 3.1: Scaling factors for the centrifuge tests (Taylor, 1995)

Parameter	Scaling factor (Model/prototype)	Value
Length	1/N	1/60
Strain	1/1	1
Velocity	1/1	1
Frequency	N/1	60
Acceleration	N/1	60
Dynamic time	1/N	1/60
Stress	1/1	1
Axial force	$1/N^2$	1/3600

3.2.2 Stress error

Generally, the gravitational acceleration of the Earth (g) is uniform for the practical range of soil depths encountered in civil engineering and this leads to a linear vertical stress field for a soil with a constant density ρ, see Equation 3.5. However, the inertial gravitational acceleration field provided by a centrifuge varies with depth due to the inertial acceleration (a) being a function of radius: $a = \omega^2 r$. ω is the angular rotational speed of the centrifuge; for geotechnical centrifuge testing, ω can be calculated using:

$$Ng = \omega^2 R_e \tag{3.4}$$

where R_e is the effective centrifuge radius for the model where the inertial acceleration is N times Earth's gravity g.

Equation 3.4 suggests the inertial acceleration above and below R_e is smaller and larger than Ng, respectively. The non-linear variation of vertical stress in the centrifuge produces a slight stress error. The vertical stresses in the prototype, σ_{vp}, and the corresponding centrifuge model, σ_{vm}, are given in Equation 3.5 and Equation 3.6, respectively. The vertical stress distributions in prototype and model are plotted against corresponding depth to make a direct comparison, shown in Figure 3.1.

$$\sigma_{vp} = \rho g h_p = \rho g N h_m \tag{3.5}$$

$$\sigma_{vm} = \int_0^{h_m} \rho a dz = \int_0^{h_m} \rho \omega^2 (R_t + z) dz = \rho \omega^2 h_m (R_t + \frac{h_m}{2}) \tag{3.6}$$

where h_p and h_m denote the soil depth in prototype and centrifuge model, respectively. R_t is the radius from the central axis of the centrifuge to the top of the soil model.

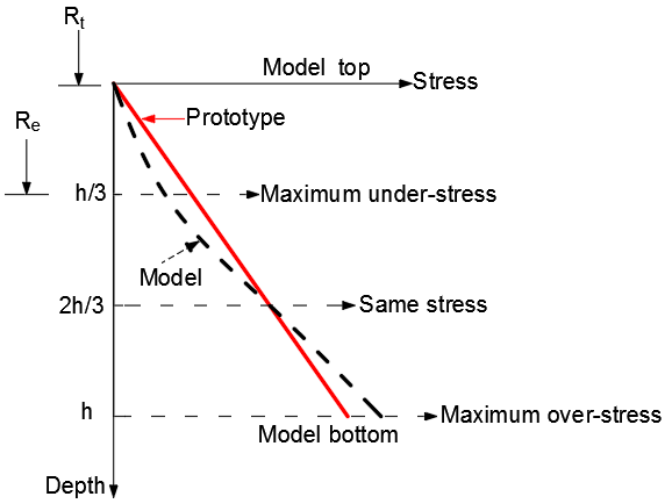


FIGURE 3.1: Comparison of stress variation with depth in prototype and its corresponding model

It can be seen from Figure 3.1 that the stresses in the upper section of the model are usually underestimated and stresses nearer the bottom are overestimated compared to the prototype. To minimize the stress error, Taylor (1995) suggests that the maximum under-stress ratio equals the maximum over-stress ratio. Consequently, the effective centrifuge radius, R_e in Equation 3.4, can be calculated and it should be measured from the central axis to one-third the model depth. This leads to the exact correspondence in stress between prototype and model at two-thirds the model depth as in Figure 3.1.

In this study, the correct modelling of soil-pile interaction is the most significant aspect. Therefore, R_e adopted in this study was from the central axis to one-third the embedded pile length. This leads to the exact correspondence in stress at two-thirds the pile length, instead of the model depth. The resulting values of R_t, R_e and ω were 1.505 m, 1.591 m and 183 rpm (revolutions per minute) in the centrifuge tests.

3.2.3 Soil material and sample preparation

Dry Congleton sand (HST95 silica sand from Minerals Marketing) was chosen to simulate the soil medium. The Congleton sand is very fine and uniformly rounded and has been used by Al-Defae (2013) to study the performance of slopes under seismic action. The basic parameters of the Congleton sand (Lauder, 2010) are

shown in Table 3.2. The Congleton sand was air pluviated, shown in Figure 3.2, using a sieve with a mesh size of 1.5 mm to obtain a relative density of approximately 85% during the centrifuge model preparation. The drop height adopted was 67 cm in this study. Six soil density calibration tests were conducted to make sure the variability of relative density of the soil was within +/- 2% of the stated relative density. The sand density is 1739.25 kg/m^3.

TABLE 3.2: Physical properties of HST95 Silica Congleton Sand (Lauder, 2010)

Parameter	Value
Specific Gravity (G_s)	2.63
D_{10}	0.09 mm
D_{30}	0.12 mm
D_{60}	0.17 mm
D_{90}	0.195 mm
Maximum dry unit weight ($\gamma_{d,min}$)	17.58 kN/m^3
Minimum dry unit weight ($\gamma_{d,max}$)	14.59 kN/m^3
Maximum Void Ratio (e_{max})	0.769
Minimum Void Ratio (e_{min})	0.467



FIGURE 3.2: Air pluviated soil

3.2.4 Scaling considerations for piles in sand and pile preparation

According to the scaling laws, the typical particle size of the model soil should be N times smaller than the prototype soil. This criterion suggests a remarkable reduction in particle size used in the centrifuge model. Therefore, sand would be used to model gravel and clay would be utilized to model sand. However, the behaviours of the three soils are different in many ways. Usually, the prototype soil is used in the centrifuge test. The ratio of the pile diameter to the soil particle size may alter the soil-pile interaction mechanisms as well as boundary effects. Therefore the below suggestions should be taken into consideration.

In order to reduce the scale effect, the minimum ratio of pile diameter (D_p) to average grain size (D_{50}) should be 20 suggested by Bolton et al. (1999) based on pile driving tests. To minimize the boundary effects on the pile tip resistance, the ratio of distance between the wall and the pile to the pile diameter should be greater than 10 (Bolton et al., 1999). To correctly model the pile shaft friction, it was suggested that the ratio D_p/D_{50} should be greater than 100 by Garnier (1998) and 50 by Fioravante (2002). In addition, it was concluded that if the ratio of model diameter to average grain size is larger than 35, no significant problem would be caused by sand particle size effect (Liu, 2009).

This study focuses on medium sized (480 mm in diameter) friction piles at prototype scale installed in dry sand and investigate the transmission of ground borne vibrations generated from a single pile. An 8 mm diameter aluminium rod was manufactured to model the pile. The ratio of pile diameter to average grain size (D_{50}) was approximately 50 to minimise the scale effect. A thin layer of Congleton sand was stuck to the surface of the pile to achieve a rough soil-pile interface. The rough interface was used to remove uncertainty for the numerical simulation of the tests, detailed in Section 6. The pile with an embedded length of 280 mm in model scale (16.8 m in prototype scale) was placed by burial at the predetermined location (see Figure 3.3) to avoid the need to quantify the effects of pile installation on the stress distribution near the pile (Lehane et al., 2005). This methodology simulates bored piles (Chiang and Lee, 2007). As shown in Figure 3.3, a frame, composed of two threaded bolts and two aluminium angles, was used to hold the pile approximately in the center of the container prior to sand pouring. The pile cap was machined with two threaded holes to allow attachment of the pile cap. The sand pouring and pile installation process is detailed in Section 3.2.9.

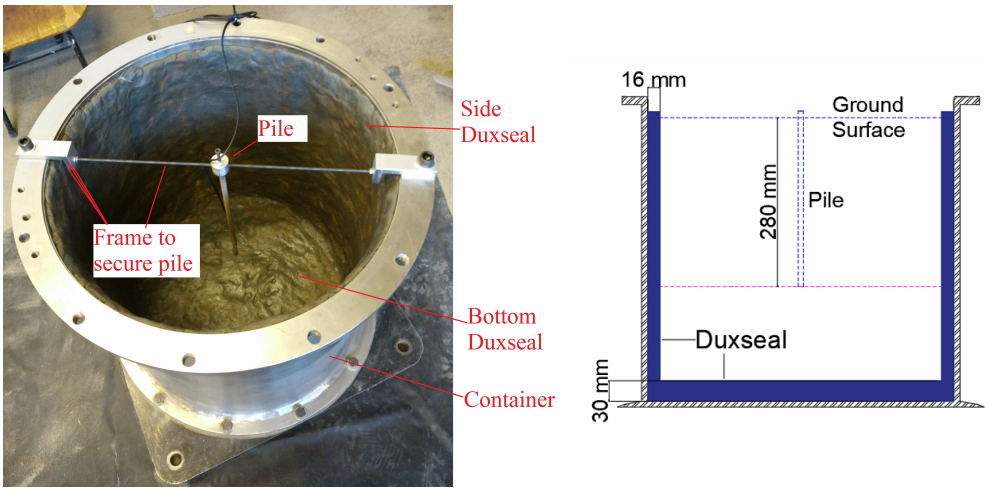


FIGURE 3.3: Side and bottom Duxseal

3.2.5 Model container and boundary effects

In this study, a cylindrical steel container with a diameter of 500 mm and a depth of 500 mm was used and Duxseal was used to absorb the vibrations at the model container boundaries. Duxseal has been previously used by several researchers (Cheney et al., 1990, Cilingir, 2009, Madabhushi, 1991, Pak and Guzina, 1995, Steedman et al., 1990, Yang, 2011) and the properties of Duxseal has been detailed in Section 2.3.3.2. In terms of the boundary effects on pile resistance, the ratio between the distance of the pile from the wall and the pile diameter was 28, which is above the minimum values discussed in Section 3.2.4. The steel container was lined with Duxseal to a thickness of 16 mm along the sides and a thickness of 30 mm on the bottom of the container, as shown in Figure 3.3. To investigate the effects of Duxeal on the initial K_0 condition, air hammer tests and bender element tests were carried out to back-calculate the lateral earth pressure coefficient in the centrifuge model. Air hammer tests and bender element tests are detailed in Section 3.3 and testing results are presented in Chapter 4.

3.2.6 Excitation method

There are two types of excitation methods typically used in the centrifuge: impact test and shaker test. The method adopted in the centrifuge testing must meet the requirements listed as follows:

- Limited by the space in the centrifuge, the excitation source must be small, easy to be installed and controlled;
- Frequency range of train induced vibration is between about 2 and 250 Hz (Lombaert et al., 2015). The frequency range of interest in

this study is 2 to 120 Hz in prototype scale. The reason for selecting this frequency range is that the piezoelectric accelerometers, used to measure the vibrations, have a linear response between 10 Hz and 7 kHz and deviate by up to 10% between 7 kHz and 10 kHz. Therefore, care should be taken when using the instruments to monitor any higher harmonics experienced during the tests. According to the scaling law, the corresponding frequency range of interest is 120 Hz to 7200 Hz in model scale. The excitation source must provide such a wide excitation frequency range;

- The input signal parameters: frequency, amplitude and duration must be easy to be controlled and maintained in every test to make sure the test is repeatable.

The impact test is implemented by using a ball dropping system such as that tested by Luong (1994) and Itoh et al. (2002). The impact force is applied onto the structure by releasing the ball from a certain height above the model foundation (an aluminium cylinder). When the ball hits the foundation, the applied force is measured by the dynamic load cell inside the foundation. The force amplitude is controlled by the ball weight and the drop height. The excitation frequency range is controlled by the stiffness of the ball and the foundation. The stiffer the ball and the foundation, the wider the excitation frequency range is obtained. As mentioned, this study aimed to achieve frequencies above 7000 Hz, which is very difficult to achieve using a ball dropping system.

Another commonly used excitation device is electromagnetic shakers. An electromagnetic shaker mainly consists of a heavy magnet, a coil and an armature. The armature is the movable component of the shaker and it is usually connected to the test structure with a stinger (a threaded bolt in this study). The basic working principle of an electromagnetic shaker is electromagnetic induction: when the electric current passes through the coil, a force is generated. The force magnitude is proportional to the current and the magnetic flux density and its direction varies with the direction of electric current. The armature moves cyclically with the electric current to excite the structure. The dynamic force amplitude is controlled with a signal generator by changing the input voltage amplitude. In addition, the signal generator is capable of generating a wide range of frequencies. Therefore, good control over both force amplitude and frequency range can be achieved by the electromagnetic shakers. A disadvantage of a shaker test is the response of the structure may be significantly affected by the mass and stiffness of the shaker attachment. The stinger, as mentioned above, is used to uncouple the effects of

the shaker from the structure. However, the effects cannot be ignored. An impact test does not have influences on the response of the structure.

As discussed above, each method has its own advantages and disadvantages. Even though the shaker attachment can affect the response of the structure (the pile in this study), this research is mainly concerned with ground borne vibrations. Therefore, the shaker test was chosen to excite the model in this study, considering the requirements mentioned before. In this study, a small shaker which is able to provide sinusoidal forces from 5 to 13000 Hz was employed. A signal was first generated by the signal generator which was then amplified by a power amplifier before sending to the electromagnetic shaker. A 6 mm diameter threaded steel rod (stinger) was used to connect the armature to a dynamic load cell to excite the pile, as shown in Figure 3.5. A sinusoidal signal was used in the tests and the input signal parameters (frequency, amplitude and duration) are detailed in Section 3.2.12.

3.2.7 Instrumentation and equipment specifications

3.2.7.1 Loading system and transducers

The instrumentation and equipment used to study ground borne vibrations can be divided into two main categories: loading system and transducers. The loading system included the loading frame, the dead load and the dynamic load applied to the top of the pile. The transducers had three main types: force, displacement and acceleration. Table 3.3 details the instrumentation and equipment used and the corresponding roles in the tests.

TABLE 3.3: Instrumentation and equipment

Category		Instrumentation/ equipment	Role
Loading system	Dead load	76.2 mm diameter brass discs	Provide surcharge mass
	Dynamic load	Shaker	Impose vibrations
Transducers	Force	Static load cell	Measure dead load on pile
		Dynamic load cell	Measure dynamic load on pile
	Displacement	LVDT-G	Measure displacement of ground surface (G) and pile (P)
		LVDT-P	
	Acceleration	Piezoelectric accelerometer	Measure vibrations of pile and ground

3.2.7.2 Model layout

The model layout and specified locations of the instrumentation and equipment are provided in Figure 3.4. Two 10 g piezoelectric accelerometers were attached vertically and horizontally (PCV and PCH, respectively) on the top of the pile (Figure 3.4). PCH was mounted horizontally to evaluate the rocking of the pile. To monitor the progression of the vertical waves within the soil generated by the oscillating load on the pile during the main tests, an array of piezoelectric accelerometers were used (Figure 3.4). Six 5 g piezoelectric accelerometers (VPNP3, VPDP3, VPNP2, VPDP2, VPNP1, VPDP1) were buried in the soil at 20%, 60% and 100% of the embedded depth of the pile (L) to monitor the vertical vibrations. Two 5 g piezoelectric accelerometers (HPNP3, HPNP1) were used to monitor the horizontal vibrations within the soil. The DJB Instruments A/120 piezoelectric accelerometers were denoted as 'Piezos' in this thesis. The Congleton sand (model soil) was glued to the surface of Piezos to ensure good coupling between Piezos and the soil.

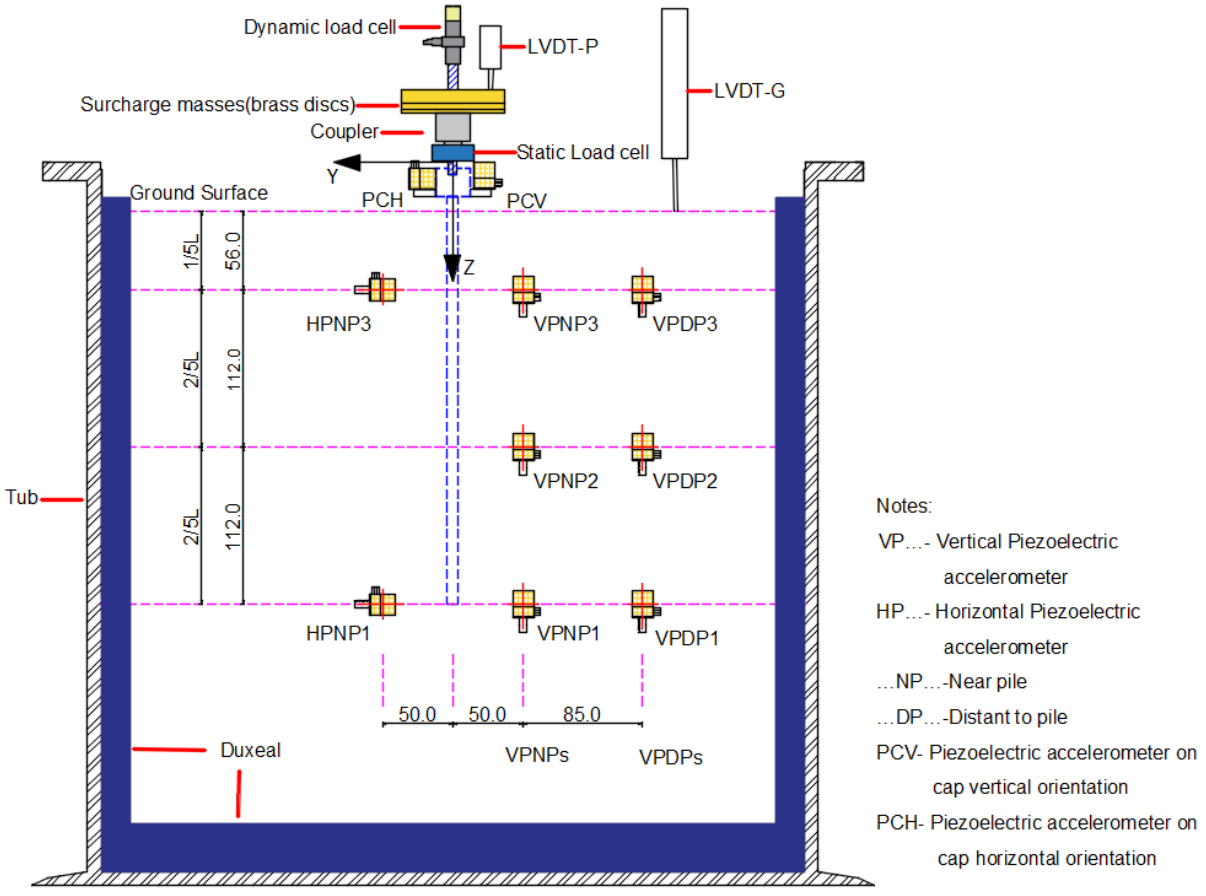


FIGURE 3.4: Schematic view of model layout in centrifuge testing (all in mm)

Two LVDTs were used to monitor the displacement of the pile (LVDT-P) and the ground surface (LVDT-G). A 500 N capacity static load cell (Richmond Industries

210 Series inline load cell) was employed to measure the dead load being applied to the top of the pile. The dead load was applied using three 76.2 mm diameter brass discs which were located above the static load cell (capable of low frequency measurements). It should be noted that a large portion of dynamic force may be lost because the static load cell is relatively soft compared to other items, and this may result in very low vibrations in the soil. The vibration level in the soil was checked during the preliminary tests (Pre01 and Pre02, detailed in Section 3.2.11) to ensure that detectable vibrations were generated. The brass discs screw onto a central steel rod and were locked in place by a nut. This setup allowed the mass to be changed easily between different flights with minimal disturbance to the pile. Three different surcharge masses (see Figure 3.5) were employed in the formal ground borne vibration test (Test GBV, summarized in Section 3.2.13) to investigate the effects of dead load on the behaviour of the pile and soil. The weights of three surcharge masses are shown in Table 3.4. The measured dead loads will be illustrated in Chapter 5 and compared with the pile bearing capacity. It should be noted that even when no surcharge mass was used, the dead load applied to the pile was not zero because of the existence of the coupler, static load cell, and the dynamic load cell. The combined weight of the three items were 170 g.

TABLE 3.4: Surcharge masses on the top of the pile

Test	Surcharge mass	Weight of surcharge mass(g)
GBV_m1	m1	726.5
GBV_m2	m2	350.5
GBV_m3	m3	115

In this study, the dynamic load was applied by an electromagnetic shaker (LDS V201) to excite the model (see Figure 3.5). The small shaker can provide a peak force of 17.8 N across a frequency range of 5 to 13,000 Hz. The supporting system for the shaker is detailed in Section 3.2.11.4 and the input signal to control the shaker is discussed in Section 3.2.12. The dynamic load cell (ICP 221B02) was connected to the shaker with a threaded steel rod to measure the dynamic load being applied during the test. The dynamic load cell is capable of measuring frequencies from 10 Hz up to 15 kHz.

3.2.8 Data acquisition system and signal processing

According to the Nyquist Theorem, the sampling rate should be at least twice the highest frequency used in the study (7200 Hz) to avoid aliasing. A National Instruments Ethernet Rio expansion chassis (NI-9149) forms the backbone of the

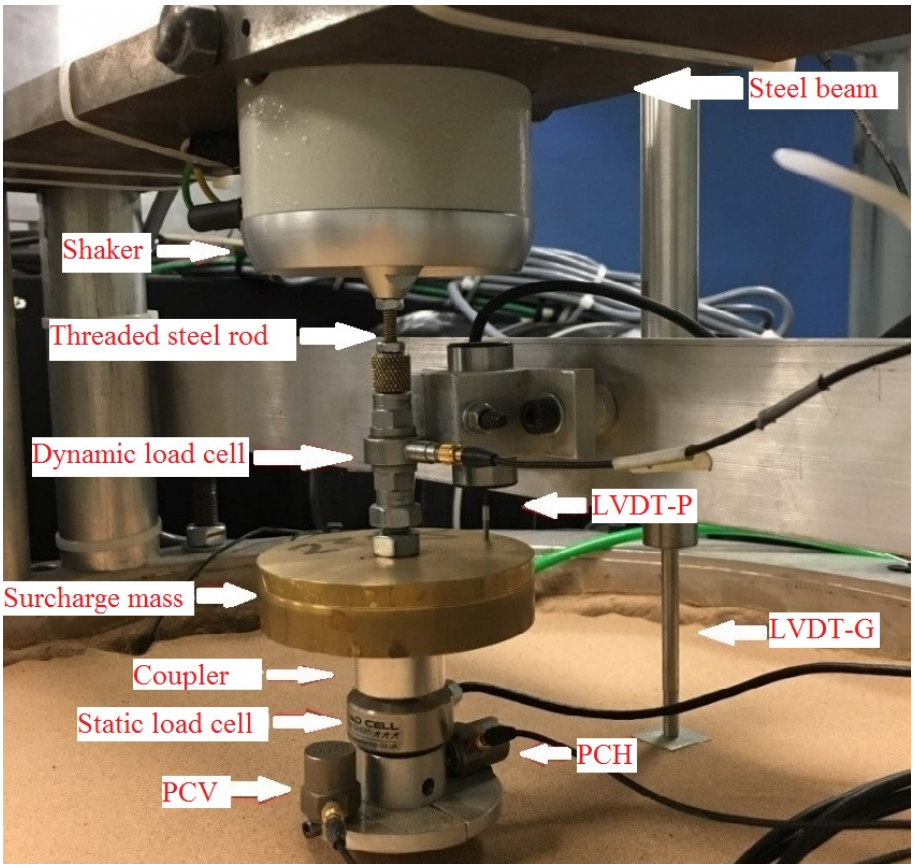


FIGURE 3.5: A view of devices and transducers used in centrifuge testing

data acquisition system on the University of Nottingham centrifuge. In the tests, the dynamic load cell (DLC) and piezoelectric accelerometers (Piezos) are the IEPE (integrated electronic piezoelectric) instruments. The dynamic load cell data and piezoelectric accelerometer data were recorded using the National Instruments NI-9234 modules (high speed IEPE module), which is capable of a synchronous sampling frequency of 51.2 kHz.

The voltage output instruments (static load cell and displacement transducers), despite not being high-frequency instruments, were connected to a junction box and then to a NI-9220 module. The junction box was used as intermediate modules between the transducers and the data acquisition system. It can supply power to the transducers and amplify the analog output signals coming from the transducers. The NI-9220 module is capable of a synchronous sampling frequency of 100 kHz. This high speed module was also needed for recording MEMS (Micro-Electro-Mechanical Systems) accelerometers which were used in the tests to measure the in-flight dynamic properties of the soil (detailed in Section 3.3.1). Both data acquisition modules (NI-9234 and NI-9220) allowed for the recording of frequencies well in excess of the Nyquist frequency (3.5 times for the Piezos). Details of the data acquisition system (DAQ system) are shown in Table 3.5, including

the sampling frequency (Fs), channel number (Ch), resolution (Res), voltage input. Locations of Piezos, the dynamic load cell (DLC), the static load cell (SLC) and LVDTs are shown in Figure 3.4 and Figure 3.5. Locations of MEMS used in air hammer testing are shown in Figure 3.30, see Section 3.3.2. Specifications of all the transducers are provided in the Appendix.

TABLE 3.5: Transducers and DAQ system in centrifuge tests

Transducer	Model number	Location	NI module type	Fs (kHz)	Ch	Res (bits)	Voltage input
Piezos	DJB A/120v	VPNP1	NI-9234	51.2	1	24	5 V
Piezos	DJB A/120v	VPDP1	NI-9234	51.2	2	24	5 V
Piezos	DJB A/120v	VPNP2	NI-9234	51.2	3	24	5 V
Piezos	DJB A/120v	VPDP2	NI-9234	51.2	4	24	5 V
Piezos	DJB A/120v	VPNP3	NI-9234	51.2	5	24	5 V
Piezos	DJB A/120v	VPDP3	NI-9234	51.2	6	24	5 V
Piezos	DJB A/120v	PCV	NI-9234	51.2	7	24	5 V
Piezos	DJB A/120v	PCH	NI-9234	51.2	8	24	5 V
Piezos	DJB A/120v	HPNP1	NI-9234	51.2	9	24	5 V
Piezos	DJB A/120v	HPNP2	NI-9234	51.2	10	24	5 V
Dynamic load cell	ICP 221B02	DLC	NI-9234	51.2	11	24	5 V
Static load cell	Richmond Industries 210 Series	SLC	NI-9220	100	1	16	10 V
LVDT	S015.0	LVDT-G	NI-9220	100	2	16	10 V
LVDT	DFg5	LVDT-P	NI-9220	100	3	16	10 V
MEMS	ADXL001-70	AHA-M1	NI-9220	100	5	16	5 V
MEMS	ADXL001-70	AHA-M2	NI-9220	100	6	16	5 V
MEMS	ADXL001-70	AHA-M3	NI-9220	100	7	16	5 V
MEMS	ADXL001-70	AHA-M4	NI-9220	100	8	16	5 V

Before the preparation of each model, all the transducers were calibrated first. Then the original data (all raw readings in volts) were multiplied by the calibration factor of each transducer to obtain the acceleration (m/s^2), displacement (mm) and force (N) respectively. A variety of Matlab programs were used to calculate the power spectra, frequency response function and coherence function from the measured vibration data. Details of these calculations are described in Chapter 5.

3.2.9 Model preparation

This part summarises the model preparation process undertaken before centrifuge testing.

- 10 mm thick dry Congleton sand was air pluviated into the model container with side and bottom Duxseal.
- The air hammer device, which was used to generate shear waves, was installed, detailed in Section 3.3.2.
- The pile was positioned and secured by a frame, see Figure 3.3, which allows for the MEMS accelerometers array (explained in Section 3.3.2) to be installed above the air hammer to measure the shear waves generated by the air hammer.
- Sand was poured until the bottom of the pile and then the accelerometers were placed at the relevant locations.
- Sand pouring continued until the next level of instruments where the transducers were positioned followed by the further sand pouring. This was repeated until the sand level reached the required height.
- The sand surface was levelled to ensure a constant height.
- The model was loaded onto the centrifuge platform.
- The static load cell, brass discs and dynamic load cell were connected to each other, and finally the shaker was positioned by a supporting system.
- Two LVDTs (LVDT-G and LVDT-P) were installed to measure the displacement of the soil surface and the pile.
- All the connections were made.

3.2.10 Test procedure

After the completion of the model preparation, some simple checks were made to ensure all the systems were working correctly, and the following steps were carried out:

- The centrifuge was spun up to 183 rpm (60 g) and down to 100 rpm (10 g) 5 times (cycles) as a stabilisation process. This was because the Duxseal used can derform over a long period of time. This process helps to ensure that all the further tests were carried out under consistent conditions. The maximum surcharge mass (m1=719.4 g) was used first during this process. Two LVDTs were used to measure the displacement of the ground surface and the pile. After four cycles in this test, a marginal difference in displacement of the ground surface and the pile (less than 0.1 mm) was noted between the third and fourth cycles.

- Once stabilised at 60 g, the air hammer test (explained in Section 3.3.2) was conducted. The air pressure needed to actuate the air hammer was obtained by trial and error. Then the air hammer was triggered at least 8 times to evaluate the average shear wave velocity.
- The shaker was actuated to vibrate the top of the pile to perform ground borne vibration tests. The details of input excitation signals are specified in Section 3.2.12.
- The air hammer tests were conducted again.
- The centrifuge was stopped.
- The mass on the top of the pile was changed (see Table 3.4) and the preceding steps were repeated.

3.2.11 Model development: centrifuge and shaker induced interference

Some preliminary tests (Pre01, Pre02, Pre03 and Pre04) were conducted first to solve centrifuge and shaker induced noise and vibration problems and wind effects, as well as determining appropriate input signals for the shaker and magnitude of excitation for shear wave velocity measurements (see Section 3.3.2). This section presents results related to the centrifuge and shaker induced interference. The determination of input signals for the shaker is discussed in Section 3.2.12. Some centrifuge induced problems were found in Test Pre01 and approaches were adopted in Test Pre02 to solve these problems. The effects of two supporting systems were checked in Test Pre03 and Pre04, and results are presented in Section 3.2.11.4. Table 3.6 summarises these preliminary tests conducted before the formal ground borne vibration tests (Test GBV).

3.2.11.1 Isolation from the vibration sources with rubber mat

As discussed in Section 2.1.1.5, the train induced vibration amplitudes are small. Therefore, in the centrifuge tests it is very important to know/limit the interference on measurements from the running centrifuge and the shaker. There are two main factors that can distort the real vibration level that the pile and soil are experiencing: electric noise and physical vibrations. Electric noise cannot be 100% eliminated, and the noise level is constant during the test. However, physical vibrations generated by the centrifuge and shaker vary with frequency and can be reduced by isolation from the vibration sources.

TABLE 3.6: Details of preliminary tests

Test name	Test description	Presented section
Pre01_T01	centrifuge induced vibrations at 60 g without rubber mat	3.2.11.1
Pre02_T01	centrifuge induced vibrations at 60 g with rubber mat	3.2.11.1
Pre02_T04	centrifuge induced vibration properties during spin-up	3.2.11.2
Pre01_T02	wind effects at 60 g without wind shield	3.2.11.3
Pre02_T02	wind effects at 60 g with wind shield	3.2.11.3
Pre03_T01	centrifuge induced vibration at 60 g with old supporting system	3.2.11.4
Pre04_T01	centrifuge induced vibration at 60 g with new supporting system	3.2.11.4
Pre04_T02	shaker induced vibration at 60 g with new supporting system	3.2.11.4

In the preliminary test Pre01, it was found that centrifuge induced vibrations at 60 g can propagate through the support system and the container into the soil. Therefore, a 6 mm thick rubber mat was placed between the centrifuge platform and the model container in test Pre02, as shown in Figure 3.7, to reduce the unwanted vibrations. Two centrifuge tests (Pre01_T01 and Pre02_T01) were carried out to estimate the pile and soil responses caused by the running centrifuge without and with the rubber mat at 60 g. It should be noted that no excitations were applied to the pile to purely measure the centrifuge induced interference. The measured accelerations in frequency domain from two representative Piezos (PCV on the pile top and VPNP3 in the soil) are illustrated in Figure 3.6.

It can be seen that, without and with the rubber mat, the frequency responses were quite similar within the frequency range of 0 to 600 Hz for both pile top and interior of the soil. The rubber mat reduced the vibration levels on the pile top from about 23 mm/s^2 to 3 mm/s^2 within 600 Hz to 1300 Hz and it significantly decreased the spikes to about 4 mm/s^2 within the range of 3500 Hz to 8000 Hz. In terms of the soil, the acceleration amplitude was reduced from about 10 mm/s^2 to 3 mm/s^2 within the frequency range of 600 Hz to 1300 Hz. In the frequency range of 1500 Hz to 8000 Hz, the acceleration amplitude in the soil was reduced to less than 1 mm/s^2. Therefore, it was concluded that it is necessary to employ the rubber mat between the centrifuge and the model container to reduce the effects of the centrifuge on the pile and soil responses during the investigation of small ground-borne vibrations. Moreover, a high pass filter with a high pass frequency of 600 Hz will be used to filter out noise based on the noise test results.

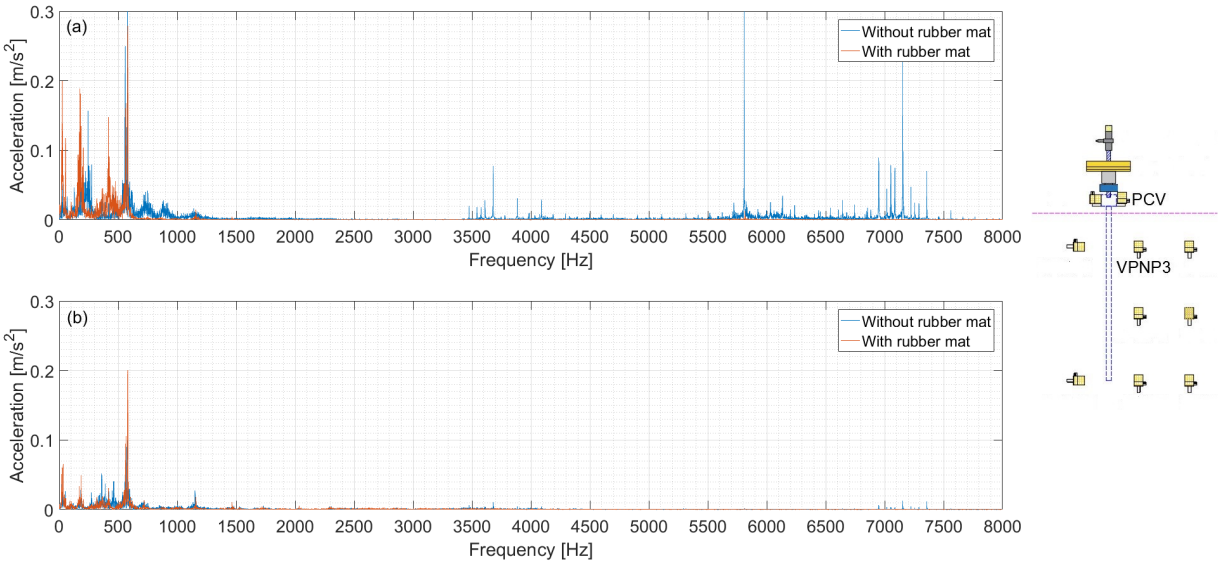


FIGURE 3.6: Frequency range and vibrations from centrifuge at 60 g: (a) PCV and (b) VPNP3

3.2.11.2 Centrifuge induced vibration properties during spin-up

To fully understand the properties of centrifuge induced vibrations and the resulting effects on pile and soil responses, a series of vibration tests were conducted during the spin-up of the centrifuge (Test Pre02_T04). The background noise and vibration test was conducted without applying harmonic excitation with the shaker. The vertical and horizontal vibrations on the pile top and within interior of the soil were measured during the spin-up, see Figure 3.7. In addition, two accelerometers (CFV and CFH) were mounted onto the centrifuge platform to evaluate the vertical and horizontal vibrations at 10 g, 20 g, 30 g, 40 g, 50 g and 60 g, see Figure 3.7. The corresponding angular velocities were 75 rpm, 106 rpm, 130 rpm, 150 rpm, 168 rpm and 183 rpm in this test.

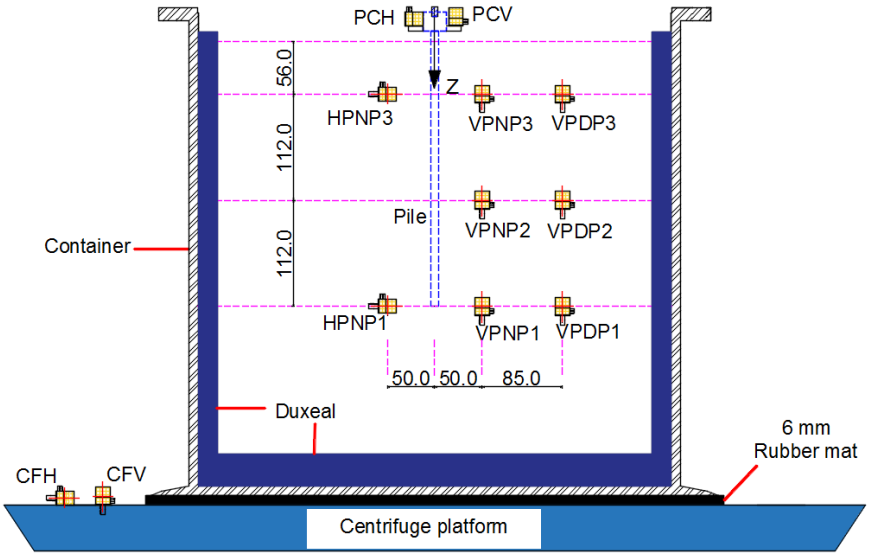


FIGURE 3.7: Vibration measurement location

The vibrations on the centrifuge platform measured from CFV and CFH in time domain at different g_levels were transferred to frequency domain. As discussed in Section 3.2.6, the frequency range of interest is between 120 and 7200 Hz in model scale. Therefore, the acceleration spectrum with a wider frequency range of 0 to 8000 Hz is shown in Figure 3.8. A smaller frequency range of 0 to 1000 Hz is shown in Figure 3.9 to clearly show the angular speed effects on lower frequency range and to compare the results with pile and soil responses, shown in subsequent figures. It can be seen that:

- The vertical vibrations at most frequencies generated by the centrifuge were larger (2-3 times) than the horizontal vibrations at most frequencies.
- At 10 g, the vibration amplitudes were very small at most frequencies, except for some lower frequency components (0 to 200 Hz) and some higher frequencies (around 5800 Hz). The vibration amplitudes increased with increasing g-level (angular velocity), especially at about 5800 Hz.
- Figure 3.9 indicates the vibrations within about 200 Hz were relatively high and constant. However, the second peak frequency increased with the increase of angular velocity. It occurred at 240 Hz (10 g), 342 Hz (20 g), 418 Hz (30 g), 481 Hz (40 g), 536 Hz (50 g) and 587 Hz (60 g), respectively. According to the curve fitting analysis, the relationship between the second peak frequency f_{peak} and the g_level

(N) is $f_{peak} = 76\sqrt{N}$. This may be caused by the increasing angular velocity of the centrifuge or the running frequency of the motor that drives the centrifuge.

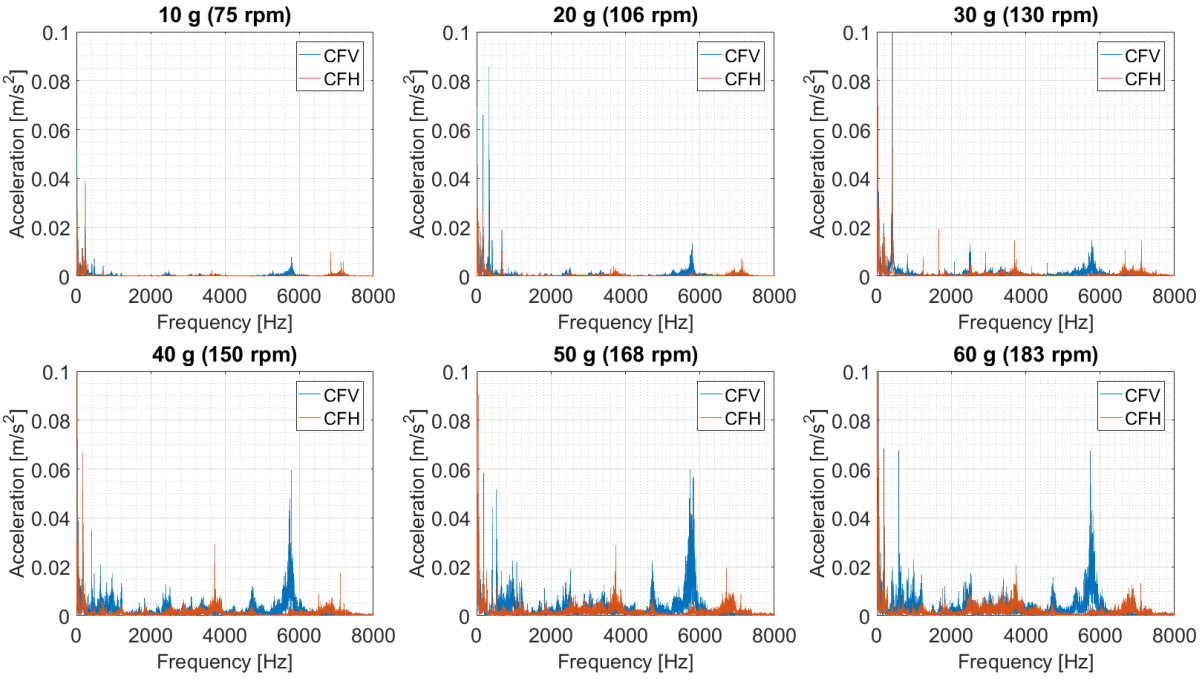


FIGURE 3.8: Accelerations on centrifuge platform during spin-up (within 8000 Hz)

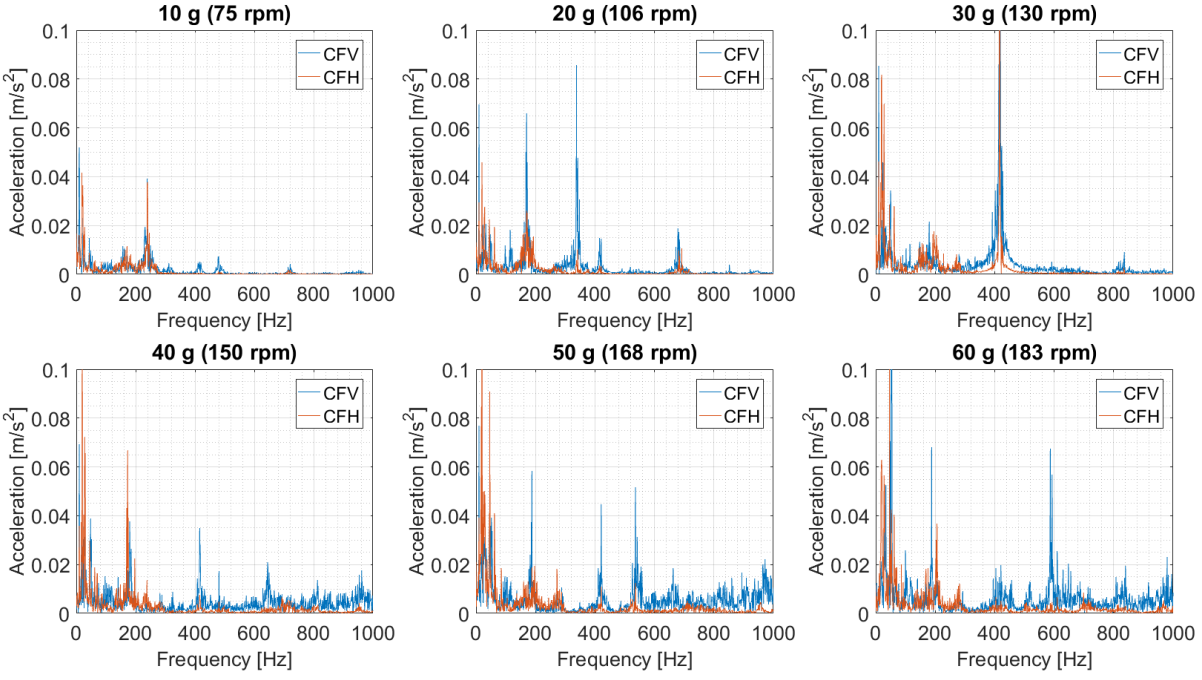


FIGURE 3.9: Accelerations on centrifuge platform during spin-up (within 1000 Hz)

The accelerations in frequency domain measured from PCV and PCH at different g-levels are shown in Figure 3.10 (0-8000 Hz) and Figure 3.11 (0-1000 Hz). It can be seen that:

- Similar to the centrifuge platform, the vertical vibrations at most frequencies were larger (2 to 5 times, depending on the frequency) than the horizontal vibrations.
- The vibration amplitudes were significant, around 40 mm/s^2, at low frequency components (0 to 600 Hz). Within the range of 600 Hz to 8000 Hz, the vibration amplitudes were relatively small and constant at most frequencies, less than 3 mm/s^2.
- Similar to the centrifuge platform, Figure 3.11 indicates the acceleration vibrations within 200 Hz were relatively high and constant. The second peak frequency increased with the increasing angular velocity. It occurred at 235 Hz (10 g), 335 Hz (20 g), 409 Hz (30 g), 474 Hz (40 g), 529 Hz (50 g) and 580 Hz (60 g), respectively.

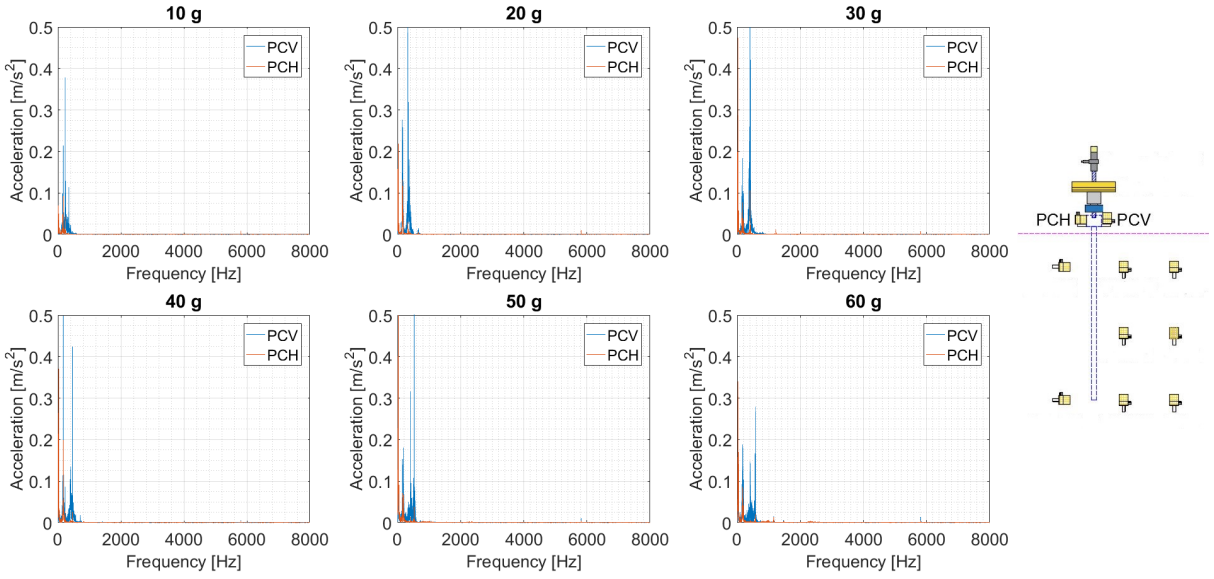


FIGURE 3.10: Accelerations on pile top during spin-up (within 8000 Hz)

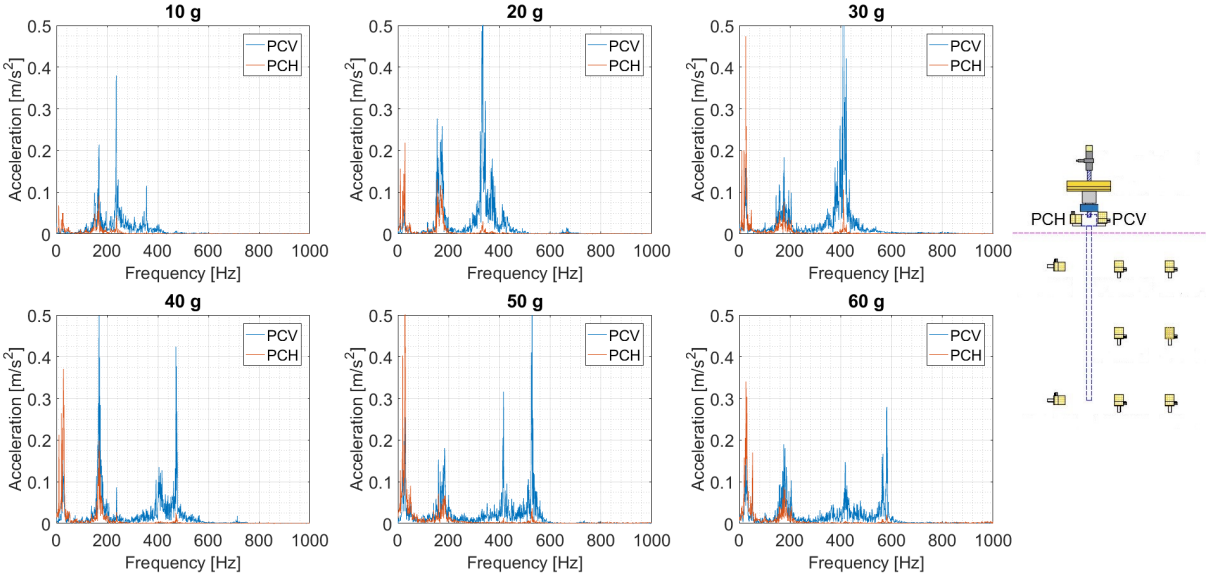


FIGURE 3.11: Accelerations on pile top during spin-up (within 1000 Hz)

As shown in Figure 3.12, centrifuge-induced vibrations within the soil were similar to the pile top: the vertical vibrations at most frequencies were larger than the horizontal vibrations and the vibration amplitudes were only significant within 0 to 600 Hz. At 60 g, the most significant frequency range was 550 Hz to 600 Hz.

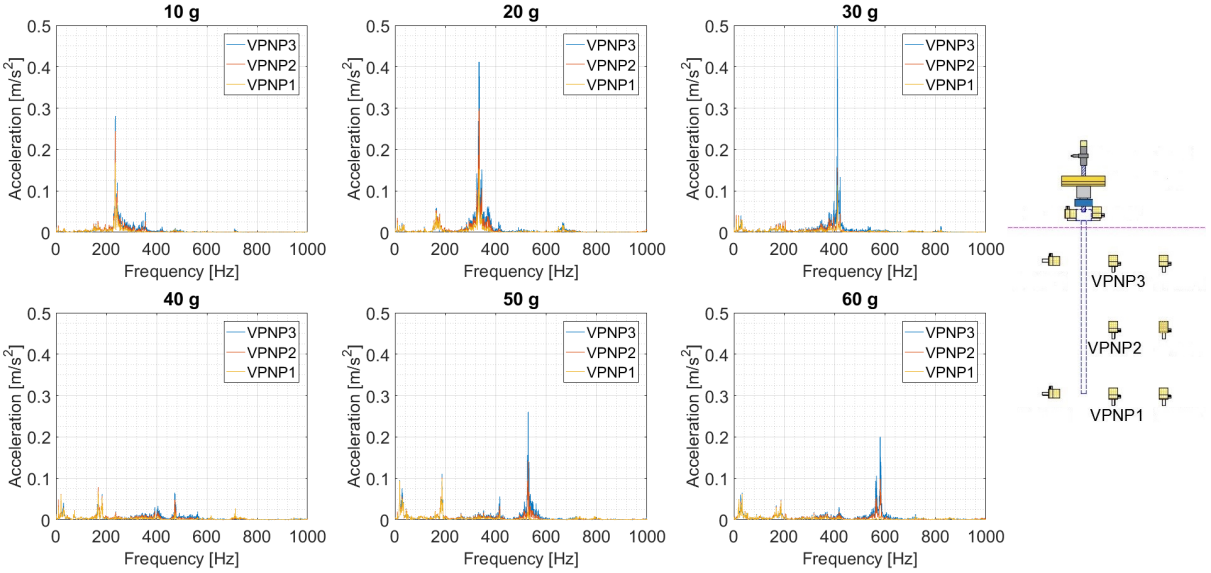


FIGURE 3.12: Accelerations within the soil during spin-up (within 1000 Hz)

3.2.11.3 Wind effect from centrifuge

Another challenge faced with the centrifuge tests was related to the effect of wind buffeting on the shaker armature and upper portion of the pile, which protruded above the top of the centrifuge container. The centrifuge rotates at 3 cycles per second at the specified centrifugal acceleration, thus generating undesirable wind buffeting. Two exposed accelerometers on the top of the pile, PCV and PCH were vulnerable to the wind effects. The wind effect was examined by recording the accelerations with and without a wind shield, as shown in Figure 3.13. A 6 mm thick aluminum plate with a projection area onto the windward plane of $22 \times 70\,\text{cm}^2$ (height$\times$width) was used. The wind shield was higher than the shaker top and wider than the model container so that the two Piezos were protected, to a degree, from the wind. The results, shown in Figure 3.14, indicate that the wind had an adverse effect on the response of PCV and PCH. Therefore, the wind shield was used for all the tests presented in the following sections.

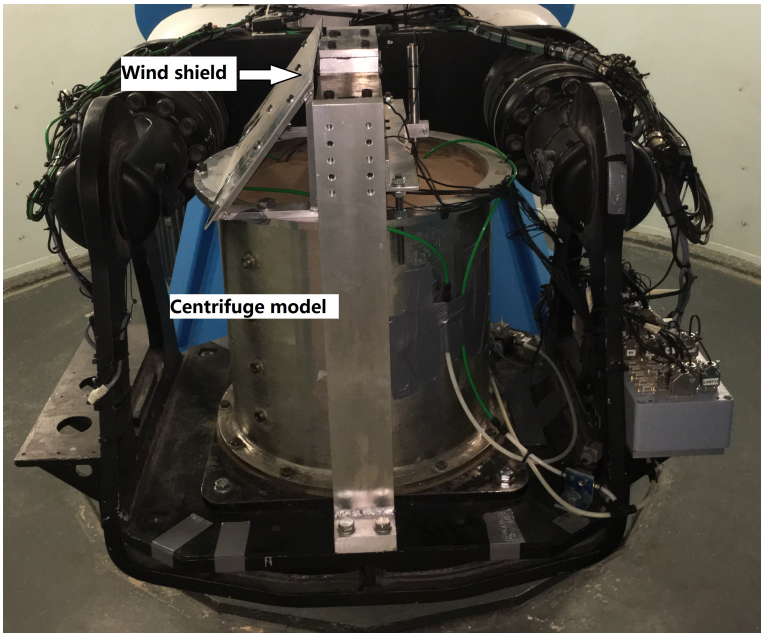


FIGURE 3.13: Wind shield

3.2.11.4 Supporting systems and noise and vibration from shaker

This study intended to investigate the vibrations generated through soil-pile interaction. However, in addition to the intended vibrations being transmitted to the pile, the shaker may transmit vibrations through its support which then pass through the model container and into the soil hence affecting the real signals. It was found that the unwanted electrical noise and physical vibrations from the shaker could affect the tested signals, which leads to low signal-to-noise ratios.

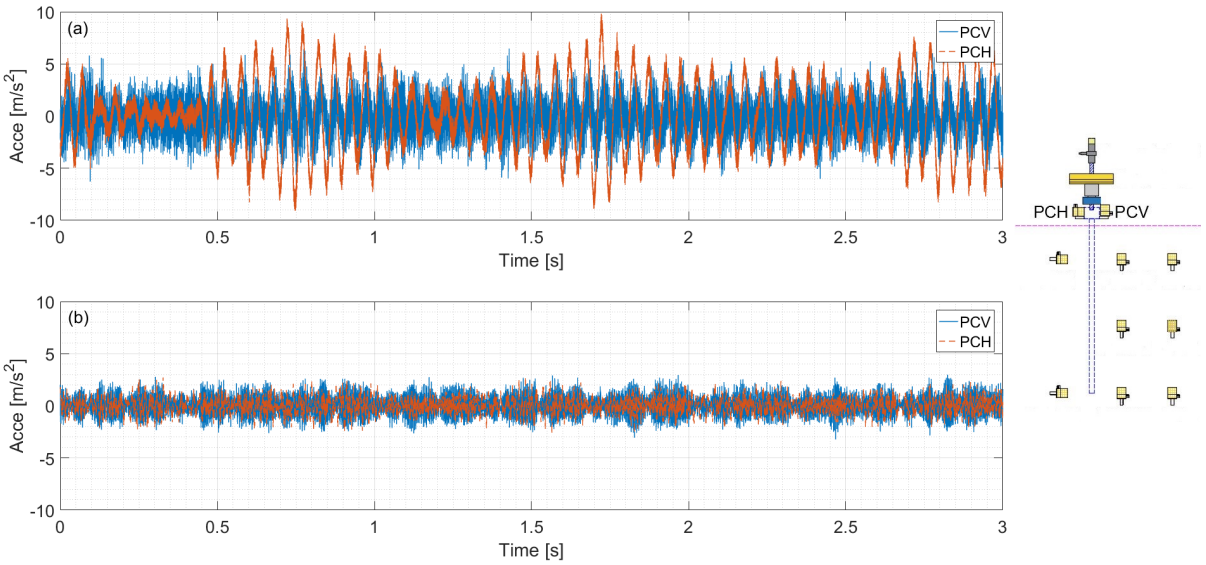


FIGURE 3.14: Wind effect on PCV and PCH: (a) without wind shield and (b) with wind shield

Two supporting systems were designed in this study to conduct ground borne vibration tests and the effectiveness was examined.

For the old supporting system, the shaker was connected to the model container through four aluminium columns, as shown in Figure 3.15. The four aluminium columns were mounted onto the centrifuge container. In Test Pre03_T01, the effectiveness of the old supporting system was examined. A new loading system that was not fixed to the container was designed to support the shaker, thereby reducing the effect of vibrations which propagate directly through the container into the soil, see Figure 3.16. The new system consists of a stainless steel beam and two aluminium rectangular bars. The two aluminium bars are mounted directly on the centrifuge platform instead of the model container to isolate the container/soil from the unwanted vibrations of the shaker. The effectiveness of the new supporting system was examined in Test Pre04_T01, and a comparison was made between two systems. For both configurations, a 6 mm rubber mat was placed between the centrifuge platform and the container to further reduce the vibrations from the centrifuge.

First, two centrifuge induced vibration tests with the old and new supporting systems were conducted and the results are shown in Figure 3.17. It should be noted the shaker was not applying dynamic loads to the pile top during these tests. First of all, it can be seen that vibrations within the soil, VPNP3, were almost the same for both supporting systems. Compared to the old supporting system, it is observed that, with the new supporting system, the pile top experienced smaller vibrations especially within 0 to 500 Hz. Within 500 Hz to 600 Hz, vibrations at

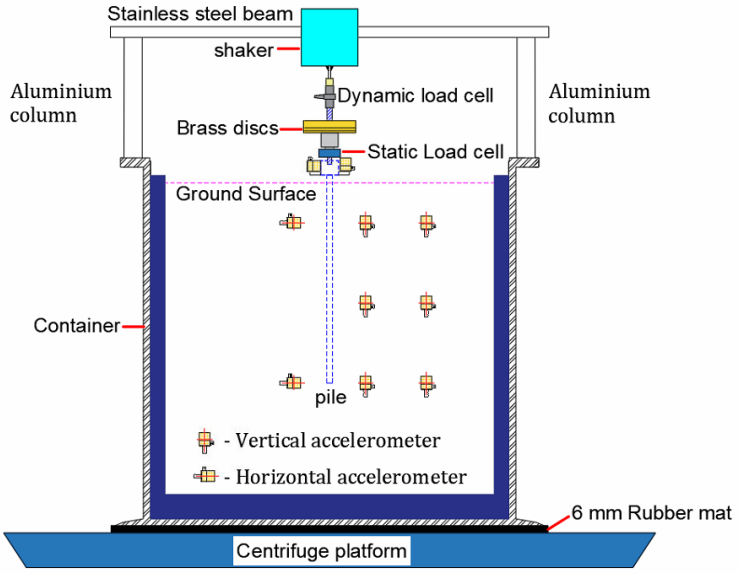


FIGURE 3.15: A schematic view of old supporting system and transducers in Test Pre03_T01

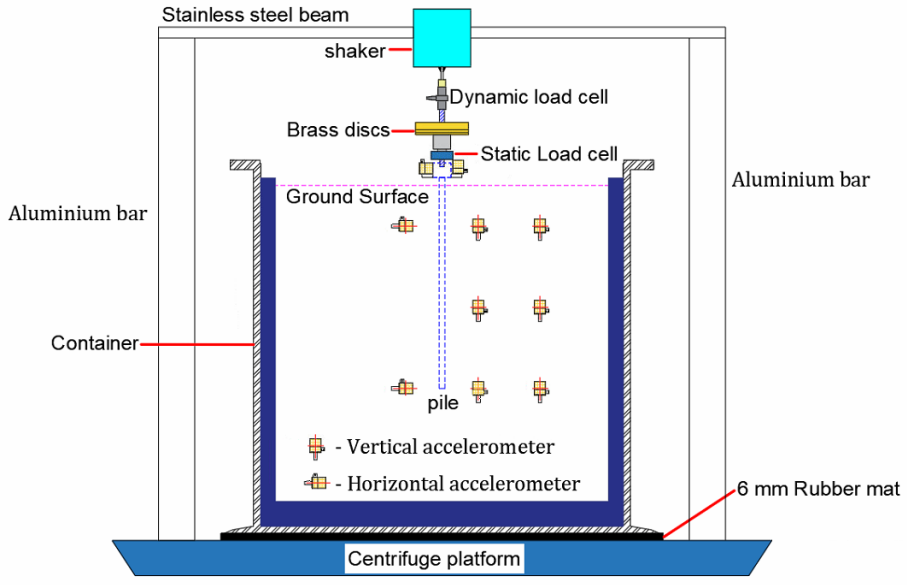


FIGURE 3.16: A schematic view of new supporting system and transducers in Test Pre04_T01

the pile top were almost the same for both supporting systems. However, larger pile responses can be observed with the new supporting system from Figure 3.17 within 600 Hz to 8000 Hz. This indicates that the new supporting system was capable of reducing low frequency vibrations. However, the new supporting system was mounted onto the centrifuge platform and the high frequency vibrations can still propagate through the aluminium bars and the beam to the pile. The model container and the old supporting system were isolated by the rubber mat, which can reduce the high frequency vibrations within the range of 600 Hz to 8000 Hz, as discussed in Section 3.2.11.1.

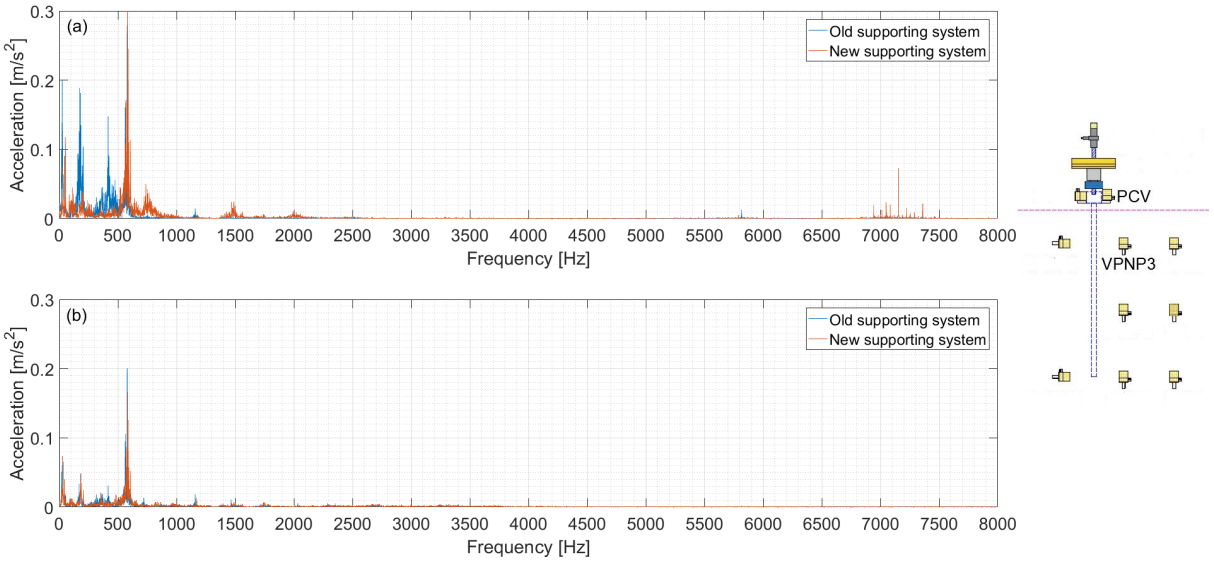


FIGURE 3.17: Vibrations from centrifuge with old and new supporting system: (a) PCV and (b) VPNP3

The purpose of using the new supporting system was to reduce shaker induced vibrations. To verify the effectiveness of the new supporting system, another noise and vibration test at 60 g (Test Pre04_T02) was conducted to estimate noise level unrelated to the soil-pile interaction by disconnecting the shaker with the pile. At the same time, the movable component of the shaker (armature) was fixed by an aluminium angle mounted to the steel beam, shown in Figure 3.18. Therefore, all the recorded signals were influenced by the electric noise or the physical vibrations from the centrifuge and the shaker. In this case, ground-borne vibration generated by soil-pile interaction has no contribution to the recorded signals. A 20 second sweep signal with a frequency range of 2-7200 Hz was used. The input voltage amplitude was 500 mV.

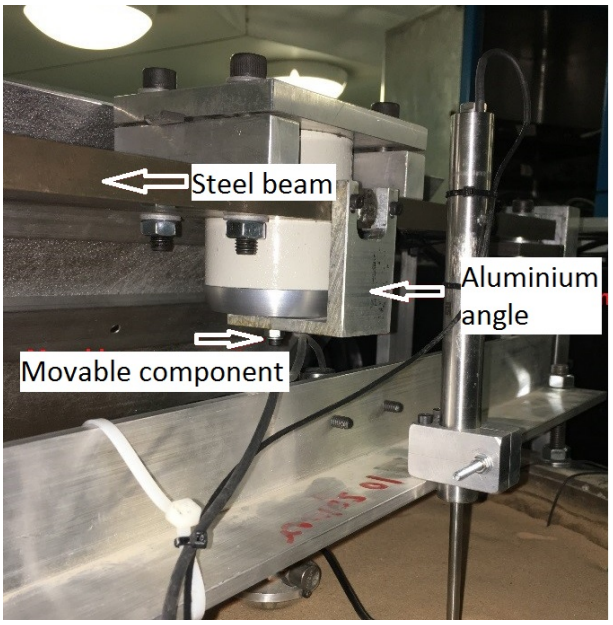


FIGURE 3.18: Aluminium angle mounted to the steel beam

The measured signals in time domain from DLC and piezoelectric accelerometers are illustrated in Figure 3.19 and Figure 3.20. The amplitudes of recorded forces at most frequencies related to electric noise and vibrations were about 0.025 N, see Figure 3.19. The measured dynamic forces in the normal tests were about 1 N and up to 40 N, as presented in Section 5.2.4. The ratio is relatively small, about 2.5% at most frequencies. Test results indicate the dynamic load cell (DLC) is slightly affected by electric noise and physical vibrations.

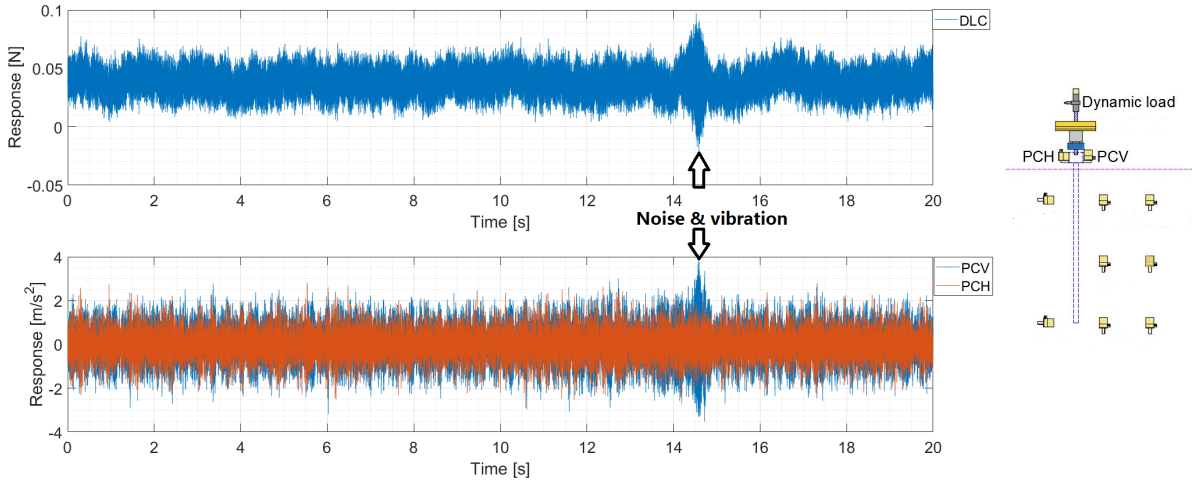


FIGURE 3.19: Noise levels of dynamic load cell and accelerometers on pile in time domain

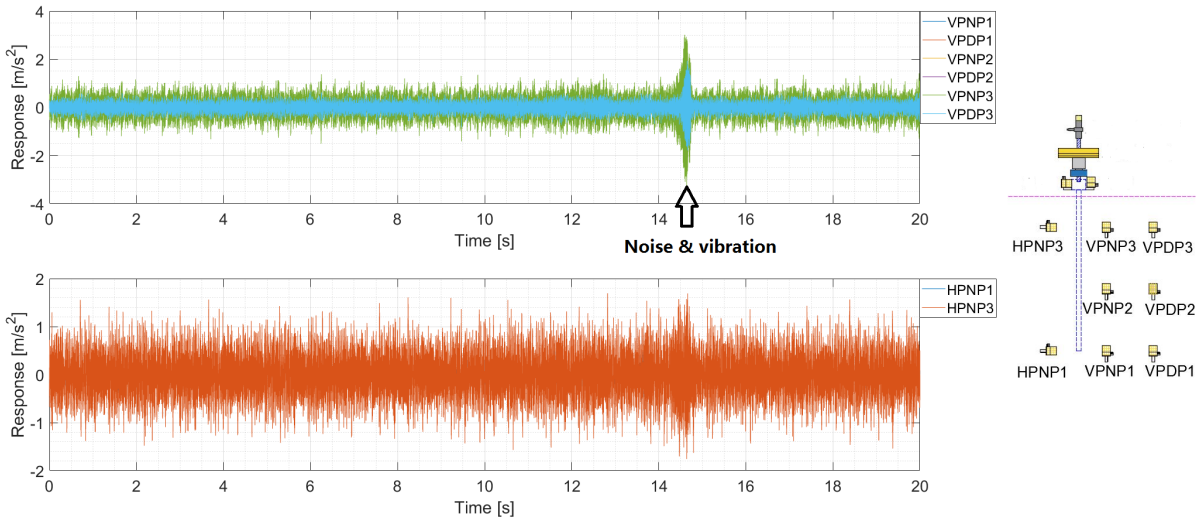


FIGURE 3.20: Noise levels of vertical and horizontal accelerometers in soil

Figure 3.19 and Figure 3.20 shows vibration levels in both horizontal and vertical directions and they indicate the accelerations were almost constant at most of the times. A considerable vibration can be observed during approximately the fourteenth second from the time history data. Compared with the horizontal accelerometers (PCH, HPNP1 and HPNP3), the vertical piezoelectric accelerometers are significantly affected by the physical vibrations generated by the action and reaction at some frequencies. The vertical accelerations caused by the vibrations were up to 3 m/s^2. However, the acceleration at PCH remained constant (2 m/s^2); accelerations at HPNP1 and HPNP3 were still about 1 m/s^2. This is due to the direction of the harmonic loads is mainly vertical.

The results indicate vibrations could still propagate into the soil through rubber mat, container and duxseal. During the test, the noises and physical vibrations from the centrifuge are relatively constant. The shaker applies harmonic loads to the aluminium angle (to the pile in the normal test), and the applied frequency ranges from 2 Hz to 7200 Hz. The acceleration level caused by the action and reaction may vary with frequency. The frequency range of the significantly affected signals is obtained by conducting a Fast Fourier Transform of the extracted time history data. Only the vertical accelerometer signals in the soil are analysed and shown in Figure 3.21. It is clear that there are two frequency ranges (less than 1000 Hz) which could affect the real signal. One range is from 550 Hz to 600 Hz, another is from 900 Hz to 1000 Hz. Figure 3.17 and Figure 3.21 suggest the noise and physical vibrations do consist of two parts: constant part from the centrifuge and varying part from the shaker, as discussed above.

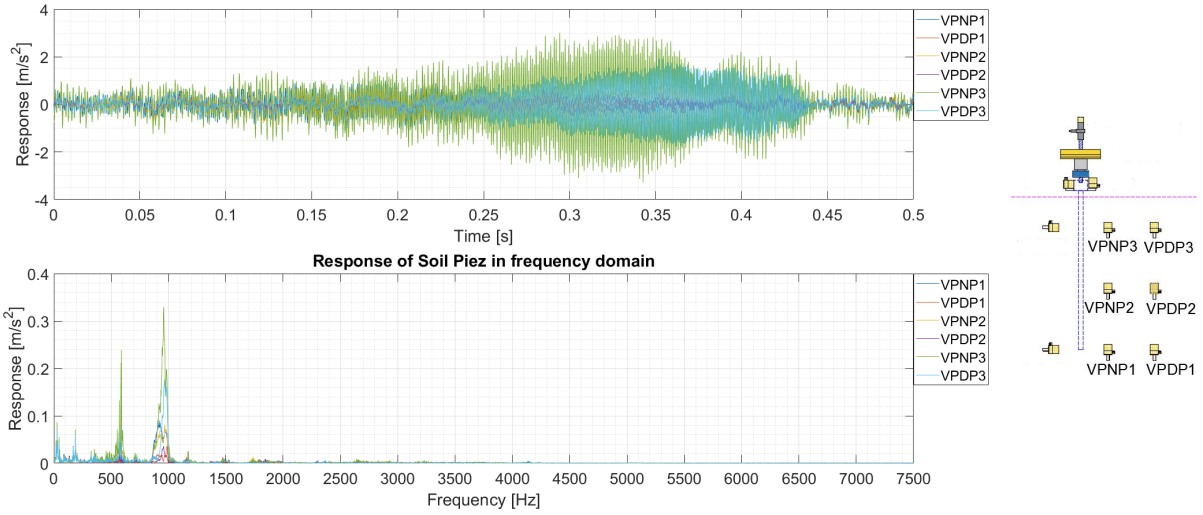


FIGURE 3.21: Frequency range of background noises and vibrations from centrifuge and shaker (data extracted from the whole time history data shown in Figure 3.20)

Results presented in this section indicate that the vibrations at the pile top were similar and significant for the old and the new supporting systems within 0 to 600 Hz. However, the old supporting system is capable of providing a smaller centrifuge induced vibration level within the frequency range of 600 Hz to 8000 Hz compared with the new system. Additionally, the new supporting system can not effectively reduce vibrations from the shaker during excitation. Therefore, the old supporting system was employed to conduct the formal ground borne vibration tests (Test GBV). Another reason for using the old supporting system is presented in the following section.

3.2.12 Model development: input signal for shaker

In this study, the shaker was selected as the excitation method in the centrifuge tests. The advantages and disadvantages of performing shaker testing have been discussed in Section 3.2.6. This section discusses the input signal for the shaker. Table 3.7 presents all the tests carried out to determine appropriate input signals for the shaker in terms of amplitude and signal type. The parameters illustrated in Table 3.7 are detailed in the following subsections. All the results presented in this section are in model scale.

3.2.12.1 Input signal

In this study, a sinusoidal signal was selected to conduct the vibration analysis. Two different types of vibration signals were used in this study: sine chirp signal and single frequency signal. The two vibration signals both consist of sinusoidal

TABLE 3.7: Details of dead loads and input signal in preliminary tests

Test name	Surcharge mass(g)	Amplitude (mV)	Vibration signal	Frequency range(Hz)	Supporting system	Rubber mat
Pre01_T03	726.5	300/500/800	sweep signal	600-7200	old	without
Pre01_T04	350.5	300/500/800	sweep signal	600-7200	old	without
Pre01_T05	115.0	300/500/800	sweep signal	600-7200	old	without
Pre02_T03	726.5	300/500/800	sweep signal	600-7200	old	with
Pre02_T04	350.5	300/500/800	sweep signal	600-7200	old	with
Pre02_T05	115.0	300/500/800	sweep signal	600-7200	old	with
Pre03_T02	350.5	800	sweep signal	600-7200	old	with
Pre03_T03	350.5	800	single frequency	600-7200	old	with
Pre04_T03	350.5	800	single frequency	600-7200	new	with

signals. The difference, advantages and disadvantages of these two input excitation signals are summarised below (Avitabile, 2001).

- Sine chirp signal

The first type is a sweep signal, in which the frequency varies across the whole frequency range (i.e. 600 Hz to 7200 Hz) with a short duration (i.e. 5 s). This type of signal is called the sine chirp and an example is presented in Figure 3.22. The advantage of a sine chirp signal is the short testing time, which minimizes data file size and allows a wider range of parameters to be investigated during one centrifuge flight. However, the rate of change of frequency is very quick, especially for the low frequencies. This is because a signal generator usually breaks the total frequency range into a certain amount of steps, i.e. 2000 steps. In this case, each frequency component only lasts 0.003 seconds (5/2048=0.003). Within an extremely short period, the model response may not reach steady state. Increasing the duration for a sweep signal can reduce the rate of change of frequency. However, the model response may still not reach a steady state at low frequencies.

Secondly, the longer duration cannot solve the 'leakage' problem related to signal processing, explained herein. In dynamic analysis, time history data needs to be transformed to frequency domain to understand the soil or structure responses at different frequencies. Another disadvantage of the sweep signal relates a digital signal processing effect referred to as leakage when transforming time domain data to frequency domain data (Brigham, 1974). This is because the Fourier transform process requires the sampling duration to be an integer multiple of the period for a certain excitation frequency (Brigham, 1974). However, the sampling duration for a certain excitation frequency is not controllable if sweep signal is employed. To reduce leakage, window functions are used to process the data. A window function, also known as an tapering function, is a mathematical function that is zero-valued

outside of some chosen interval. This kind of function is symmetric around the middle of the interval. They usually have a maximum in the middle, and taper away from the middle. However, window functions still cause some distortion of the data and should be avoided whenever possible.

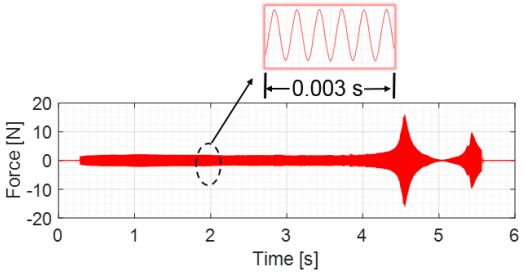


FIGURE 3.22: An example of sine chirp input signal (dynamic load)

It should be noted that Figure 3.22 indicates the measured dynamic load amplitude was not constant. It has been mentioned in Section 3.2.6 that the force magnitude provided by the shaker is proportional to the current and the magnetic flux density. However, the force magnitude applied to the test object (all the instruments below the shaker, as shown in Figure 3.16) is also determined by the supporting system, the shaker body, the armature, and the test object. This is because the supporting system, the shaker body, the armature and the test object form a spring/mass/damper vibration system with multiple degree-of-freedom. The response of this multiple degree-of-freedom system is frequency dependent, thus leading to the varying measured force with frequency.

- Single frequency signal

The second signal is a single frequency sinusoidal signal with a short duration. This signal is named single frequency signal in this study. This type of signal can guarantee that the steady state response of the model is measured. This is because the duration of each single frequency can be controlled to last long enough so that soil has adequate time to reach a steady state response. In addition it can avoid the leakage error because the sampling duration for each excitation frequency is controllable.

An example of the harmonic loads under a certain single frequency (4600 Hz) is shown in Figure 3.23. It can be seen that the recorded duration of each single frequency input signal was around 1 s. It should be noted that only about 0.4 s of data corresponded to the action of the dynamic load. The reason for the 1 s data being recorded is due to the control system taking approximately 0.3 s to send the command from the signal generator to the shaker and for the system to respond. The 0.4 s of useful data was extracted from the data stream to carry out subsequent analysis.

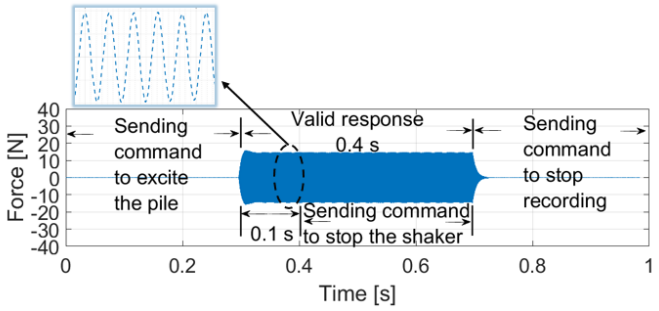


FIGURE 3.23: An example of single frequency input signal (dynamic load)

In this study, the frequency range of interest is 120 Hz to 7200 Hz in model scale, explained in Section 3.2.6. Centrifuge induced interference tests, presented in Section 3.2.11, indicated that low frequency noise was significant below 600 Hz. Therefore, the input frequencies used for the single frequency signal ranged from 600 Hz to 7200 Hz. The scaling factor for frequency was N=60, so 6 Hz (0.1 Hz in prototype) was chosen as the frequency spacing. A total of 1101 input frequencies: 600, 606, 612 ..... 7200 Hz (10, 10.1, 10.2, 10.3 ... 120 Hz in prototype scale) were used one by one to excite the model. The estimated total time was about 1200 s considering that thousands of frequencies employed in this study and that each frequency took about 1 s to excite the model. This type of signal took much longer time than the sweep signal (5 s) and resulted in a large amount of data to be processed.

3.2.12.2 Selection of input signal

In terms of the input signal, the challenge relates to the selection of an appropriate input signal type to ensure the soil-pile system can reach a steady state level of response. However, with the large number of frequencies being investigated, combined with the potential for very large data files due to high sampling frequency (see Table 3.5), input signals should be short enough to achieve efficient testing.

As discussed in the previous section, measured signals are affected by the electric noise and physical vibrations. Even though just two frequency ranges can affect the real signal significantly, at the other frequencies, the real signal which is supposed to be just the result of soil-pile interaction may be distorted by unwanted noise and vibrations. This is because the amplitude of ground-borne vibrations investigated in this study is very small and therefore vulnerable to electrical noise and vibration sources. In this study, the coherence function (detailed in Section 5.2.3) between the input signal and the output measurements is used to examine whether the model reached a steady state, evaluate the quality of measurements, and explore which type of input signal provides the best model response within an acceptable

testing time. The coherence is a value between zero and one. Zero indicates no correlation between the measured response (outputs = acceleration data from the Piezos) and the measured excitation (inputs = applied forces from the dynamic load cell) and one indicates the measured response is 100% aligned with the measured excitation.

Another important input parameter is the input voltage amplitude for the shaker. The dynamic load amplitude applied to the pile top which is provided by the shaker is proportional to the input voltage amplitude, hence so are the vibration level and shear strain level within the soil. As discussed in Section 2.1.1.5, railway-induced vibration is small and the shear strain level within the soil is still within the very small range. The soil behaviour is assumed to be in the linear elastic range. On the other hand, the relatively soft static load, as discussed in Section 3.2.7.2, may lead to a very small vibration level in the ground. Therefore, it is very important to ensure the input voltage amplitude for the shaker is high enough to generate observable vibrations, but not too high to avoid the generation of large shear strains. Some preliminary tests (Pre01_04, Pre01_05, Pre01_06, Pre02_04, Pre02_05 and Pre02_06) indicated 500 and 800 mV were appropriate voltage amplitudes for the shaker. The linearity of the model will be detailed in Chapter 5.

3.2.12.3 Test results and determination of input signal

The test results using two types of signals are compared in this section. All the tests presented were carried out under the same dead load (350.5 g) and with the same amplitude of 800 mV for the shaker so that only one influence factor, type of input signal, is being investigated. The coherence values between the dynamic forces measured by the dynamic load cell and accelerations in the interior of soil (VPNP1 and VPNP3) and on the top of the pile (PCV) are selected to make a comparison between two signal types.

- Sine chirp signal

The coherence values obtained using a sine chirp signal (Pre03_T02: input signal varies from 600 Hz to 7200 Hz within 5 seconds) are shown in Figure 3.24. It can be seen that the coherence between the input signal (dynamic force) and the output (accelerations) was low at the frequency range of 600 Hz to 4000 Hz. This is because the sweep signal from the signal generator was broken into 2048 steps. Each frequency component only lasts 0.003 seconds (5/2048=0.003) which is shorter than the period of frequency components below 410 Hz (1/410=0.003). This phenomenon means that the lasting time of each excitation frequency component may affect the response of the model. Figure 3.24 also indicates that the

coherence was larger than 0.9 at most frequencies above 4000 Hz. Given that the period of 4000 Hz is 0.0003 seconds, and 0.003 seconds is about 10 times the period of 4000 Hz, this suggests that each frequency component needs at least ten periods to vibrate the model to obtain a good response.

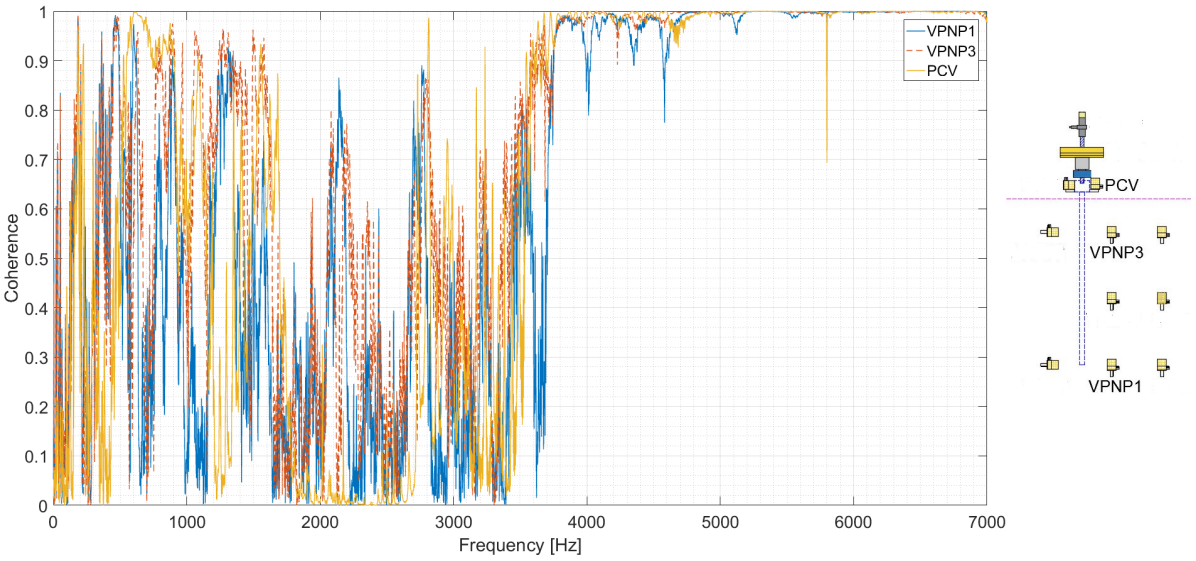


FIGURE 3.24: Coherence at VPNP1, VPNP3 and PCV

- Single frequency signal

Results from the sine chirp signal indicated that to obtain a good response, the duration of each excitation frequency component was about 10 times the period. To clearly explain this, time history data measured from the dynamic load cell and the soil accelerometers (VPNP3 and VPDP3) under a certain single frequency (4600 Hz) from Test Pre03_T03 is shown in Figure 3.25. It can be seen that there was a time delay between the input signal and the output signal, approximately 0.0006 s and 0.002 s for VPNP3 and VPDP3, respectively. This is because the shear wave generated at the soil-pile interface takes time to travel to the measurement locations. If the duration for a certain input frequency is too short, poor soil response is recorded and this can result in a low coherence. In addition, Figure 3.25 suggests a clear and steady soil response was detected after about 10 cycles. Therefore, the duration for each frequency component adopted in this study should be at least 20 periods to measure steady state model response.

In this study, a total of 1101 input frequencies: 600, 606, 612 ..... 7200 Hz (with a frequency spacing of 6 Hz) were used in the centrifuge tests. 0.4 s was chosen as the duration for every single frequency which was larger than 20 times the period of every frequency, as shown in Figure 3.23. An example of coherence function value from Test Pre03_T03 and Test Pre04_T03 is shown in Figure 3.26

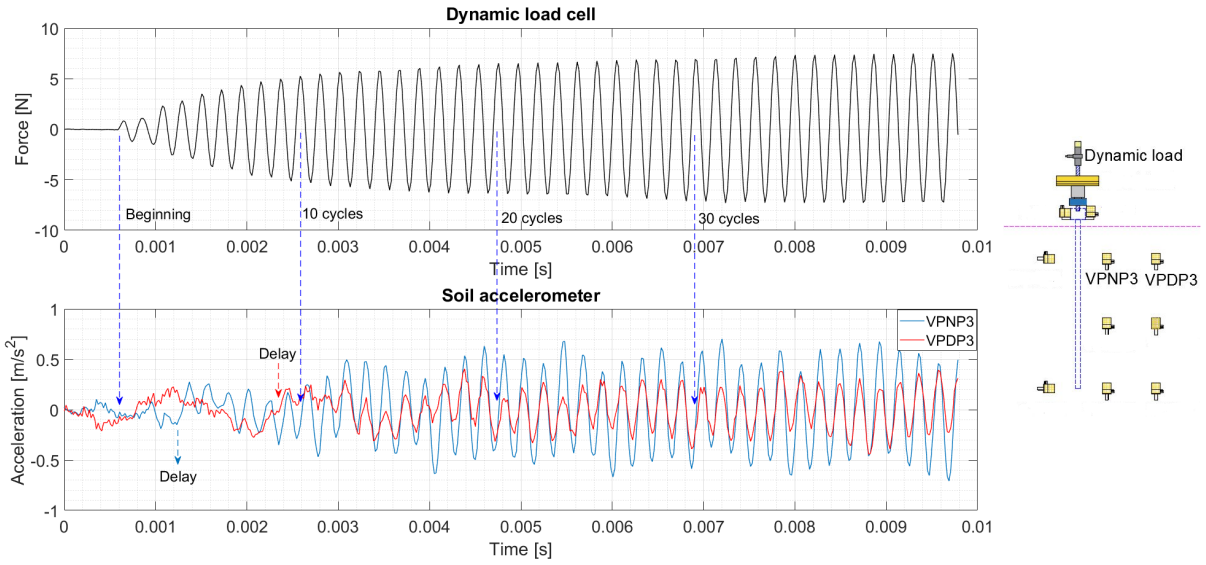


FIGURE 3.25: Steady state response of soil (4600 Hz)

and Figure 3.27 respectively. Results show good coherence was obtained using the two different supporting systems. It can be seen that the coherence values at selected locations were much better (close to 1) than that using the sine chirp signal. Therefore, the single frequency signal with a good control over frequency, amplitude and duration was adopted in the remainder of the study to obtain high quality and high resolution signals despite the drawbacks of long test durations and management of large data files. It can also be seen that more low coherence values were obtained using the new supporting system in Test Pre04_T03 to secure the shaker. This is another reason for not using the new supporting system.

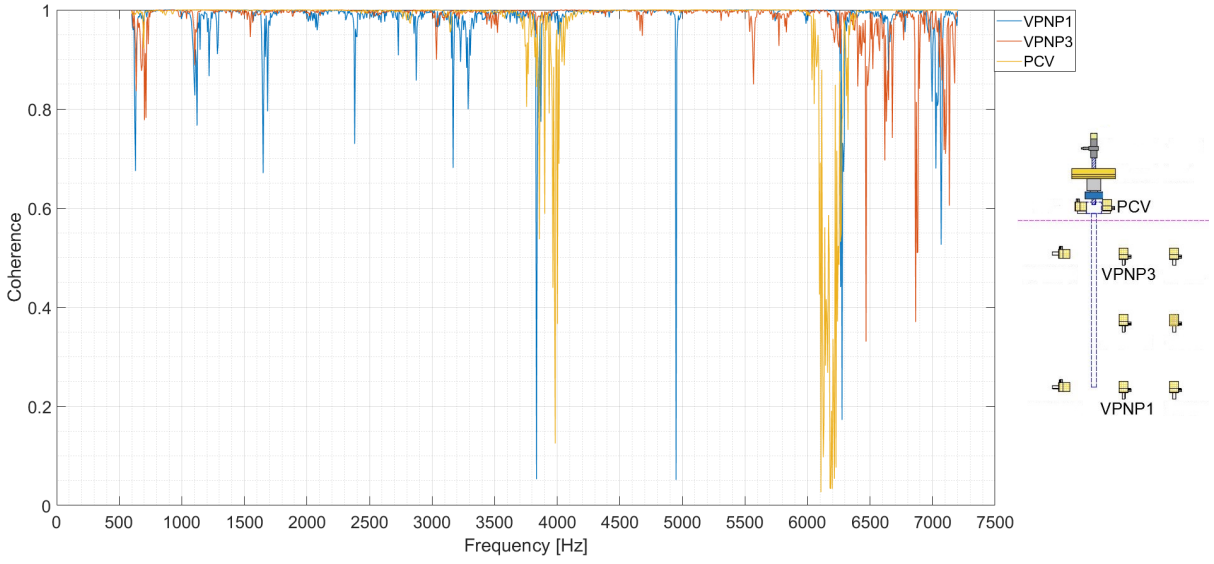


FIGURE 3.26: Coherence at VPNP1, VPNP3 and PCV (Pre03_T03: old supporting system)

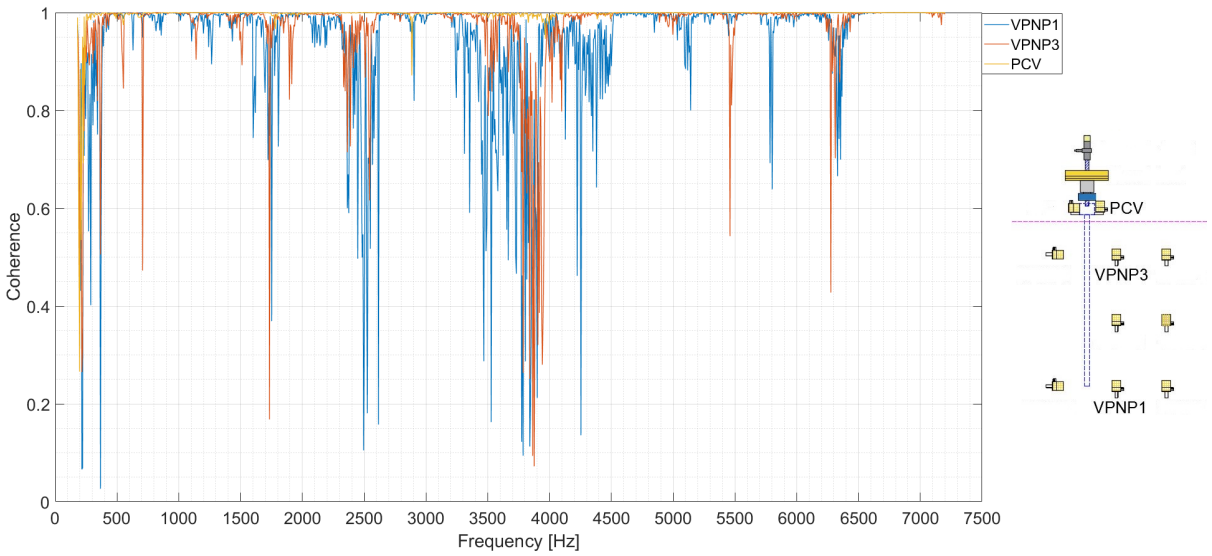


FIGURE 3.27: Coherence at VPNP1, VPNP3 and PCV (Pre04_T03: new supporting system)

It should be noted that an objective of this study was to understand how the pile-soil system responds at specific frequencies to subsequently allow for the calibration of a numerical model using results from the centrifuge test. Although the vibrations emanating from a train vary rapidly in terms of amplitude and frequency, this transient behaviour can only be investigated once the simpler response to a single frequency input is fully understood and can be captured within the numerical analysis.

3.2.13 Summary of ground-borne vibration tests

Model development results related to centrifuge and shaker induced interference and the input signal for the shaker have been presented in the Section 3.2.11 and Section 3.2.12, respectively. As discussed above, the old supporting system and the single frequency signal with a frequency range of 600 Hz to 7200 Hz were used in formal ground borne vibration tests (Test GBV). A series of tests were carried out within Test GBV to investigate the soil-pile interaction and the transmission of ground-borne vibrations generated from the excitation of the top of a single pile.

A series of combinations of dead loads (surcharge mass) and dynamic loads (shaker excitation) were chosen to investigate their effects on pile and soil behaviours. Details of input signals for the shaker and dead loads used in Test GBV are listed in Table 3.8 (all at model scale). All the test results are presented in Chapter 5.

TABLE 3.8: Details of dead loads and input signal in GBV (model scale)

Test name	Surcharge mass(g)	Amplitude (mV)	Vibration signal	Frequency range(Hz)	Frequency spacing (Hz)
GBV_m1	726.5	500/800	single frequency	600-7200	6
GBV_m2	350.5	500/800	single frequency	600-7200	6
GBV_m3	115.0	500/800	single frequency	600-7200	6

3.3 Shear wave velocity measurement using air-hammer and bender elements

3.3.1 Introduction

In order to obtain the in-flight measurements of soil stiffness profiles in the range of elastic deformations, the air hammer test was employed to measure the shear wave velocity v_s of the soil. However, limited by the small model in the centrifuge, shear wave velocities of only three soil layers were measured, which was not representative of the entire soil profile. Therefore, bender element tests incorporated into a triaxial cell were conducted to obtain a second evaluation of soil stiffness depending on confining stress. Another reason for performing the bender element tests is only v_s could be obtained from air hammer testing. Therefore, pressure wave velocity was measured using bender element testing to obtain the elastic modulus of the soil. The obtained data and profiles of soil stiffness were subsequently used as inputs for the numerical modelling, as described in Chapter 6.

As discussed in Section 2.3.3.2, the use of Duxseal may alter the initial K_0 condition of the centrifuge model. The combined results from the air hammer and bender element tests can be manipulated to back-calculate the lateral earth pressure coefficient along depth in the the centrifuge model. Therefore, the effects of the Duxseal on lateral stress and soil properties can be evaluated. These two methods are detailed in this section and results are presented in Chapter 4.

3.3.2 Air hammer test in the centrifuge

As mentioned in Section 2.2.2.2, several methods have been developed by centrifuge modellers to measure in-flight shear wave velocity. In this test, a miniature air hammer, see Figure 3.29, was used to generate the shear waves. The air hammer is a 10 cm long tube with a 20 mm long pellet inside. The pellet was made of 2 PTFE hollow cylinders, an iron cylinder and 2 bolts, as shown in Figure 3.28. The internal diameter of the tube is 6 mm. To generate the shear waves within the soil, air is supplied from one end to the other end, and the pellet is forced to impact

the end of the tube. Consequently, the tube moves slightly in the soil resulting in a small shear wave. A series of preliminary tests were conducted first to determine the appropriate air pressure for the air hammer test in the centrifuge. Results indicated that 50 kPa to 100 kPa was enough in this study to generate the impact while minimising the shear strain level in order to get a value for shear modulus as close to G_{max} as possible.

The progression of the shear waves is monitored by an array of MEMS accelerometers (AHA-M). A vertical array of MEMS accelerometers (ADXL001-70BEZ) were positioned at various depths above the air hammer to detect and record the shear waves. Four MEMS accelerometers with a range of +/- 70 g were mounted on a continual flexible plastic sheet (as shown in Figure 3.29) which offers greater accuracy regarding inter-instrument spacing. The measurement range of the MEMS is considerably greater than the measured accelerations generated from the shear wave, however MEMS with a smaller measurement range and a high frequency range were not commercially available. The sensitive axis for the MEMS accelerometers monitoring the shear wave was horizontal.

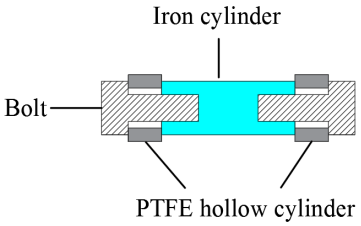
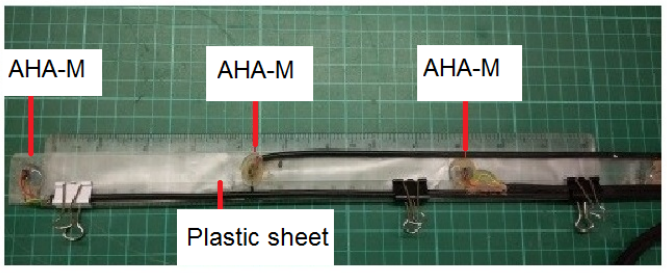


FIGURE 3.28: Air hammer pellet



MEMS accelerometers array



Air hammer

FIGURE 3.29: Air hammer and MEMS accelerometers

The model depth in the centrifuge test was 440 mm (26.4 m in the prototype). Air hammer MEMS accelerometers were installed at 60 mm, 180 mm, 300 mm and 420 mm in model scale (3.6 m, 10.8 m, 18 m and 25.2 m in prototype scale, shown in Figure 3.30) to measure the average shear wave velocity ($v_{s,AHA,1}$, $v_{s,AHA,2}$ and $v_{s,AHA,3}$) of each soil layer (L1, L2 and L3).

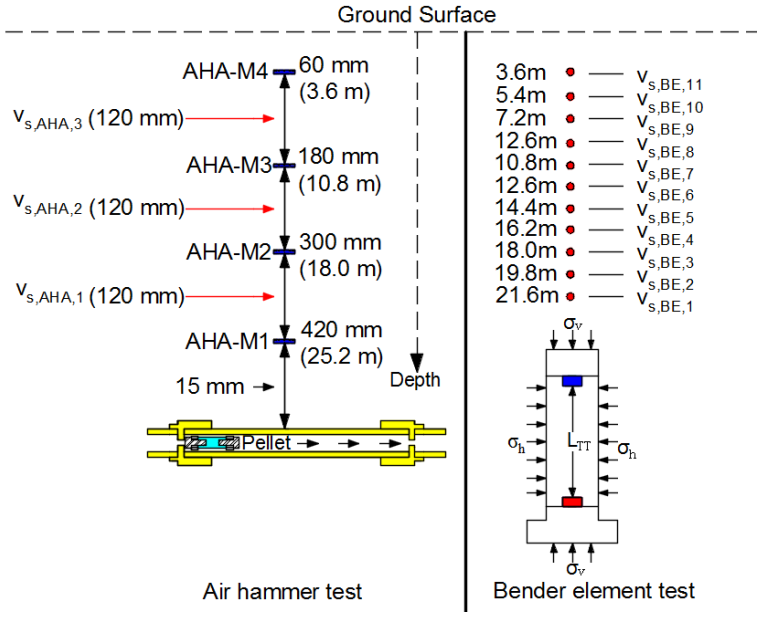


FIGURE 3.30: Air hammer and bender element test setup

The average shear wave velocity in a soil layer can be calculated by obtaining the elapsed time the wave takes between two adjacent accelerometers and the corresponding distance. A high sampling rate of 100 kHz was used to record the acceleration time histories from the four MEMS to create a sufficiently small sampling interval relative to the shear wave travel time to avoid low-resolution estimates (Lee et al., 2014). The data processing is presented in Chapter 4.

3.3.3 Bender element test in the triaxial cell

To supplement the results from the air hammer tests and obtain a better estimation of soil stiffness profile, wave velocities were determined at 11 depths, corresponding to 11 levels of confining stress within prototype soil, as shown on the right-hand side in Figure 3.30. The 11 depths used in bender element testing were selected based on the embedded MEMS depths in the centrifuge tests.

3.3.3.1 Operating principle of a bender element system

A bender element is typically composed of two piezo-ceramic plates rigidly bonded together. When a driving voltage is applied to the element, the plates deform.

Similarly, when the element is forced to deform, the imposed deformation generates a measurable electrical signal (Mitaritonna et al., 2010). The former works as a source and the latter works as a receiver of the wave motion. If the elements are inserted into a soil and have good coupling, the perturbation generated by a source will transfer into the soil and be detected by a receiver (Camacho-Tauta et al., 2012, Kumar and Madhusudhan, 2010, Lee and Santamarina, 2005). The source and receiver can be placed at each end of a specimen, shown in Figure 3.33, and the travel time from source to receiver can be obtained by analyzing the signals, detailed in Chapter 4. Furthermore, the shear wave velocity or pressure wave velocity can be calculated.

3.3.3.2 GDS Bender Element System

In this study, the GDS Bender Element System (GDS-BES) supplied by the GDS Instruments, UK, was used to conduct the shear and pressure wave velocity test. The system, see Figure 3.31, consists of the following components:

- Two bender element inserts with adapted top cap and pedestal (Figure 3.32)
- External control box
- High speed PC data acquisition and control card
- Windows based Bender Element System control and acquisition software

As shown in Figure 3.32, the GDS bender elements are manufactured as an insert that can be mounted in a top cap or pedestal. A single pair of bender elements (BE) are incorporated into a triaxial cell which can apply vertical (σ_v) and horizontal (σ_h) stress to the soil specimen (50 mm in diameter (D) and 100 mm in height (L)), see Figure 3.33. The GDS bender elements can generate pressure and shear waves separately, as shown in Figure 3.33. Both shear wave velocity and pressure wave velocity can be measured at each depth, see Figure 3.30. The two bender elements must be placed in line so that the signal sent by a source could be received by a receiver due to the polarisation of the source bender element. This is because the polarisation determines not only the direction of motion of the shear wave generated by a source bender element but also the expected deformation direction of a receiver. If the two bender elements are placed out of line, the source signal may not be received.

An extremely high sampling rate of 2000 kHz was adopted in this test to obtain high resolution estimates; the reasons are discussed in the next section. A sine wave

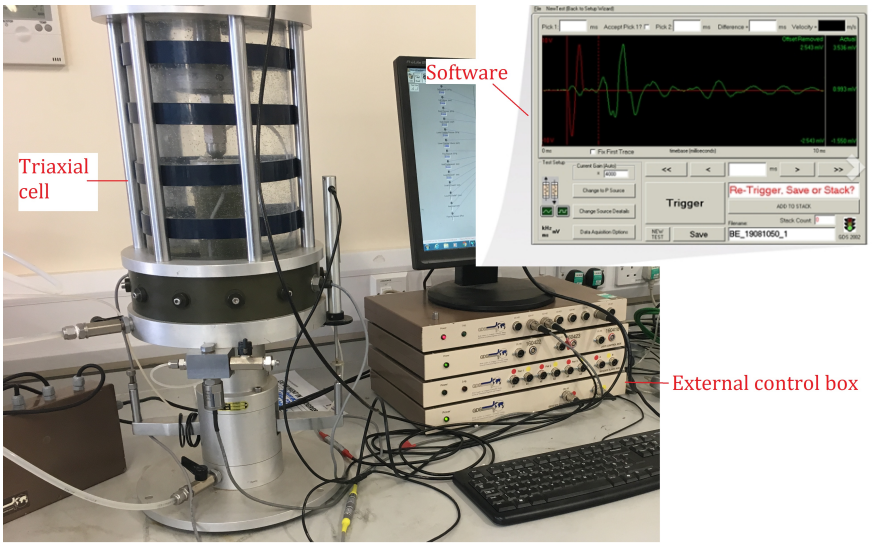


FIGURE 3.31: GDS Bender Element System

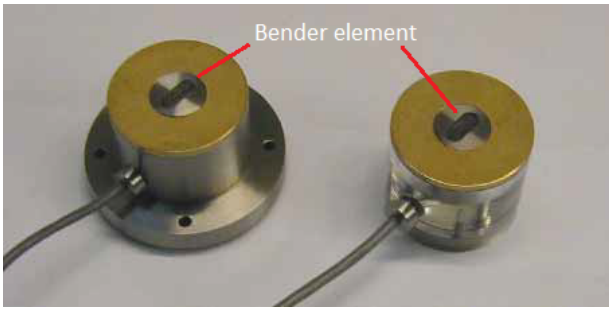


FIGURE 3.32: Pedestal (left) and top cap (right) with bender elements

signal (commonly used input signal) was used throughout this study to perform bender element tests. The wave velocities (v_s and v_p) can be obtained by measuring the distance (L_{TT}) between the tips of two bender elements and the travel time (t). Methods used to determine the travel time are discussed in Chapter 4.

3.3.3.3 Factors affecting the accuracy of bender element testing

Several requirements described as follows must be taken into consideration to make sure the tests are conducted correctly (Camacho-Tauta et al., 2012, El-Sekelly et al., 2013):

- Length of two bender elements (4 mm in this study) must be subtracted from the soil specimen height (L) to obtain the tip-to-tip distance: L_{TT}. This means L_{TT} is less than 96 mm in this study.
- Slenderness ratio of soil specimen (L_{TT}/D) is less than 2 to reduce the effects of the reflections from the lateral boundaries affect the signals.

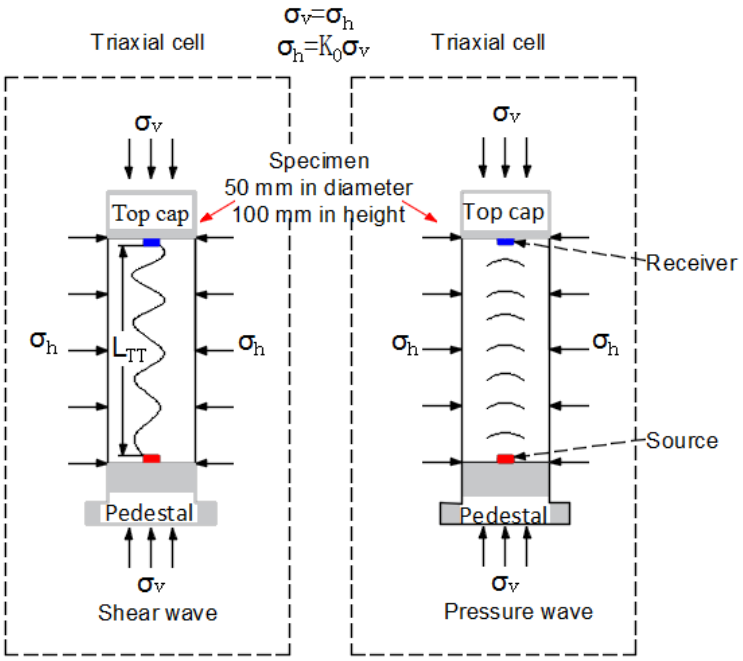


FIGURE 3.33: A schematic view of bender element testing in triaxial cell

- Equipment time delay of the system (the travel time in electronic equipment, cables and connections) must be subtracted from the total travel time to obtain the real tip-to-tip travel time. The equipment time delay can be tested by placing two tips of the two bender elements in direct contact (Bartake and Singh, 2007) and measuring the calibration time t_c between the electrical pulse sent by the source and received by the receiver. The time delay can be determined at the first deflection point from the receiver signal. Equipment time delay of GDS-BES used in this study was measured and it was 6 μs, as shown in Figure 3.34.

- If the source is too close to the receiver, the arrival of the shear wave is masked by the pressure wave generated together with the shear wave, this being defined as the near field effect. The near field effect leads to the difficult identification of the first arrival of shear waves. To avoid near field effect, the tip-to-tip distance L_{TT} and the wavelength λ must satisfy: $2 < L_{TT}/\lambda < 9$ (Camacho-Tauta et al., 2012). λ equals shear wave velocity times the period T: $\lambda = v_s T$. According to the air hammer test results, the period for the shear wave velocities were estimated as 0.05-0.1 ms to carry out bender element tests.

- Given that the estimated period was 0.05-0.1 ms (10-20 kHz), the

sampling rate adopted in this test was 2000 kHz to obtain high resolution data.

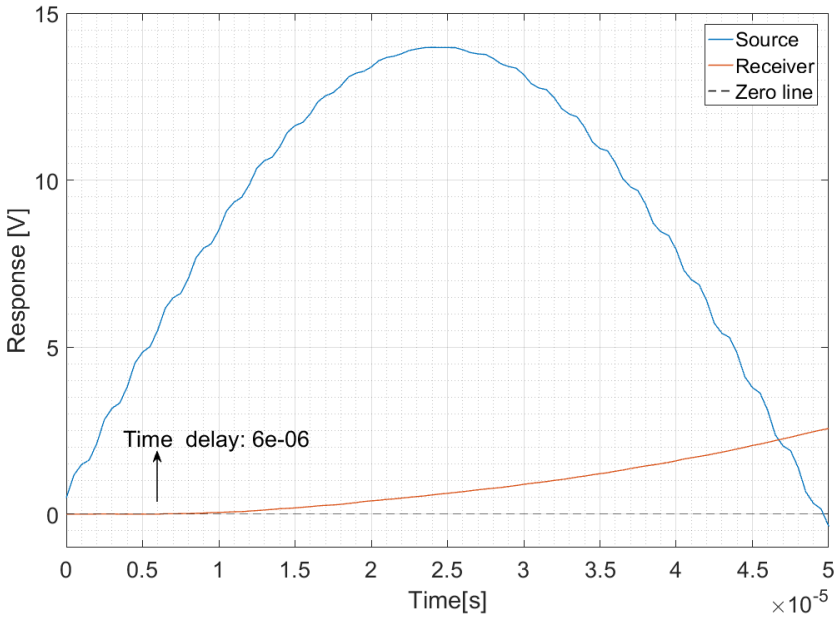


FIGURE 3.34: Equipment time delay of GDS-BES

3.3.3.4 Preparation and deformation measurement of soil specimen

A split mold was used to prepare the soil specimen. In order to force the membrane to stick to the split mold, the mold was sealed by the silicon grease and a vacuum pump was employed. The dry HST95 Congleton sand was air pluviated to obtain a relative density of approximately 85%, which is the same as the centrifuge tests. After the top cap was placed on the top of the specimen and the membrane and O-rings were used to seal the specimen, 20 kPa of vacuum was applied onto the interior of the specimen to secure the specimen and the mold was removed. The specimen was placed in position and the triaxial cell was filled with water. The vacuum was replaced by cell pressure gradually.

The specimen deforms after confining stress is applied, therefore the tip-to-tip distance L_{TT} changes with stress. In order to measure the deformation of the specimen, two vertical local LVDTs capable of measuring small displacement were installed, as shown in Figure 3.35. The displacement range of the local LVDT is $\pm$2.5 mm, and the resolution using 16 bit data acquisition is 0.1 μm, allowing the detection of very small axial strains.

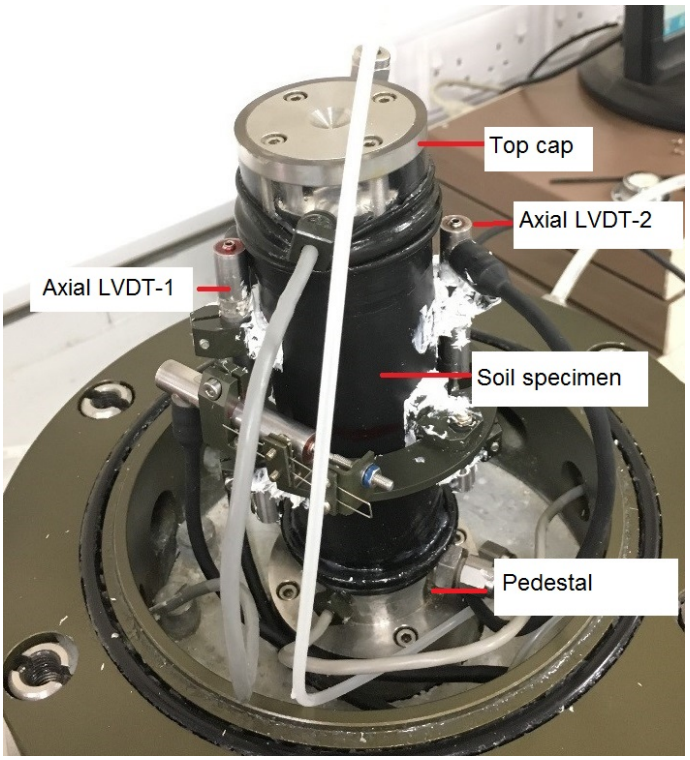


FIGURE 3.35: Bender element test in triaxial cell

3.3.3.5 Stress state on the specimen: isotropic versus anisotropic

As discussed in Section 2.2.2.3, the following general equation can be used to predict G_{max} of normally consolidated round-grained dry sands (Hardin and Richart, 1963). The constant B in Equation 3.7 depends on the grain shape and the grain-size distribution, and varies slightly with sand types. One of the objectives in this project is to obtain the constant B for the HST95 Congleton sand, and results are detailed in the next chapter.

$$G_{max} = B\frac{(2.17-e)^2}{1+e}(\sigma_m^{'})^{0.5} \tag{3.7}$$

where G_{max} is dynamic shear modulus (kPa), e is the void ratio of the soil model and $\sigma_m^{'}$ is the mean effective stress (kPa).

For a shear wave travelling in the soil, particle motion is perpendicular to the direction of wave propagation. Due to the nature of shear waves, the stress state (the vertical stress and horizontal stress) could affect the value of the shear wave velocity. It has been found by Stokoe et al. (1985) that for shear waves which travel vertically in the soil, the vertical and horizontal effective stresses (σ_v' and σ_h') contribute equally to the value of the shear wave velocity, which implies that σ_m' in Equation 3.7 can be taken as:

$$\sigma'_m = (\sigma'_v)^{0.5}(\sigma'_h)^{0.5} \tag{3.8}$$

Equation 3.8 was examined by El-Sekelly et al. (2014) using the centrifuge based bender element tests. According to Equation 2.6, Equation 3.7 and Equation 3.8, the equation to calculate v_s can be expressed by:

$$v_s = \sqrt{B\frac{(2.17-e)^2}{(1+e)\rho}\sigma_v'^{0.125}\sigma_h'^{0.125}} \tag{3.9}$$

Equation 3.9 also suggests the constant B is a stress state independent factor. To verify this point, two stress states were conducted in the bender element test to obtain the constant B:

- Isotropic stress state: $\sigma_v^{'} = \sigma_h^{'}$
- Anisotropic stress state:

$$\sigma'_h = K_0\sigma'_v \tag{3.10}$$

where K_0 is the at rest earth pressure coefficient.

For normally consolidated dry sand, Equation 3.11 can be used to calculate K_0 (Jaky, 1944). The critical angle of internal friction for dry sand ϕ is usually around 30°-40° (El-Sekelly et al., 2013). Therefore, K_0 is less than 1. When the air hammer test was performed in the centrifuge, the stress state within the soil was anisotropic ($\sigma_h^{'} = K_0\sigma_v^{'}$), which means the anisotropic stress state should be used to carry out the bender element test to compare the bender element test results with the air hammer testing. In this study, the critical friction angle of dry Congleton sand was 31° by Lauder (2010), and K_0 was obtained by Equation 3.11 (K_0=0.5).

$$K_0 = 1 - \sin(\phi) \tag{3.11}$$

To distinguish the vertical effective stress in the prototype from the vertical stress on the specimen, the vertical effective stress in the prototype is denoted by $\sigma_{v,p}^{'}$ and the vertical and horizontal effective stresses on the specimen is denoted by $\sigma_{v,s}^{'}$ and $\sigma_{h,s}^{'}$ in this study. The stresses applied using two types of stress states, as shown in Table 3.10 can be calculated by the equations listed in Table 3.9.

In Table 3.9, $p^{'}$ is defined as effective confining stress and it was the same in both isotropic and anisotropic stress state tests. $\sigma_{v,p}^{'}$ can be calculated using:

TABLE 3.9: Equations to calculate $\sigma'_{v,s}$ and $\sigma'_{h,s}$ in two stress state tests

Anisotropic stress state test	Isotropic stress state test
$\sigma'_{v,s} = \sigma'_{v,p}$	$\sigma'_{v,s} = \frac{2}{3}\sigma'_{v,p}$
$\sigma'_{h,s} = K_0\sigma'_{v,p}$	$\sigma'_{h,s} = \frac{2}{3}\sigma'_{v,p}$
$p' = \frac{\sigma'_{v,s} + 2\sigma'_{h,s}}{3} = \frac{2}{3}\sigma'_{v,p}$	$p' = \frac{\sigma'_{v,s} + 2\sigma'_{h,s}}{3} = \frac{2}{3}\sigma'_{v,p}$

$$\sigma'_{v,p} = \rho g h \tag{3.12}$$

where: ρ is the dry density of the sand (1739.25 kg/m^3), g is gravitational acceleration (9.8 m/s^2), h is the depth (see Table 3.10).

TABLE 3.10: Stresses applied in two types of stress state tests

Anisotropic stress state test					Isotropic stress state test		
Step	Depth (m)	$\sigma'_{v,s}$ (kPa)	$\sigma'_{h,s}$ (kPa)	p' (kPa)	Step	Depth (m)	$\sigma'_{v,s} = \sigma'_{h,s} = p'$ (kPa)
1	3.6	61.36	30.68	40.91	1	3.6	40.91
2	5.4	92.04	46.02	61.36	2	5.4	61.36
3	7.2	122.72	61.36	81.81	3	7.2	81.81
4	9	153.40	76.70	102.27	4	9	102.27
5	10.8	184.08	92.04	122.72	5	10.8	122.72
6	12.6	214.76	107.38	143.18	6	12.6	143.18
7	14.4	245.44	122.72	163.63	7	14.4	163.63
8	16.2	276.12	138.06	184.08	8	16.2	184.08
9	18	306.80	153.40	204.54	9	18	204.54
10	19.8	337.48	168.74	224.99	10	19.8	224.99
11	21.6	368.16	184.08	245.44	11	21.6	245.44

In addition, Equation 3.9 and Equation 3.10 can be manipulated to obtain expressions for v_s:

$$v_s = \sqrt{B\frac{(2.17-e)^2}{(1+e)\rho}\sigma_v'^{0.25}K_0^{0.125}} \tag{3.13}$$

Equation 3.13 indicates that the at rest earth pressure coefficient, K_0, of a certain soil layer can be back calculated if the values of the others are already known. The process to back calculate K_0 is detailed in Chapter 4. This can be used to investigate the effects of Duxseal on lateral earth pressure coefficient and the soil stiffness in the centrifuge. Test results related to v_s, G_{max}, K_0 and constant B are presented in Chapter 4.

Chapter 4

Estimation of soil stiffness and Duxseal effect in the centrifuge

4.1 Introduction

This chapter discusses the methods used to process the data obtained from the air hammer tests in the centrifuge and the bender element tests incoporated into a trixial cell, detailed in Section 4.2. Two empirical equations were used, as shown in Section 2.2.2.2, to calculate the shear modulus of the soil. The tested and calculated results are illustrated and compared in Section 4.3.1, Section 4.3.2 and Section 4.4.

Two stress states, anisotropic and isotropic, were employed, shown in Table 3.10, to compare the bender element test results with the air hammer testing and investigate the effects of stress state on wave velocities. In addition, the constant B in Equation 3.13 which should not be affected by the stress state can be obtained. These two tests are denoted as BE-aniso and BE-iso respectively in this study and the test results are presented in Section 4.3.3.

In addition, the effect of Duxseal on lateral earth pressure coefficient within the centrifuge model was studied by analyzing the results obtained from the air hammer tests and the bender element tests. Two formal centrifuge based air hammer tests were carried out to measure the shear wave velocities of three soil layers: one with Duxseal (vibration absorbing material, see Section 3.2.5) along the sides of the container and one without Duxseal: AHA-C1 and AHA-C2. In each test, the air hammer was triggered over 10 times so that average shear wave velocities can be obtained. Duxseal was attached on the bottom of the container in both tests to only investigate the side Duxseal effects on soil stiffness in the centrifuge. The detailed procedure to back calculate K_0 is presented in Section 4.5. Furthermore,

the potential effects of Duxseal on the horizontal stress field within the centrifuge is investigated. The results are used to calibrate the static numerical models in FLAC3D, see Chapter 6.

Table 4.1 illustrates all the tests carried out to investigate the stress state effect and the Duxseal effect.

TABLE 4.1: Details of dead loads and input signal in preliminary tests

Test name	Test ID	Test description
Bender element in the triaxial cell	BE-aniso	Anisotropic stress state test (see Table 3.10)
Bender element in the triaxial cell	BE-iso	Isotropic stress state test (see Table 3.10)
Air hammer in the centrifuge	AHA-C1	with Duxseal along the sides of the container
Air hammer in the centrifuge	AHA-C2	without Duxseal along the sides of the container

4.2 Signal processing method

The typical measured signals from both the air hammer and bender element tests are illustrated first to show the signal properties from both tests. Then, the advantages and disadvantages of different signal processing methods are discussed and reasons for choosing the cross correlation method are explained.

4.2.1 Typical data from air hammer and bender element tests

Typical data from the air-hammer (AHA) and bender element (BE) tests are shown in Figure 4.1 and Figure 4.2, respectively. The data from a depth of 3.6 m was chosen here as an example. Data from AHA and BE tests at all depths had a similar pattern.

Figure 4.1 indicates the relatively low resolution signals measured from the air hammer tests in the centrifuge. This is because a sampling frequency of 100 kHz, the highest sampling frequency the data acquisition system could achieve, was used and the shear waves generated by the air hammer impact had a frequency of about 10 kHz, which was determined by performing a Fourier transform analysis. Therefore, only about 9 to 10 data points over one cycle were recorded, shown in Figure 4.1. This low resolution data can affect the accuracy of the travel time determination methods, as discussed in the next section. In addition, reflected waves from the rigid container boundaries or elements embedded in the model soil, such as the pile, piezoelectric accelerometers and cables, decay of the wave signals, electrical noise and mechanical vibrations from the centrifuge can also distort the detected signals.

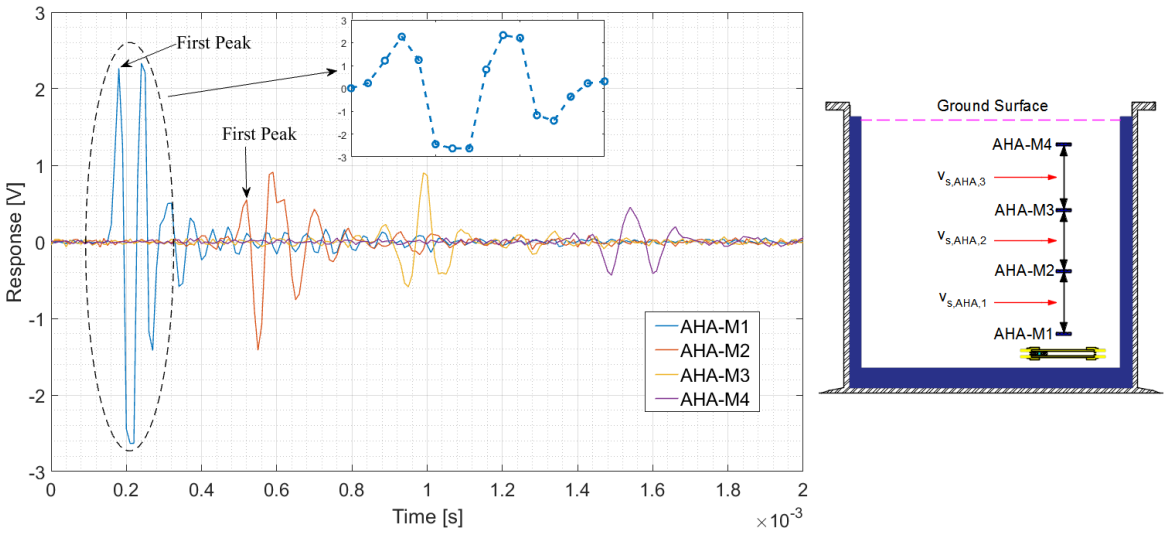


FIGURE 4.1: Typical data from a centrifuge based air-hammer test

In contrast, high resolution signals, due to the high sampling rate of 2000 kHz used, obtained from the bender element tests (Figure 4.2) suffer to a lesser degree from these issues mentioned above. This is because the running of a traxial test does not generate noise and vibrations as that in the centrifuge.

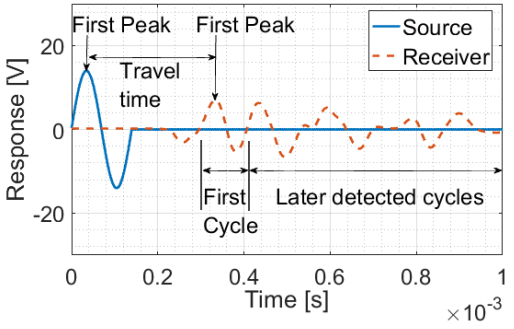


FIGURE 4.2: Typical data from a triaxial based bender element test (depth=3.6 m)

4.2.2 Methods to determine travel time

A key challenge is determining the travel time between two transducers; the travel distance between two transducers is already known, detailed in Section 3.3. The travel time can be calculated by comparing time records from two accelerometers or the two bender elements. There are two main types of methods to determine the travel time: direct time methods and indirect time methods (Karl, 2005).

4.2.2.1 Direct time methods

Direct time methods are based on the interpretation of the time histories, as shown in Figure 4.1 and Figure 4.2, obtained from transducers. Some characteristic points, such as the first arrival points and the first peak points, in the signals are picked up and their shifts in time are used to calculate the wave velocity.

The direct time methods are the most straightforward way to obtain the travel time. However, the identification of the chosen characteristic points is very difficult and requires some experience from the operator. This is due to the measured signals from air hammer or bender element tests being masked by the near field effect, explained in Section 3.3.3, and distorted by the noise and vibrations from surrounding equipment and reflections from the centrifuge model container. Additionally, the limited sampling rate can affect the accuracy of the time shift obtained from the direct time methods, as well as the cross correlation method, detailed in the following sections.

Among these two types of points, the first peak points are much easier to identify compared to the first arrival points, especially for the signals from AHA-M3 and AHA-M4 whose amplitudes were relatively low. Despite this, the low resolution of data still poses a challenge for implementing the peak to peak method. This is because the measured peak point on a discrete curve may be not the real peak point on a analog signal. As shown in Figure 4.1, 9 to 10 data points over one cycle were recorded, and this low resolution data can reduce the accuracy of the peak to peak method.

4.2.2.2 Indirect time methods

The cross correlation (xcorr) method is probably the most popular indirect time method, which is still performed in the time domain. The cross-correlation method determines the travel time between two correlated signals, i.e. source signal and receiver signal from bender element testing, by performing a point-wise multiplication to determine where two signals are best aligned. The source signal is shifted step by step and the point-wise multiplication is performed at each step to obtain the cross correlation function. The time shift between two correlated signals is obtained at the maximum (or minimum if the signals are negatively correlated) of the cross correlation function, as shown in Figure 4.3. Two correlated discrete signals are denoted as $s[k]$ and $r[k]$ and the cross correlation function $T_{sr}[n]$ is defined as (Rabiner and Gold, 1975):

$$T_{sr}[n] = \sum_{m=-\infty}^{\infty} s[m]r[m+n] \tag{4.1}$$

where the parameter n is an integer between positive and negative infinity.

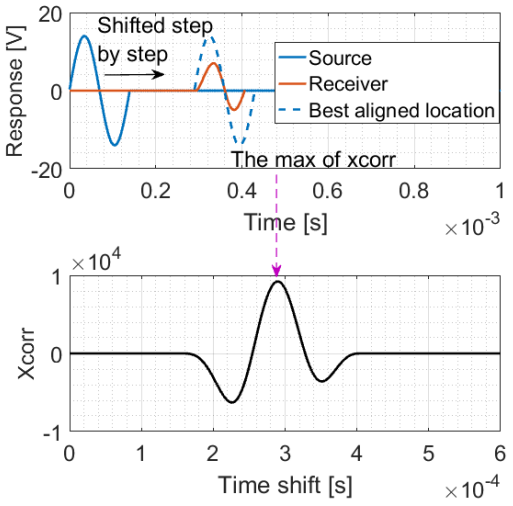


FIGURE 4.3: Cross correlation method (an example from BE test)

The output of the cross correlation method is also affected by the same signal quality issues mentioned above when processing air hammer test data. However, the cross correlation method avoids complications with picking characteristic points (i.e. first peak) from discrete signals. On the other hand, by including more distorted data (i.e. the later detected cycles, shown in Figure 4.1 and Figure 4.2), the determined time difference between two signals from the cross correlation method can be impacted, discussed as following.

To investigate the effect of data length on the cross correlation results, the mean value of $v_{s,AHA,1}$, see Figure 4.1, for the bottom soil layer (L_1) from 8 air-hammer strikes using different data lengths was calculated. One cycle, one and a half cycles and two cycles of measured data were extracted from the entire data length to perform the cross correlation method. Table 4.2 shows results and indicates that a longer data length resulted in lower estimations of $v_{s,AHA,1}$. This outcome highlights the importance of considering data with the highest possible signal-to-noise ratio.

In addition, three approaches were used to calculate v_s profile from the triaxial BE data: xcorr using the entire data length (normal xcorr), xcorr using the first cycle of the shear wave (first cycle xcorr), and the first peak to peak method (peak to peak), as shown in Figure 4.4. Results indicate that the peak to peak method agrees well with the first cycle xcorr method, but that using the full length of the

TABLE 4.2: Shear wave velocity from air-hammer testing using different data lengths

Data length	Strikes	Mean $v_{s,AHA,1}$
1 cycle	8	293.7 m/s
1.5 cycles	8	281.1 m/s
2 cycles	8	264.8 m/s

data set results in a lower estimate of v_s as well as an unrealistic scattered pattern of v_s with depth. This indicates that the first cycle xcorr method can provide more accurate estimate of the travel time.

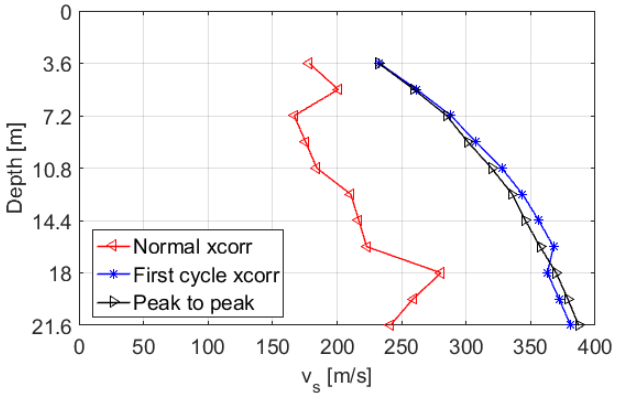


FIGURE 4.4: Shear wave velocity comparison using three approaches to analyse BE data

In conclusion, all methods mentioned above are affected by several factors. In terms of the high resolution signals obtained from the BE tests (Figure 4.2), both the peak to peak and cross correlation methods prove to be reliable, compared in Section 4.2.2.2. Given that low resolution signals are obtained from the air hammer tests limited by the relatively small sampling frequency, the cross correlation method was adopted in this study due to the fact that this method is less subjective, i.e. it avoids picking characteristic points. However, it is necessary to remove distorted data in order to obtain a higher degree of correlation and hence a more accurate value for the travel time, as discussed in Section 4.2.2.2.

Another issue associated with the accurate manipulation of this method is led by the change in the shear wave period along soil depth in the centrifuge, as discussed in detail in the following section.

4.2.2.3 Changing wave period effect on all methods

Another problem relates to the varying shear wave period with soil depth, see Figure 4.1. It can be seen from Figure 4.1 that the wave period at the bottom

(AHA-M1) is smaller than the top (AHA-M4). This is due to soil stiffness increasing with depth which results in the gradual decrease of shear wave period with increasing depth. It should be noted that the air hammer device only generates an impact, and this impact wouldn't affect the shear wave velocity and the shear wave frequency of the soil. The shear wave velocity and the shear wave frequency of the soil are determined by the properties of soil. In the centrifuge based air hammer tests, the varying shear wave period with depth can lead to a travel time error obtained from the first cycle xcorr method.

To explain the error from all methods caused by the changing period with depth, two artificial sinusoidal signals are used, as shown in Figure 4.5. Shear waves, generated by an impact, travel within the soil and are detected by two transducers one after another. If shear waves are not affected by any noise, vibrations, or reflections, and soil material damping is zero, two perfect smooth signals with the same amplitude should be measured, denoted as Signal 1 and Signal 2.

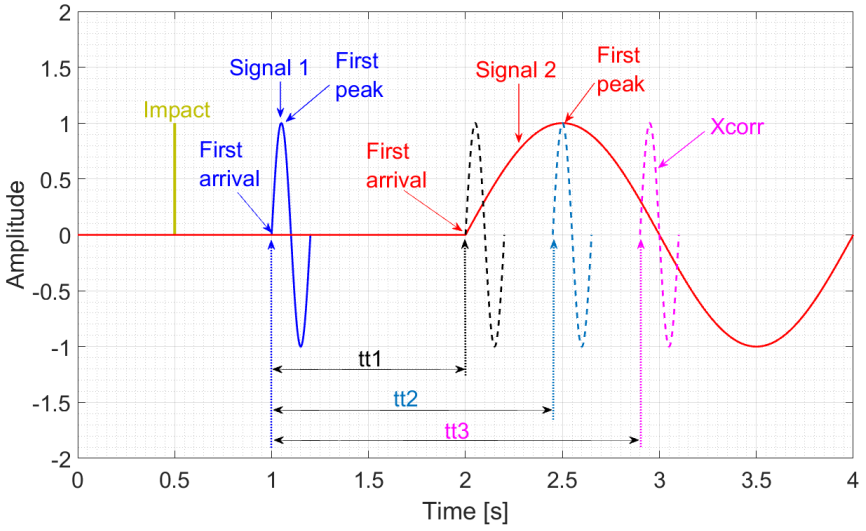


FIGURE 4.5: Error from cross correlation method by changing period

As shown in Figure 4.5, three dotted lines are used to show the travel time, tt1, tt2 and tt3, obtained from three methods: the first arrival method, the peak to peak method and xcorr method. The periods of two signals are denoted as T1 and T2. To clearly show the difference, only one cycle data is presented in Figure 4.5 and T2 is much lager than T1. If T1 equals T2, the three methods give the same travel time. If T1 is different from T2 (i.e. T2 is larger than T1 in this study), three methods give three different results. The real travel time, tt1, should be the time difference between the first two arrival points even if the two signals have different periods. However, the travel time obtained from the peak to peak method and

the xcorr method are tt2=tt1+(T2-T1)/4 and tt3=tt1+(T2-T1)/2 and the travel time errors are (T2-T1)/4 and (T2-T1)/2, respectively.

Theoretically, this indicates the shear wave velocities obtained from the two methods can be smaller than the real values because the two methods provide larger travel times. It is therefore important to quantify this error. To obtain the shear wave period at each depth, $T_{AHA,1}$, $T_{AHA,2}$, $T_{AHA,3}$ and $T_{AHA,4}$, the first cycle data was extracted from the signals measured by AHA-M1, AHA-M2, AHA-M3 and AHA-M4 to perform Fast Fourier Transform (FFT). The peak values and the corresponding frequencies, $f_{AHA,1}$, $f_{AHA,2}$, $f_{AHA,3}$ and $f_{AHA,4}$, can be obtained from the frequency domain. Then the shear wave periods can be calculated and v_s can be corrected. Table 4.3 shows the mean shear wave periods and mean v_s obtained from over 10 air hammer test strikes with side Duxseal along the centrifuge container (AHA-C1).

It can be seen from Table 4.3 that the wave period decreases with soil depth. Compared with the bottom three positions, the wave period at the top depth, $T_{AHA,4}$, was much larger than the others. The error in wave velocity resulting from the varying period was approximately 3.7% for the top soil layer. Consequently, the resulting error in G_{max} can reach up to 8% for the top soil layer. This error cannot be ignored and all the soil stiffness related parameters from the air hammer test illustrated in the following sections have had this correction applied.

TABLE 4.3: Mean wave period and v_s from AHA-C1 before and after correction

Shear wave period	Mean v_s before correction	Mean v_s after correction	Error
$T_{AHA,4}$: 12.6×10^{-5} s	-	-	-
$T_{AHA,3}$: 8.18×10^{-5} s	$v_{s,AHA,3}$: 229.05 m/s	$v_{s,AHA,3}$: 237.83 m/s	3.7%
$T_{AHA,2}$: 7.78×10^{-5} s	$v_{s,AHA,2}$: 304.13 m/s	$v_{s,AHA,2}$: 308.75 m/s	1.5%
$T_{AHA,1}$: 6.28×10^{-5} s	$v_{s,AHA,1}$: 342.85 m/s	$v_{s,AHA,1}$: 350.36 m/s	2.1%

4.3 Shear wave velocity: air-hammer and bender element test results

4.3.1 Bender element data versus empirical curves

The proposed empirical expression for the shear modulus, presented in Section 2.2.2.3, is applicable to the round grained Congleton sand used in this study. Results from the bender element test and the empirical equation are compared in this section. To make a direct comparison, equations to calculate the shear wave velocity are derived, since the wave velocity is determined directly from all the measurement

methods instead of the shear modulus. Given that the stress state was assumed to be anisotropic when performing air hammer testing, shear wave velocities presented in this section are all obtained under anisotropic stress (K_0=0.5).

Equation 2.9 for G_{max} proposed by Hardin and Richart (1963), Equation 3.8, Equation 3.10 and Equation 3.12 can be can be manipulated to obtain expressions for v_s:

$$v_s = \sqrt{7000\frac{(2.17-e)^2}{(1+e)\rho}}(\rho g)^{0.25}K_0^{0.125}h^{0.25} \tag{4.2}$$

Shear wave velocities from BE tests, along with results using Equation 4.2 are shown in Figure 4.6. It can be seen from this figure that Equation 4.2 agrees very well with the bender element test results, with differences less than 1 m/s (0.5%). This suggests Equation 2.9 can be used to calculate the shear modulus of dry Congleton sand.

According to Equation 4.2, the basic relationship between v_s and h is:

$$v_s = a \times h^{0.25} \tag{4.3}$$

where a is a fitting parameter.

The curve fitting results conducted in MATLAB were obtained based on the above relationship using bender element test results, denoted as BE-curve fitting in Figure 4.6. This curve is used for the analysis in the following section.

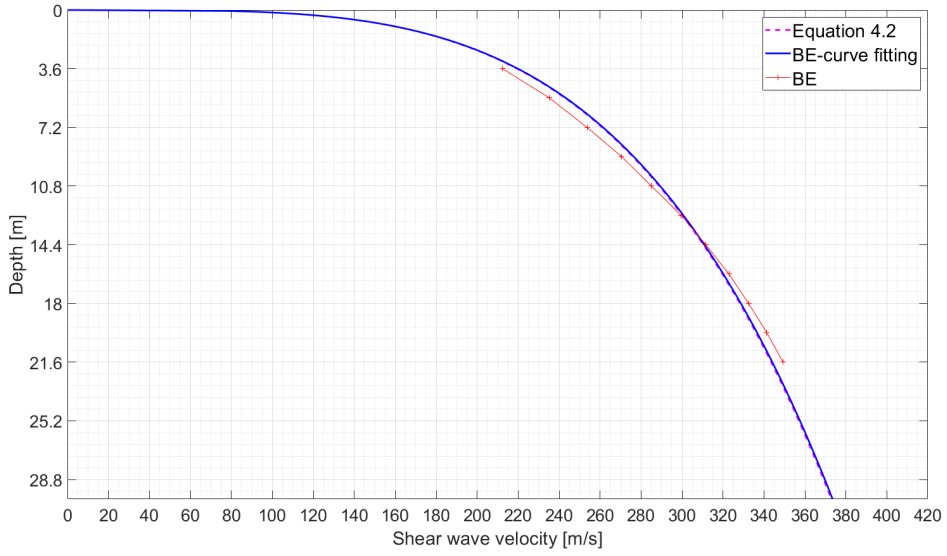


FIGURE 4.6: Shear wave velocities from BE and Equation 4.2

4.3.2 BE data versus air-hammer data

Results from the air hammer and bender element tests are compared in this section. The ratio of horizontal to vertical stresses applied in the BE tests was 0.5 to match the anisotropic stress state in the centrifuge with an assumed $K_0 = 0.5$. In the air hammer test, the shear wave velocity is the mean value of a soil layer. Tens of strikes were conducted to obtain the mean shear wave velocities of three soil layers. However, the bender element test provides the shear wave velocity at a certain depth. In order to compare the AHA with the BE directly, the averaged velocities of these three soil layers were calculated by integrating the equation $v_s = a \times h^{0.25}$ obtained from bender element testing with respect to h. The parameter a was 159.6 based on the curve fitting results from the previous section. Given that a shear wave travelling with a velocity of v_s from h_1 to h_2, the elapsed time t can be calculated by:

$$t = \int_{h_1}^{h_2} \frac{dh}{v_s} = \int_{h_1}^{h_2} \frac{dh}{a \times h^{0.25}} = \frac{h_2^{0.75} - h_1^{0.75}}{a \times 0.75} \tag{4.4}$$

Then the average velocity v_a from bender element testing is obtained by:

$$v_a = \frac{h_2 - h_1}{t} = \frac{0.75a(h_2 - h_1)}{h_2^{0.75} - h_1^{0.75}} \tag{4.5}$$

Shear wave velocities of three soil layers from AHA and BE tests are listed in Table 4.4. Results indicate the bottom two average velocities from AHA have a good agreement with the BE results. The differences are 1.7% and 0.6%, respectively, which is deemed acceptable. For $v_{s,3}$, the AHA data is 8.5% smaller than the BE data. It should be noted that, $v_{s,2}$ from AHA results is very close to that from BE. However, $v_{s,1}$ from AHA is larger than that from BE results. Possible reasons for the above observations are listed as follows:

- The low stress levels in this shallow region, causing a relatively poor coupling between the soil and the top accelerometer;
- The signal is very low, as shown in Figure 4.1, when shear waves arrive at the top transducer because of damping. Moreover, the low signal is more vulnerable to the reflected waves and the background noise, which can increase errors of data processing.
- As discussed in Section 2.2.2.3, the confining stress is the main factor which can influence v_s significantly. Figure 4.7 shows the stress error of the centrifuge testing in this study and it indicates that the vertical stresses near the model top are smaller and stresses near the

model bottom are larger than that in the prototype. Given that the vertical stresses applied in the BE tests were calculated based on the linear stress relationship as in prototype, Equation 3.5, this may lead to a smaller measured $v_{s,3}$ (top soil layer) and larger $v_{s,1}$ (bottom soil layer) than the BE data.

- The vertical underestimated stress error was about 3% and the vertical overestimated stress error was approximately 5% in this study. Therefore, the difference for $v_{s,3}$ should be smaller than $v_{s,1}$. By contrast, the difference for $v_{s,3}$ (8.5%) is much larger compared to $v_{s,1}$ (1.7%). Given that both the vertical and horizontal stresses can affect the shear wave velocity, this much larger difference for $v_{s,3}$ may indicate that not only the vertical stresses near the model top, but also the horizontal stresses decrease, namely, the lateral earth pressure coefficient at shallow depths in the centrifuge is less than 0.5. Therefore, the lateral earth pressure coefficient (K) is back calculated and the reasons for the reduction in horizontal stress are further investigated, detailed in Section 4.5. As will be presented later, the use of Duxseal can reduce the horizontal stress field in the centrifuge.

Overall, it was found that the air hammer is a reliable method to measure the in-flight shear wave velocity in the centrifuge. It is a relatively low cost and easily deployable solution. However, a higher level of scepticism should be applied to air-hammer measurements with distorted or weak signals, or those obtained near the ground surface.

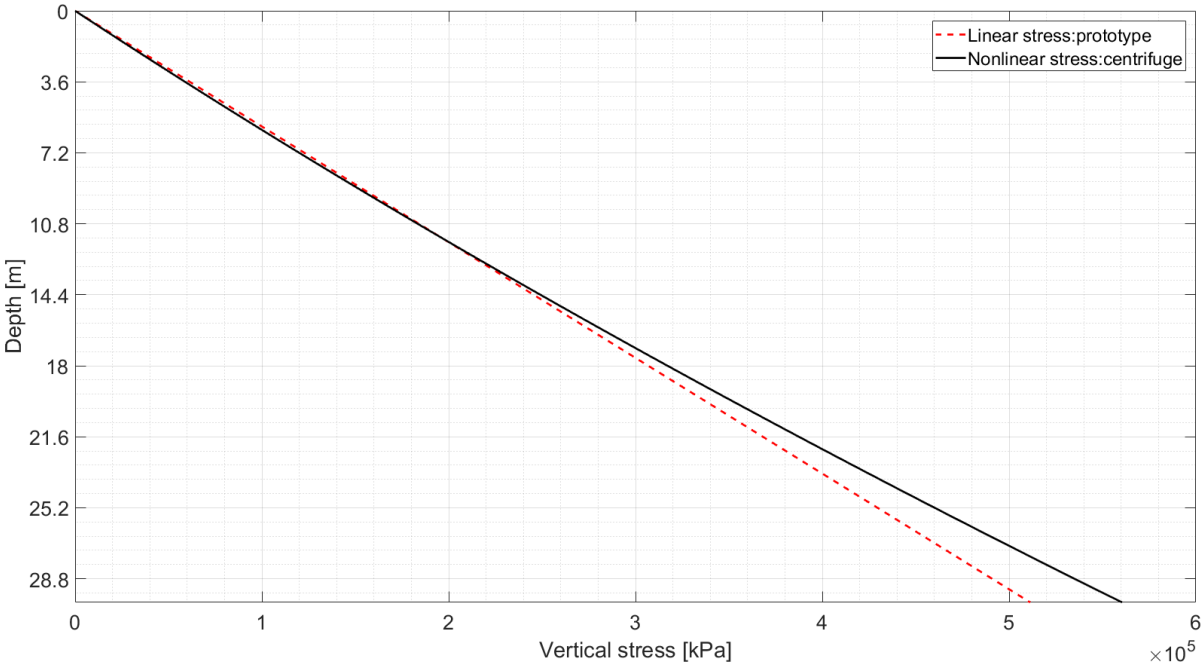


FIGURE 4.7: Stress error in this study

TABLE 4.4: Shear wave velocities from AHA and BE

Soil layer	Soil depth	AHA (m/s)	BE (m/s)	Difference
$v_{s,3}$	3.6 m-10.8 m	237.83	258.37	8.5%
$v_{s,2}$	10.8 m-18.0 m	308.75	310.64	0.6%
$v_{s,1}$	18.0 m-25.2 m	350.36	344.43	1.7%

4.3.3 Bender element: isotropic versus anisotropic

To investigate the effect of stress state on shear modulus and demonstrate that the constant B in Equation 3.9 is not affected by the stress state, as discussed in Section 3.3.3.5, both isotropic and anisotropic stress states were used to perform bender element tests, as detailed in Section 3.3.3.5.

The test results are shown in Figure 4.8. It can be seen that shear wave velocities under an isotropic stress state are a little smaller than with an anisotropic stress state, however, they are close to each other. The parameter a in the equation $v_s = a \times h^{0.25}$ for isotropic and anisotropic stress states was 156.3 and 159.6, respectively. This means the stress state has a slight effect on shear wave velocity when the confining stress is the same (2% difference).

According to the curve fitting analysis, the constant B in Equation 3.9 for isotropic and anisotropic stress states were 6937 and 7023, respectively. The difference is about 1%, which indicates that the constant B in Equation 3.9 is stress state independent. The mean value of constant B for dry Congleton sand obtained by this study is 6980, which is used to back-calculate the lateral earth pressure coefficient, as detailed in Section 4.5.

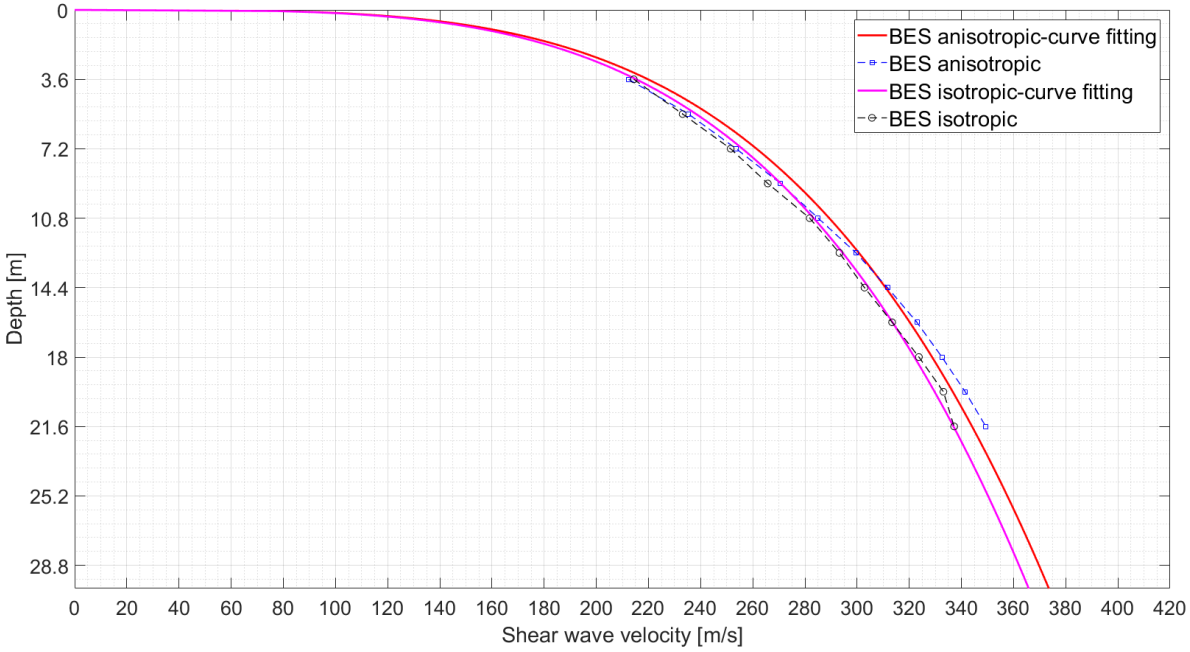


FIGURE 4.8: Shear wave velocity: isotropic versus anisotropic (BE)

4.4 Shear modulus and elastic modulus

As discussed in Section 2.2.2.3, both shear modulus and elastic modulus can be obtained from the bender element test by measuring the shear wave and pressure wave velocities. This section presents the pressure wave velocity results from the BE tests, as well as the shear modulus and elastic modulus profiles of the soil.

4.4.1 Pressure wave velocity

It has been discussed that v_s is affected by the stress state. In this study, v_p was also measured under both stress states in the bender element tests to investigate the effects on v_p. According to Equation 2.11, v_p can be calculated by:

$$v_p = \sqrt{\frac{2-2\mu}{1-2\mu}} v_s \tag{4.6}$$

Equation 4.6 suggests the relationship between v_p and depth h is similar to v_s, $v_s = a \times h^{0.25}$, and it satisfies Equation 4.7. The curve fitting results were also obtained based on this relationship. The parameter b for isotropic and anisotropic stress states are 232.6 and 247.2 respectively. Pressure wave velocities are shown in Figure 4.9. This figure indicates the pressure wave velocity is more affected by the stress state within the soil: 6% difference. As explained in Section 3.3.3.5, the vertical stress and horizontal stress could affect the shear wave velocity because particle motion is perpendicular to the direction of wave propagation for a shear wave. The combined effect of vertical and horizontal stress variations on the shear wave velocity is relatively small. Unlike the shear wave, the particle motion is in parallel with the direction of wave propagation for a pressure wave travelling vertically in the soil. In this case, only the vertical stress applied to the specimen can affect the pressure wave velocity. It can be seen from Table 3.10 that the vertical stress difference in both tests was approximately 30%. This may lead to a bigger difference in the pressure wave velocity.

$$v_p = \sqrt{\frac{2-2\mu}{1-2\mu}} a h^{0.25} = b h^{0.25} \tag{4.7}$$

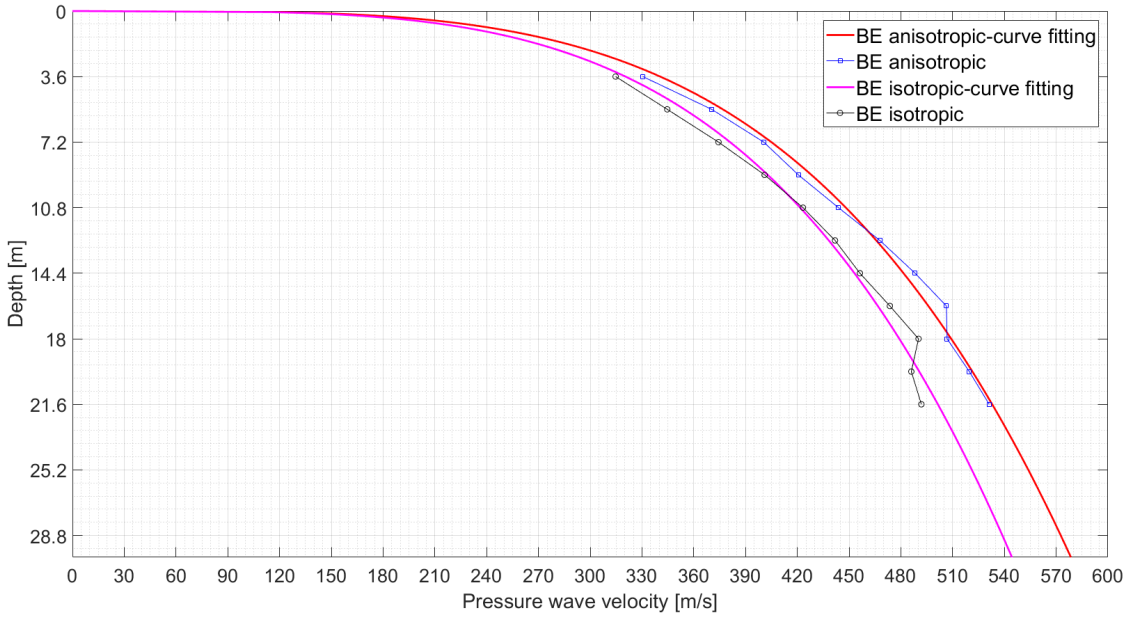


FIGURE 4.9: Pressure wave velocity: isotropic VS anisotropic (BE)

4.4.2 Soil moduli

The anisotropic stress state testing results are used to calculate shear modulus G and elastic modulus E considering the stress state within the soil is anisotropic

in the prototype. v_s and v_p profiles are obtained using the curve fitting method discussed above. The velocity profile and soil stiffness profile are shown in Figure 4.10 and Figure 4.11. These important soil model parameters will be used to conduct numerical modelling presented in Chapter 6.

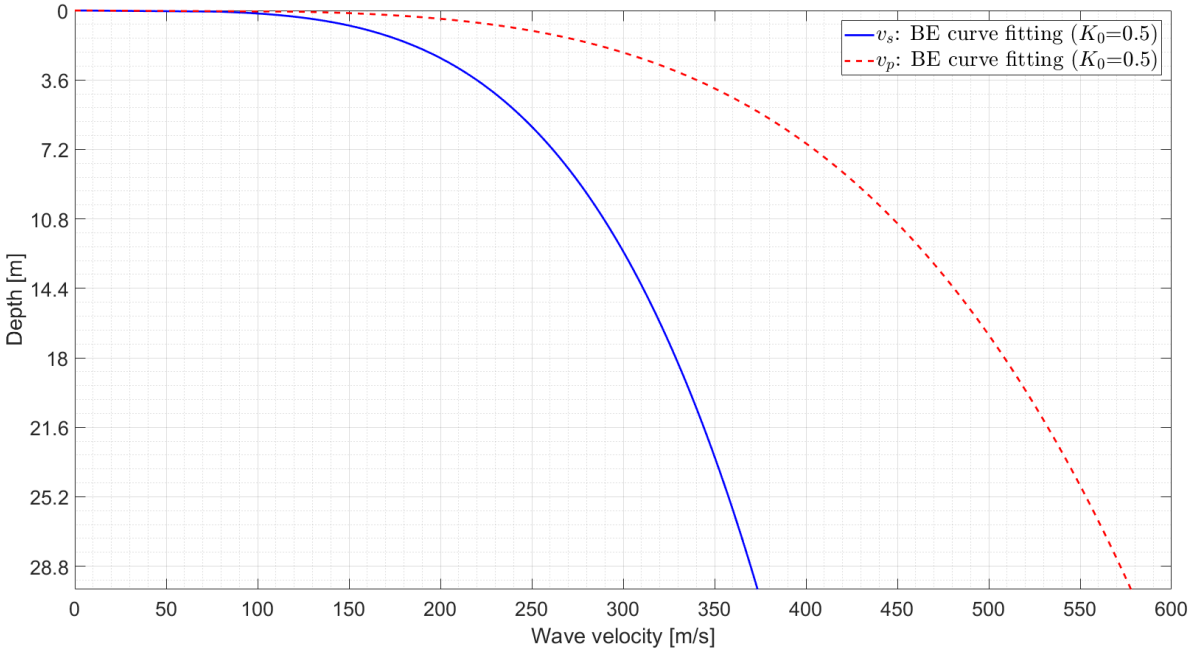


FIGURE 4.10: Shear wave and pressure wave velocity (BE)

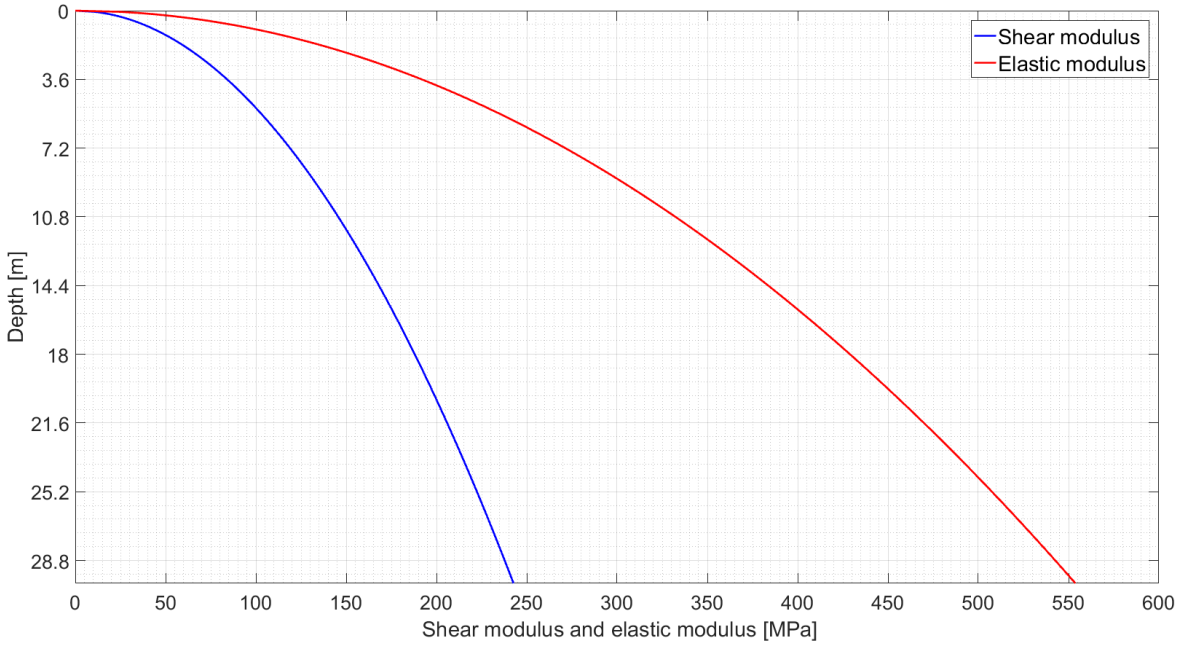


FIGURE 4.11: Shear modulus and elastic modulus (BE)

4.5 Effect of Duxseal on horizontal stress in the centrifuge

Data analysis in Section 4.3.2 suggests that the vibration absorbing material (Duxseal) can potentially reduce the horizontal stress in the centrifuge model, especially at shallow depths. Therefore, an individual air hammer test in the centrifuge without side Duxseal on the model container, see Figure 3.3, was carried out to measure the shear wave velocities of the same three soil layers, shown in Figure 3.30. Furthermore, the effects of Duxseal on the horizontal stress in the centrifuge can be examined by back-calculating the lateral earth pressure coefficient (K), also detailed in this section.

4.5.1 Procedure to back-calculate K in the centrifuge

The basic idea to calculate K in the centrifuge is assuming that K of a soil layer is constant. If v_s of a certain soil layer can be expressed as a function of K. Then the AHA results can be employed to back-calculate K. The procedure to obtain K of each soil layer in the centrifuge involves the data from BE tests, an empirical equation, the non-linear centrifuge stress field, as well as the AHA results.

4.5.1.1 Empirical equation to calculate v_s at depth h_m

As presented in Section 4.3.3, the mean value of constant B in Equation 3.13 obtained from two stress state tests was 6980. Consequently, the empirical equation to estimate v_s of Congleton sand at depth h_m in the centrifuge can be obtained by manipulating Equation 2.6 and Equation 3.13:

$$v_s = \sqrt{6980 \frac{(2.17-e)^2}{(1+e)\rho} (\sigma'_{vm})^{0.5} (K)^{0.25}} \tag{4.8}$$

where σ'_{vm} in Equation 4.8 is the vertical effective stress at h_m in the centrifuge, as given by Equation 4.9, a nonlinear equation. The values of e, ρ, ω and R_t in Equation 4.8 and Equation 4.9 have been illustrated in Chapter 3.

$$\sigma'_{vm} = \rho \omega^2 h_m (R_t + \frac{h_m}{2}) \tag{4.9}$$

Therefore, v_s at a certain depth h_m in the centrifuge is given by:

$$v_s = \sqrt{6980 \frac{(2.17-e)^2}{(1+e)\rho} (\rho \omega^2 h_m R_t + \rho \omega^2 \frac{h_m^2}{2})^{0.5} (K)^{0.25}} \tag{4.10}$$

4.5.1.2 Empirical equation to calculate v_s of a soil layer

Equation 4.10 suggests v_s at a certain depth h_m is a function of K. Theoretically, the same method, as detailed in Section 4.3.2, can be employed to calculate the mean wave velocity of a soil layer by assuming K is constant. As a consequence, the travel time, dt, within an infinitely thin soil layer, dh_m, is given by:

$$dt = \frac{dh_m}{v_s} \tag{4.11}$$

The travel time, t, within a soil layer, thickness=ΔH, can be obtained by integrating the above equation with respect to h_m from h_1 to h_2:

$$t = \int_{h_1}^{h_2} \frac{dh_m}{v_s} = \int_{h_1}^{h_2} \frac{dh_m}{\sqrt{6980 \frac{(2.17-e)^2}{(1+e)\rho} (\rho\omega^2 h_m R_t + \rho\omega^2 \frac{h_m^2}{2})^{0.5} (K)^{0.25}}} \tag{4.12}$$

Finally, K of a certain soil layer can be obtained from the equation below:

$$v_{s,AHA} = \frac{\Delta H}{t} \tag{4.13}$$

where $v_{s,AHA}$ is the measured mean shear wave velocity of a soil layer from the AHA.

However, the integrand function in Equation 4.12 is a non-integrable function. Therefore, K of a certain soil layer cannot be obtained directly using the above equations. Instead of solving this equation analytically, a numerical method is proposed to calculate K.

A simple method was adopted in this study to calculate K by discretizing a thick soil layer ΔH into multiple equal thiner soil layers Δh. Shear wave velocity at the middle point of each sub soil layer is taken as the mean velocity due to Δh being very small: 1 mm in this study. The elapsed time within each sub soil layer and the total travel time within each thick soil layer can be obtained, as well as the mean shear wave velocity, as detailed in the following section. It should be noted that this method is based on the following assumptions: vertical stresses are not affected by the Duxseal and soil density remains constant during centrifuge spin-up.

4.5.1.3 Step-by-step procedure to calculate K of a soil layer

The procedure to obtain the theoretical v_s of a soil layer in the centrifuge and to back-calculate K of a soil layer using AHA results is summarized as follows:

- BE tests under two stress states are conducted to obtain the empirical relationship Equation 4.10, to estimate v_s of the soil used in the centrifuge at a certain depth h_m.
- Each 0.12 m, ΔH, thick soil layer (L_1, L_2 and L_3) in the centrifuge is divided into 120 sub soil layers with a thickness of Δh=0.001 m, (i.e. $L_{1,1}$, $L_{1,2}$ ... $L_{1,120}$).
- v_s is a function of K and K is assumed to be constant within each soil layer L_i. Shear wave velocity at the middle point, $h_{m(i,j)}$, of each sub soil layer, $L_{i,j}$, is taken as the mean velocity, $v_{s(i,j)}$. The travel time $t_{i,j}$ within a thin sub soil layer $L_{i,j}$ can be obtained by:

$$t_{i,j} = \frac{\Delta h}{v_{s(i,j)}} \tag{4.14}$$

where i =1, 2, 3, and j =1, 2, 3 ... 120.

- The travel time t_i within a thick soil layer L_i can be obtained by:

$$t_i = \sum_{j=1}^{120} t_{i,j} \tag{4.15}$$

- The theoretical mean shear wave velocity $v_{s,i}$ within L_i can be obtained by:

$$v_{s,i} = \frac{\Delta H}{t_i} = \frac{\Delta H}{\Delta h} D^{0.5} (K_i)^{0.125} \sum_{j=1}^{120} (E h_{m(i,j)}^2 + F h_{m(i,j)})^{0.25} \tag{4.16}$$

where $D = 6980 \frac{(2.17-e)^2}{(1+e)\rho}$, $F = \rho \omega^2 R_t$ and $E = \frac{\rho \omega^2}{2}$.

- The measured mean velocity $v_{s,AHA,i}$ within L_i from air hammer tests should equal $v_{s,i}$, which gives:

$$v_{s,AHA,i} = \frac{\Delta H}{t_i} \tag{4.17}$$

- Equation 4.16 and Equation 4.17 can be manipulated to obtain measured K_i of L_i in the centrifuge:

$$K_i = \left(\frac{v_{s,AHA,i} \Delta h}{\Delta H D^{0.5} \sum_{j=1}^{120} (E h_{m(i,j)}^2 + F h_{m(i,j)})^{0.25}} \right)^8 \tag{4.18}$$

4.5.2 K in the centrifuge: with and without side Duxseal

Following the procedure detailed above, the theoretical mean shear wave velocities ($v_{s,1}$, $v_{s,2}$ and $v_{s,3}$) of the three soil layers can be calculated with Equation 4.16 by assuming K_i=0.5. In addition, the equivalent lateral earth pressure coefficients (K_1, K_2 and K_3) can be calculated from Equation 4.18 using the AHA results ($v_{s,AHA,1}$, $v_{s,AHA,2}$ and $v_{s,AHA,3}$) under two conditions: with and without side Duxseal. The results are illustrated in Table 4.5.

4.5.2.1 Without side Duxseal

It can be seen from Column 7 in Table 4.5 that K is relatively constant, about 0.52, within all three soil layers without Duxseal. The values are a little larger than 0.5. A possible reason is: under the high confining stress, the soil relative density became a little larger at 60 g than that at 1 g, which can lead to a larger measured $v_{s,AHA,i}$ from the air hammer tests. However, the soil density used to calculate K_i was the original value.

Overall, the measured K without Duxseal is close to the assumed at-rest earth pressure coefficient K_0 obtained from Equation 3.11 by Jaky (1944). This proves that the soil mass is in a state of elastic equilibrium and normally consolidated dry sand can be obtained in the centrifuge under rigid boundary conditions.

4.5.2.2 With side Duxseal

Tested values with Duxseal, see Column 5 in Table 4.5, indicate that K increases with depth. K within the bottom two soil layers is quite close to 0.5. However, K is very low, about 0.3, at shallow depths. According to Rankine's theory of active earth pressure (Rankine, 1857), the coefficient of active earth pressure, K_a, for a cohensionless soil with a friction angle of 31 degrees is about 0.3, which can be calculated by Equation 4.19.

Duxseal stiffness (G) was tested using the bender element test in a triaxial cell by measuring the shear wave velocity. The sample preparation process was similar to the soil specimen preparation, detailed in Section 3.3.3.4. The only difference was Duxseal was compacted in a split mold instead of air pluviated. A Poisson$'$s ratio of 0.47 given by Cilingir (2009) was employed to calculate the elastic modulus of Duxseal using Equation 2.10. A very weak signal was detected due to its high damping. The measured E was about 16 MPa which is very low compared with the soil, see Figure 4.11. This suggests the side Duxseal can provide a relatively flexible boundary condition. In the centrifuge, there is a lateral component of acceleration

Taylor (1995). This flexible Duxseal wall near the ground surface is allowed to move away from the soil mass and may be squeezed away from the upper soil under the action of lateral acceleration and lateral earth pressure, hence reducing the soil density and the horizontal principal stress. Therefore, the soil near the model top, 3.6-10.8 m, may have reached an active state of plastic equilibrium.

$$K_a = \tan^2(45 - \frac{\phi}{2}) \tag{4.19}$$

TABLE 4.5: v_s and K in the centrifuge with and without Duxseal

Soil layer	Soil depth (m)	Centrifuge (K_i=0.5) $v_{s,i}$ (m/s)	With $v_{s,AHA,i}$ (m/s)	With K_i	Without $v_{s,AHA,i}$ (m/s)	Without K_i
L_3	3.6-10.8	255.4	237.8	0.28	256.7	0.52
L_2	10.8-18.0	310.0	308.8	0.48	311.8	0.52
L_1	18.0-25.2	346.9	350.4	0.54	349.4	0.53

Additionally, it can be seen from Table 4.5 that the lateral earth pressure coefficient increases with depth. This indicates the stiffness of Duxseal may also be stress dependent. Duxseal stiffness is larger under higher confining stress and the horizontal movement decreases with depth.

4.5.2.3 Duxseal effect on soil stiffness

The theoretical shear modulus in both prototype and centrifuge, and the measured shear modulus with and without Duxseal in the centrifuge are plotted against depth, in Figure 4.12. It can be seen that the shear modulus of the top soil layer obtained with Duxseal is much smaller than that without Duxseal, about 14% smaller. This is a result of the reduced horizontal stress at the shallow depths. Measured shear modulus of the middle and bottom soil layer is very close to the theoretical estimates.

Measured data from air hammer tests can only provide values at discrete locations; three soil layers in this study. To further investigate the effects of Duxseal stiffness on horizontal stress distribution within the centrifuge, a FLAC3D model was built to simulate the centrifuge model. The FLAC3D model was calibrated using the AHA and BE test data and the Duxseal non-homogeneity effects on stress field and soil stiffness were further examined, as detailed in Chapter 6.

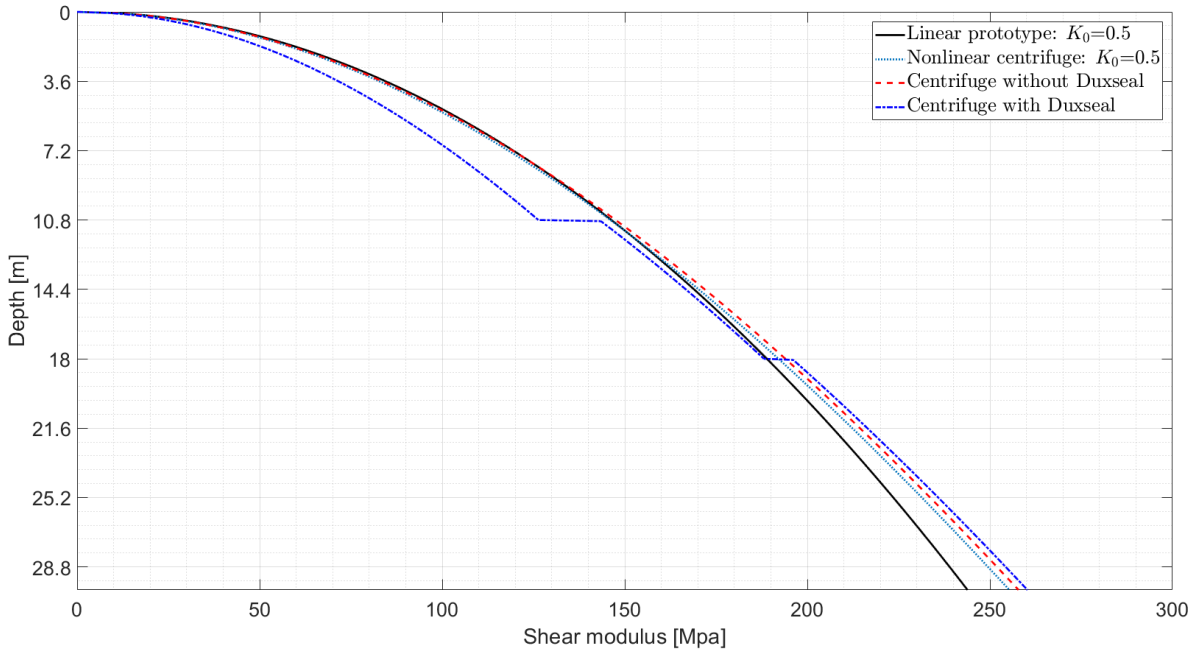


FIGURE 4.12: Comparison of shear modulus: theory versus measurements with and without Duxseal in centrifuge

4.6 Chapter summary

Methods used to process the data obtained from the centrifuge based air hammer testing and the triaxial based bender element testing were discussed in this chapter. The tested shear wave velocity from bender element testing and empirically estimated results were compared. In addition, the procedure to back-calculate the lateral earth pressure coefficient of each soil layer in the centrifuge was presented. Furthermore, centrifuge based air hammer testing with and without Duxseal was conducted and the effect of Duxseal on horizontal stress in the centrifuge model was investigated. The following is a summary of the findings:

- Signals from air hammer tests were affected by several factors: reflected waves, decay of the wave signals, electrical noise and mechanical vibrations from the centrifuge. Low resolution time history signals were obtained from the air hammer tests limited by the sampling frequency. The reasons mentioned above can mask or distort the real first peaks and first arrival points which can lower the accuracy of the direct time methods. Therefore, a less subjective method (cross correlation method) was employed to process the shear wave signals measured from experiments in this study because this method can avoid the need to pick characteristic points.

- The effects of data length (adopted to conduct cross correlation method) and the varying shear wave period with depth in the centrifuge on cross correlation results were investigated. Results indicated that using the full length of the data set can lead to a lower estimate of shear wave velocity and the first cycle data should be extracted from the full data set to obtain more accurate estimate of the travel time from the cross correlation method. Varying shear wave period can also lead to an error in v_s (3.7%) and G_{max} (up to 8%). This error cannot be ignored and air hammer test results from the cross correlation method should be corrected.

- A round grained sand (HST95 Congleton sand) was used in this study as the model soil. The empirical equation developed by Hardin and Richart (1963) was applicable for sand with round-grained particles. Values of v_s obtained from the bender element tests were compared against the two empirical equations. Results indicated that Equation 2.9 by Hardin and Richart (1963) agreed well with the bender element test results and can be used to estimate G_{max} of dry Congleton sand.

- Both isotropic (K_0=1) and anisotropic (K_0=0.5) stress states were used to perform bender element tests. The test results indicated shear wave velocities under isotropic stress state were a little smaller than anisotropic stress state and the stress state had a slight effect on shear wave velocity when the effective confining stress was the same. Based on bender element curve fitting results, the measured constant B in Equation 3.13 under both states were 6937 and 7023, respectively. The slight difference (about 1%) demonstrated the constant B in Equation 3.13 was insensitive to the stress state.

- The procedure to estimate the theoretical mean shear wave velocity and to back-calculate the equivalent lateral earth pressure coefficients K of a soil layer was detailed. Two equations were deduced based on the procedures. Centrifuge based air hammer tests (with and without side Duxseal, see Figure 3.3) were carried out to investigate the effects of side Duxseal on horizontal stress field and the soil stiffness. Test results indicated that K was constant (0.52) at all depths when no Duxseal was attached to the sides of the model container. However, with side Duxseal, K was very low, about 0.3, at shallow depths (3.6-10.8 m). This suggested the flexible Duxseal wall near the ground surface may move away from the soil mass and the horizontal principal

stress decreases. Consequently, the soil stiffness near the model top was much smaller (about 14%) than that without Duxseal.

Chapter 5

Centrifuge Test Results and Analysis

5.1 Introduction

As summarized in Section 3.2.13, the dynamic pile and soil behaviour under a series of dead and dynamic loads were investigated in this study. This chapter mainly presents vibration related results from centrifuge tests. The static ultimate bearing capacity of the pile is estimated and the dynamic linearity of the model under three dead loads are examined using the frequency response function defined in Section 5.2. In addition, the static pile and soil displacements with and without dynamic excitation are also examined and discussed in Section 5.2. This is followed by the presentation of dynamic pile and soil response amplitudes under different dead weights but with the same dynamic load, in Section 5.3. Two simplified mechanical models are proposed in Section 5.3 to explain the pile and soil responses, as well as the soil-pile interaction. The shear strain level within the soil and the damping ratio of the soil along depth are estimated and presented in Section 5.4, as well as the vibration attenuation properties. In this chapter, all results are presented in prototype scale unless otherwise stated.

5.2 Linearity of model

5.2.1 Introduction

In the centrifuge tests, the loading process is divided into two stages: the static loading stage (stage 1) and the dynamic loading stage (stage 2). The axial static and dynamic loads are imposed to the pile top using brass discs and the shaker,

respectively. Three dead loads were used to investigate the effect of the dead load magnitude on the dynamic pile behaviour and the ground-borne vibration. Section 5.2.2 discusses the two loading stages, as well as the effect of the dead load magnitude.

As discussed in Section 2.1.1.5, the railway-induced vibration is small and linear soil and pile behaviours are expected to be obtained from the centrifuge tests, thus proving that the conducted tests could simulate the relevant problem and conducting different tests with varying static loads using the same soil sample is appropriate. The frequency response function, detailed in Section 5.2.3, is employed in this study to examine the linear model behaviour by comparing the results obtained under two different amplitudes of excitation. Results related to the pile and soil linearity are presented in Section 5.2.4 and Section 5.2.5, respectively.

5.2.2 Loading stages in the centrifuge tests

5.2.2.1 Stage 1: Static loading

As shown in Figure 5.1, the vertical dead load (F_s) applied to the pile top is transferred into the soil by shear stress (τ_s) along the pile shaft. As the load is increased, the full shaft resistance (Q_S) is mobilized and part of the load starts to be carried by the pile base (Q_P) (Viggiani, 2012). Q_P may be zero if F_s is much smaller than the shaft resistance capacity.

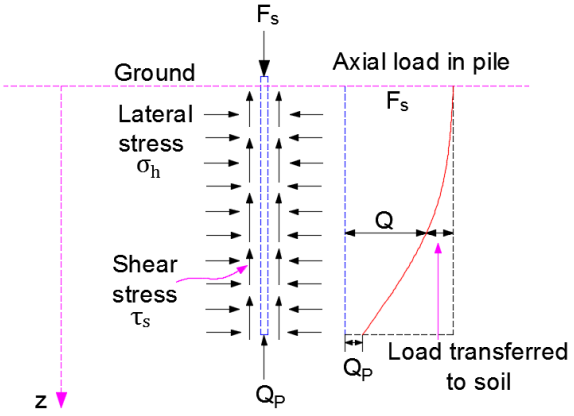


FIGURE 5.1: Axially loaded pile and load distribution along pile depth

Under static compressive loads, the pile settles and a typical pile load-displacement curve is shown in Figure 5.2. It can be seen that the pile behaviour becomes nonlinear as the load increases. Therefore, the magnitude of the static load applied to the pile top is an important parameter with the static load determining the

initial load and displacement distribution along the pile, thus further affecting the pile behaviour and the soil-pile interaction during dynamic loading.

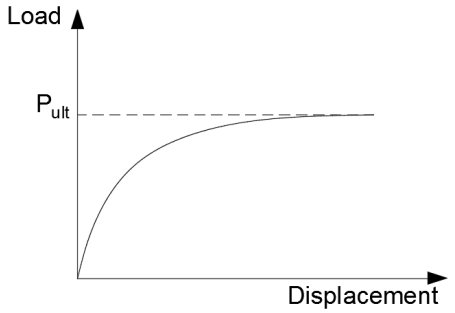


FIGURE 5.2: Typical pile load-displacement curve

In this study, to investigate the effects of initial static loads on the dynamic pile behaviour, three different dead weights modelled by the brass discs were used in stage 1. The applied dead load (F_s) and the resulting displacement at the pile top (u_s) were measured by the static load cell and LVDT-P, see Figure 3.4. The ultimate bearing capacity of the single pile embedded in the dry Congleton sand in this study is estimated using the following equation:

$$P_{ult} = Q_S + Q_P \tag{5.1}$$

The shaft resistance Q_S for a pile in cohesion-less soil is given by :

$$Q_S = \pi d \int_0^H K\sigma_v^{'} \tan\delta dz \tag{5.2}$$

where d is the pile diameter (0.5 m), H is the embedded pile depth (16.8 m), $\sigma_v^{'}$ is the vertical effective stress at depth z, δ is the friction angle between the pile shaft and the soil.

$\sigma_v^{'}$ can be calculated by Equation 4.9. A K value of 0.7 was recommended by Fleming et al. (2008) to calculate the ultimate bearing capacity of bored piles. In this study, a thin layer of sand was attached to the pile shaft and δ was assumed to be soil internal effective friction angle (31 degrees by Lauder (2010)).

The end bearing resistance Q_P for a pile in cohesion-less soil is given by :

$$Q_P = A_p \sigma_v^{'} N_q \tag{5.3}$$

where A_p is the cross-section area of the pile base. N_q is the bearing capacity factor; a value of 40 was assumed, as recommended by Reese (2006) for dense sand.

Based on the above equations, the estimated ultimate bearing capacity of the pile in this study was evaluated to be 3600 kN in prototype scale. The measured dead load F_s and pile top displacement u_s are shown in Table 5.1, as well as the ratio of F_s/P_{ult} and the safety factor. It can be seen the ratios of F_s and P_{ult} were approximately 12%, 24% and 44%, respectively. The dead load applied in Test GBV_m1 was about two times and four times the dead load in GBV_m2 and GBV_m3. This indicates the dead load applied increased linearly from GBV_m3 to GBV_m1. However, the pile top displacement difference between GBV_m1 and GBV_m2 (1.2 mm) was twice the difference between GBV_m2 and GBV_m3 (0.6 mm). This suggests the pile top displacement u_s increased non-linearly with the increasing dead load F_s.

TABLE 5.1: Dead load, pile top displacement and safety factor (Test GBV)

Test name	F_s (kN)	u_s (mm) (model scale)	$P_{ult}(kN)$	Ratio (F_s/P_{ult})	Safety factor
GBV_m1	1576.8	9.6	3609	43.7%	2.3
GBV_m2	864.0	8.4	3609	23.9%	4.2
GBV_m3	421.2	7.8	3609	11.6%	8.6

5.2.2.2 Stage 2: Dynamic loading

In stage 2, the harmonic load ($F_d(t)$) with a frequency of f from the shaker was applied to vibrate the pile. The input frequency ranged from 10 Hz to 120 Hz with a frequency spacing of 0.1 Hz during each complete excitation process. The dynamic load amplitude was controlled by the input voltage amplitude for the shaker and two amplitudes were used (500 mV and 800 mV) for each dead weight. In this stage, the axial dynamic load ($F_d(t)$) carried by the pile varied with time, as shown in Figure 5.3, and the pile vibrated harmonically. In this study, only the dynamic pile top response was measured by the accelerometer PCV and pile top behaviour under both dead and dynamic loads are discussed in Section 5.2.4. It should be noted that the compression force is taken to be positive considering the combined axial loads were compressive (downwards) loads in this study due to the static load being larger than the dynamic load.

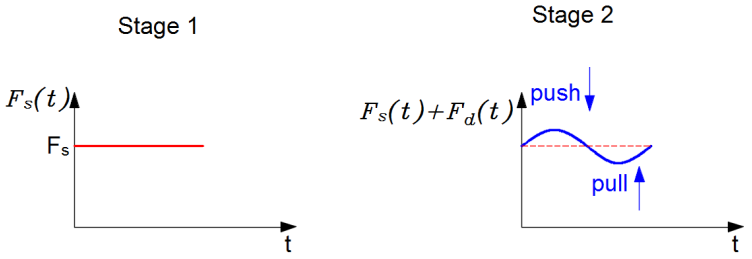


FIGURE 5.3: Loading stages in the centrifuge test

5.2.3 Frequency response function and coherence function

Two important functions, the frequency response function and coherence function, are defined in this section. They are used to evaluate the model behaviour and correlation between inputs and outputs, respectively. In this study, input signals are applied dynamic forces provided by the shaker and measured by the dynamic load cell. Output signals are accelerations measured by piezoelectric accelerometers. The velocity and displacement data can be calculated by integrating the acceleration data.

5.2.3.1 Frequency response function

If the soil/structure behaviour is within the linear elastic range, the measured responses (output signal) at all locations are linearly proportional to the applied harmonic load (input signal), or at least the ratios of output to input are insensitive to the input amplitude. If nonlinear behaviour occurs, the ratio of output to input varies with the input amplitude of the excitation. To investigate whether the observed behaviour was linear, two input amplitudes of excitation (500 mV and 800 mV) were used in Test GBV and results are presented in the following section.

The time history data of applied dynamic force and the responses (acceleration, velocity and displacement) are denoted as F(t) and R(t) in this study. The original time history data can be converted to a representation in frequency domain and the corresponding response amplitude in frequency domain are denoted as F(w) and R(w). F(w) and R(w) are calculated by conducting the Fourier transforms of F(t) and R(t) respectively in MATLAB. The frequency response functions (FRFs) at each measured point were calculated. If the soil and pile behaviour is linear, the FRFs should be constant under different input amplitudes. The FRF is defined as:

$$H(w) = \frac{R(w)}{F(w)} \tag{5.4}$$

This process described above can be accomplished easily using the Fast Fourier Transform (FFT) function in MATLAB. To make sure the magnitude of the captured signal is accurate when transforming time domain data to frequency domain data, as discussed in Section 3.2.12, an integer multiple of the period of the sampled data (20 periods) was extracted from the total data to conduct the FFT.

Ideally, Equation 5.4 is used to calculate the FRF if the measured input and output signals are not affected by anything. However, the centrifuge and the shaker induce interference which may introduce random errors. Therefore, a random vibration approach was used in this study to process the measurement data. The random vibration approach considers that the excitation, or input, is non-deterministic, and treats the samples as signals from random process. The structural response to random vibration is usually treated using statistical or probabilistic approaches. This approach defines the FRF by the input auto-spectrum $S_{FF}(\omega)$, the output auto-spectrum $S_{RR}(\omega)$, and the cross-spectrum between the output and input signals $S_{FR}(\omega)$ and $S_{RF}(\omega)$, as shown in Equation 5.5 to Equation 5.8 (Ewins, 2000).

$$S_{FF}(\omega) = \frac{1}{N_s^2}\left[\sum_{n=0}^{N_s-1} F(t)_n e^{-\frac{2\pi imn}{N_s}}\right]^2 \text{ ... ... for } m = 0, 1 \text{ ... } N_s - 1 \tag{5.5}$$

$$S_{RR}(\omega) = \frac{1}{N_s^2}\left[\sum_{n=0}^{N_s-1} R(t)_n e^{-\frac{2\pi imn}{N_s}}\right]^2 \text{ ... ... for } m = 0, 1 \text{ ... } N_s - 1 \tag{5.6}$$

$$S_{RF}(\omega) = \frac{1}{N_s^2}\left[\sum_{n=0}^{N_s-1} R(t)_n e^{-\frac{2\pi imn}{N_s}}\right]\left[\sum_{n=0}^{N_s-1} F(t)_n e^{-\frac{2\pi imn}{N_s}}\right] \text{ ... ... for } m = 0, 1 \text{ ... } N_s - 1 \tag{5.7}$$

$$S_{FR}(\omega) = \frac{1}{N_s^2}\left[\sum_{n=0}^{N_s-1} F(t)_n e^{-\frac{2\pi imn}{N_s}}\right]\left[\sum_{n=0}^{N_s-1} R(t)_n e^{-\frac{2\pi imn}{N_s}}\right] \text{ ... ... for } m = 0, 1 \text{ ... } N_s - 1 \tag{5.8}$$

where: N_s is the sampling number.

There are two alternative equations for the FRF defined by the above equations:

$$H_1(\omega) = \frac{S_{FR}(\omega)}{S_{FF}(\omega)} \tag{5.9}$$

$$H_2(\omega) = \frac{S_{RR}(\omega)}{S_{RF}(\omega)} \tag{5.10}$$

Theoretically, Equation 5.9 and Equation 5.10 are expected to provide the same results. However, noise analysis indicates that the noise has a more severe effect on the acceleration measurement compared to dynamic force measurement, as discussed in Section 3.2.11.1. Generally, $H_1(\omega)$ is more susceptible to noise in the dynamic force measurement. By contrast, $H_2(\omega)$ is more susceptible to noise in the acceleration measurement (Ewins, 2000). In this study, $H_1(\omega)$ is employed to calculate FRFs. This is because the centrifuge and shaker induced interference test results indicate the measured dynamic force was slightly affected by electric noise and physical vibrations compared to the accelerations measured by the Piezos.

In order to obtain $H_1(\omega)$, the values of $S_{FF}(\omega)$, $S_{RR}(\omega)$, $S_{RF}(\omega)$ and $S_{FR}(\omega)$, as shown in Equation 5.5 to Equation 5.8 respectively, are required. In this study, the extracted sampled data for each single frequency excitation was processed using the same procedure outlined below to calculate the auto-spectrum and cross-spectrum of the measured data.

- Divide the N_s data points into K overlapping segments;
- Apply a Hanning window to the data to reduce the end effect and further reduce the leakage effect;
- Calculate the the auto-spectrum or cross-spectrum of the measured data using Equation 5.5 to Equation 5.8;
- Calculate the average auto-spectrum or cross-spectrum over the K^{th} segment.

All the calculations stated above were conducted in MATLAB. There are two ways to present the FRF: one is called linear scale and another is dB scale, or named logarithmic scale, calculated as:

$$R_{dB} = 20\log_{10}(H_1(\omega)) \tag{5.11}$$

According to the definition of FRF, the units for FRFs are m/s^2/N, m/s/N and m/N for the acceleration, the velocity and the displacement in linear scale. Therefore, the units, dB$_{\text{ref}}$(m/s^2/N), dB$_{\text{ref}}$(m/s/N) and dB$_{\text{ref}}$(m/N), are used in all the figures when FRFs are presented in dB scale.

5.2.3.2 Coherence function

Another important aspect is that the measured output signals should only be caused by the inputs from the shaker. In addition to the FRF, the coherence

function is computed to evaluate how much of the output signal is related to the measured input signal. The coherence function is a frequency domain function computed to show the degree of relationship between two signals and it indicates the quality of the FRF measurement. The value of the coherence function ranges between zero and one, where a value of zero indicates there is no relationship between the signals. A value of one indicates the existence of linear frequency response between the two signals. The coherence function is defined as:

$$\gamma^2(\omega) = \frac{H_1(\omega)}{H_2(\omega)} = \frac{S_{FR}(\omega)S_{RF}(\omega)}{S_{FF}(\omega)S_{RR}(\omega)} \tag{5.12}$$

5.2.4 Linearity of pile behaviour

In this study, accelerations at different locations (pile top and within the soil) are measured by the Piezos directly, instead of the velocity and the displacement. To obtain the time history data of the velocity and the displacement, a trapezoidal integration is conducted in MATLAB. First the original acceleration data is filtered with a high pass frequency of 600 Hz to filter out noise based on the noise test results, see Section 3.2.11. Then the acceleration data is integrated with time to obtain the velocity time history and the displacement time history. To eliminate drift errors during integration, a high pass filter is used at a low frequency of 20 Hz after each integration. This method is employed in this study to process the data and all the velocity and displacement results presented in the following sections are obtained by the above process. It should be noted that the displacement data obtained from the above approach is referred to as dynamic displacement through out this study. It was found the time history data is not capable of providing a clear view of the signals due to rather high frequencies being used in this study. Therefore, time domain data is transformed into frequency domain by using FFT and most results are presented in frequency domain unless otherwise stated.

The measured dynamic load amplitudes by the dynamic load cell (DLC), vertical dynamic displacement amplitudes at the pile top by PCV and FRFs (displacement/force) in frequency domain obtained from Test GBV_m1, GBV_m2 and GBV_m3 are presented in Figure 5.4, Figure 5.5 and Figure 5.6. The ratios of the dead load F_s to the ultimate bearing capacity P_{ult} were approximately 44%, 24% and 12% for GBV_m1, GBV_m2 and GBV_m3, respectively.

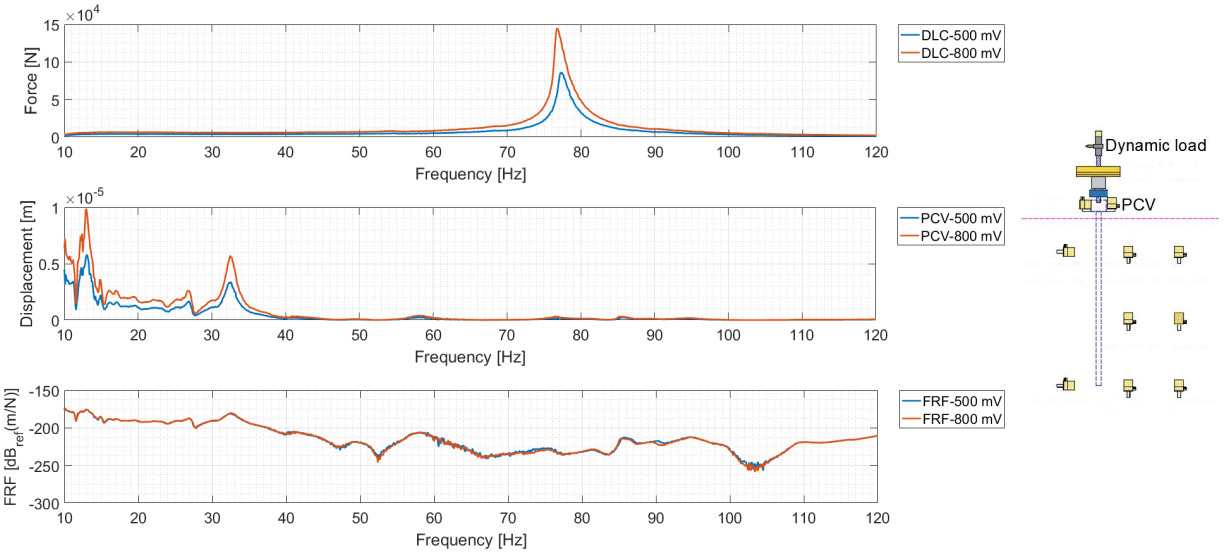


FIGURE 5.4: Dynamic force, pile displacement and FRF (GBV_m1:F_s/P_{ult}=44%)

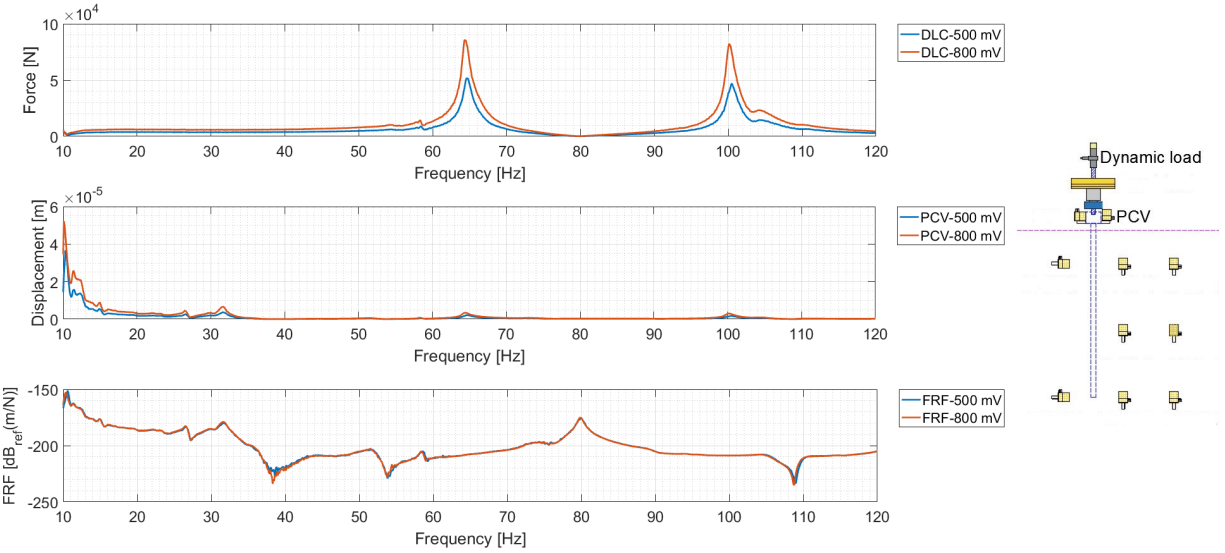


FIGURE 5.5: Dynamic force, pile displacement and FRF (GBV_m2:F_s/P_{ult}=24%)

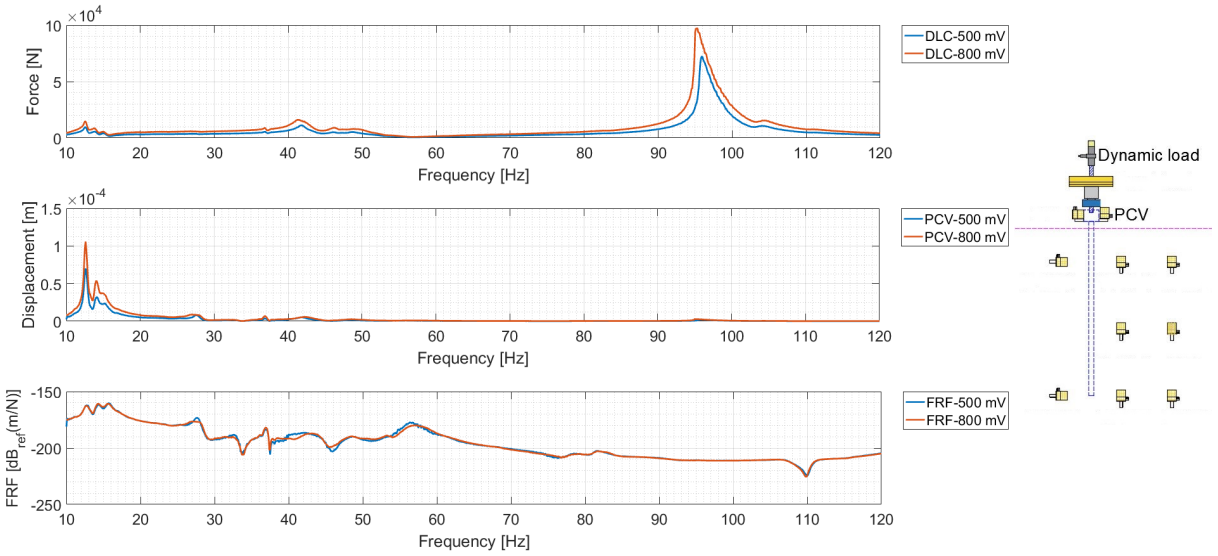


FIGURE 5.6: Dynamic force, pile displacement and FRF (GBV_m3:F_s/P_{ult}=12%)

It can be seen from Figure 5.4, Figure 5.5 and Figure 5.6 that both the dynamic force amplitude F_d and the resulting pile top displacement increase with the input voltage amplitude for the shaker. However, it can be clearly seen that the FRFs (displacement/force) are almost constant at each frequency component even though the input voltage amplitude increased significantly. This indicates the dynamic pile behaviour is in the linear range or at least not sensitive to the combined static and dynamic loads when F_s/P_{ult}<44% (safety factor>2). It should be noted that FRFs (displacement/force) in dB scale are used instead of linear scale data, this is because the linear scale data is very small at many frequencies and very hard to distinguish responses. The use of dB scale data can give a better fit over the whole frequency range. However, the dB scale can hide some information due to the property of dB scale data. For example, a 5 dB difference around 41 Hz, see Figure 5.6, indicates one is twice as much as the other.

The linear pile top response is because the dynamic load level was very small (F_d<150 kN and F_d/P_{ult}<3.5%) and the resulting dynamic displacement being extremely small (approximately 0.01 mm at most frequencies, as shown in Figure 5.4, Figure 5.5 and Figure 5.6). Therefore, dynamic pile behaviour was still in the linear range and no obvious irrecoverable displacement (accumulation of permanent displacement) occured during the dynamic loading. To prove that no accumulated pile displacement occurred, the static displacements of the pile top and the ground surface measured by LVDT-P and LVDT-G respectively, are examined. To distinguish the dynamic displacement obtained from the Piezos, the displacement measured by LVDT-P and LVDT-G is referred to as static displacement. The results are analysed as following.

Figure 5.7 presents the static displacement time history and the displacement rate under three dead weights with the input voltage of 500 mV during one complete excitation process (10 Hz to 120 Hz). Approximately 1100 seconds (20 minutes) of data was recorded during one complete excitation process. In addition, 16 seconds of data was recorded without dynamic loading, as shown in Figure 5.8. It can be seen from Figure 5.7 and Figure 5.8 that under the same dead weight, both the pile and the ground settled at almost the same rate: approximately 0.03 μm/s for m1, 0.02 μm/s for m2 and 0.015 μm/s for m3. This indicates the soil and the pile experienced the same displacement at the interface and the dynamic load applied to the pile top would not result in accumulated pile displacement. Therefore, the soil-pile interface can be treated as a perfectly bonded interface in this study.

In addition, Figure 5.7 and Figure 5.8 suggest the static pile and ground displacement rates without dynamic loading were quite similar with the results obtained during dynamic loading, indicating that the static pile and soil settlements were independent of dynamic loading. In this study, Test GBV_m1 was carried out first, followed by Test GBV_m2 and Test GBV_m3. It can be seen that under three dead weights, the displacement rate decreased gradually with the ongoing test during GBV. This indicates the whole model was still settling even after 40 minutes under 60 g. For a dry sand, the consolidation process should finish instantly. This gradually decreased displacement rate indicates the flexible Duxseal attached to the bottom of the container may be still deforming under high confining pressure even after a long period of time. As mentioned in Section 2.3.3.2, Duxseal is an oil based material with a very low permeability and remains pliable and useable even when exposed to air over a long time (Cilingir, 2009). It was found that amount of oil occurred in the sand adjacent to the Duxseal when emptying the container. This indicates the oil within the Duxseal was squeezed out gradually during the centrifuge test in this study. This suggests that it was the Duxseal that may lead to the settlement of the whole model and the displacement rate reduces over time as the Duxseal essentially consolidates under the applied loading.

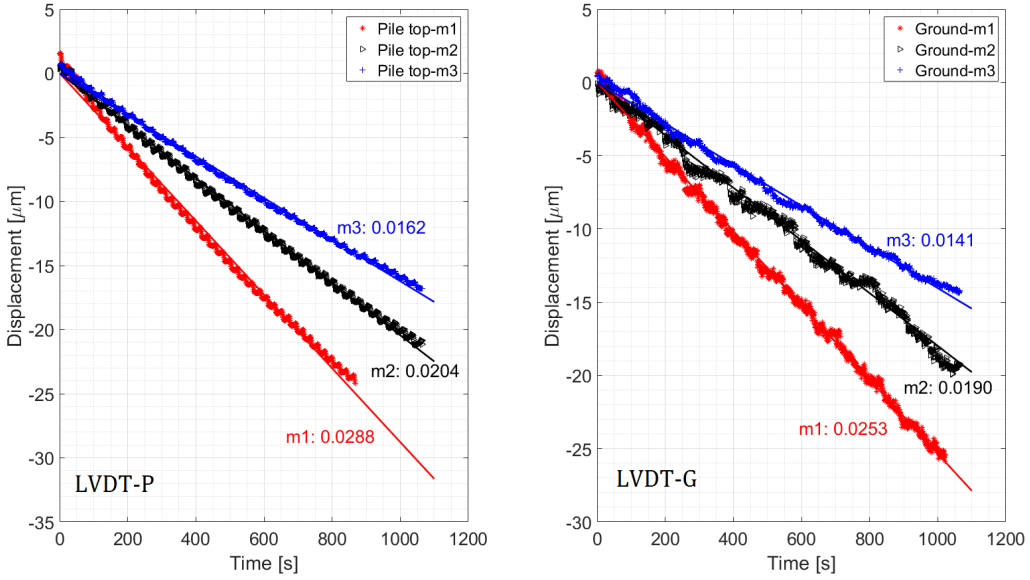


FIGURE 5.7: Static pile and soil displacement during excitation under 500 mV

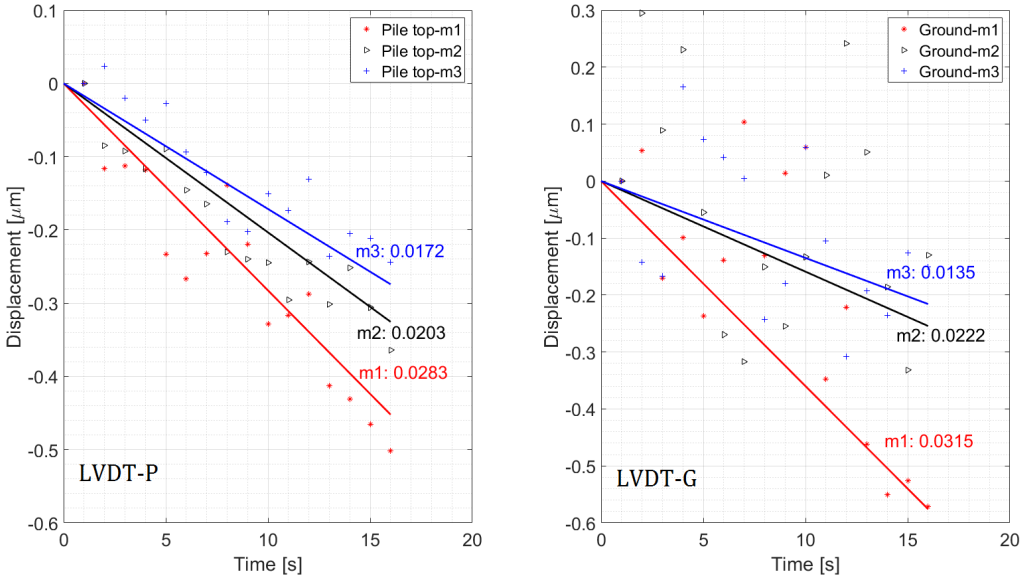


FIGURE 5.8: Static pile and soil displacement without dynamic loading

5.2.5 Linearity of soil behaviour

The linearity of the soil is also examined by calculating the FRFs under three dead weights (m1, m2 and m3). Soil responses in dB scale at two selected positions (VPNP3: nearest location from the excitation source and VPDP1: furthest observation location from the excitation source) are presented in Figure 5.9, Figure 5.10 and Figure 5.11

Figure 5.9, Figure 5.10 and Figure 5.11 imply all the FRFs of the soil are almost the same except at some frequencies. The results also indicate that the FRFs of soil were independent of excitation amplitude which implies a linear response of the soil. At some frequencies (i.e. 64 Hz for GBV_m1 and 42 Hz for GBV_m2), there are relatively large differences of the FRFs. At these frequencies, a feature observed is that they occurred at the low coherence values (troughs of the corresponding coherence curves). This indicates the measured data may have been affected by other factors, such as noise and reflections from the boundaries.

It can be found from these three figures that the coherence values increased with increasing input amplitudes to some extent. It is also observed that the coherence decreased with increasing distance from the excitation source. This is due to the fact that the soil response decreased with distance, as detailed in Section 5.4. Therefore, the proportion of interference to response was larger at deeper locations and the interference had a more significant impact on the measured smaller amplitude signals.

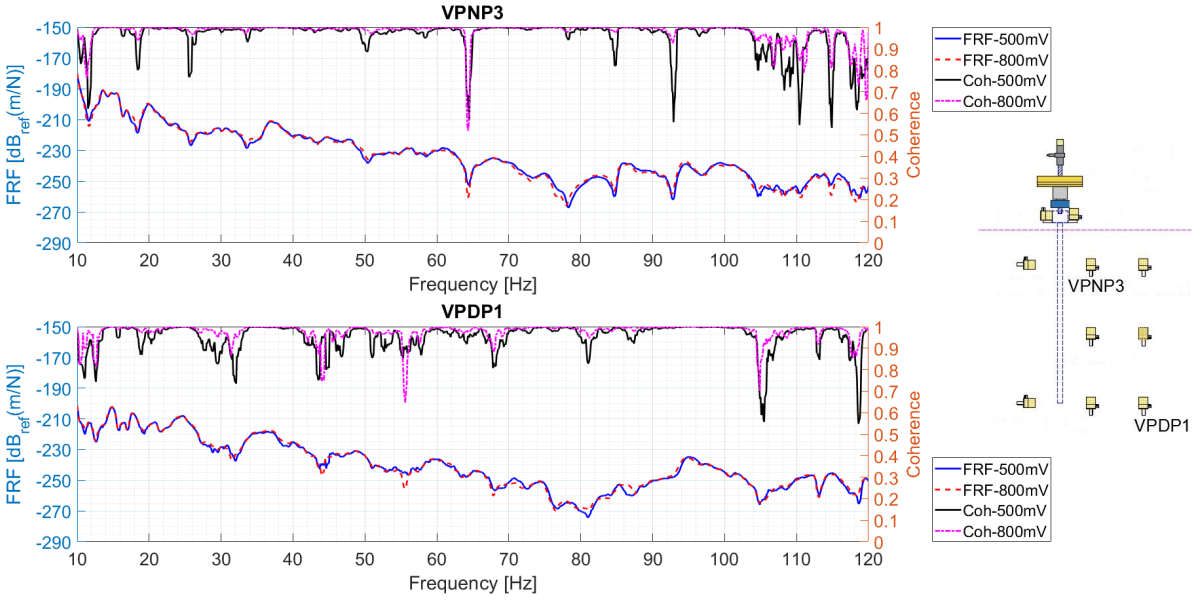


FIGURE 5.9: The FRF and coherence at VPNP3 and VPDP1 (GBV_m1)

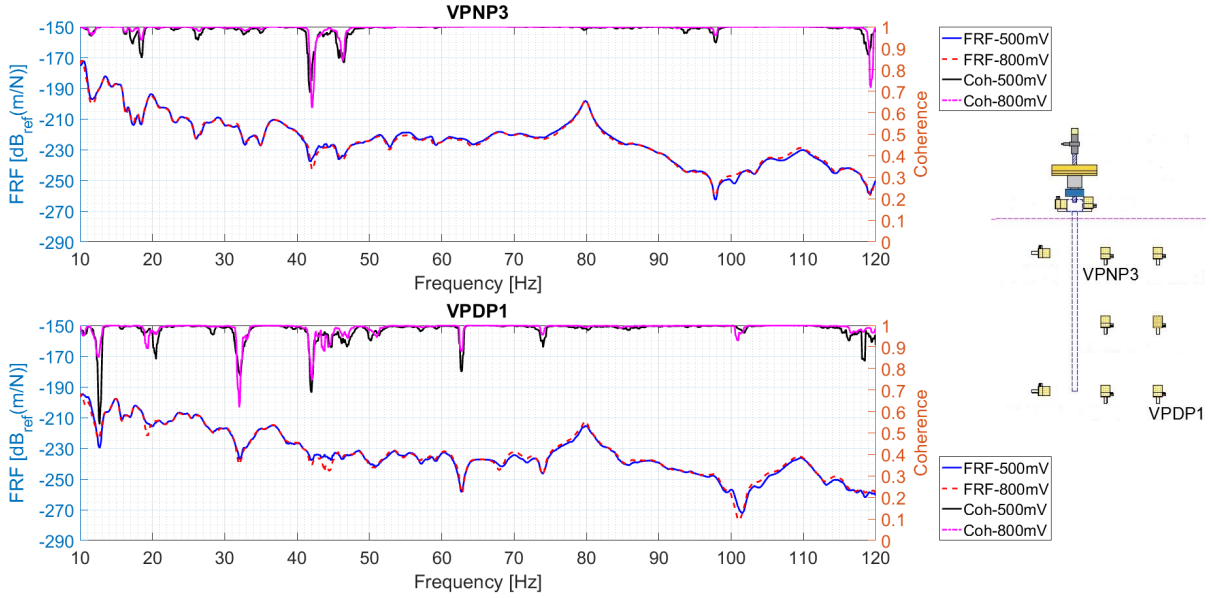


FIGURE 5.10: The FRF and coherence at VPNP3 and VPDP1 (GBV_m2)

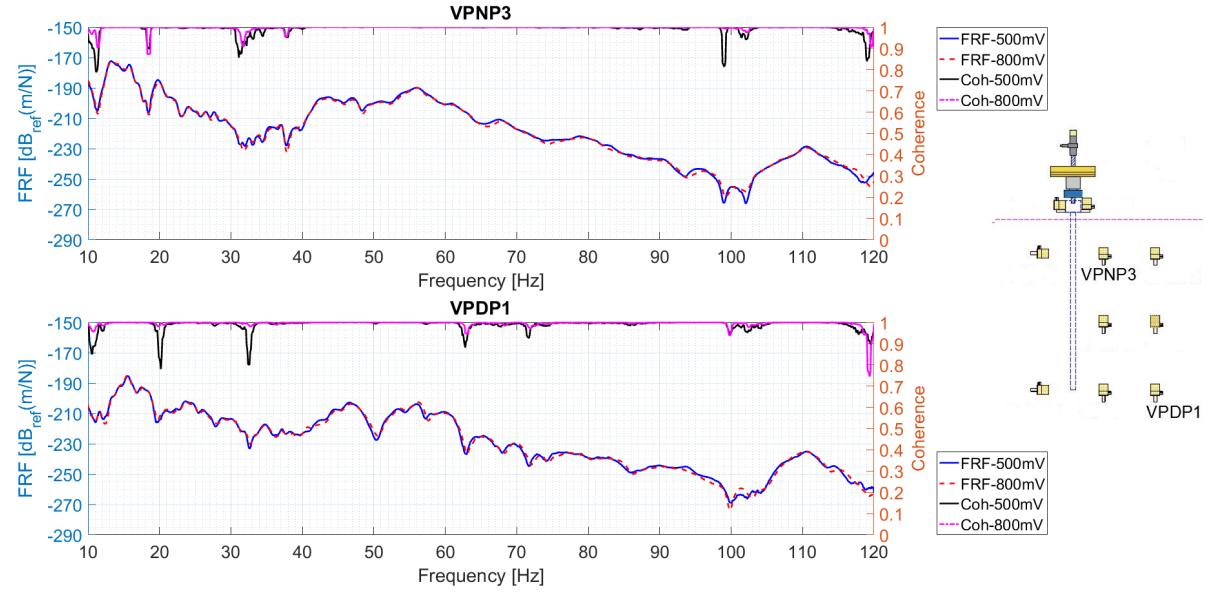


FIGURE 5.11: The FRF and coherence at VPNP3 and VPDP1 (GBV_m3)

5.3 Dead weight effect on pile and soil response amplitude

As has been discussed in Section 5.2, the model behaviour (soil and pile) was linearly proportional to the input amplitude of excitation under each dead weight. To investigate the dead weight effect on model response amplitude, the FRFs (velocity/force) under the same input voltage amplitude of 500 mV are used in this section to make a direct comparison, as presented in Section 5.3.1. The reason

for presenting the velocity data instead of displacement or acceleration is that historically researchers have used velocity data to quantify train induced vibration levels within the ground. Section 5.3.2 places the focus on the interpretation of the findings presented in Section 5.3.1, two simplified mechanical models are proposed in Section 5.3.2 to analyse the pile behaviour and the soil-pile interaction.

5.3.1 Pile and soil responses

FRFs of PCV (pile top) and VPNP3 (nearest measurement location from the excitation source) under three dead weights (m1>m2>m3, see Table 5.1) in linear scale are shown in Figure 5.12. It can be seen that the linear scale data is very small at many frequencies and very hard to distinguish responses. Therefore, dB scale data of PCV and VPNP3 are presented in Figure 5.13 which show the response differences more clearly.

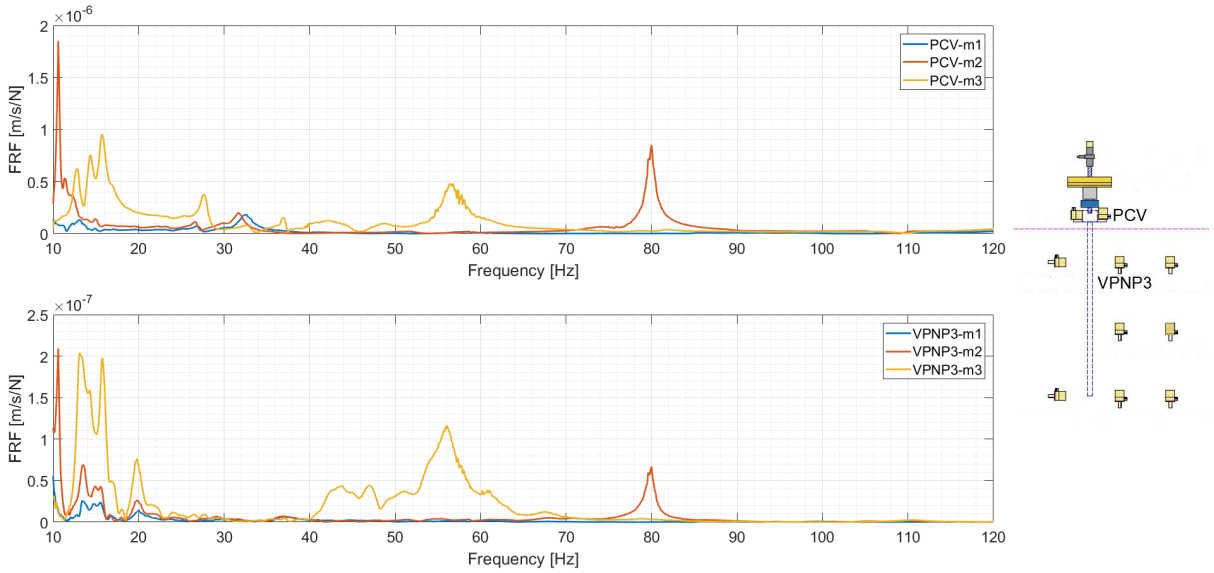


FIGURE 5.12: FRFs (velocity/force) at PCV and VPNP3 (linear scale)

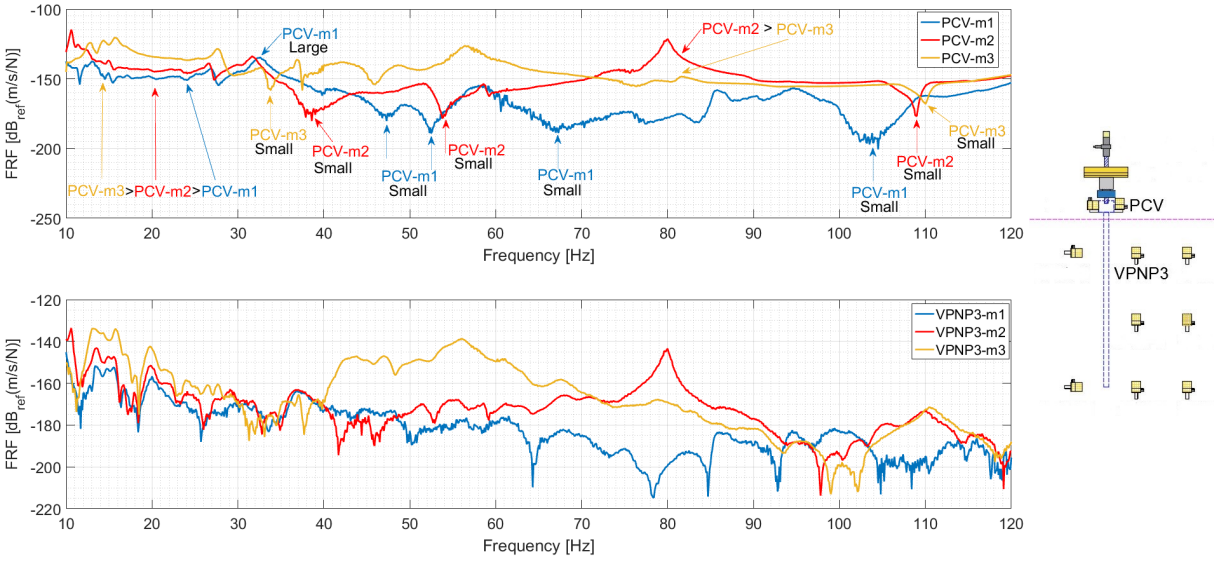


FIGURE 5.13: FRFs (velocity/force) at PCV and VPNP3 (logarithmic scale)

Some observations from Figure 5.12 and Figure 5.13, are illustrated below, with the explanations provided in the following section.

(1) In general, at most frequencies, the model response level (both pile and soil) decreased with increasing dead weight under the same dynamic load: PCV-m3 >PCV-m2>PCV-m1 and VPNP3-m3>VPNP3-m2>VPNP3-m1 (such as 10 Hz-30 Hz , 43 Hz-54 Hz and 60 Hz-71 Hz).

(2) PCV-m1 was quite similar to or even greater than PCV-m2 and PCV-m3 within the frequency range of 30 Hz to 43 Hz.

(3) Within 54 Hz to 60 Hz, PCV-m2 was quite close to PCV-m1.

(4) As marked in Figure 5.13, PCV-m2 was much greater than PCV-m3 within the frequency range of 71 Hz to 105 Hz. However, both PCV-m2 and PCV-m3 were still larger than PCV-m1 in this frequency range.

(5) PCV-m2 was quite close to PCV-m3 within the frequency range of 105 Hz to 120 Hz, but both PCV-m2 and PCV-m3 were still larger than PCV-m1.

(6) At most frequency components, soil responses have the same trend as the pile top. This indicates soil behaviour was consistent with the pile top.

It can be seen from Figure 5.12 that it is very difficult to quantify the response difference between the three dead weights due to a large amount of frequencies

which were used and the FRFs fluctuation with frequency. To make a better comparison, the ratios (PCV-m3/PCV-m2, PCV-m2/PCV-m1, VPNP3-m3/VPNP3-m2 and VPNP3-m2/VPNP3-m1) are calculated. The distributions of the ratio for PCV and VPNP3 are shown in Figure 5.14 and Figure 5.15, respectively. It should be noted that some ratios were considerable (larger than 30 and even up to 100). The reasons are discussed in the following section. These values are not shown in Figure 5.14 and Figure 5.15 due to the percentage value being low and it makes the ratios less than 30 unable to be seen clearly.

It can be found from Figure 5.14 that approximately 15% of the PCV-m2/PCV-m1 ratios are less than 1. 85% of them are larger than 1 and most of the ratios (about 50%) are within 1 to 9. Similarly, approximately 30% of the PCV-m3/PCV-m2 ratios are less than 1. 70% of them are larger than 1 and most of the ratios (about 50%) are within 1 to 9. It can be seen from Figure 5.15 that approximately 18% of the VPNP3-m2/VPNP3-m1 ratios are less than 1. 82% of them are larger than 1 and most of the ratios (about 60%) are within 1 to 9. In terms of the VPNP3-m3/VPNP3-m2 ratios, approximately 30% of them are less than 1. 70% of them are larger than 1 and most of the ratios (about 50%) are within 1 to 9.

This indicates that at most frequencies, the lighter the dead weight, the bigger the pile top and soil responses. The average ratios are calculated and shown in Table 5.2. It can be seen that both PCV and VPNP3 ratios were approximately 2. Therefore, it can be concluded that the pile and soil responses are inversely proportional to the dead weight applied on the pile when the ratio of dead weight and the ultimate bearing capacity is no more than 44%.

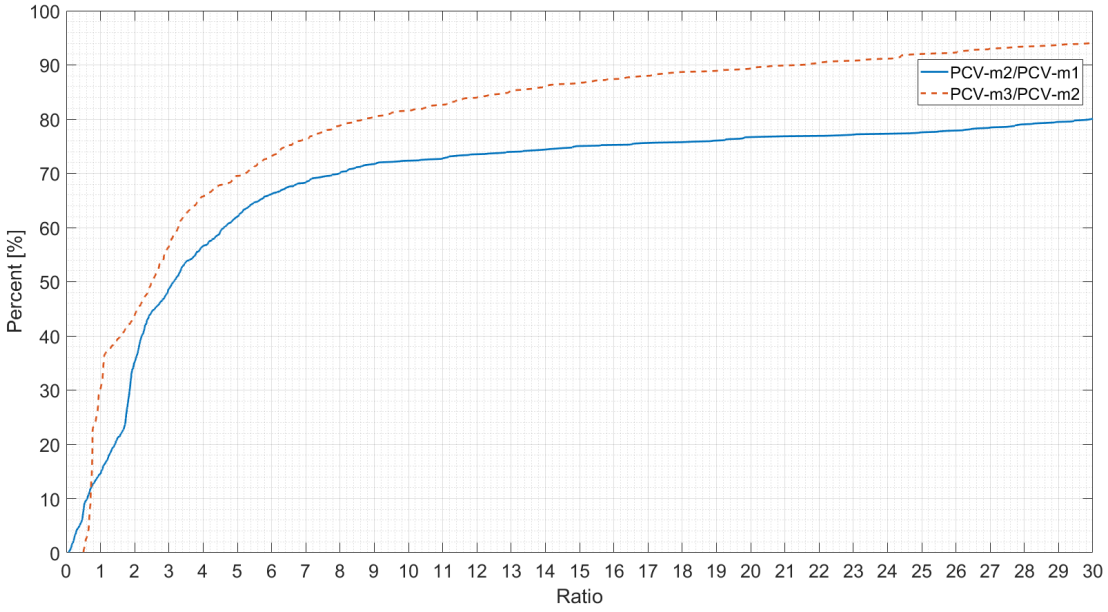


FIGURE 5.14: Response ratios at PCV under different dead weights

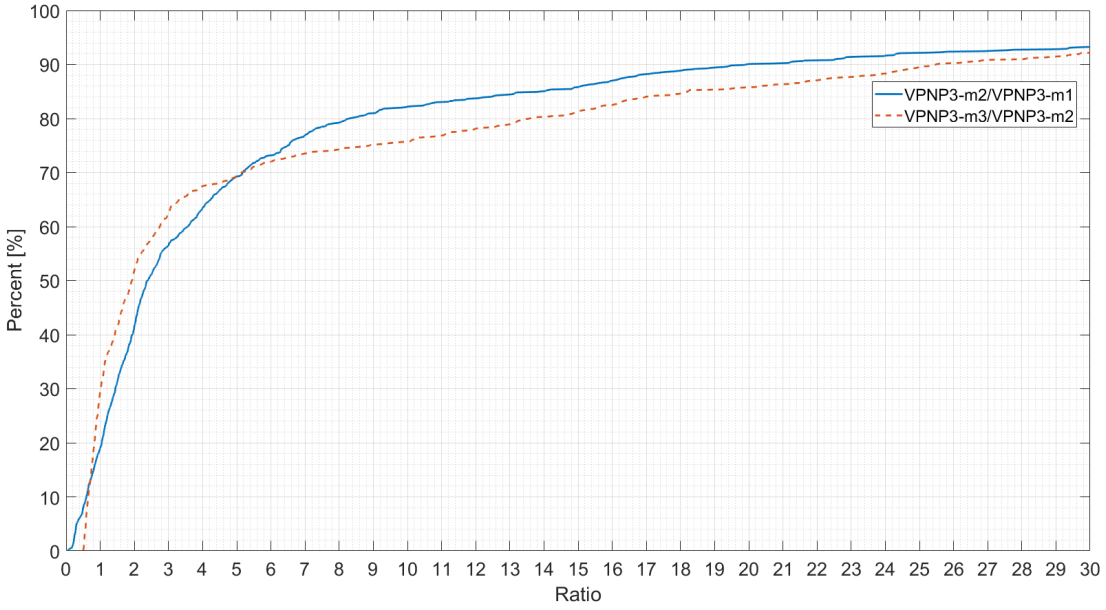


FIGURE 5.15: Response ratios at VPNP3 under different dead weights

TABLE 5.2: Dead load ratios and mean pile top and soil response ratios

Ratio (dead weight)	Mean ratio (PCV)	Mean ratio (VPNP3)
m2/m1=0.55	PCV-m2/PCV-m1=2.14	VPNP3-m2/VPNP3-m1=2.02
m3/m2=0.49	PCV-m3/PCV-m2=2.45	VPNP3-m3/VPNP3-m2=1.98

5.3.2 Result discussion

To explain the above observations, simplified mechanical models are proposed in this section. Section 5.3.2.1 discusses the pile top behaviour and Section 5.3.2.2 details the soil-pile interaction and soil behaviour under dynamic loading.

5.3.2.1 Pile top behaviour under axially dynamic loading

To explain the first five observations illustrated in Section 5.3.1, a simplified multiple degree of freedom (MDOF) system is proposed, as shown in Figure 5.16. In the centrifuge, the model consists of three systems (the supporting system, the loading system and the soil-pile system) and the three systems interact with each other. The vertical oscillation of the above ground loading system and the pile top can be regarded as a two degree of freedom system: two masses (mass 1 denotes the dead weight and mass 2 denotes the pile top) connected by springs (k_1 and k_2 denote spring constants) and dash-pots (c_1 and c_2 denote damping coefficients) in series under the action of an external harmonic load, $F_d(t)$, see Figure 5.16.

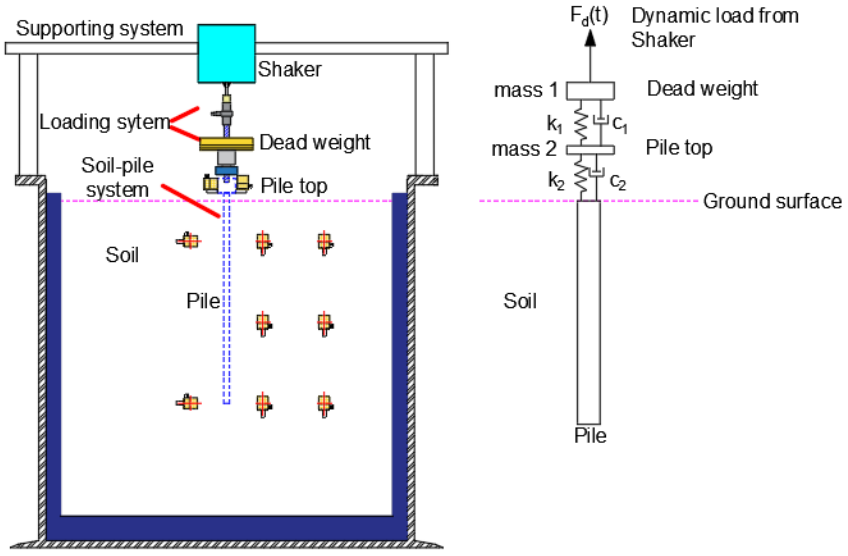


FIGURE 5.16: Simplified MDOF system of above ground system in the centrifuge

In the centrifuge test, the dynamic excitation was applied to the dead weight directly. Under the same dynamic load, the larger the dead weight the smaller the acceleration response if Newton's second law is applied to the dead weight. As a consequence, the vibration level at pile top decreased with the increasing dead weight. For a harmonic oscillation with a frequency of f, the relationship between the displacement amplitude u, the velocity amplitude v and the acceleration amplitude a is given by Equation 5.13. This equation indicates the velocity and the displacement are proportional to the acceleration and they also decrease with the increasing dead weight. This explains why PCV-m3 >PCV-m2>PCV-m1 at most frequencies.

$$a = 2\pi f v = (2\pi f)^2 u \tag{5.13}$$

In addition, measured responses from the dynamic load cell and PCV in frequency domain are shown in Figure 5.17, Figure 5.18 and Figure 5.19 to explain why pile top response did not always decrease with increasing dead weight (observation 2, 3, 4 and 5).

For the two degree of freedom system, the input dynamic force and the resulting response of the pile top are dependent on the mass and the stiffness of the whole system. It can be seen from Figure 5.17, Figure 5.18 and Figure 5.19 that the dynamic force was not constant even though the input voltage amplitude was constant. The dynamic loads varied both with dead weight and frequency. This is because the dead weight on the pile top changes the stiffness and the mass of the

loading system, thus changing the natural frequency and the frequency response behaviour of the loading system. At most frequency components, the input dynamic force amplitude was approximately 4 kN. At some frequencies (77 Hz for GBV_m1, 65 Hz and 100 Hz for GBV_m2 and 96 Hz for GBV_m3), the dynamic load amplitude was much higher than that at other frequencies. The corresponding dynamic force amplitudes were 82.8 kN for GBV_m1, 50.4 kN and 46.8 kN for GBV_m2 and 36.0 kN for GBV_m3. This means the forcing frequency was close to one of the resonance frequencies of the system. On the other hand, at a special frequency for the forced damped spring mass system (i.e. 80 Hz for GBV_m2), the amplitude of dynamic force dropped to almost zero (10 N for GBV_m2). This indicates the forcing frequency was close to the anti-resonance frequency of the loading system. However, this is not the anti-resonance frequency of the soil-pile system, which resulted in relatively larger values of PCV/Force near the anti-resonance frequency of the loading system, as shown in Figure 5.18.

In terms of PCV-m1, it can be seen from Figure 5.17 the force was quite constant within the 30 Hz to 43 Hz range. However, the pile top response was considerable (marked by the black arrow), which indicates the forcing frequency was close to the natural frequency of the pile top. As a consequence, the normalised pile response (PCV/Force) increased and PCV-m1 was similar to or greater than PCV-m2 and PCV-m3 within 30 Hz to 43 Hz.

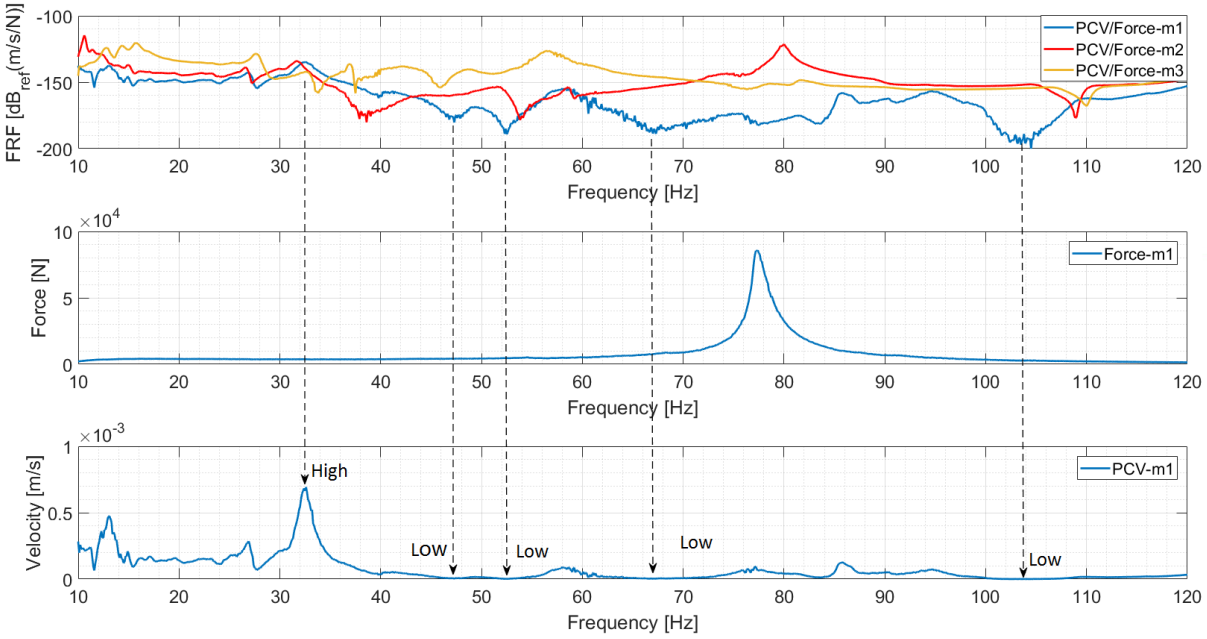


FIGURE 5.17: Dynamic load, pile top velocity and FRFs for PCV (GBV_m1)

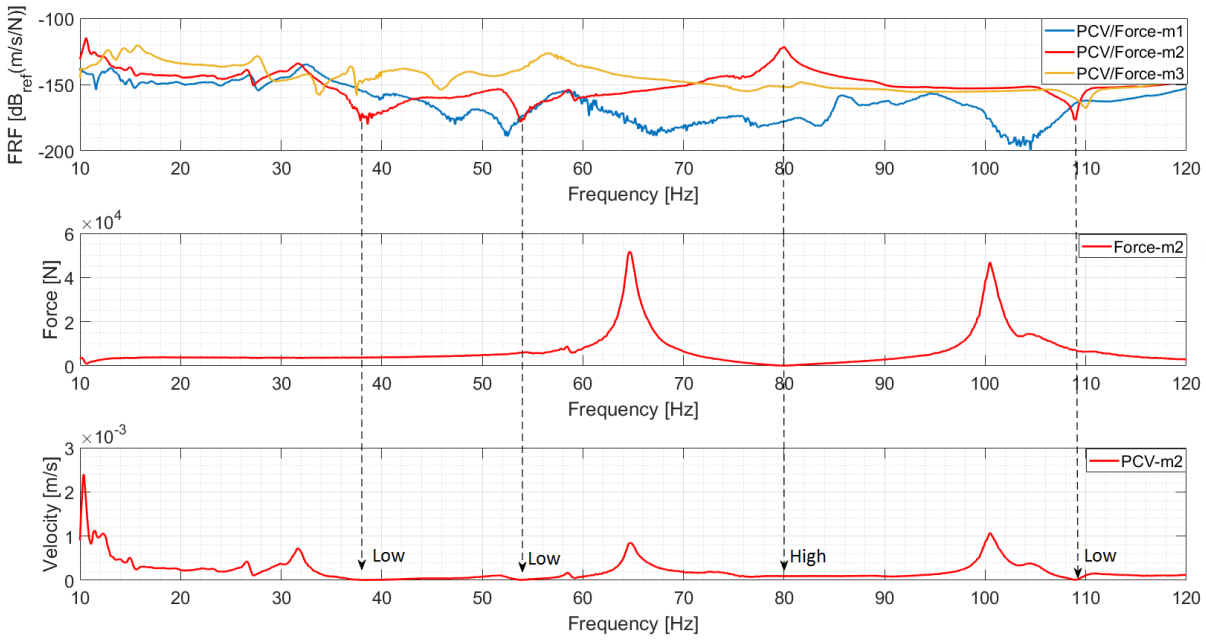


FIGURE 5.18: Dynamic load, pile top velocity and FRFs for PCV (GBV_m2)

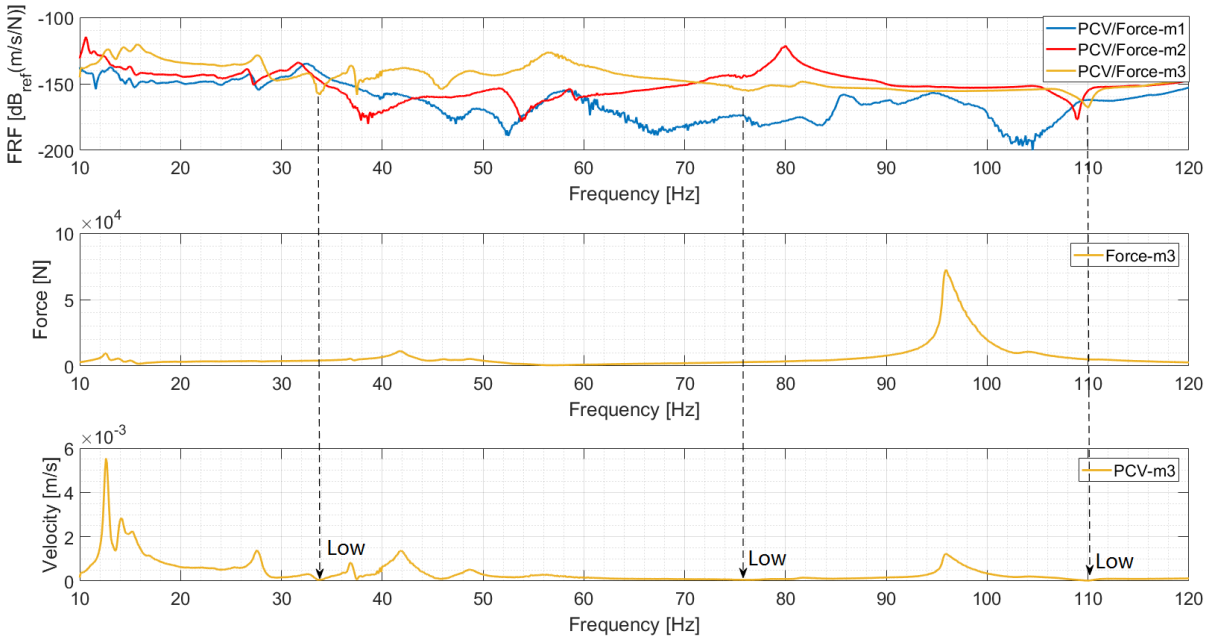


FIGURE 5.19: Dynamic load, pile top velocity and FRFs for PCV (GBV_m3)

It can also be found that within some frequency ranges, the pile top velocity is quite low (marked by the black arrows in Figure 5.17, Figure 5.18 and Figure 5.19), thus resulting in unexpected low FRFs. The possible reason for obtaining very low pile top responses is the forcing frequency was close to the anti-resonance frequency of the system, as explained above. In this case, the external dynamic load would not contribute to the pile response and the resulting coherence between the dynamic

load and the pile top response should be very low. The FRFs and the coherence values of PCV are presented in Figure 5.20. It can be seen that most of low FRFs for each dead weight correspond to the low coherence values (troughs), marked by the arrows.

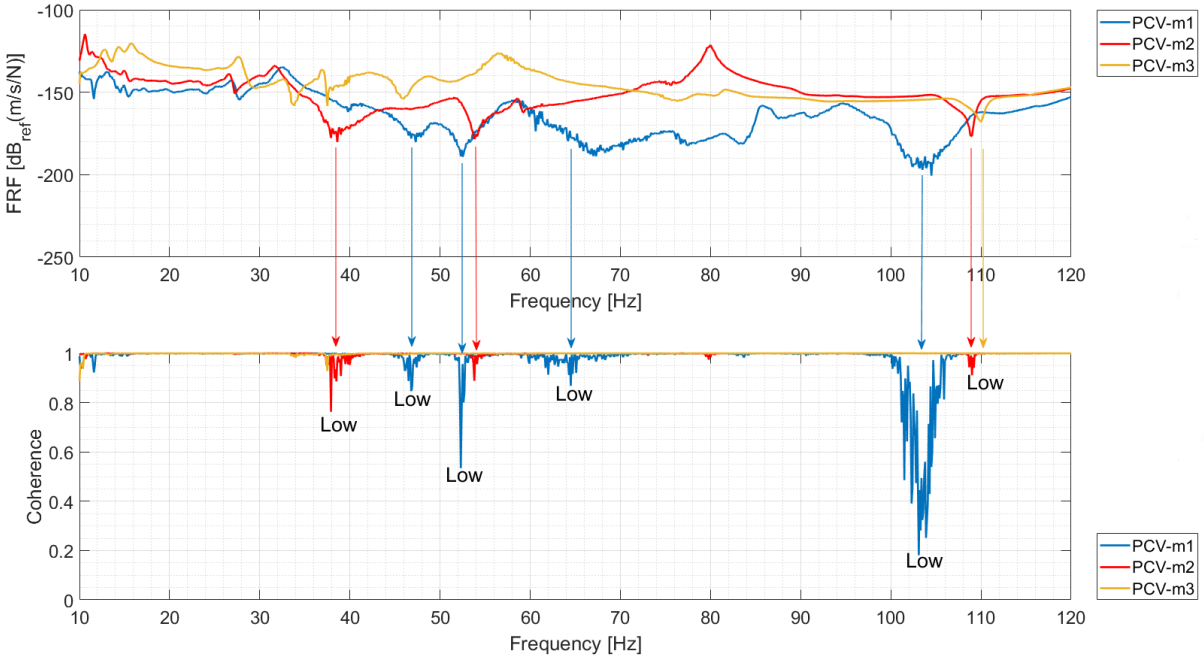


FIGURE 5.20: FRFs and coherence values of PCV

5.3.2.2 Soil-pile interaction under axially dynamic loading

This section explains observation 6 illustrated in Section 5.3.1: the soil response trend is consistent with the pile top, which is related to the dynamic soil-pile interaction. To fully understand the soil-pile interaction, the compressibility of the pile is examined first by analysing the signals measured by the Piezos. Then, a simplified soil-pile mechanical model is proposed based on the findings. Finally, the centrifuge test data is used to verify the proposed the model.

- Compressibility of the pile

For the settlement behaviour of a single axially loaded pile, there are two possible assumptions: compressible pile (Coyle and Reese, 1966) and incompressible pile (Poulos and Davis, 1968). If the pile is assumed to be incompressible, the entire pile must suffer an equal vertical displacement and zero radial displacement. Discussions in Section 5.2 indicate the soil-pile interface can be treated as a perfectly bonded interface during dynamic loading. Therefore, shear waves are generated through shaft friction along the entire pile length at the same time and travel into

the soil. Given that the shear wave velocity increases with depth, it takes less time for the shear waves to arrive at VPNP2 compared to VPNP3, as shown in Figure 5.21. The accelerometers (VPNP3, VPNP2) were placed at the same distance (50 mm in model scale) from the pile with embedded depths of 56 mm and 168 mm. The shear wave velocities at the two depths can be calculated by Equation 4.10 and they are 200 m/s and 281 m/s, respectively. The travel time between the pile shaft and the two accelerometers can be calculated (2.3×10^{-4} s and 1.63×10^{-4} s) and the travel time difference between VPNP3 and VPNP2 is 6.7×10^{-5} s. In addition, the measured responses at VPNP3 should be smaller than VPNP2 due to the damping ratio decreases with depth, as discussed in Section 5.4.

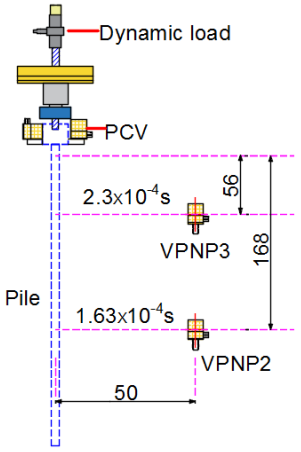


FIGURE 5.21: Travel time difference in the soil for incompressible pile (model scale: in mm)

To investigate whether the test results are consistent with the calculated travel time difference (6.7×10^{-5} s) by assuming the pile is incompressible, the travel time difference between VPNP3 and VPNP2 in the centrifuge test is calculated. An example of measured time history data from Test GBV_m2 is shown in Figure 5.22. The input dynamic load and measured accelerations from PCV, VPNP3 and VPNP2 in model scale are presented in Figure 5.22. First, it can be seen that there was a slight time delay between the input signal (dynamic load) and the output signal (PCV). This suggests the vibration generated by the shaker took some time to travel to PCV and the above ground system cannot be treated as an incompressible system. It can also be seen from Figure 5.22 that the shear wave did travel to VPNP2 earlier than VPNP3. However, the travel time difference between VPNP3 and VPNP2 (mean value from three tests) was 3.6×10^{-5} s, which was shorter than the estimated 6.7×10^{-5} s obtained above. The peak to peak method, detailed in Chapter 4, was used to determine the travel time. This means the pile is compressible and the pressure wave generated within the

pile travelled along the pile from the top to the bottom, which can reduce the time difference between VPNP3 and VPNP2. In this study, the pile was made of aluminium. The pressure wave velocity of the pile can be estimated using Equation 2.6, Equation 2.10 and Equation 2.11. The elastic modulus, the shear modulus and the density of aluminium used to obtain the pressure wave velocity are 70 GPa, 27 GPa and 2700 kg/m^3, respectively. Thereafter, the travel time the pressure wave needs from the depth of 56 mm to 168 mm can be estimated and it is 2.2×10^{-5} s. This value (2.2×10^{-5} s) is close to the difference between the theoretically estimated travel time difference and the measured travel time difference (6.7×10^{-5} s-3.6×10^{-5} s=3.1×10^{-5} s).

It can also be seen that the response amplitude at VPNP3 was larger than VPNP2. This also indicates that the pile in this study was compressible. Otherwise, VPNP3 should be smaller than VPNP2, as explained above.

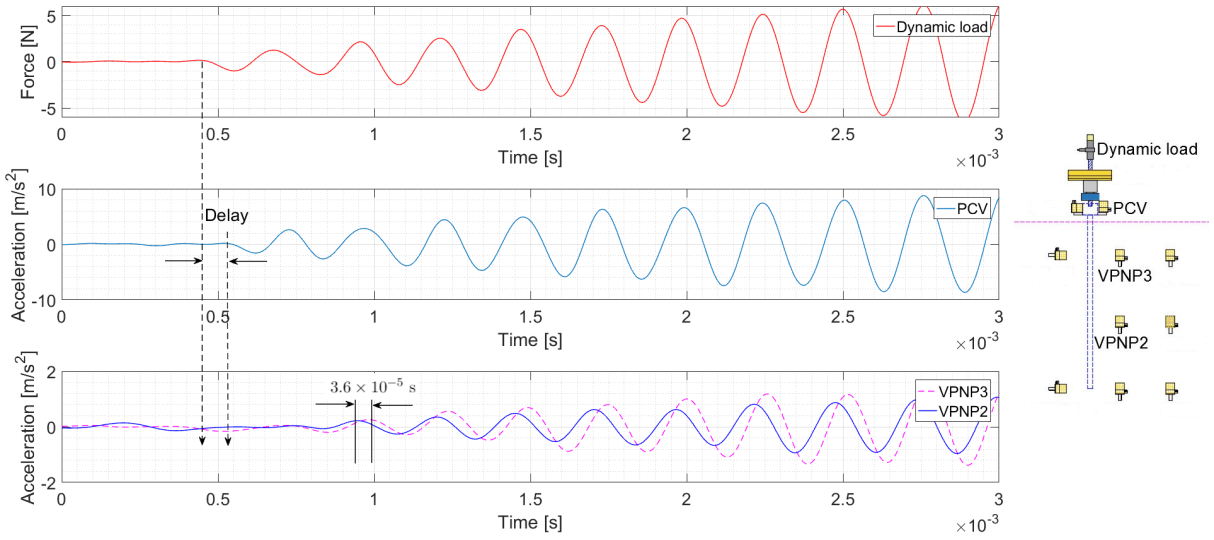


FIGURE 5.22: An example of travel time difference in the soil from GBV_m2_500mV (model scale)

- Simplified soil-pile model

As shown in Figure 5.23, the soil-pile system is simplified as a number of pile segments connected by springs ($k_{p,n}$ denotes the pile spring constant) and dashpots ($c_{p,n}$ denotes the pile damping coefficient) under the action of dynamic loads ($Q_d(t)$) transmitted to the pile. Meanwhile, the interaction between the pile and the soil is assumed to be determined by independent springs distributed along the pile shaft ($k_{s,n}$ denotes the springs constant of the soil in the vicinity of the pile) and at the pile base (k_b and c_b denote the spring constant and the damping coefficient at the pile base). An element of pile at a depth z from ground surface is also shown in Figure 5.23.

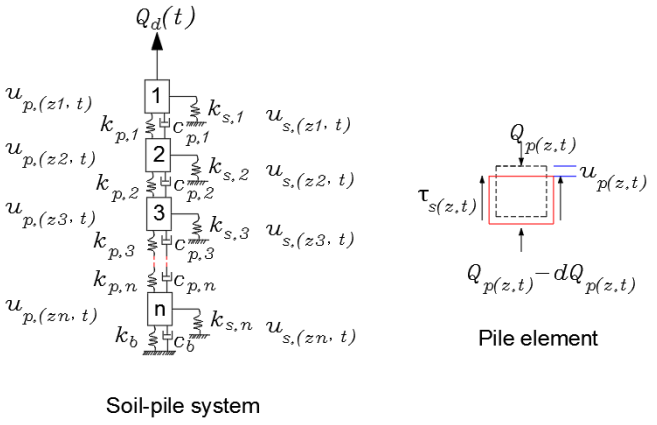


FIGURE 5.23: Simplified soil-pile system in the centrifuge

At a certain depth z, the vertical displacement of a cylindrical pile is represented by $u_{p(z,t)}$ under dynamic loads, $Q_{p(z,t)}$. The pile is compressible, as concluded above, and the displacement of the pile element is assumed to be purely caused by the axial elastic deformation $du_{p(z,t)}$ which equals:

$$du_{p(z,t)} = \frac{Q_{p(z,t)}dz}{AE} \tag{5.14}$$

where $Q_{p(z,t)}$ is the axial load, dz is the length of the pile element, A is the cross-sectional area of the pile and E is the elastic modulus of the pile.

The difference in axial forces at the top and bottom of the element is $dQ_{p(z,t)}$. The difference $dQ_{p(z,t)}$ equals the shear force carried by the soil:

$$dQ_{p(z,t)} = \pi d\tau_{s(z,t)}dz \tag{5.15}$$

where d is the diameter of the pile and $\tau_{s(z,t)}$ is the shear stress acting over a circumferential section of a segment dz.

It was shown in Section 5.2 that the pile and soil experienced the same displacement at the interface during dynamic loading: $u_{p(z,t)} = u_{s(z,t)}$. Therefore, the shear stress $\tau_{s(z,t)}$ is given by:

$$\tau_{s(z,t)} = k_s u_{p(z,t)} \tag{5.16}$$

where k_s is the spring constant of the soil in the vicinity of the pile segment.

From Equation 5.15 and Equation 5.16, the following equation can be formulated:

$$dQ_{p(z,t)} = \pi d k_s u_{p(z,t)}dz \tag{5.17}$$

The above simplified soil-pile model and equations indicate the dynamic load is transferred into the soil through friction at the soil-pile interface. Consequently, the dynamic axial load within the pile decreases with depth, thus resulting in the decreasing axial elastic deformation of the pile along depth. Therefore, the soil displacement at the interface also decreases with depth. As explained in Section 5.3.2.1, the relationship between the displacement amplitude u, the velocity amplitude v and the acceleration amplitude a indicates velocity and acceleration within the soil also decrease along depth because they are proportional to the displacement. It should be noted that the dynamic load and responses (displacement, velocity and acceleration) mentioned above vary with time, thus generating harmonic vibrations within the ground.

- Soil particle velocity

The proposed model suggests the particle velocity within the interior of the soil generated by the vibrating pile should be the same if the pile top experiences the same velocity even under different dead weights. To verify this, the ratios of measured velocity from VPNP3 (interior of soil) and that from PCV (pile top) under three dead weights are shown in Figure 5.24 as an example. Ratios in both linear scale and log scale are presented to clearly show the results due to some values in linear scale being very small.

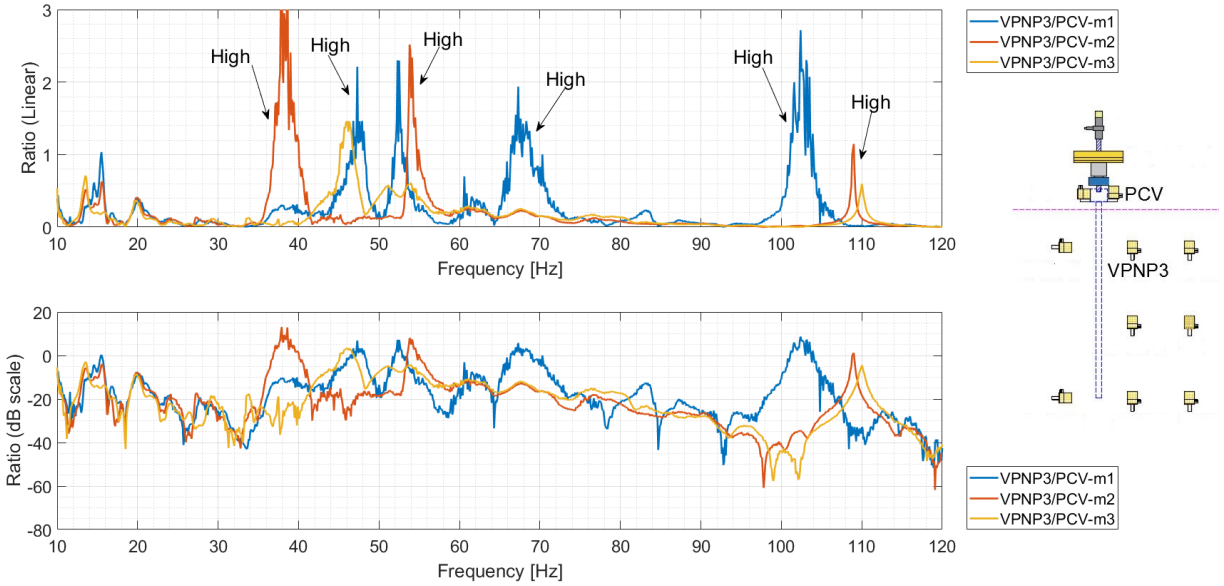


FIGURE 5.24: Response ratio (VPNP3/PCV) in linear and log scale

The data in Figure 5.24 indicates that ratios under three dead weights were almost the same at most frequencies and they were less than 1 (within 10 Hz to 35 Hz and

70 Hz to 95 Hz for the three dead weights). Especially for GBV_m2 and GBV_m3, the ratios were almost the same at all frequencies. This indicates that the vibration within the soil is dominated by the deformation of the pile. As discussed above, the soil-pile interface is bonded. Therefore, the dynamic velocity amplitude within the soil is proportional to the dynamic velocity of the pile, thus leading to the same VPNP3/PCV ratios even under different dead weights. However, at some frequency ranges, as marked by the black arrows, the ratios were larger than 1, such as 45 Hz to 55 Hz and 65 Hz to 70 Hz for m1. This leads to a large difference between different dead weights.

To explain why some ratios were larger than 1, the pile rocking effect and centrifuge induced interference effect are examined. In this study, the horizontal movement of the pile was measured by the accelerometer PCH. The ratios (VPNP3/PCV) and the velocities measured by PCV and PCH are shown in Figure 5.25, Figure 5.26 and Figure 5.27. In addition, centrifuge induced effects on the measured vertical soil velocity are evaluated. Ratios of measured velocity during shaker excitation and centrifuge interference induced velocity without shaker excitation at VPNP3 are calculated and presented in Figure 5.25, Figure 5.26 and Figure 5.27 in linear scale (denoted as SNR). Some extremely high SNR values are not presented in these three figures to make most values visible.

First, it can be seen that the SNR was very large at most frequencies: approximately 400 for GBV_m1, 1400 for GBV_m2 and 2200 for GBV_m3. This indicates the centrifuge induced interference was insignificant and would not lead to such high VPNP3/PCV ratios. Similar to the FRFs of PCV, see Figure 5.17, Figure 5.18 and Figure 5.19, the relatively large VPNP3/PCV ratios were a result of the very small vertical pile top velocities within these frequency ranges compared to the velocities of VPNP3. This is possibly because these frequency ranges were close to the anti-resonance frequency of the pile-soil system in the vertical direction. However, it can be seen that horizontal velocities at PCH were relatively high compared with PCV within these frequency ranges. Therefore, it can be concluded that the horizontal movement of the pile may generate pressure waves in the soil and the pressure waves can alter the vertical movement of soil particles. As a consequence, the VPNP3/PCV ratios were relatively high and even larger than 1 within these frequency ranges. Overall, presented results indicate vertical soil behaviour was consistent with the vertical pile top response at most frequencies.

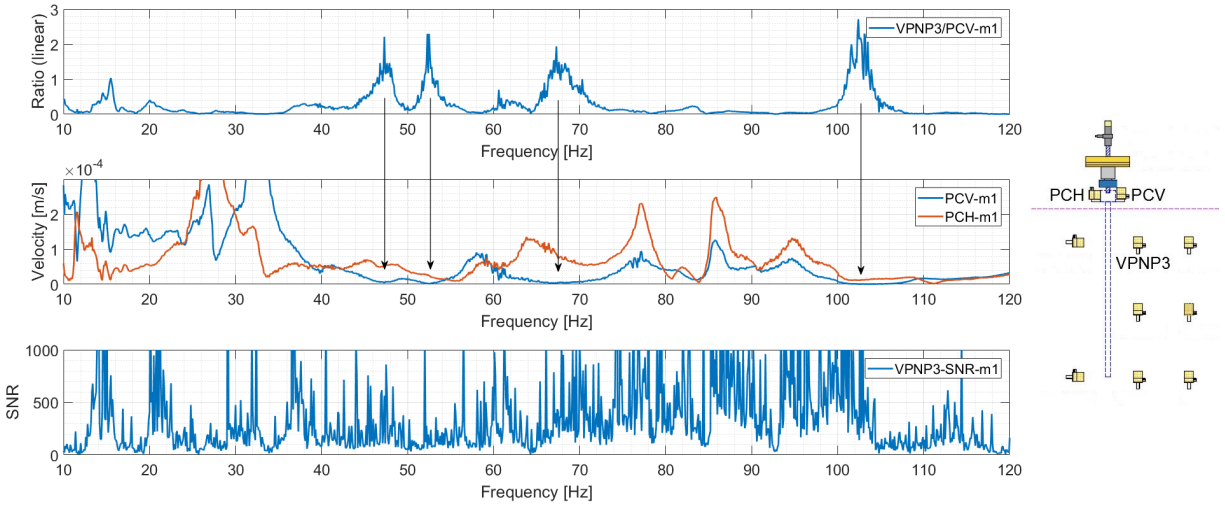


FIGURE 5.25: Response ratios and velocity responses at PCV and VNPN3 (GBV_m1)

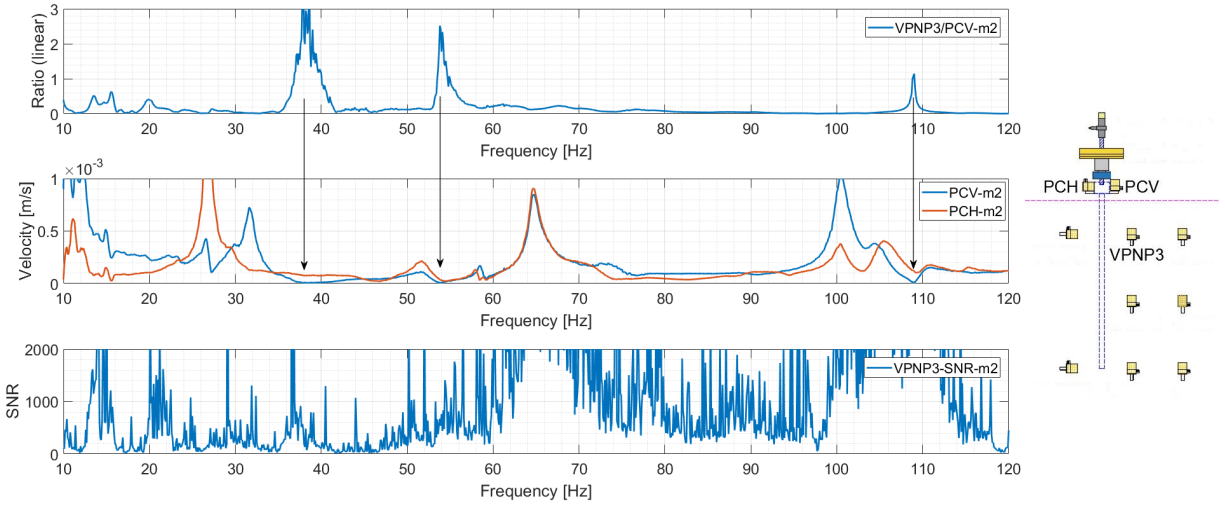


FIGURE 5.26: Response ratios and velocity responses at PCV and VNPN3 (GBV_m2)

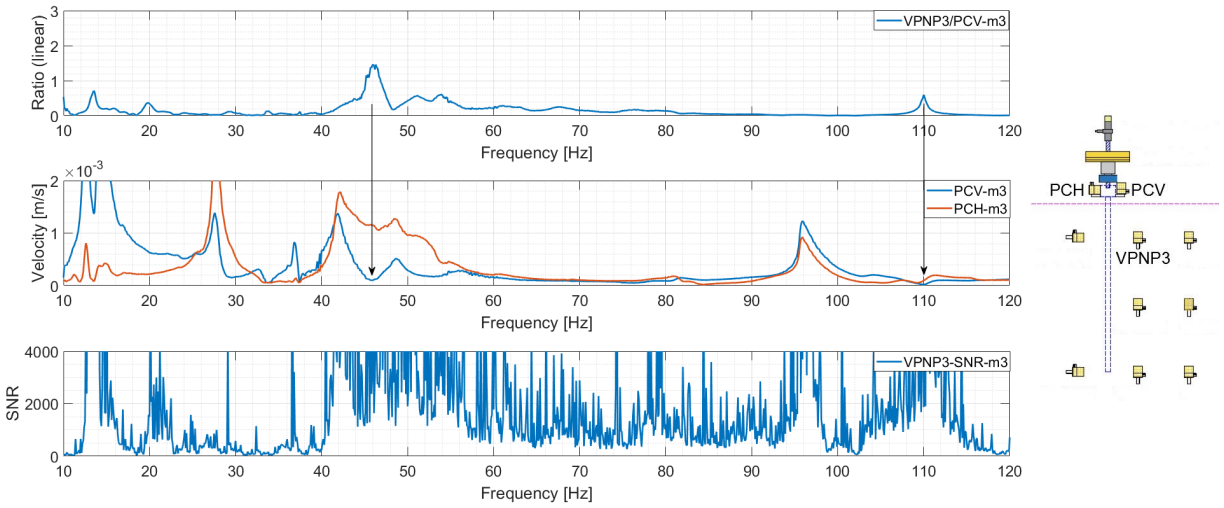


FIGURE 5.27: Response ratios and velocity responses at PCV and VNPN3 (GBV_m3)

5.4 Soil damping along depth and vibration propagation

It has been concluded that the vertical vibration level generated at the soil-pile interface decreases with depth. The vertical vibrations generated at the interface propagate radially in the soil. The vertical vibration level within the soil along depth at a certain radial distance from the pile is affected by the vibration level at the interface and the damping ratio of soil along depth. To fully understand the vibration propagation in the soil, the shear strain amplitude within the soil caused by vertical vibrations and the damping ratio along depth are estimated in Section 5.4.1. The vibration attenuation properties along radial distance are discussed in Section 5.4.2.

5.4.1 Soil damping ratio

As discussed in Section 2.2.3.2, the damping ratio of sand is affected strongly by shear strain and effective principal stress: the damping ratio increases with increasing shear strain and decreasing effective principal stress. Therefore, it is very important to estimate the shear strain level in the soil. Additionally, soil damping ratio in the centrifuge model is calculated using the logarithmic decrement method, detailed in this section.

5.4.1.1 Logarithmic decrement method

The vertical vibration of the pile or soil in this study can be simplified as a damped single degree of freedom (SDOF) system. The logarithmic decrement method can be used to determine the damping ratio of a damped SDOF system from the free vibration response. As shown in Figure 5.28, the response amplitude (A_i) of the free vibration of a damped SDOF system decreases with time and the damping ratio (D) can be calculated using Equation 5.18 (De Silva, 2007). A_i is the amplitude of the i^{th} peak, see Figure 5.28.

$$D = \sqrt{\frac{\left(\ln\frac{A_i}{A_{i+n}}\right)^2}{\left(\ln\frac{A_i}{A_{i+n}}\right)^2 + 4\pi^2 n^2}} \tag{5.18}$$

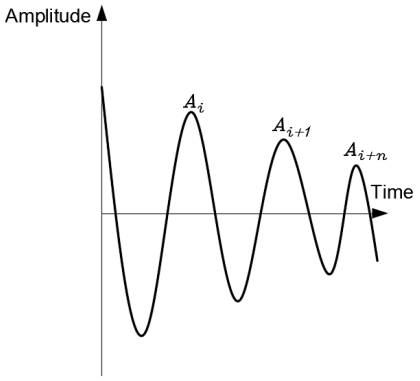


FIGURE 5.28: Logarithmic decrement method

5.4.1.2 Shear strain of soil in the centrifuge model

The shear strain amplitude can be calculated using the following equation (Kim and Lee, 2000).

$$\gamma = \frac{\dot{\mu}}{v_s} \tag{5.19}$$

where γ is the shear strain amplitude, $\dot{\mu}$ is the particle velocity, and v_s is the shear wave velocity.

As shown in Figure 5.29, soil particle motion is perpendicular to the direction of wave propagation for shear waves. Within an infinitesimal time interval (d_t), the shear displacement of soil is $\dot{\mu}d_t$ and the initial length can be regarded as $v_s d_t$. The shear strain can be calculated using Equation 5.19. The shear wave velocity of soil v_s can be calculated by Equation 4.10 obtained from the bender element test,

see Chapter 4. Particle motion velocity $\dot{\mu}$ is obtained by integrating the vertical accelerations from the piezoelectric accelerometers. This method is based on the recordings from just one accelerometer and it is referred to as one point based equation in this study.

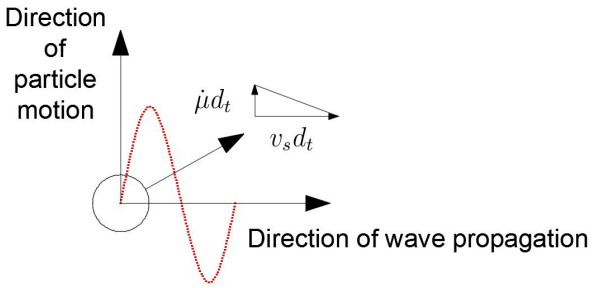


FIGURE 5.29: shear strain calculation using particle velocity

As discussed in Section 5.2.5, soil response is proportional to the input amplitude of excitation. The vertical soil response from GBV_m1_800mV, GBV_m2_800mV, and GBV_m3_800mV (largest input amplitude under three dead loads) was employed to calculate soil shear strain, as shown in Figure 5.30, Figure 5.31 and Figure 5.32. Test results indicate the shear strain the soil experienced at 6 locations was within the very small range (less than 1.0×10^{-6} at all frequency components) and the shear strain amplitude under three dead weights was quite similar. It can be seen from that the overall trend is shear strain amplitudes are larger within the frequency range of 10 Hz to 20 Hz than that within 20 Hz to 120 Hz. Another important feature is the amplitudes of shear strain are 1.0×10^{-7} at almost all the frequencies under three dead weights. The shear strain amplitude near the pile shaft, say 1 mm from the pile, can be estimated using Equation 5.20, as detailed in Section 5.4.2. In summary, this equation can calculate the soil response at point B (the soil near pile in this case) if the soil response at point A (the soil response at VPNP3) is already known. The estimated shear strain amplitudes are within the range of 1.0×10^{-5} to 1.0×10^{-6} at all frequencies.

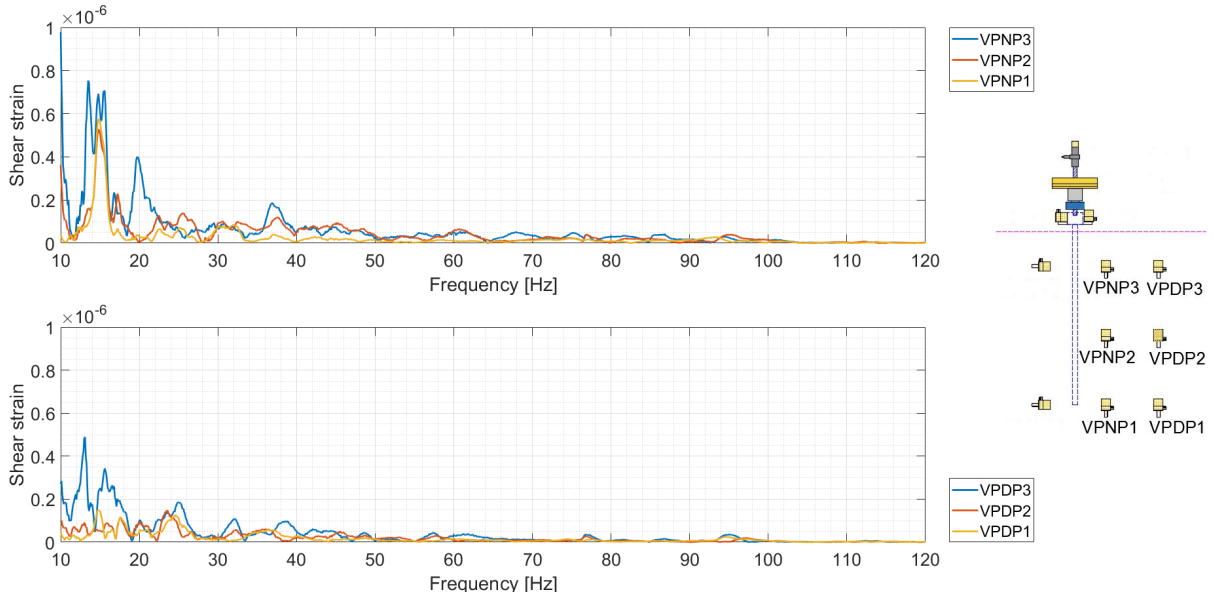


FIGURE 5.30: Shear strain of soil (GBV_m1_800mV)

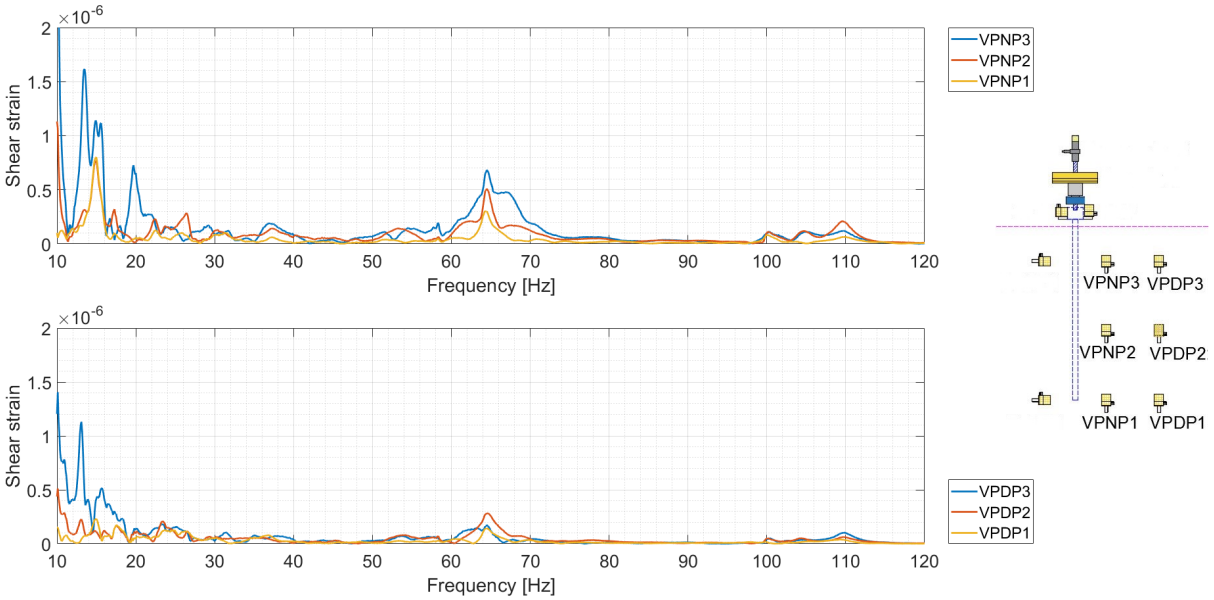


FIGURE 5.31: Shear strain of soil (GBV_m2_800mV)

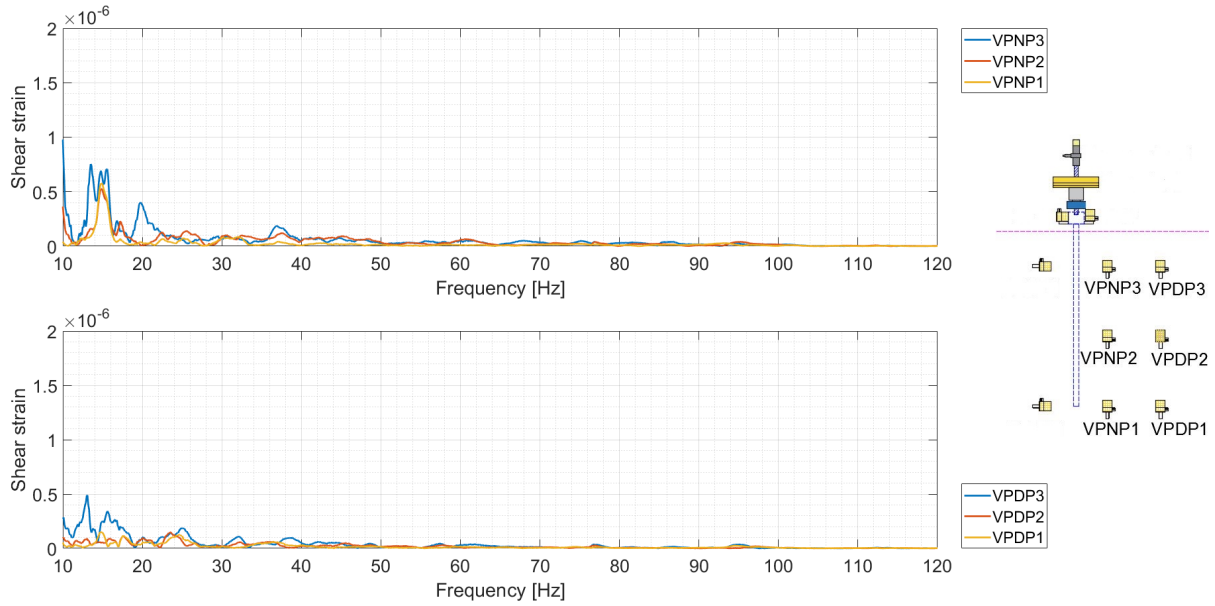


FIGURE 5.32: Shear strain of soil (GBV_m3_800mV)

5.4.1.3 Damping ratio of soil along depth

It was reported by Seed et al. (1986) that the damping ratio of sand under very the small strain is approximately 1% to 2%, see Figure 5.33. The findings can provide reference values for the damping ratio of dry sand used in this study under very small strain.

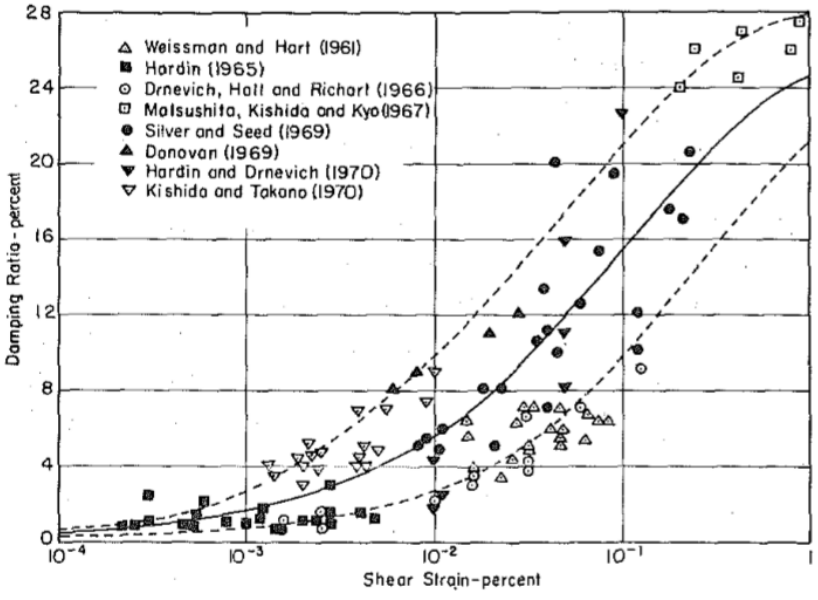


FIGURE 5.33: Soil damping for dry sand (Seed et al., 1986)

The logarithmic decrement method was used in this study to calculate the damping ratio of the soil using data recorded by VPNP3, VPNP2 and VPNP1. After

the excitation from the shaker stops, the response amplitudes can be obtained from the measured vertical free vibration data and Equation 5.18 can be used to calculate the damping ratio. An example from Test GBV_m2 at 3876 Hz is shown in Figure 5.34 and it can be seen that soil responses decrease with time after the excitation stops. The original acceleration data was used to calculate the damping ratio instead of the velocity or the displacement data due to integrated and filtered data may provide less accurate results.

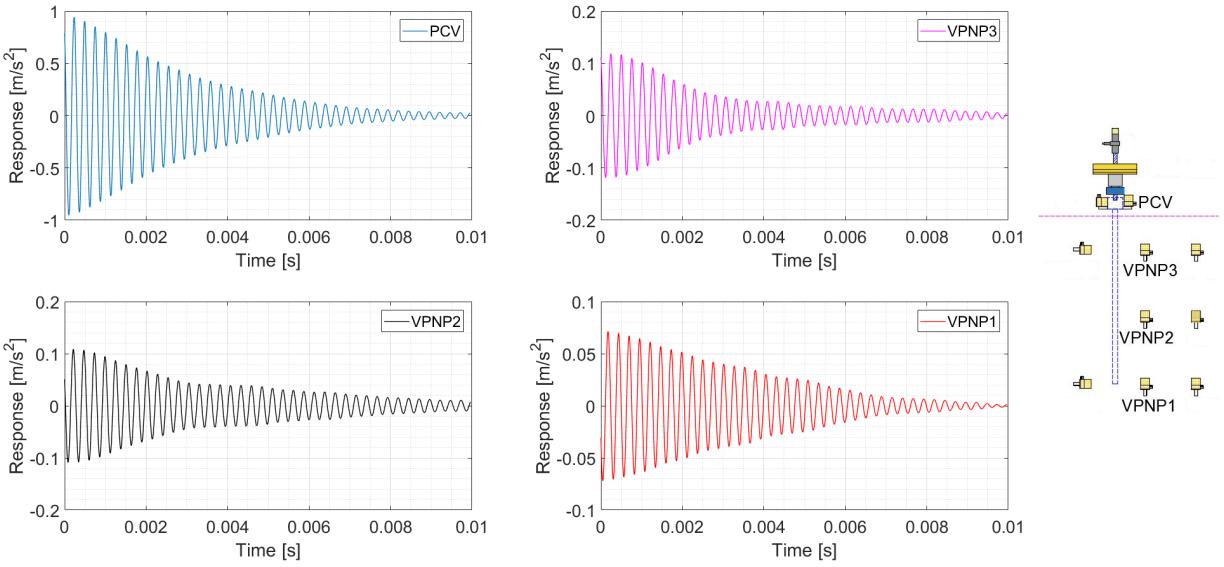


FIGURE 5.34: Soil damping (an example from GBV_m2)

Theoretically, the free vibration data should be used to calculate the damping ratio. However, it is found from Figure 5.34 that the pile is still vibrating after the shaker stops moving and the vibrating pile is still generating vibrations in the soil. Therefore the recorded data by soil Piezos is not the free vibration signal due to data being affected by the free-vibrating pile. Moreover, it is very difficult to determine when the effects of the vibrating pile stops because the signal is getting smaller and affected by the noise and reflected vibrations. However, it is believed that the impact from the free-vibrating pile on the soil response is getting smaller due to the pile vibration amplitude decreasing with time.

According to Equation 5.18, two peaks (A_i and A_{i+n}) are needed to calculate the damping ratio. Ideally, A_{i+n} is smaller than A_i for the free vibration. A feature observed from Figure 5.34 is that the two adjacent peaks (A_i and A_{i+1}) are very similar and A_{i+1} is even larger than A_i. This is because the soil vibration level is very small and vulnerable to centrifuge related interference. However, it can be seen that the overall trend is the soil vibration amplitude decreases with time,

especially for the first 14 peaks. Therefore, a n value of 2 (A_i and A_{i+2}) is used to evaluate the change in damping with time, and results are presented in Figure 5.35.

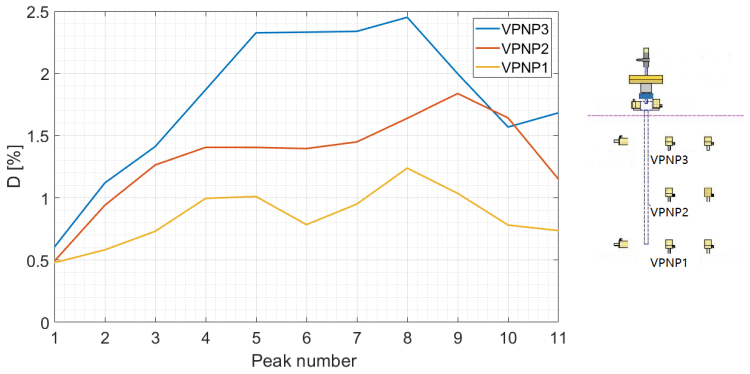


FIGURE 5.35: Soil damping at VPNP3, VPNP2 and VPNP1

It can be seen that the damping ratio increases with time and then tends to be constant from the the 4^{th} peak number. Finally, the damping ratio starts to decrease from the 9^{th} peak number. This indicates interference from the vibrating pile can significantly affect the soil response at the very beginning right after the shaker stops. Therefore, the mean damping ratios at VPNP3, VPNP2 and VPNP1 are calculated using the values from the 4^{th} to the 9^{th} peak number. The damping ratios of the dry sand at three different depths (corresponding confining stresses: 40 kPa, 120 kPa and 200 kPa) tested in this study are: 2.2% at VPNP3, 1.5% at VPNP2, and 1.0% at VPNP1. Compared to VPNP3 and VPNP2, the damping ratio of VPNP1 is the smallest. This is because VPNP1 is the deepest observation point and the vibration level is smaller than VPNP3 and VPNP2. These damping ratios are used in this study to perform the numerical modelling. The damping ratio profile of dry Congleton sand adopted by this study is shown in Figure 5.36.

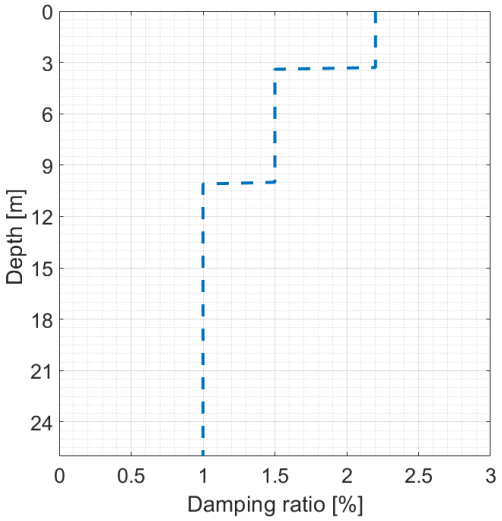


FIGURE 5.36: Soil damping ratio with depth in prototype scale

5.4.2 Vibration attenuation with radial distance

As mentioned before, the proposed soil-pile interaction model in Section 5.3.2.2 indicates soil response generated at the soil-pile interface decreased with depth. However, results in Figure 5.36 suggest damping ratio of the soil also decreased with depth. This indicates the soil vibration level at shallower depths may be smaller than that at deeper locations due to soil damping being larger at shallower depths. To investigate this point, the vibration attenuation property with radial distance is discussed in this section. First of all, the centrifuge test results are used to verify a theoretical equation which is capable of predicting the vibration propagation in the soil. Then, this equation is used to investigate the vibration attenuation and to examine the reflected vibration levels from the rigid boundary.

5.4.2.1 Theoretical estimation

As reviewed in Section 2.1.1, several vibration prediction equations were developed by previous researchers to predict ground vibrations. Of them, Equation 2.1 has a good agreement with field testing results, and every parameter in Equation 2.1 can be obtained experimentally in this study. Therefore, Equation 2.1 is used to make a comparison with the centrifuge test results. For a vertically loaded friction pile, the geometric damping coefficient n is 1.0 based on Table 2.1. This vibration prediction equation can be represented by:

$$W_2 = W_1 \left(\frac{r_1}{r_2} \right) e^{-\frac{2\pi D f}{c}(r_2 - r_1)} \tag{5.20}$$

The definition of every parameter is explained in Section 2.1.1. Of them, the damping ratio, D, is shown in Figure 5.36 and the wave velocity, c, can be obtained by Equation 4.10.

5.4.2.2 Centrifuge test results versus theory

In this study, VPNP1, VPNP2 and VPNP3 (VPNPs) were placed at 3.0 m away from the pile center and VPDP1, VPDP2 and VPDP3 (VPDPs) were placed at 8.1 m away from the pile center. The soil response ratio of two points at the same depth (VPDPs/VPNPs) can be estimated by Equation 5.20 by assuming the vibration amplitude (W_1) at point 1 (VPNPs) is the same at all depths and W_1 equals 1. The distance (r_1 and r_2) is regarded as the horizontal distance from the centre of the accelerometers to the pile centre, as shown in Figure 3.4. The vibration amplitude (W_2) at point 2 (VPDPs) can be calculated using W_2/W_1 due to W_1=1. The soil damping ratio with depth under the shear strain of 10^{-6}, illustrated in Figure 5.36, and the measured shear wave velocities at three depths were used to calculate W_2/W_1. In addition, the measured velocity responses at VPDPs and VPNPs were used to calculate the response ratios and results from GBV_m2 and GBV_m3 are presented in Figure 5.37 and Figure 5.38. The reason for not presenting results from GBV_m1 is that vertical soil responses at a lot of frequencies were affected by the pile rocking, as shown in Figure 5.25.

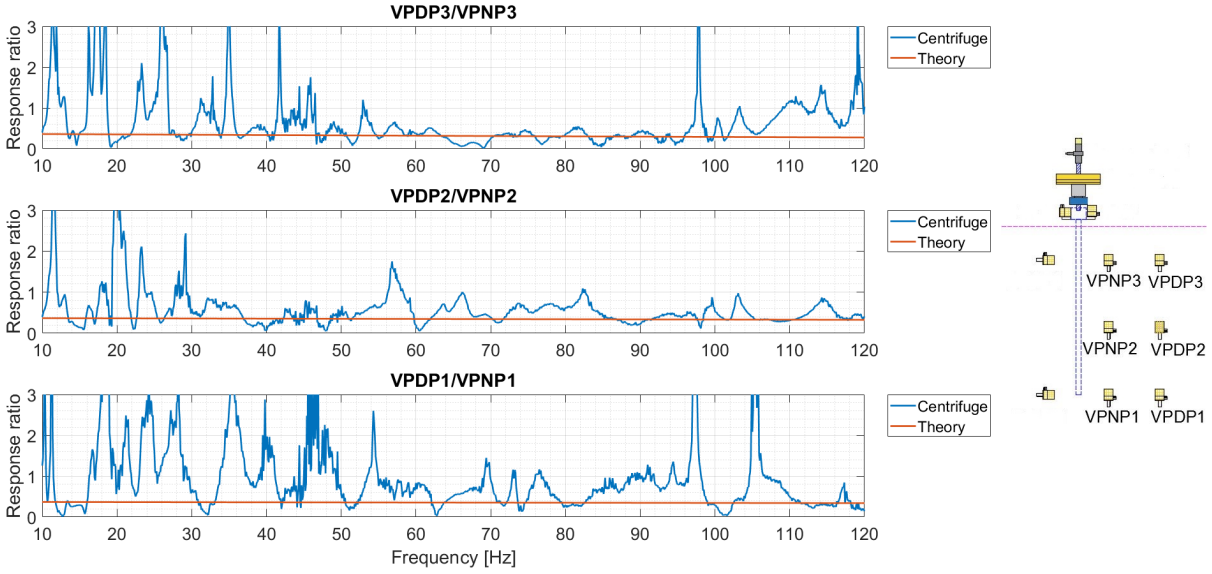


FIGURE 5.37: Response ratio: centrifuge versus theory (GBV_m2)

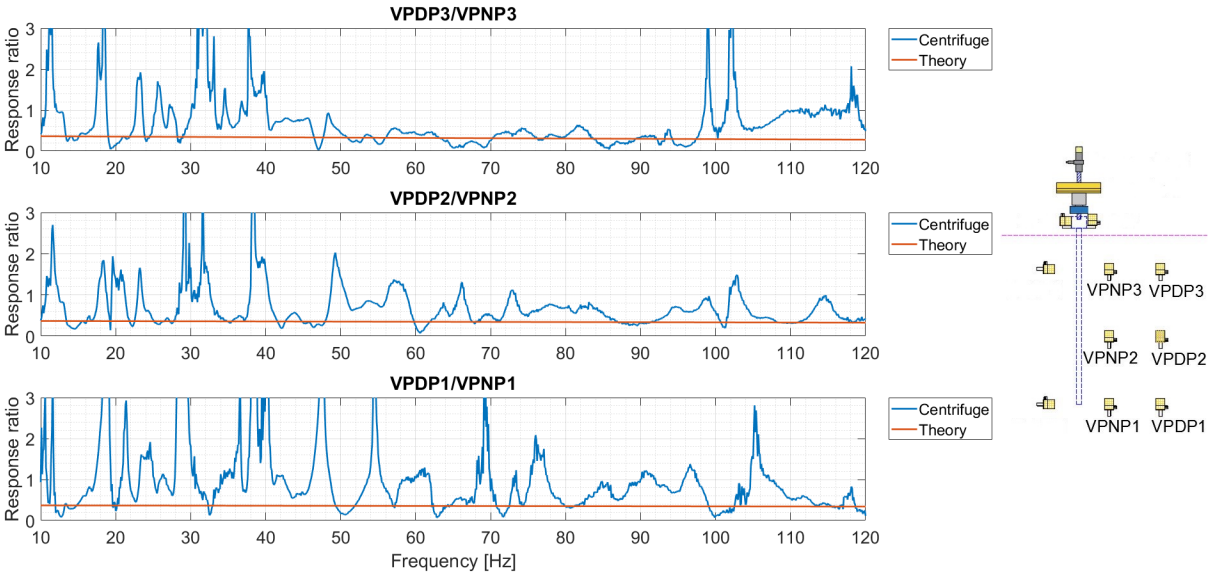


FIGURE 5.38: Response ratio: centrifuge versus theory (GBV_m3)

It can be seen from Figure 5.37 and Figure 5.38 that response ratios are less than 1 at most frequencies. However, it is noted that some values were more than 1, even larger than 3. These may be a result of the combined effects of horizontal pile movement and the reflections from the container boundary. Of these reasons, pile rocking effects have been discussed in Section 5.3.2.2. For the values less than 1, most of them are in the range of 0.2 to 0.6, which is close to the theoretically estimated value, approximately 0.4. To make a better comparison, the ratio distributions at three depths are calculated and shown in Figure 5.39 and Figure 5.40.

It can be seen from Figure 5.39 that 83% of VPDP3/VPNP3 ratios, 82% of VPDP2/VPNP2 ratios and 70% of VPDP1/VPNP1 ratios are less than 1. For the ratios less than 1, 51% of VPDP3/VPNP3, 50% of VPDP2/VPNP2 and 40% of VPDP1/VPNP1 are within the range of 0.2 to 0.6. Similar findings are obtained from Figure 5.39. 83% of VPDP3/VPNP3, 92% of VPDP2/VPNP2 and 71% of VPDP1/VPNP1 are less than 1. For the ratios less than 1, 55% of VPDP3/VPNP3, 49% of VPDP2/VPNP2 and 34% of VPDP1/VPNP1 are within the range of 0.2 to 0.6. Therefore, it can be concluded that most of the ratios are reasonably close to the theoretical estimation, 0.4. This indicates Equation 5.20 can be used to predict the ground borne vibration from the oscillation of a single pile.

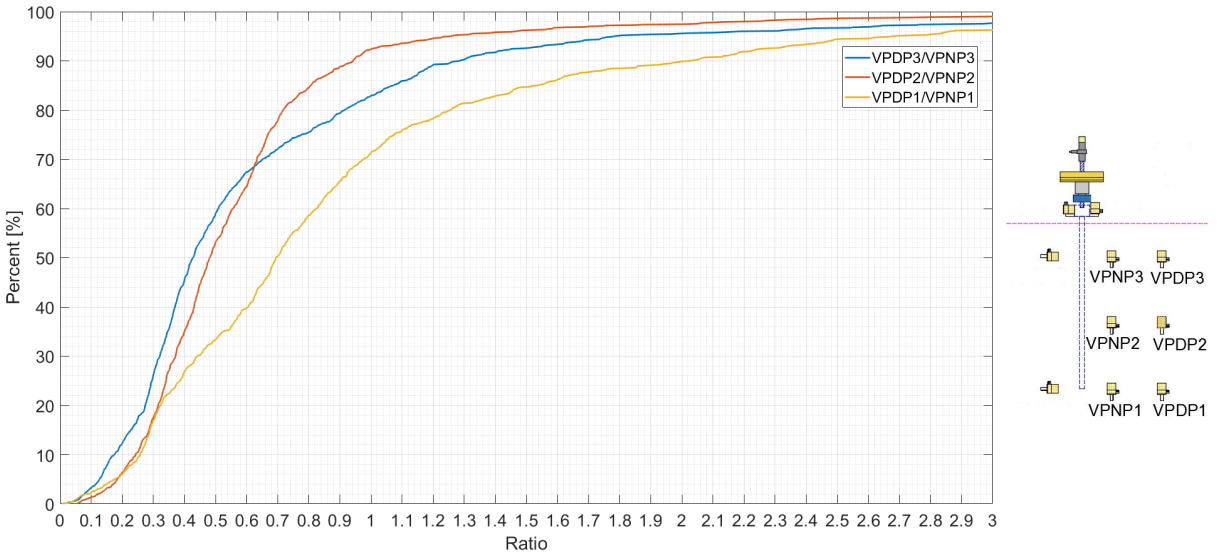


FIGURE 5.39: Response ratio distribution (GBV_m2)

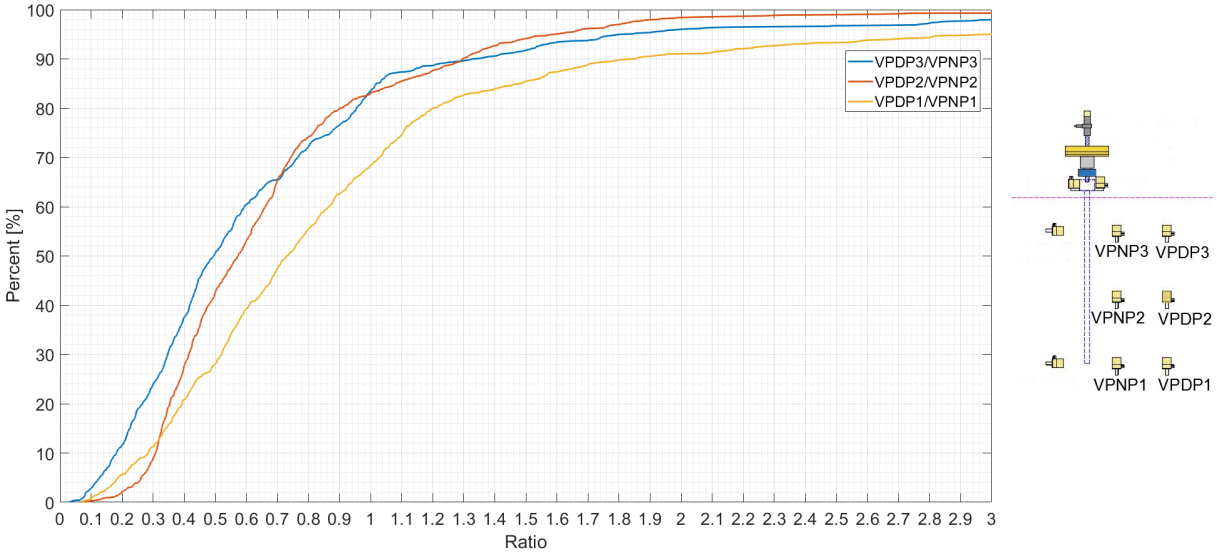


FIGURE 5.40: Response ratio distribution (GBV_m3)

5.4.2.3 Vibration propagation

To investigate the vibration propagation in the soil and to examine the reflected vibration levels, the mean response ratios (VPNPs/PCV) and Equation 5.20 are used to estimate how much of the vibration can propagate to the centrifuge container boundary.

The response ratios (VPNPs/PCV) can show how much of the vibration generated at the pile top is transmitted into the soil near the pile. The mean response ratios (VPNPs/PCV) are calculated and shown in Table 5.3. It can be seen that VPNPs/PCV decreases with depth. Approximately 22%, 16% and 8% of the

vibration generated at the pile top can propagate to VPNP3, VPNP2 and VPNP1 respectively and this indicates the vibration level at the same horizontal distance from the pile decreases almost linearly with depth. This suggests vertical vibrations generated at soil-pile interface decreased with depth which agrees with the previous discussion in Section 5.3.2.2 that the pile segment was moving less at depth. It also means the very small shear strain damping has insignificant effect on vibration attenuation near the pile.

TABLE 5.3: Mean FRFs and response ratios

Location	mean VPNPs/PCV
VPNP3 (3m, 20% L)	VPNP3/PCV=21.7%
VPNP2 (3m, 60% L)	VPNP2/PCV=15.6%
VPNP1 (3m, 100% L)	VPNP1/PCV=7.5%

The mean response ratios (VPNPs/PCV) are substituted into Equation 5.20 to predict the vibration level with radial distance. It can be seen from Figure 5.41 that the vibration attenuates very quickly from 3 m (VPNPs) to 15 m (boundary). At the depth of 3.36 m, 10 m and 16.8 m, approximately 3.1%, 2.7% and 1.5% of the vibration can reach the boundary. Compared with the response ratios at VPDPs (8.1 m from the pile), they are about half the vibration levels at VPDPs: 6.8%, 5.4% and 2.7%. The reflected vibrations may interfere with the propagating waves, which makes the soil response ratios much more complicated and different from the theoretically estimated values. It can also be seen that the vibration attenuation rate becomes quite small when the distance from the pile is larger than 15 m. A feature observed from Figure 5.41 is that the soil vibration level at 3.36 m is smaller than that at 10 m when the distance from the pile is larger than 21 m. This is because the damping ratio at 3.36 m is greater than that at 10 m.

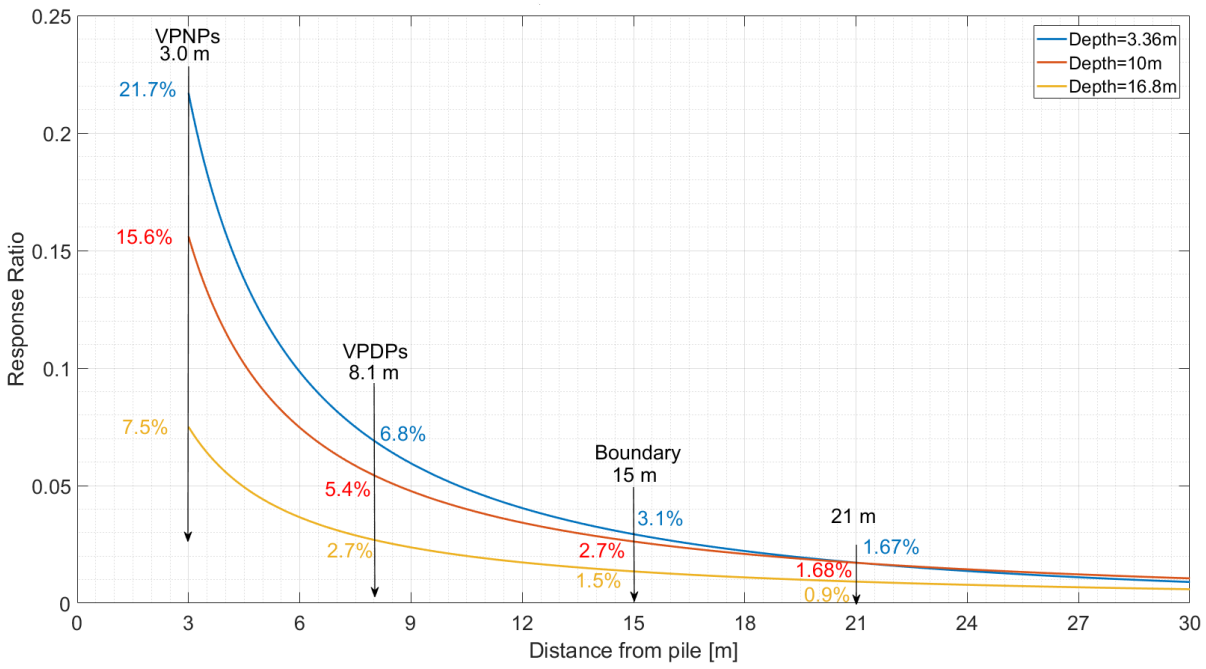


FIGURE 5.41: Ratio of soil response and pile top with distance at three depths

5.5 Chapter summary

Results from the centrifuge test (Test GBV) were presented and discussed in this chapter. The dynamic linearity of the model (both pile and soil) and the accumulated pile and soil displacements with and without the dynamic excitation under three dead loads were examined first. In addition, the dead weight effect on the dynamic pile and soil response amplitude properties were investigated and two simplified mechanical models were proposed to explain the pile and soil responses. Finally, the shear strain level within the soil and the damping ratio of the soil along depth were estimated, as well as the vertical vibration level in the soil along depth and vibration attenuation properties. The following is a summary of the findings:

- A typical pile load-displacement curve indicates the pile behaviour is dead load dependent and the pile may experience a nonlinear response with increasing dead load. Three dead loads with a safety factor of approximately 8, 4 and 2 were employed in this study to investigate the effect of the static load amplitude on the dynamic pile and soil behaviour. Two different input dynamic forces were applied to the pile top under each dead load and the frequency response function (response/force) was employed to evaluate the model behaviour. It was found that both dynamic pile and soil behaviours were in linear

range. This indicated the dead load would not affect the dynamic soil-pile interaction at least when the safety factor was greater than 2.

- In addition to the model linearity, the static pile and soil displacements were examined and results indicated both the pile and the ground settled at almost the same rate. This indicated the soil and the pile experienced the same displacement at the interface and the dynamic load applied to the pile top would not result in accumulated pile displacement. Therefore, the soil-pile interface can be treated as a perfectly bonded interface under all the combined forces applied in this study. The settlement of the whole model (pile and soil) may be a result of the flexible Duxseal attached to the bottom of the container.

- Under three dead loads, the pile top response amplitudes under the same excitation force (FRFs) were compared. It was found that the overall trend was the pile responses decreased with the increasing dead load. However, at some frequencies, contrary results were obtained. A simplified two degree of freedom system was proposed to explain the pile top behaviour. The analysis indicated the anti-resonance frequency of the system may result in the paradoxical phenomenon at some frequencies.

- To understand the soil-pile interaction and analyse the soil particle behaviour under axially dynamic loading, the compressibility of the pile was examined first. It was found that the pile was compressible and a simplified soil-pile mechanical model was employed to analyse the soil-pile interaction. This model was proposed based on the two findings mentioned above: the soil-pile interface was perfectly bonded and the displacement of the pile element was purely caused by the axial elastic deformation. This model indicated axial load within the pile decreased with depth, thus resulting in the decreasing axial elastic deformation of the pile and soil particle displacement along depth. This model also indicated that even under different dead weights, the particle velocity within the interior of the soil generated by the vibrating pile was the same if the pile top experienced the same velocity. The response ratio of soil velocity and pile top velocity under three dead weights was calculated and it was found that test results were consistent with the the proposed model except for some frequencies. Further analysis indicated centrifuge induced interference should not pose significant impacts on the model behaviour. However, the lateral pile movement may affect the vertical soil responses at those frequencies.

- The shear strain amplitude within the soil at three depths was estimated using particle velocities measured from accelerometers and shear wave velocities obtained from the bender element test. Estimated shear strain amplitude was approximately 1.0×10^{-6}, which indicated the shear strain within the soil was in very small range. The damping ratio of soil along depth was calculated by assuming the shear strain was 1.0×10^{-6}. In addition, the logarithmic decrement method was used to calculate the damping ratios at three depths using data measured by the accelerometers. It was found the logarithmic decrement method results agreed well with the results obtained from the empirical equation under the shear strain of 1.0×10^{-6}. The estimated damping ratios were approximately 1.0% at three depths with a slight difference. This indicated material damping may have a slight effect on the vibration attenuation at three depths.

- The vertical vibration level along depth at the same distance from the pile was examined. It was found that approximately 22%, 16% and 8% of the vibration generated at the pile top can propagate to VPNP3, VPNP2 and VPNP1 respectively and this indicated the vibration level at the same horizontal distance decreased almost linearly with depth. This suggested vertical vibrations generated at soil-pile interface decreased with depth which agreed with the proposed model that the pile segment is moving less at depth. It also proved the damping effect on vibration attenuation within very small shear strain range was insignificant.

- The vibration attenuation property along radial distance was evaluated by comparing the ratio of vibration responses measured by two accelerometers with the same embedded depth. It was found that test results agreed well with the theoretical estimation at most frequencies. The vibration attenuation curves at three depths (3.36 m, 10 m and 16.8 m) were calculated. It was found that within 3 m to 15 m, the vibration attenuated very quickly. The curves tended to be flat when the distance from the pile was greater than 27 m. A feature observed from the vibration attenuation curves was that the soil vibration level at 3.36 m was smaller than that at 10 m when the distance from the pile was larger than 21 m. This was because the damping ratio at 3.36 m was greater than that at 10 m.

Chapter 6

Numerical Modelling in FLAC3D and Comparison with Centrifuge Test Results

6.1 Introduction

Experimental results relating to the soil stiffness and stress field, and ground-borne vibration from the oscillation of a single pile were presented in Chapters 4 and 5. Advantages of centrifuge testing over numerical modelling or analytical methods are that less modelling assumptions are required (Connolly et al., 2014) and the soil behaviour and the soil-pile interaction can be realistically modelled. However, centrifuge testing has some drawbacks for the investigation of small ground-borne vibrations induced by railways, see Section 2.1.1.5, in the centrifuge and these can be overcome by the numerical modelling, as detailed below.

Experimental results relating to the ground-borne vibrations obtained with Duxseal have been presented and discussed in Chapter 5. One of the disadvantages is that the employed vibration absorbing material, Duxseal, can remarkably reduce the lateral earth pressure coefficient and the soil stiffness at shallow depths (within 1/3 the model depth from the ground surface), as detailed in Chapter 4. In the presence of Duxseal, shear wave velocities of only three soil layers were obtained from the air hammer tests, which were used to back-calculate the lateral earth pressure coefficient and the change in soil stiffness. However, the lateral earth pressure coefficient and the soil stiffness across the whole model cannot be represented by three soil layers. Moreover, the resulting effects due to the change in the stress and the stiffness on the dynamic pile and soil behaviours was not

examined by the centrifuge tests. This is because experimental results in the absence of Duxseal are required to make a comparison to examine the Duxseal effect on ground-borne vibrations. However, it is very difficult to replicate exactly the same centrifuge model without Duxseal, such as consistent soil density along depth and same embedded positions of piezoelectric accelerometers (Piezos) can not be ensured. This motivates the use of numerical modelling to investigate Duxseal effects on the static and dynamic model behaviours. This is because the numerical modelling does not suffer from these problems.

In addition, the presence of Piezos in the soil (referred to as soil Piezos) may also affect the centrifuge measurements. This is because the sensor housing is made of steel and the stiffness and the density of Piezos are larger than the soil. The presence of soil Piezos can also generate reflected waves in the soil, which may alter the centrifuge measurements. The Piezos effects are also examined by the numerical modelling.

Fast Lagrangian Analysis of Continua in 3 Dimensions (FLAC3D) is a numerical modelling software, which is often used for geotechnical engineering applications (Itasca, 2008). A brief overview of FLAC3D modelling is presented in Section 6.2. The reliability of the FLAC3D modelling is verified first. Section 6.3 presents the calibration of the FLAC3D models by direct comparison with the centrifuge model. Thereafter, the same numerical modelling procedure is used to develop new FLAC3D models and the calibrated models are used to investigate the Duxseal effects and Piezos effects on the centrifuge measurements, presented in Section 6.4 and Section 6.5, respectively.

6.2 FLAC3D modelling

6.2.1 Overview of FLAC3D

FLAC3D (Itasca, 2008) is a three dimensional explicit finite difference program that has been widely used in geotechnical engineering. The program can be used to simulate the behaviour of three-dimensional objects built of soil, rock or other materials using the various constitutive models provided or by using user-defined models. A FLAC3D model is represented by polyhedral elements, which form a three-dimensional grid (another term for grid is mesh) that is adjusted by the user to fit the shape of the object to be modelled. Each zone behaves according to a prescribed constitutive model (linear or nonlinear stress/strain law) in response to the applied forces or boundary restraints. In addition to the zones, an interface which can represent a physical discontinuity (such as a fault, contact plane)

or interface between two different materials (soil-structure interface) can also be modelled in FLAC3D.

FLAC3D was originally developed for analysis and design in mining engineering and underground construction. The program has been extended and many optional modules have been developed, such as dynamic analysis and writing user-defined constitutive models. FLAC3D can be operated from a command-driven mode and it contains the powerful built-in programming language (FISH language) which allows user designed functions to be implemented in the program, such as user-prescribed property variations in the grid.

In FLAC3D, the solution to a problem requires a number of computational steps. During computational stepping, the information associated with the phenomenon under investigation is propagated across the zones in the finite difference grid. A certain number of steps is required to arrive at an equilibrium state for a static solution. Before reaching the equilibrium state, the FISH language allows the user to change material properties during computational stepping. This is because the stepping can be halted when a certain condition is detected. When using the dynamic analysis option, STEP refers to the actual timestep for the dynamic problem. Other terms for step are timestep and cycle. The default calculation mode in FLAC3D is for static mechanical analysis. Full dynamic analysis is provided by the dynamic analysis module in FLAC3D. The full equations of motion are used to solve the problem in FLAC3D in static analyses as well as dynamic analyses.

6.2.2 Numerical analysis with FLAC3D

Both static and dynamic simulations can be performed in FLAC3D. Three fundamental components of a problem are required to be defined before performing a numerical simulation with FLAC3D.

- the finite difference grid
- the constitutive model and material properties
- boundary and initial conditions

The finite difference grid represents the geometry of the problem under study. Constitutive model behaviour and associated material properties dictate the type of response the model will display upon disturbance. Boundary and initial conditions define the in-situ state. After these conditions are defined in FLAC3D, the initial equilibrium state is calculated for the model. Thereafter, alterations can be made (e.g., excavate material or apply dynamic excitation), and the resulting

response of the model is calculated. The three main components are discussed in the following sections, as well as the dynamic excitation.

6.2.2.1 Finite difference grid

The geometric information of a FLAC3D model is provided by the finite difference grid. FLAC3D provides 13 built-in primitive mesh shapes (predefined grid patterns) so that a model composed of multiple shapes can be simulated. The FLAC3D grid can be distorted to fit arbitrary and complicated regions. The size of the grid must be determined to balance the accuracy of results and the necessary computational time. In general, a model with the finer mesh (smaller grid) gives better results, but requires longer computational time.

The dynamic analysis requires a minimum size for the grid. This is because the numerical accuracy of wave transmission is affected by the ratio of the wavelength and the grid size in a dynamic analysis. Practically, according to Nyquist–Shannon sampling criteria (Ewins, 2000), the grid size should be smaller than half of the wavelength. According to Itasca (2008), Kuhlemeyer and Lysmer suggest that the grid size should be smaller than approximately $1/8^{\text{th}}$ of the lowest wavelength in the model to accurately represent the wave transmission through a model. Both the input wave frequency and the wave speed characteristics of the model can affect the wavelength. The lowest wavelength is determined by the smallest wave velocity at the highest input frequency.

6.2.2.2 Constitutive models and material properties

There are 15 basic constitutive models available in FLAC3D which can be identified into three groups: null, elastic and plastic models. A null material model is used to represent material that is removed or excavated. The elastic constitutive models are used to simulate linear, path-independent stress-strain material behaviour without failure criterion. Materials with a property that includes some degree of permanent, path-dependent deformation (failure) and the consequence of nonlinear stress-strain relations can be represented by the plastic models. More details about the representative material of the models and their corresponding applications can be found in Itasca (2008).

6.2.2.3 Boundary condition

FLAC3D provides two forms of boundaries to model the physical object: real and artificial boundaries. Real boundaries exist in the physical object (i.e. the ground

surface), whereas artificial boundaries do not. For a physical problem with large or infinite geometry, such as semi-infinite soils, artificial boundaries are required to reduce the geometry of the physical object being modelled, thus limiting the computational time and computer memory. This can be achieved by using artificial boundaries which can be realistically placed at some distance from the problem domain of interest. The model boundary usually refers to the periphery of the finite difference grid. Internal boundaries, such as holes within the grid, are also model boundaries.

In FLAC3D, fixed artificial boundaries can be used in static analyses. However, fixed artificial boundaries can lead to the reflection of propagating waves which may superimpose with the incident waves and affect the behaviour of the model in dynamic analyses. Instead of fixed boundaries, absorbing boundaries, referred to as quiet boundaries in FLAC3D, are used in dynamic modelling to minimise this effect. Independent dashpots in the normal and shear directions are applied at the artificial boundaries to simulate quiet boundaries. It should be noted that the quiet boundary can effectively absorb waves with incident angles of greater than 30 degrees (angles are measured relative to the perpendicular to the boundary surface). It is however not capable of perfectly eliminating waves with lower incident angles and these residual reflected waves may still affect the model behaviour.

Boundary conditions can be defined through prescribing displacement or stress conditions in FLAC3D, such as a fixed displacement or applying forces or stresses to the boundary for mechanical problems. By default, the boundaries of a FLAC3D grid are free of stress and any constraint.

6.2.2.4 Dynamic excitation

The dynamic analysis option permits three-dimensional, fully dynamic analysis with FLAC3D. FLAC3D performs the calculation in the time domain to solve the full equations of motion using lumped grid-point masses derived from the real density of surrounding zones. The dynamic input applied to the model is the time history dynamic excitation, including an acceleration history, a velocity history, a stress history and a force history. These four dynamic excitations can be all applied to the model boundaries, whereas only accelerations, velocities and forces can be applied to interior grid points. Dynamic input can be applied in the x-direction, y-direction or z-direction corresponding to the axes for the model, or in the normal and shear directions to the model boundary.

6.3 Calibration of the FLAC3D model against centrifuge model

In this research project, FLAC3D was used to perform the numerical study of the centrifuge tests for modelling ground-borne vibration from the oscillation of a single pile. All the centrifuge tests were simulated in model scale, so that the calibration of the FLAC3D models can be done by direct comparison with centrifuge models. Section 6.3.1 presents the FLAC3D model developed to simulate the centrifuge tests. The numerical modelling procedure is summarized in Section 6.3.2. The centrifuge modelling process can be identified into two stages: the static stage and the dynamic stage. Both stages were simulated with FLAC3D and discussed in Section 6.3.2. The results obtained from the shear wave velocity measurement using air-hammer and bender elements (presented in Chapter 4) and the measured dynamic pile and soil responses during harmonic loading (presented in Chapter 5) were used to calibrate the FLAC3D models in two stages, presented in Section 6.3.3 and Section 6.3.4, respectively.

6.3.1 Description of FLAC3D model

6.3.1.1 FLAC3D model mesh

Two 3D numerical models were developed in FLAC3D based on the centrifuge models. It should be noted that three surcharge masses (m1>m2>m3, see Table 5.1) were used in the centrifuge tests. The centrifuge model with the largest surcharge mass (GBV_m1) was not modelled in the numerical modelling because the vertical soil response from GBV_m1 at more frequencies were affected by the centrifuge induced interference or the pile rocking effect compared with GBV_m2 and GBV_m3, explained in Section 5.3.2.2. Another reason is the dynamic analysis in FLAC3D takes very long computational time and it is not necessary to make a comparison with all the centrifuge models. The FLAC3D models with the smallest surcharge mass (m3) and the middle surcharge mass (m2) were built and they are referred to as FLAC3D-m3 and FLAC3D-m2 in this study. The corresponding centrifuge models are denoted by Centrifuge-m3 and Centrifuge-m2 in this chapter, instead of GBV_m3 and GBV_m2.

Figure 6.1 presents the mesh of the model FLAC3D-m2. Because the centrifuge model is symmetric, the FLAC3D model is a quarter of the problem, as shown in Figure 6.1. The domain of the whole model is a quarter cylinder with a height of 468 mm and a radius of 250 mm. The domain of the soil is a quarter cylinder with a height of 438 mm and a radius of 234 mm. The side Duxseal is a quarter hollow

cylinder with an inner radius of 234 mm and an outer radius of 250 mm (16 mm in thickness). To ensure the numerical model behaves as close as possible to the centrifuge model, all the items detailed in Section 3.2 were modelled, including the side and bottom Duxseal, soil, the pile, the surcharge mass, the static load cell, the dynamic load cell, Piezos and couplers, see Figure 6.1.

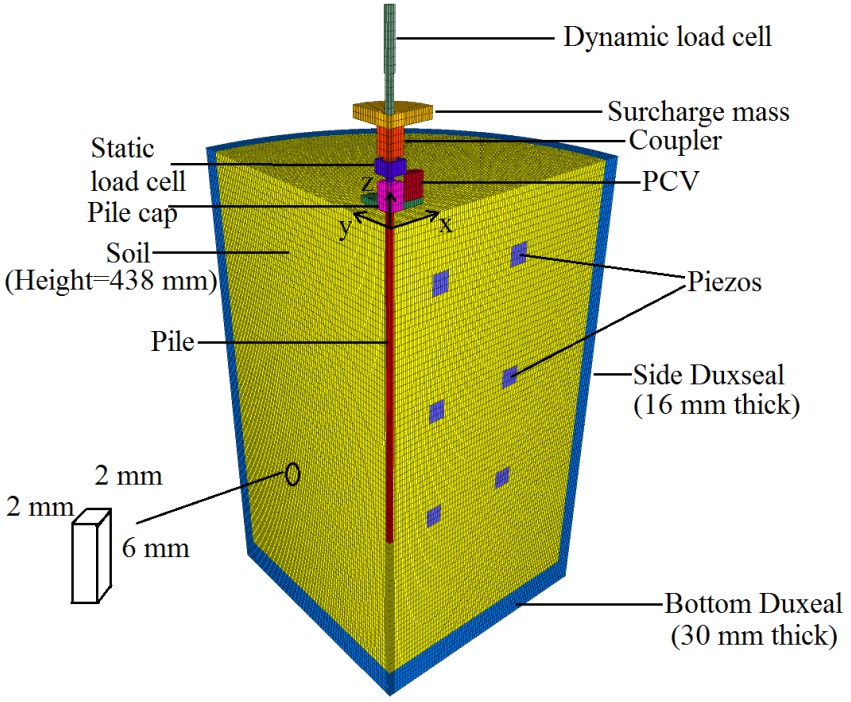


FIGURE 6.1: FLAC3D model used to simulate the centrifuge model (FLAC3D-m2)

A cross-section of the model FLAC3D-m2 at the ground surface is shown in Figure 6.2. A system of reference axes was selected, with origin located at the center of the ground surface, as indicated in Figures 6.1 and 6.2. An approximate geometry was employed in the FLAC3D model to replicate the domain at the soil-pile interface and the soil-Duxseal interface. This is because it was very difficult to build a model that can perfectly replicate the domains of the pile and the soil, which are cylinders with circular arcs. It can be seen from Figure 6.2 that trapezoids and triangles were used at the interfaces to approximate the cylinders with circular arcs. It was concluded in Section 5.2.4 that the soil and the pile experienced the same vertical displacement at the interface. Therefore, in the numerical model, a perfectly bonded soil-pile interface was adopted. In terms of the soil-Duxseal interface, Duxseal and sand nodes were also bonded considering the formation of a thin sand layer on the Duxseal due to the sticky property of Duxseal (Cilingir, 2009).

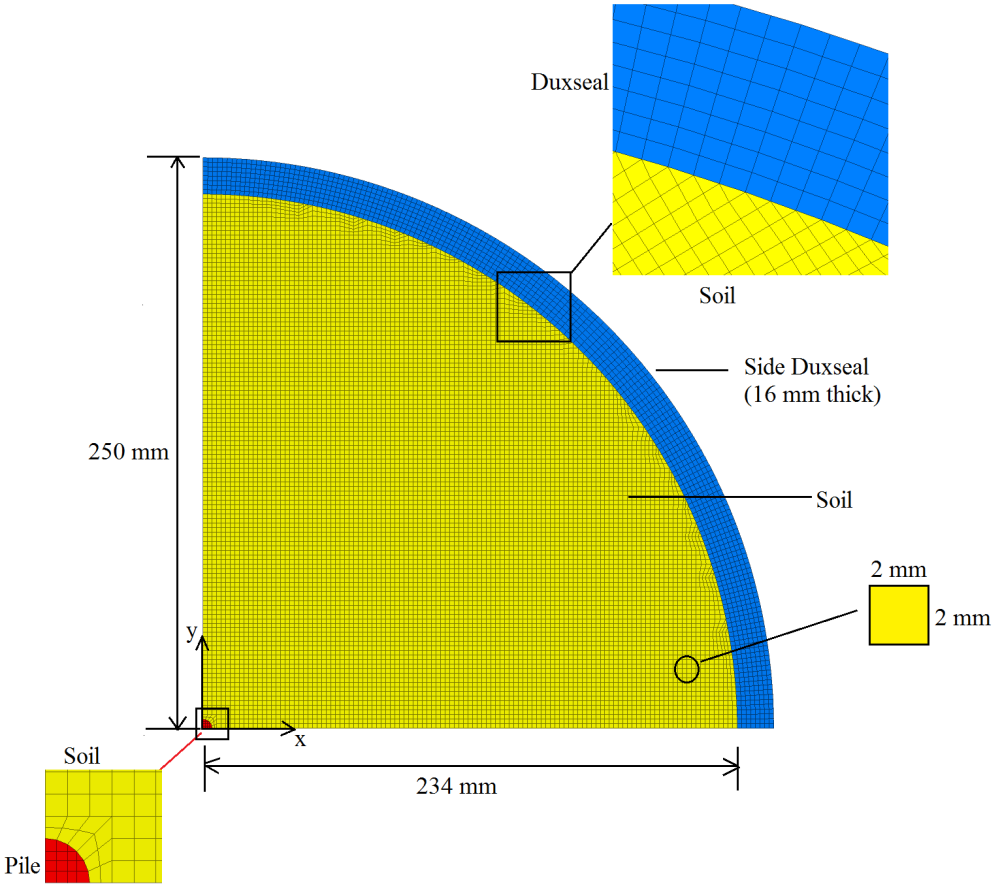


FIGURE 6.2: Cross-section of the model FLAC3D-m2 at the ground surface

In this research project, both static and dynamic analyses were performed using the same FLAC3D model. Therefore, there was a minimum size requirement for the soil grid associated with the smallest wave speed and the highest frequency component. In the centrifuge tests, the highest input frequency was 7200 Hz in model scale. In terms of the determination of smallest wave speed, some factors should be taken into account to obtain a balance between accuracy of modelling results and computational time, detailed below.

- As discussed in Chapter 2, an impact on the top of a friction pile could generate pressure waves, shear waves and Rayleigh waves. Of them, the Rayleigh wave has the smallest wave velocity. However, shear waves carry most of the energy and the shear wave velocity is the second smallest wave velocity of these three. Moreover, this study is focusing on the shear waves generated by the shaft friction. Therefore, the shear wave velocity was used to calculate the smallest wavelength.
- As discussed in Chapter 4, an equation has been obtained to calculate the shear wave velocity of the soil. The shear wave velocity is

very small within the top of the model because of the low confining stress in this area. A very small wavelength is obtained if the shear wave velocity near the ground surface (i.e. at depth 1 mm) is used to calculate the wavelength, thus resulting in an extremely small grid size ($1/8^{th}$ of the wavelength=0.8 mm). However, given that the top two Piezos were embedded at the depth of 50 mm in the centrifuge model, the shear wave velocity at depth 10 mm was employed to calculate the wavelength. The corresponding grid size was 2 mm and it was adopted as the smallest grid size of the numerical model.

- The shear waves generated by impacting a friction pile mainly propagate in the horizontal direction. The grid size adopted in the horizontal direction (x-direction and y-direction) was 2 mm, see Figures 6.1 and 6.2. To reduce computational time, the grid size in the vertical direction (z-direction) used in this study was 6 mm, as shown in Figure 6.1.

6.3.1.2 Material properties

The constitutive models and material properties of all the items simulated in the numerical models are presented in Table 6.1. For train induced ground-borne vibration, the soil behaviour is expected to be linear elastic and the isotropic elastic model can be used to model the soil behaviour. However, the results from the air hammer tests suggest that in the presence of Duxseal, the soil near the model top may have reached the state of plastic equilibrium and failure in soil may occur. Therefore, a conventional plastic model, the Mohr-Coulomb model, was used to represent soil behaviour throughout this study. The other items listed in Table 6.1 were assumed to be the isotropic elastic material.

It should be noted that one of the objectives of this research is to examine the effect of embedded Piezos on soil response. The approximate density of the Piezos, 3800 kg/m^3, was calculated by weighing the Piezos and measuring the geometric size. For the other transducers, such as load cells, they were all assumed to be solid steel in this study. The housing of the Piezos is made of steel, so the stiffness of Piezos was assumed to be the steel stiffness. The elastic modulus (E) and the shear modulus (G) of all the metals are presented in Table 6.1. The stiffnesses of the soil and the Duxseal are not presented in Table 6.1 due to them varying with depth. Their stiffnesses will be discussed in detail in Section 6.3.3. The damping ratio is an important dynamic parameter for the dynamic analysis. The damping ratio profile of dry Congleton sand adopted by this study to perform the numerical modelling is shown in Figure 6.3. The soil damping ratio decreases with depth:

0.022, 0.015 and 0.01. These damping ratios are obtained from the centrifuge testing, as presented in Section 5.4.1.3. The damping ratios of three different metals (aluminium, brass and steel) measured by Himanshu (2016) were adopted in this study. A high damping ratio of 0.2 for Duxseal suggested by Cilingir (2009) was used in this numerical model.

TABLE 6.1: Constitutive model and material properties

Item	Constitutive model	Density (kg/m^3)	E (GPa)	G (GPa)	Damping ratio
Soil	Mohr-Coulomb plasticity	1739 (dry sand)	Section 6.3.3	Section 6.3.3	Figure 6.3
Duxseal	Isotropic elastic	1427	Section 6.3.3	Section 6.3.3	0.2
Pile	Isotropic elastic	2700 (aluminium)	69	27	0.004
Coupler	Isotropic elastic	2700 (aluminium)	69	27	0.004
Surcharge mass	Isotropic elastic	8500 (brass)	105	39	0.01
Static load cell	Isotropic elastic	7700 (steel)	180	77	0.007
Dynamic load cell	Isotropic elastic	7700 (steel)	180	77	0.007
Piezos	Isotropic elastic	3800	180	77	0.007

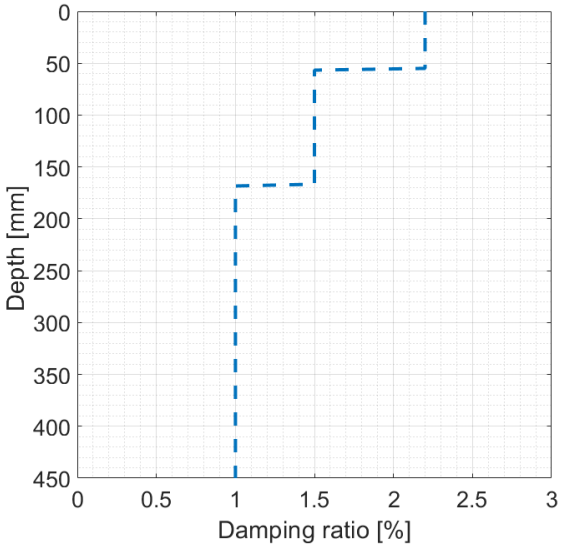


FIGURE 6.3: Soil damping ratio with depth in prototype scale

6.3.1.3 Boundary conditions

The displacement of the symmetry boundaries at x=0 and y=0 was restricted in the x-direction and the y-direction, respectively. The displacement of the side boundary (radius=250 mm) was restricted in both the x-direction and the y-direction. The model bottom was not allowed to move in the z-direction. These boundary conditions were used in both stages.

6.3.2 Numerical modelling procedure

The centrifuge test procedure has been summarized in Section 3.2.10 and the procedure can be classified into two main stages: static stage and dynamic stage. The numerical modelling procedure represents the sequence of processes that occurs in the physical modelling and it should be consistent with the centrifuge tests. The same numerical modelling procedure, summarized below, was used to calibrate the two FLAC3D models: FLAC3D-m2 and FLAC3D-m3.

In stage 1 (static stage), a scaled model was spun up from 1 g to 60 g gradually in the centrifuge and then stabilized at 60 g. To simulate this process in the numerical modelling, material properties required for the static analysis (given in Table 6.1) were assigned to the developed 3D model and boundary conditions were specified. The gradually increased gravitational acceleration level (g_level) was simplified in the numerical modelling by applying the gravitational body force to the numerical model under 1 g, 10 g, 20 g, 30 g, 40 g, 50 g and 60 g, respectively. The FLAC3D model was brought to the equilibrium state under each g_level. A key challenge in this stage is the accurate modelling of Duxseal and soil properties and this will be detailed in Section 6.3.3. To calibrate the static model, the measured lateral earth pressure coefficients of three soil layers were employed to make a comparison with the numerical modelling results. The calibrated static model was used to conduct the dynamic analysis in the next stage.

In stage 2 (dynamic stage of the centrifuge tests), a single frequency harmonic force with a duration of approximately 0.4 s was used to excite the pile top and dynamic pile and soil responses were measured. In the numerical modelling, the damping ratios of all the materials required to perform the dynamic analysis (given in Table 6.1) were assigned to the calibrated static model first. Then the harmonic force at a single frequency was applied at the top of the dynamic load cell, same as the centrifuge tests. The normalised model response under 1 N (FRF=response/force) was used to analyse the centrifuge results. Therefore, the amplitude of the harmonic force was 0.25 N due to a quarter numerical model being used. To ensure the model can reach the steady state, the dynamic excitation time used for each

frequency was 20 periods. The reason for adopting 20 periods has been discussed in Section 3.2.12.3. At each excitation frequency, the response of the FLAC3D model was calculated.

6.3.3 Static calibration

A description of the model and the numerical modelling procedure have been presented in Section 6.3.1 and Section 6.3.2, respectively. As mentioned above, the key challenge in the static calibration stage is the determination of soil and Duxseal properties and this will be detailed herein.

6.3.3.1 Soil properties

Usually, the problem of railway induced ground-borne vibration is assumed to be linear elastic and fixed material properties are assigned to a numerical model. Thereafter, the model is solved without changing the material properties during stepping in FLAC3D due to the soil behaviour being stress path independent. However, the soil properties (primarily referring to the elastic modulus, the shear modulus and the friction angle) are highly confining stress dependent. The spin-up process in the centrifuge can increase the vertical and horizontal stresses gradually. Moreover, the presence of side Duxseal can alter the horizontal stress level due to its lateral deformation and the soil near the model top may have reached the state of plastic equilibrium. This means the soil properties will change during the spin-up process and the soil property updating process should be modelled in FLAC3D.

As explained above, the Mohr-Coulomb plasticity model was used to represent the soil behaviour and the following are required properties for this model in FLAC3D:

(1) shear modulus and elastic modulus;

(2) friction and dilation angles;

(3) cohesion;

The cohesion was set to zero for the dry sand. The equation to calculate the shear modulus of the soil was obtained from the bender element tests and it is given by Equation 6.1.

$$G = 6980\frac{(2.17-e)^2}{(1+e)}(\sigma_v^{'})^{0.25}(\sigma_h^{'})^{0.25} \tag{6.1}$$

The soil elastic modulus can be calculated by Equation 2.10. The Poisson′s ratio (μ) in Equation 2.10 is needed to calculate the elastic modulus. The Poisson′s ratio was determined from the bender element tests by measuring the shear and pressure wave velocities, presented in Chapter 4. The measured Poisson′s ratio was 0.15 for the Congleton sand used in this research.

The centrifuge test condition (soil within a cylindrical container) was regarded as a triaxial strain condition and the maximum soil friction angle ϕ'_{max} can be obtained by the following equation (Bolton, 1986):

$$\phi'_{\mathrm{max}} = 3\mathrm{I_R} + \phi'_{\mathrm{crit}} \tag{6.2}$$

where ϕ'_{crit} is the critical state friction angle (31 degrees by (Lauder, 2010)) and $\mathrm{I_R}$ is the relative dilatancy index.

Equation 6.2 was valid in the range $0<\mathrm{I_R}<4$ (Bolton, 1986). $\mathrm{I_R}$ can be calculated by:

$$\mathrm{I_R} = \mathrm{I_D}(10 - \ln p') - 1 \tag{6.3}$$

where $\mathrm{I_D}$ is the relative density (0.85) and p' is the mean effective stress.

It can be seen from the above equations that the vertical and horizontal stresses are required to calculate the soil properties. These equations were used in the FLAC3D modelling to calculate the soil properties based on the stresses obtained during stepping so that the 'spin-up' process was simulated, detailed below.

Before the 'spin-up' in FLAC3D, the initial vertical stress along depth was calculated under 1 g and the initial horizontal stress was assumed to be half of the vertical stress. Then, the initial soil properties were calculated using the above equations and assigned to the model. This 1 g numerical model was brought to an initial equilibrium state.

To simulate the 'spin-up' process in FLAC3D, the gravitational body force at 10 g was applied to the model first. A stepping-updating function was programmed using the built-in FISH language to update the properties of each soil zone during the computational stepping. The FISH language allows the user to go through every zone of the FLAC3D model and extract the vertical and horizontal stresses of each zone. After every 10 steps, the stepping was halted, and the above equations were used to calculate the soil properties based on the extracted vertical and horizontal stresses. The updated soil properties were assigned to the soil and the stepping-updating process continued until the model reached the equilibrium state. The gravitational body force at 20 g, 30 g, 40 g, 50 g and 60 g was applied to the

model successively and the preceding steps were repeated. Finally, the numerical model arrived at the equilibrium state at 60 g.

6.3.3.2 Duxseal properties

Another challenge to calibrate the FLAC3D model was the determination of Duxseal stiffness. As discussed in Section 4.5.2, in the presence of Duxseal, the lateral earth pressure coefficient K increased with depth in the centrifuge model: K_3=0.28 (top soil layer), K_2=0.48 (middle soil layer) and K_1=0.54 (bottom soil layer). This indicates the stiffness of Duxseal may increase with the increasing confining stress (in other words, depth). Some preliminary numerical modelling results obtained using constant stiffness along depth also confirmed that the Duxseal stiffness can affect K: the larger the stiffness, the higher the K value. However, the stiffness of Duxseal was difficult to determine in standard laboratory tests. Only one successful bender element test was achieved and the measured elastic modulus was approximately 16 MPa, detailed in Section 4.5.2. To determine the stiffness of Duxseal and calibrate the numerical model, a parametric study was performed with FLAC3D modelling by comparing the K values of three soil layers from the numerical modelling with the K values from the centrifuge tests.

In this research, Duxseal was modelled as an elastic material, where and two properties are required: the elastic modulus and the Poisson′s ratio. A Poisson′s ratio of 0.47 suggested by Cilingir (2009) was employed through out this study. An equation to calculate the elastic modulus of Duxseal was proposed based on the equation to calculate the soil moduli, presented in Section 2.2.2.3. The basic relationship is given by:

$$E_D = c \times h^m \tag{6.4}$$

where E_D is the elastic modulus of Duxseal in MPa, h is the depth in m, c and m are fitting parameters.

Equation 6.4 is a monotonic increasing function if c and m are larger than zero. Of them, m determines the rate of change. When m is larger than 1.0, the rate of change is getting larger with increasing h. As discussed above, K increased with depth, and one feature observed was that K of the top soil layer (0.28) was much smaller than the middle (0.48) and the bottom (0.54). This indicates E_D at the top of Duxseal should also be much smaller than the middle and the bottom due to K being consistent with E_D. Therefore, m in Equation 6.4 should be larger than 1.0. Three values of m were used to conduct the parametric study in FLAC3D modelling: 2.0, 2.5 and 3.0.

In addition to m, the determination of c is of great importance. One criterion obeyed in this study when determining c was that the elastic modulus of Duxseal E_D should be smaller than the soil at the same depth. Accordingly, four values of c were used for each m to perform the parametric study, as shown in Table 6.2.

TABLE 6.2: Parameters used for parametric study

Parameter	m_1=2.0	m_2=2.5	m_3=3.0
c_1	200 (P1)	500 (P5)	1100 (P9)
c_2	300 (P2)	600 (P6)	1200 (P10)
c_3	400 (P3)	700 (P7)	1300 (P11)
c_4	500 (P4)	800 (P8)	1400 (P12)

6.3.3.3 Calibration results

In the static stage, K values of three soil layers were measured from the centrifuge based air hammer tests. As presented in Figure 6.4, in the centrifuge tests, the air hammer MEMS accelerometers array was placed at the plane where x=0 and y=135 mm from the pile center, referred to as AHA position. The calculated K values of the same soil layers at the AHA position was used to make a comparison with the air hammer test results to calibrate the static FLAC3D models.

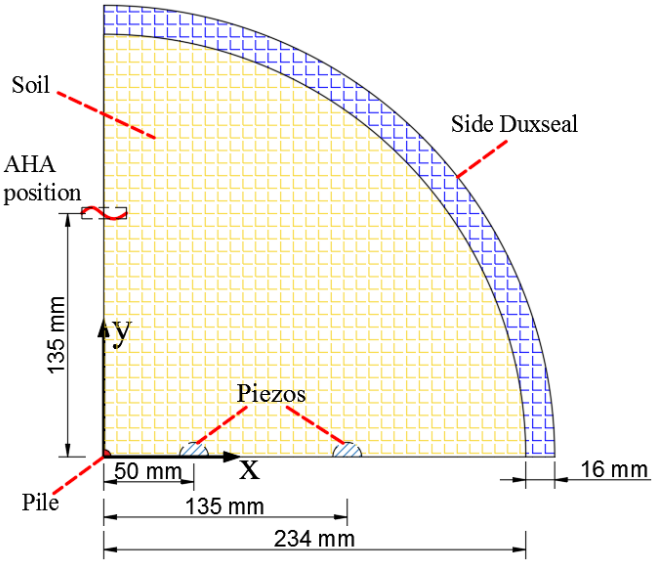


FIGURE 6.4: Air hammer MEMS accelerometers array postion (AHA position)

In order to quantify the difference between the experimental and numerical results, the RMS distances (D_{RMS}) of the K values of the experimental and numerical results were applied to the results (Owen, 2003), defined by:

$$D_{\mathrm{RMS}} = \frac{1}{3}\sum_{i=1}^{3}\left[\log_{10}\frac{K_{\mathrm{exp},i}}{K_{\mathrm{num},i}}\right]^2 \tag{6.5}$$

where $K_{\mathrm{exp},i}$ is the measured lateral earth pressure coefficient of a soil layer from the centrifuge based air hammer tests and $K_{\mathrm{num},i}$ is the calculated lateral earth pressure coefficient of a soil layer from the numerical modelling.

It should be noted that a smaller RMS distance indicates a better agreement between experimental and numerical results. As presented in Table 6.2, four values of c were used for each m to perform the parametric study. The smallest RMS distance for each m was obtained and presented in Table 6.3, as well as $K_{\mathrm{exp},i}$ and $K_{\mathrm{num},i}$. The corresponding elastic modulus of Duxseal calculated by Equation 6.4 using P3, P6 and P10 is shown in Figure 6.5.

TABLE 6.3: Lateral earth pressure coefficient obtained from the centrifuge ($K_{\mathrm{exp},i}$) and the FLAC3D modelling ($K_{\mathrm{num},i}$) and the RMS distance (D_{RMS})

Soil layer	Experimental	Numerical (P3) (m=2.0, c=400)	Numerical (P6) (m=2.5, c=600)	Numerical (P10) (m=3.0, c=1200)
L_3 (top)	$K_{\mathrm{exp},3}$=0.28	$K_{\mathrm{num},3}$=0.390	$K_{\mathrm{num},3}$=0.341	$K_{\mathrm{num},3}$=0.333
L_2 (middle)	$K_{\mathrm{exp},2}$=0.48	$K_{\mathrm{num},2}$=0.468	$K_{\mathrm{num},2}$=0.438	$K_{\mathrm{num},2}$=0.438
L_1 (bottom)	$K_{\mathrm{exp},1}$=0.54	$K_{\mathrm{num},1}$=0.523	$K_{\mathrm{num},1}$=0.518	$K_{\mathrm{num},1}$=0.524
-	-	D_{RMS}=0.0070	D_{RMS}=0.0031	D_{RMS}=0.0025

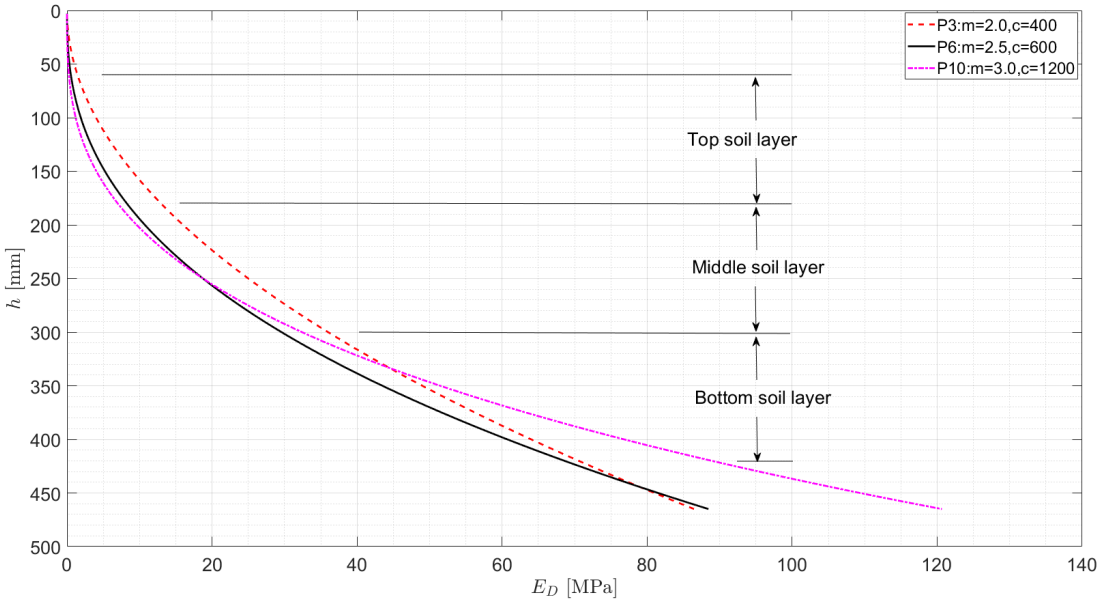


FIGURE 6.5: Duxseal elastic modulus used for numerical modelling calibration

For each curve in Figure 6.5, E_D increases with depth and this leads to the increasing K as the depth increases, see Table 6.3. Particularly, K of the top soil layer reduces to 0.333 calculated by using P10, which is quite close to the experimental results and the coefficient of active earth pressure from Rankine's theory. It can also be seen that K values of the middle and bottom soil layers calculated by using P3, P6 and P10 are quite close to each other. In terms of D_{RMS}, it can be seen from Table 6.3 that the smallest D_{RMS} is obtained by using P10, which gives the best agreement between experimental and numerical results. It is believed that adjusting the parameter c would provide better results. However, given that the parametric study process requires plenty of computational time and the results calculated using P10 are reasonably acceptable, the static models obtained using P10 were used to perform the dynamic calibration.

6.3.4 Dynamic calibration

The calibrated static models were further used to calculate the dynamic response of the model. The dynamic numerical modelling procedure has been presented in Section 6.3.2. An important parameter needed to be discussed here is the input excitation frequency. In the centrifuge tests, 1101 frequencies (ranging from 600 Hz to 7200 Hz with a frequency spacing of 6 Hz) were applied one by one to excite the pile. It was impractical to apply all the frequencies used in the centrifuge tests due to the long computational time needed for each frequency (half day to four days depending on the frequency). Therefore, 12 representative frequencies, 600 Hz to 7200 Hz with a frequency spacing of 600 Hz, were employed in the numerical modelling, namely 600 Hz, 1200 Hz, 1800 Hz, 2400 Hz, 3000 Hz, 3600 Hz, 4200 Hz, 4800 Hz, 5400 Hz, 6000 Hz, 6600 Hz and 7200 Hz. The corresponding prototype frequencies are 10 Hz, 20 Hz, 30 Hz, 40 Hz, 50 Hz, 60 Hz, 70 Hz, 80 Hz, 90 Hz, 100 Hz, 110 Hz and 120 Hz.

The pile and soil responses at different frequencies were calculated by changing the frequency of the harmonic load. At each excitation frequency, the acceleration time history data at different observation points, same as the measurement locations in the centrifuge tests, were recorded. Thereafter, the response amplitudes (acceleration, velocity and displacement) at these observation points were calculated using the same method presented in Section 5.2.4, as well as the FRFs of the model. The comparison between the experimental results and FLAC3D model results are presented in the following sections.

6.3.4.1 Pile response

The normalised pile top velocity responses (FRF=velocity/force) at all the input frequencies obtained from the centrifuge tests (Centrifuge-m2 and Centrifuge-m3) and the FLAC3D models (FLAC3D-m2 and FLAC3D-m3) are presented in Figure 6.6. The normalized velocity in log scale is presented to clearly show the results due to some values in linear scale being very small and almost invisible. It can be seen that better agreements are obtained at the low frequencies (10-70 Hz for m2 and 10-50 Hz for m3). In terms of the pile response at higher frequencies, the pile behaviour in the centrifuge tests may be affected by the mass and stiffness of the shaker attachment, as discussed in Section 3.2.6. As a consequence, the measured pile top response is quite different from the numerical results.

It has been examined by the centrifuge tests that the pile top response increases with the decreasing dead weight when the safety factor is larger than 2. It is also found from the bottom plot in Figure 6.6 that the pile top response from the numerical model FLAC3D-m3 is larger than from FLAC3D-m2 at most frequencies. This is one indicator that the numerical results are consistent with the centrifuge test results. One feature observed from the lower plot in Figure 6.6 is that FRF-PCV from FLAC3D-m3 is much larger than the FRF-PCV from FLAC3D-m2 within the frequency range of 70 Hz to 100 Hz. On the other hand, the FRF-PCV from FLAC3D-m2 is much larger than that from FLAC3D-m3 at 120 Hz. As discussed in Section 5.3.2.1, the vertical oscillation of the above ground loading system and the pile top can be regarded as a two degree of freedom system. This is probably because the resonance frequency of the system in the model FLAC3D-m3 is within 70 Hz to 100 Hz. Similarly, 120 Hz is close to the resonance frequency of the system in the model FLAC3D-m2. Near the resonance frequency, the pile behaviour is much larger, thus leading to a big difference.

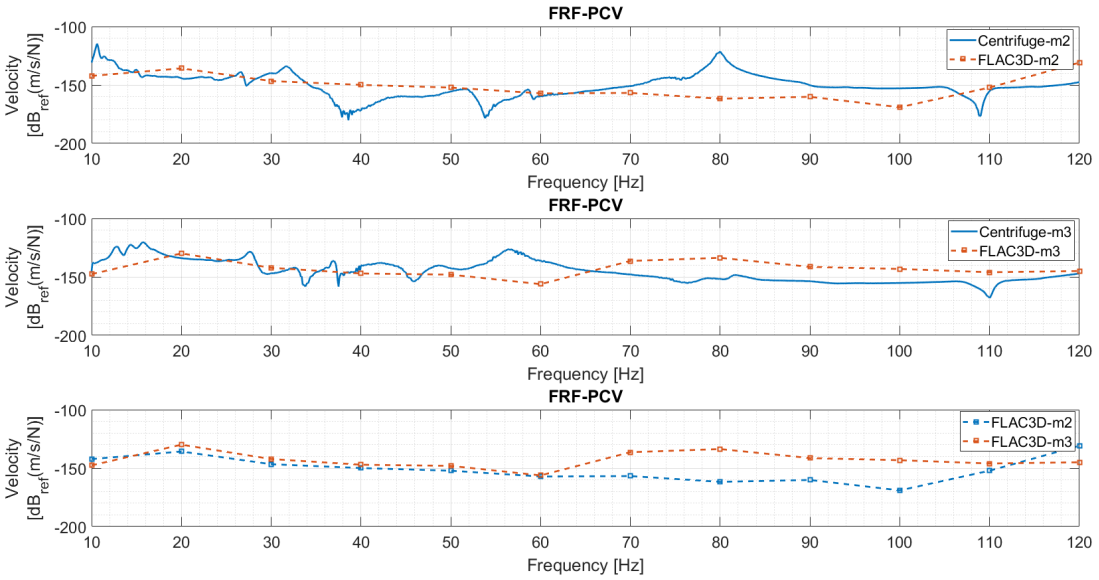


FIGURE 6.6: Comparison of the centrifuge results and numerical modelling results from FLAC3D-m2 and FLAC3D-m3 (PCV)

It is also concluded by analysing the centrifuge test data that the pile response decreases along depth. This was not directly measured from the centrifuge tests because the pile was not instrumented. The pile response along depth can be calculated by the numerical modelling. Pile responses (normalised vertical velocity) at 20%, 60% and 100% of the embedded pile depth (L), same as the embedded depths of the Piezos, calculated from the two numerical models are plotted in Figure 6.7. It can be seen that the pile response under a certain dead weight and dynamic load decreases with depth which is also consistent with the conclusion from experiments.

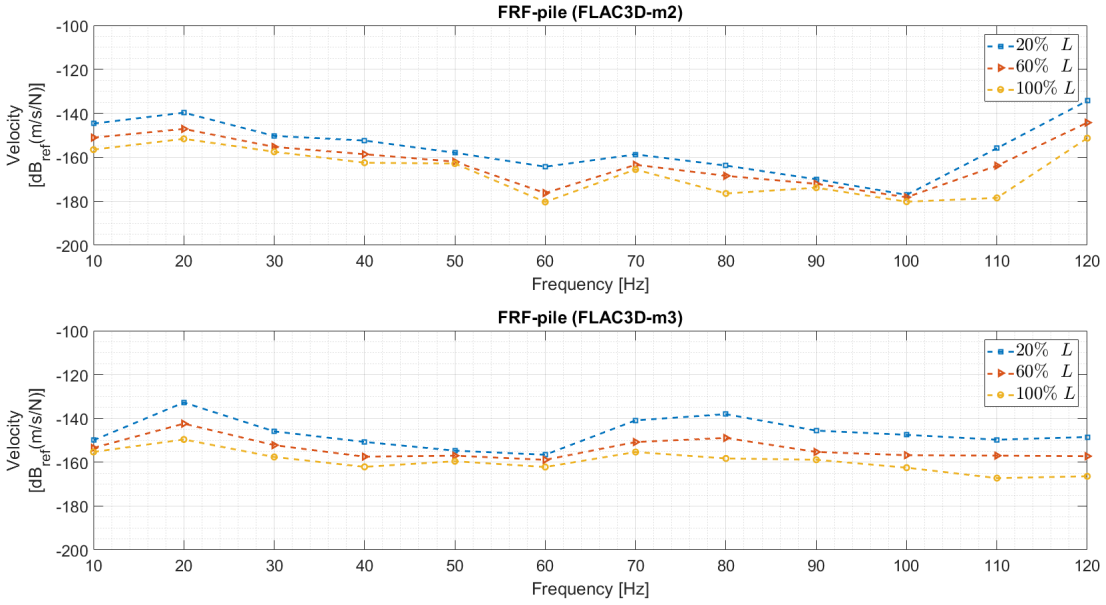


FIGURE 6.7: Pile velocity response along depth from FLAC3D-m2 and FLAC3D-m3

6.3.4.2 Soil response

The comparison of soil response between centrifuge test results and FLAC3D modelling results is shown in Figures 6.8, 6.9, 6.10 and 6.11. It can also be observed that, similar to the pile response, better estimates of soil responses are obtained at lower frequencies. Overall, the soil responses at different locations from the two numerical models are reasonably close to the experimental results.

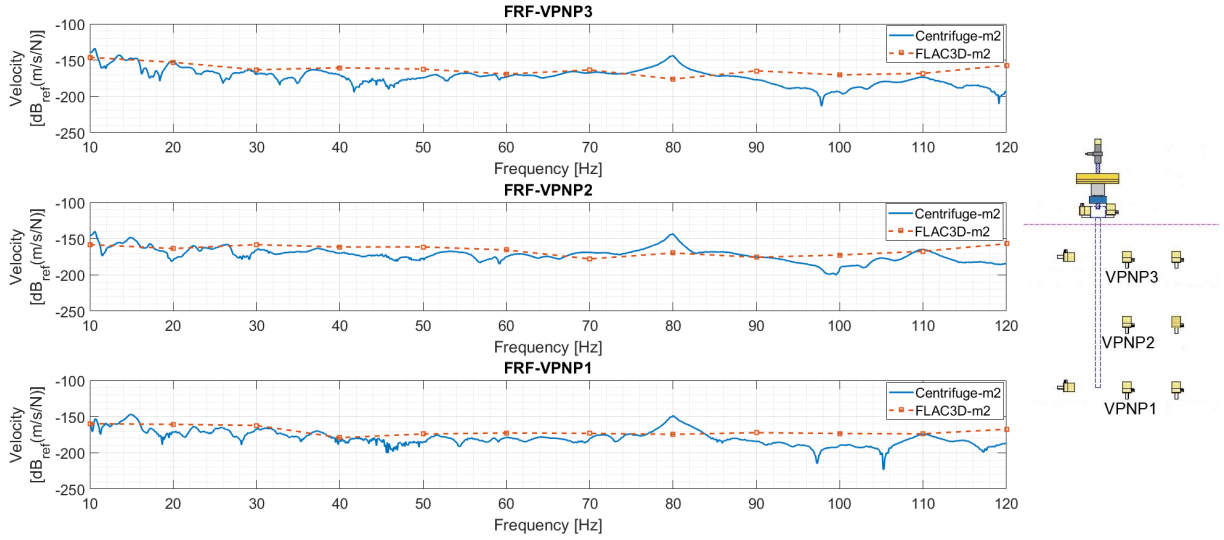


FIGURE 6.8: Comparison of the centrifuge results and numerical modelling results from FLAC3D-m2 (soil response near pile)

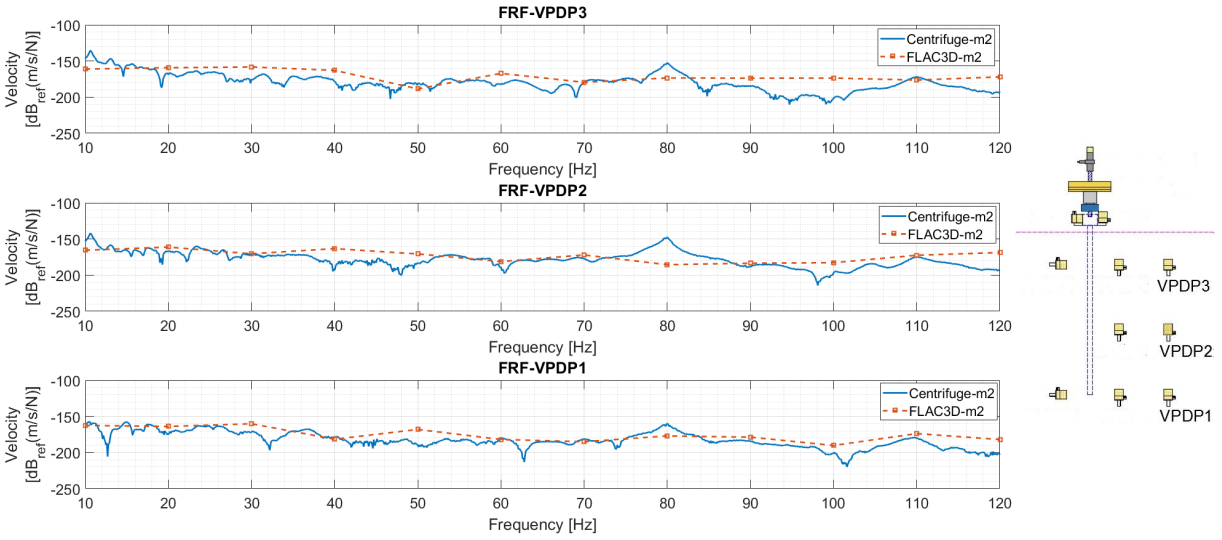


FIGURE 6.9: Comparison of the centrifuge results and numerical modelling results from FLAC3D-m2 (soil response distant to pile)

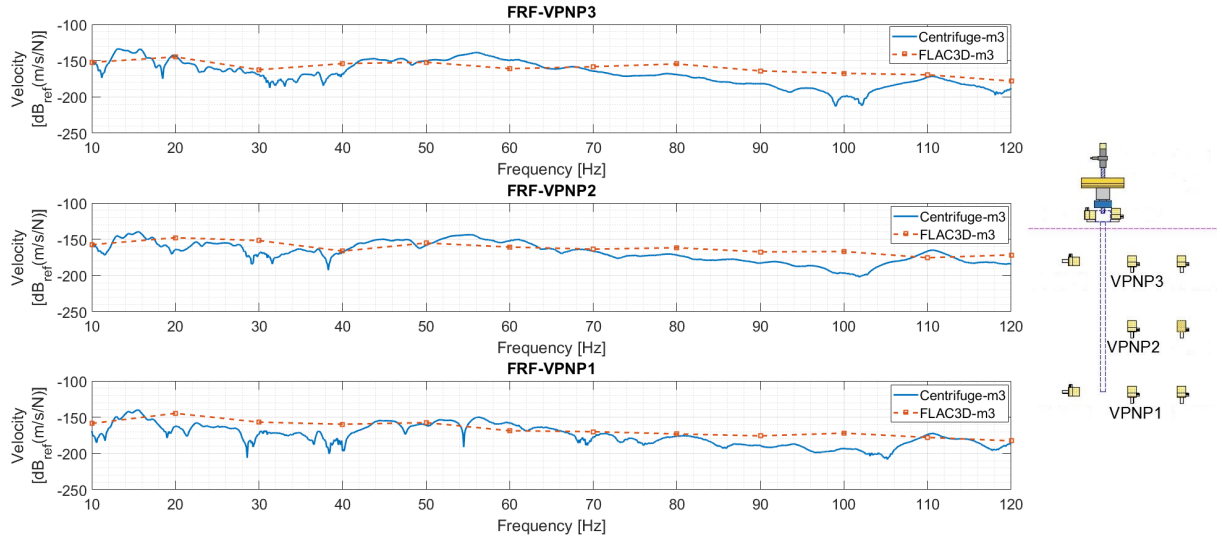


FIGURE 6.10: Comparison of the centrifuge results and numerical modelling results from FLAC3D-m3 (soil response near pile)

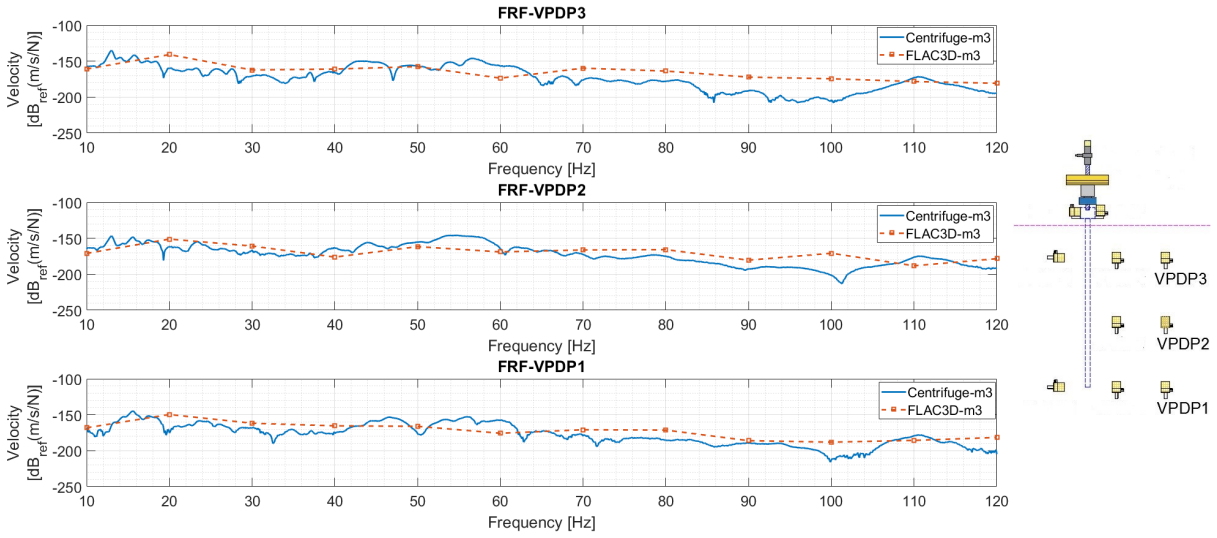


FIGURE 6.11: Comparison of the centrifuge results and numerical modelling results from FLAC3D-m3 (soil response distant to pile)

6.3.5 Brief summary

Two numerical models, FLAC3D-m2 and FLAC3D-m3, were developed in FLAC3D to simulate the centrifuge tests, as described in Section 6.3.1. The numerical modelling procedure to calibrate the two models was detailed in Section 6.3.2. The centrifuge test results were used to calibrate the two numerical models and comparisons were presented in Section 6.3.3 and Section 6.3.4. It was found that the numerical modelling results were either consistent with the centrifuge test results (such as the pile response decreased with depth and the pile top response decreased with increasing dead weight) or reasonably close to the experimental results (such as the lateral earth pressure coefficient, the pile top and soil responses at different locations). Therefore, in the following discussion, the same material properties and the numerical modelling procedure are used to develop new models and to investigate the Duxseal effect and the effect of the piezoelectric accelerometers (Piezos) on the centrifuge measurements.

6.4 Duxseal effects on soil stress field

It has been examined by the centrifuge based air hammer tests that the side Duxseal can lead to the reduction of lateral stress in the soil. To fully understand the side Duxseal effects on the stress field in the soil, two new numerical models which only accounted for the soil and the Duxseal were developed using FLAC3D. This section details the two models and compares the numerical modelling results calculated with and without the side Duxseal.

6.4.1 Description and calibration of FLAC3D models used to investigate the stress field

The first model is a flexible boundary model (FBM) due to the soil, side Duxseal and bottom Duxseal being involved. This model is referred to as FLAC3D-FBM in this study. The second one is a soil model with only bottom Duxseal, and this is to simulate the rigid boundary condition (side boundaries). This model is referred to as FLAC3D-RBM. It should be noted that whether the side Duxseal is employed or not, the boundary condition for the whole model is always rigid due to the existence of the model container. The flexible boundary model means the side Duxseal can provide a flexible boundary for the soil throughout this study. In both numerical models, the bottom Duxseal is included to demonstrate that it is the side Duxseal that can alter the stress field in the centrifuge model.

The two numerical models are shown in Figure 6.12. In both models, the dimension of the soil model was the same: 438 mm in depth and 234 mm in radius. These two models were not used to perform dynamic analysis. Therefore, the grid size was 6×6×6 mm to save computational time. Same as the model FLAC3D-m2, FLAC3D-FBM and FLAC3D-RBM were both a quarter of the problem by taking the advantage of symmetry. The models FLAC3D-m2 and FLAC3D-m3 have been calibrated based on the K values from the air hammer tests, as detailed in Section 6.3. For these two new models, the same soil properties, Duxseal properties and modelling procedure were used to simulate the 'spin-up' process. The same boundary conditions were applied at the planes where x=0, y=0, radius=250 mm (FLAC3D-FBM) and radius=234 mm (FLAC3D-RBM).

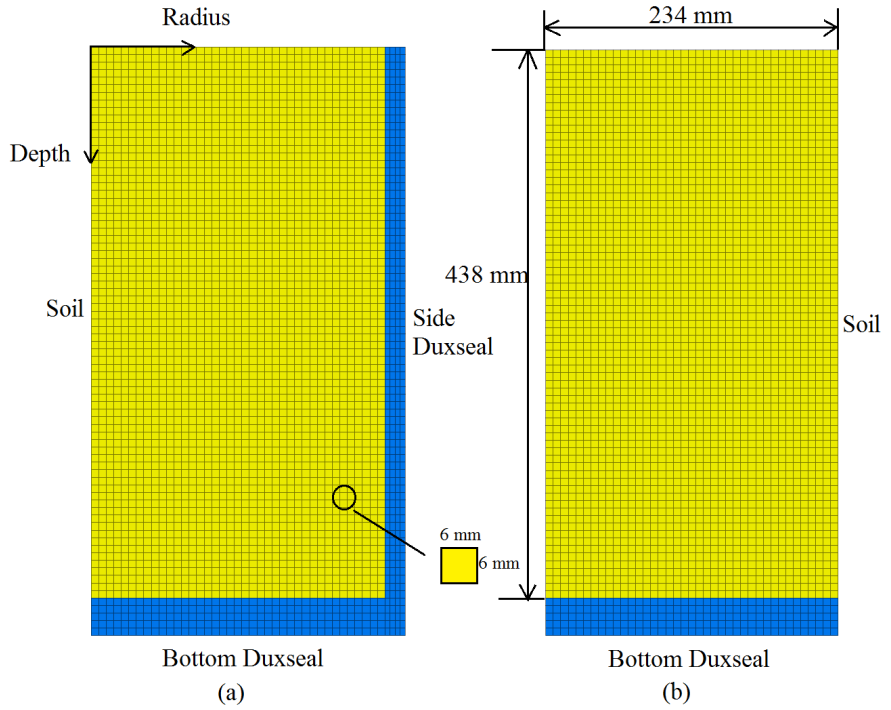


FIGURE 6.12: FLAC3D models used to investigate Duxseal effect (a) FLAC3D-FBM (b) FLAC3D-RBM

The K values of three soil layers at the AHA position, see Figure 6.4, were calculated to verify the validity of the two models, as shown in Table 6.4. The numerical results with Duxseal obtained from FLAC3D-FBM were the same as the results from FLAC3D-m2 and have been analysed in Section 6.3.3.3. The numerically calculated K values without side Duxseal were all 0.50, which was constant along depth and had a good agreement with the centrifuge test results. Table 6.4 suggests the two FLAC3D models gave reliable and accurate results and can be used to analyse the Duxseal effects on the stress field in the soil, as detailed in the following section.

TABLE 6.4: Lateral earth pressure coefficient obtained from the centrifuge ($K_{\text{exp},i}$) and the FLAC3D modelling ($K_{\text{num},i}$) with and without side Duxseal

Soil layer	Experimental (with)	Experimental (without)	Numerical (with)	Numerical (without)
L_3 (top)	$K_{\text{exp},3}$=0.28	$K_{\text{exp},3}$=0.52	$K_{\text{num},3}$=0.333	$K_{\text{num},3}$=0.50
L_2 (middle)	$K_{\text{exp},2}$=0.48	$K_{\text{exp},2}$=0.52	$K_{\text{num},2}$=0.438	$K_{\text{num},2}$=0.50
L_1 (bottom)	$K_{\text{exp},1}$=0.54	$K_{\text{exp},1}$=0.53	$K_{\text{num},1}$=0.524	$K_{\text{num},1}$=0.50

6.4.2 The stress field in the soil

The vertical and lateral stresses at the plane where y=0 were used to analyse the flexible boundary effects on the stress field in the soil. The vertical stress field in the soil and the lateral earth pressure coefficient K calculated with and without side Duxseal are shown in Figure 6.13 and Figure 6.14, respectively. The position of side Duxseal (marked by a dashed blue rectangular) is also presented in both figures.

It can be seen from the right plot of Figure 6.13 that without side Duxseal, the vertical stress increases linearly with depth thoughout the model. It can be seen from Figure 6.14 that K is constant (0.5) throughout the model without side Duxseal. This indicates the rigid boundary model (FLAC3D-RBM) can maintain zero lateral strain condition (initial K_0 condition). Figure 6.13 indicates the vertical stress with side Duxseal is almost the same as that without side Duxseal at most of the locations. This indicates the vertical stress field is slightly affected by the presence of side Duxseal. One feature observed is that the vertical stress with side Duxseal at the bottom right corner, marked by a dashed red circle, is a little higher than that without side Duxseal. Similar to the vertical stress, Figure 6.14 indicates K obtained with side Duxseal at the bottom right corner, marked by a dashed black circle, is also higher (0.55-0.6) than that without side Duxseal (0.5). This indicates the Duxseal at the bottom right corner under high vertical stress may expand laterally, thus resulting in the higher vertical and horizontal stresses within the soil.

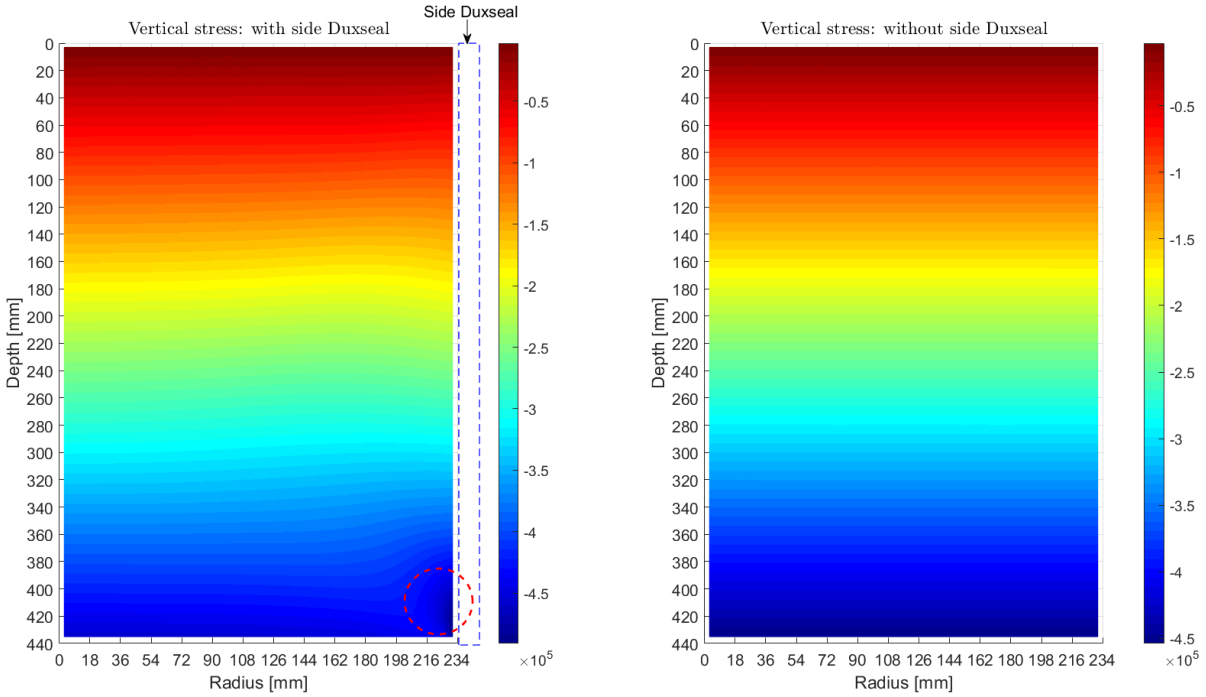


FIGURE 6.13: Vertical stress field in the soil calculated with and without side Duxseal

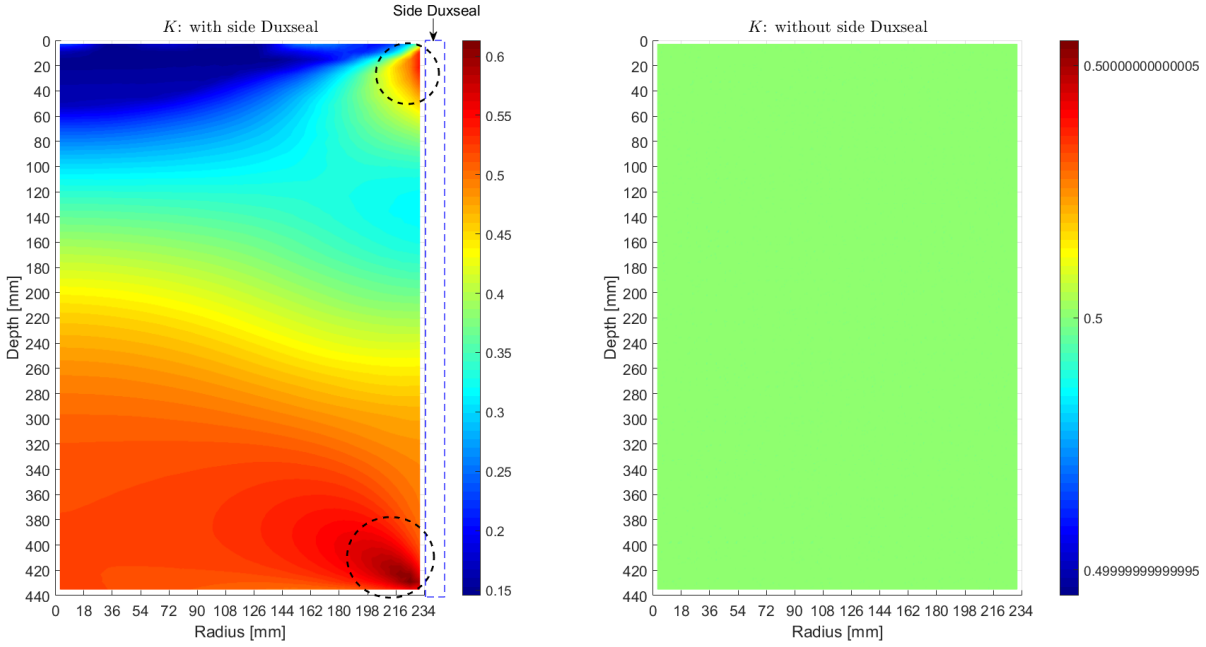


FIGURE 6.14: K calculated with and without side Duxseal

To explain the above observations, the lateral displacement vectors of the soil and the side Duxseal obtained from the model FLAC3D-FBM are shown in Figure 6.15, displayed as red and blue arrows, respectively. It is found that plotting the soil and Duxseal displacements in the same figure makes most of the arrows invisible because the displacement amplitudes within some areas are much larger than the

rest. Therefore, the soil and the Duxseal displacement vectors are plotted separately and the Duxseal displacement is presented in three subplots on the right. In addition, some bigger black arrows are used to clearly show the direction of motion due to some arrows being very small.

As shown in Figure 6.15, the lateral displacement vectors at the bottom right corner (below the depth of approximately 310 mm) imply that both side Duxseal and the soil move to the left. The left boundary is a symmetry plane and it is fixed in the numerical model FLAC3D-FBM. Therefore, the lateral stress in the soil below 310 mm is increased, as well as the vertical stress. Another increase in K values occurs at the upper right corner (0.5 to 0.55), as marked by the black circle in Figure 6.14. It can be seen from Figure 6.15, the soil and the Duxseal move towards each other in the opposite directions at this upper right corner, thus increasing the lateral stress within this area under compression.

Compared to this upper right corner, it can be seen from Figure 6.14 that, within the radius of 144 mm, K increases with depth, ranging from 0.15 at the top to approximately 0.55 at the bottom. This is because the soil above the depth of 310 mm moves towards the side Duxseal and the horizontal displacement amplitude decreases with depth. The lateral earth pressure reduction is inversely proportional to the horizontal displacement amplitude. As a consequence, K increases from 0.15 near the ground surface to 0.5 at about 310 mm. By contrast, the soil below the depth of 310 mm moves towards the fixed left boundary due to the lateral expansion of the side Duxseal under high vertical stress, as indicated by the arrows, thus leading to the increase in K.

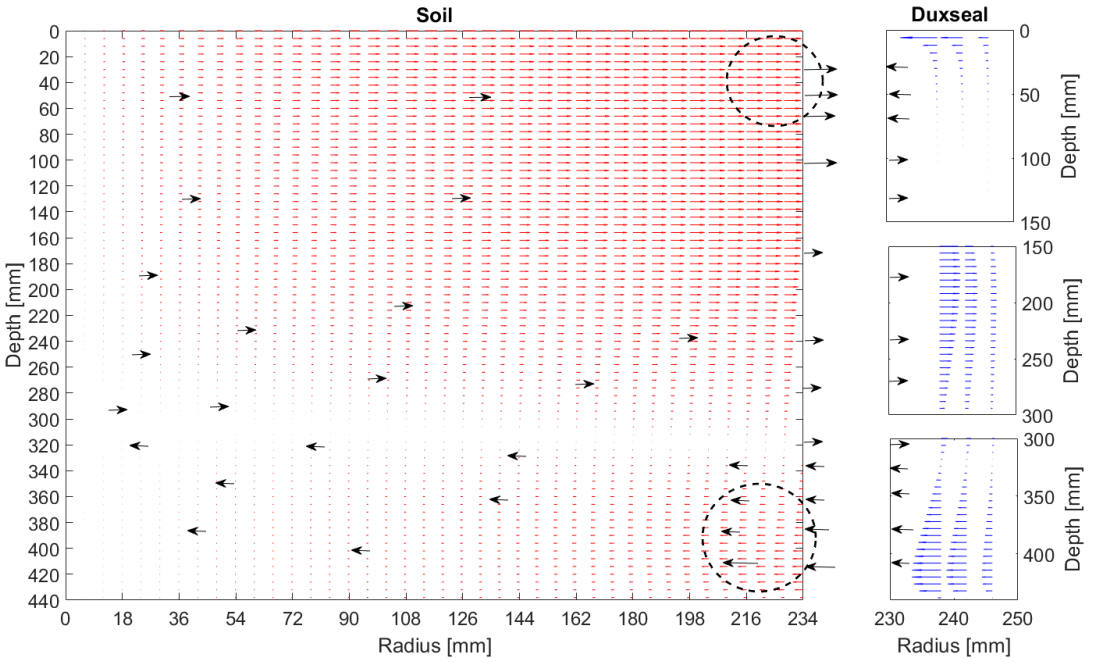


FIGURE 6.15: Lateral displacement of the soil and the side Duxseal

6.5 Duxseal effects on dynamic model response

The original purpose of the use of Duxseal was to absorb vibrations and reduce reflections from the rigid boundaries of the container. This is because the reflected waves can interact with the incident waves and adversely affect measurements. As presented in Section 6.3, the presence of side Duxseal can significantly affect the lateral stress field in the soil, thus affecting the soil-pile interaction and soil properties. This is because pile and soil behaviour are both stress dependent. Therefore, the dynamic model response may also be changed due to the presence of side Duxseal. This section discusses the potential effects of side Duxseal on the experimental results by the use of FLAC3D models.

6.5.1 FLAC3D models used to examine Duxseal effects

Two numerical models with and without side Duxseal were developed in FLAC3D. The calibrated numerical model FLAC3D-m2 represents the centrifuge model with side Duxseal, referred to as FLAC3D-m2-FBM in this section. In addition, a new model without side Duxseal, but, with the same dead weight (m2) was developed in FLAC3D to simulate the centrifuge model without side Duxseal. This model is a rigid boundary model and it is referred to as FLAC3D-m2-RBM, as shown in Figure 6.16. The K values of the three soil layers at the AHA position obtained from the model FLAC3D-m2-RBM were checked first to ensure this model can be

used to calculate the dynamic model response. This is not detailed here due to results being the same as model FLAC3D-RBM, see Table 6.4.

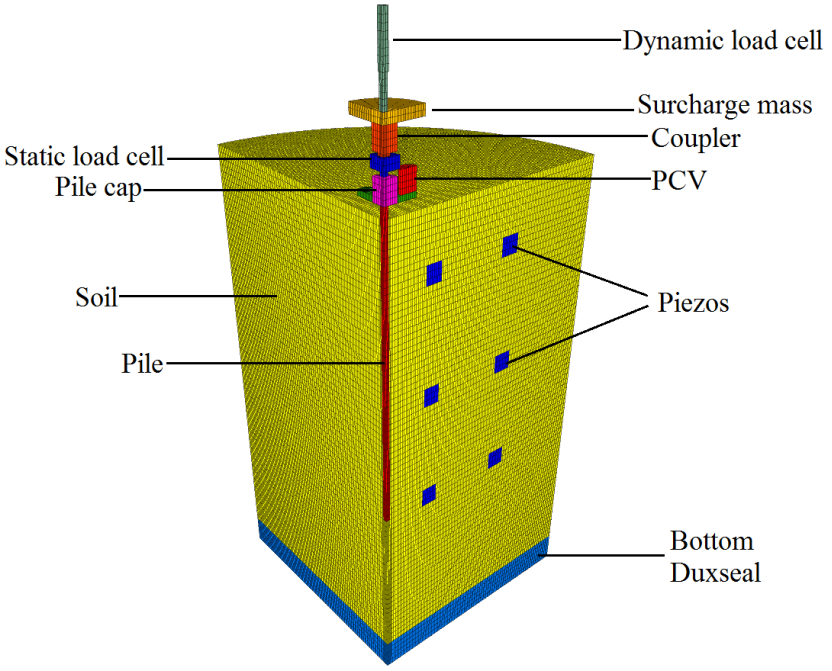


FIGURE 6.16: FLAC3D model used to simulate the centrifuge model without side Duxseal (FLAC3D-m2-RBM)

It should be noted that whether the side Duxseal is modelled or not, the boundary condition at the side walls should be fixed to realistically replicate the centrifuge model. Absorbing boundaries can be modelled in FLAC3D by applying quiet boundaries to the side walls of the model. To fully understand the effects of side Duxseal, four cases were modelled by applying two different boundary conditions at the side walls of the two models. The four cases are summarized in Table 6.5. It should be noted that the same boundary condition, fixed boundary, was applied at the bottom of all the models. In the following sections, the fixed boundary model implies the model with the fixed boundary at the side walls and the quiet boundary model implies the model with the quiet boundary at the side walls.

TABLE 6.5: Boundary conditions applied to the numerical models

Case	Name	Side Duxseal	Side walls of the model	Bottom of the model
1	FLAC3D-m2-FBM-fixed	modelled	fixed	fixed
2	FLAC3D-m2-FBM-quiet	modelled	quiet	fixed
3	FLAC3D-m2-RBM-fixed	not modelled	fixed	fixed
4	FLAC3D-m2-RBM-quiet	not modelled	quiet	fixed

6.5.2 Comparison of numerical modelling results

The Duxseal effects are discussed in detail in this section by comparing the results obtained from different cases, see Table 6.5.

6.5.2.1 Stiffness changing effect

The side Duxseal effects on the dynamic model behaviour (pile and soil response) can be found by comparing the two models with the same boundary condition (such as case 1 and case 3; case 2 and case 4). The normalised pile top and soil responses in linear scale (FRF=velocity/force) at most locations under these four different circumstances are shown in Figures 6.17, 6.18 and 6.19.

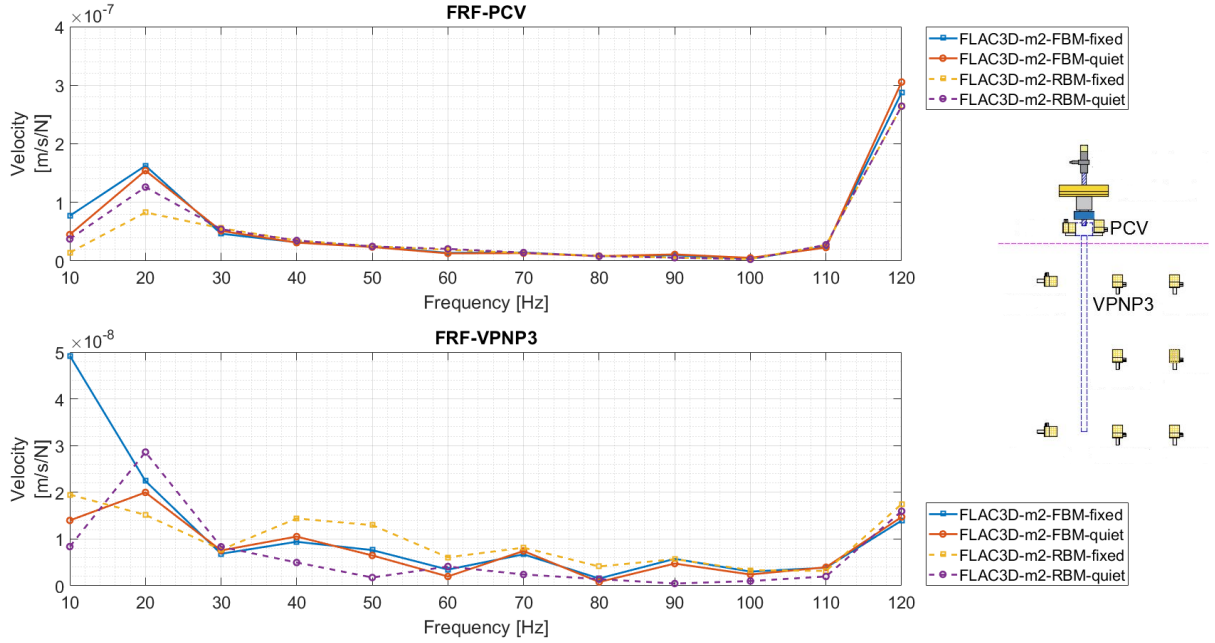


FIGURE 6.17: Pile top and soil response under different boundary conditions (PCV and VPNP3)

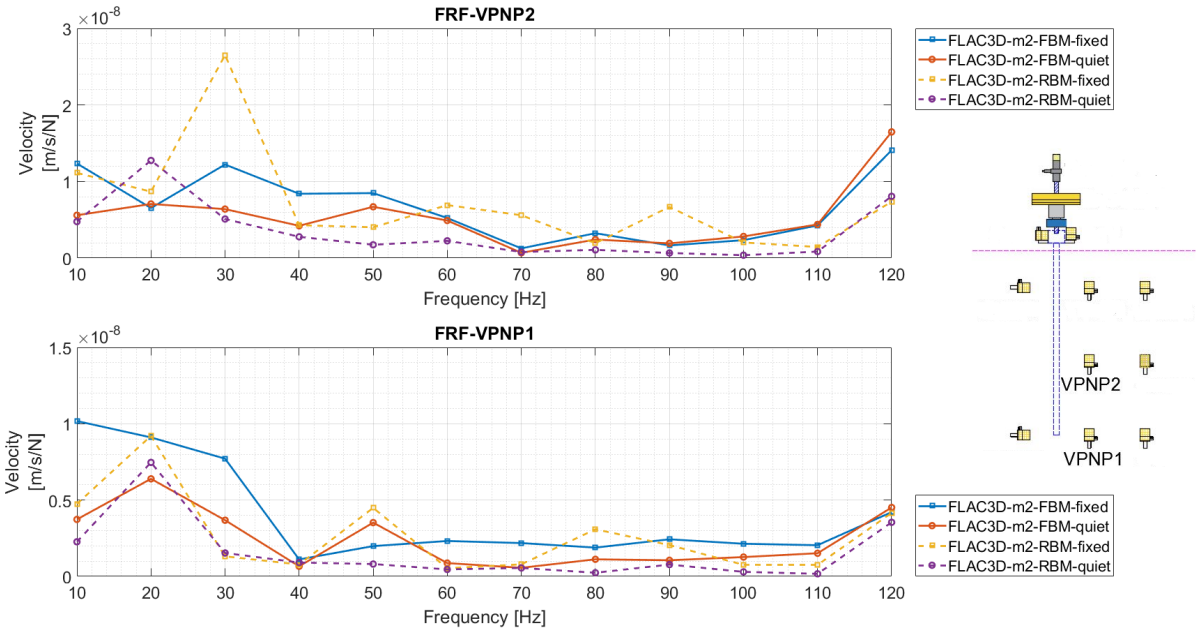


FIGURE 6.18: Soil response under different boundary conditions (VPNP2 and VPNP1)

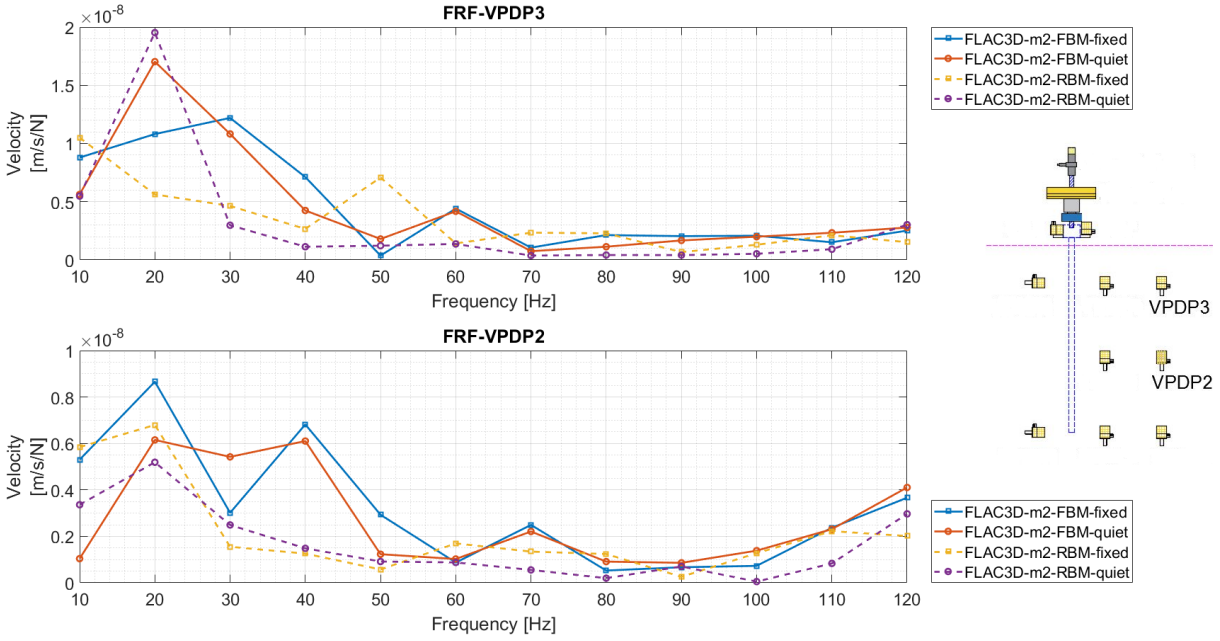


FIGURE 6.19: Soil response under different boundary conditions (VPDP3 and VPDP2)

First, it can be observed from Figure 6.17 that the pile top behaviour is slightly affected within the frequency range of 30 Hz to 110 Hz. Another feature observed from Figure 6.17 is the pile top response is higher at 20 Hz and 120 Hz. This is probably because these frequencies are close to one of the resonance frequencies of the above ground system, including the pile cap, the static load cell, the dead weight and the dynamic load cell, etc. More importantly, the boundary condition has a greater influence on the pile top behaviour at these frequencies compared

to the other frequencies. This may be due to the pile behaviour mainly being controlled by its own mass and stiffness. The pile top behaviour at most frequencies is insensitive to the changing of stresses and stiffness of the soil. However, the pile top behaviour near the resonance frequencies is more sensitive to the changing of stresses and stiffness of the soil.

Compared to the pile top, the soil response is significantly affected by the side Duxseal at most of the frequencies, see the curves of FLAC3D-m2-FBM-fixed and FLAC3D-m2-RBM-fixed in Figure 6.17, Figure 6.18 and Figure 6.19. To make a comparison, the RMS distances (defined in Section 6.3) of the pile and soil responses obtained from the two models with the same boundary condition (RMS distances of 1&3; RMS distances of 2&4) are calculated and presented in Table 6.6. It can be seen that the D_{RMS} of pile top response is less than 0.02 for both boundary conditions. However, D_{RMS} of soil responses is approximately 10 times the pile top at most locations. This is because side Duxseal can change the soil stiffness throughout the model, thus affecting the soil behaviour.

TABLE 6.6: RMS distances of the FRFs from two models with the same boundary condition

Boundary	Case	PCV	VPNP3	VPNP2	VPNP1	VPDP3	VPDP2	VPDP1
Fixed sides	1&3	0.0149	0.0320	0.1226	0.1488	0.2309	0.1439	0.1382
Quiet sides	2&4	0.0190	0.1740	0.1903	0.2044	0.1705	0.2992	0.7323

6.5.2.2 Vibration absorbing

It was found by Madabhushi (1991) that Duxseal can absorb about 65% of the incident P-waves and 60% of the incident S-waves. The ability of Duxseal to absorb vibrations was also examined in this study by the numerical models. As mentioned above, the side Duxseal was simulated in model FLAC3D-m2-FBM, however, not included in model FLAC3D-m2-RBM. Two different boundary conditions (fixed and quiet) were applied to each model. Theoretically, if side Duxseal can absorb part of the vibrations, the soil response calculated with side Duxseal under the fixed boundary are closer to the soil response obtained with side Duxseal under the quiet boundary compared to the model without side Duxseal. In other words, the FRF difference at the same location obtained from the model with side Duxseal under two different boundary conditions (FRF difference of 1&2) should be smaller than the FRF difference obtained from the model without side Duxseal under two boundary conditions (FRF difference of 3&4). This is because fewer reflections will propagate into the soil and alter the soil response.

To demonstrate this, the RMS distances of the FRFs obtained from the same model under two different boundary conditions (D_{RMS} of 1&2 and D_{RMS} of 3&4) are calculated and shown in Table 6.7. It can be seen that the D_{RMS} of 1&2 is much smaller than the D_{RMS} of 3&4 at most observation locations in the soil. This indicates Duxseal, a material with a high damping ratio, is capable of absorbing part of the vibrations and reducing reflections.

TABLE 6.7: RMS distances of the FRFs from the same model with different boundary conditions

Duxseal	Case	PCV	VPNP3	VPNP2	VPNP1	VPDP3	VPDP2	VPDP1
With	1&2	0.0033	0.0143	0.0236	0.0852	0.0582	0.0323	0.2564
Without	3&4	0.0036	0.2536	0.2786	0.2186	0.2190	0.2761	0.5972

6.5.2.3 Flexible boundary versus rigid boundary

It can be concluded from the above analysis that the use of Duxseal possesses advantages (absorbing vibrations) and disadvantages (altering dynamic model behaviour). In order to determine whether the vibration absorbing material, Duxseal, should be used in the dynamic centrifuge tests, the RMS distances of FRFs obtained from models with different boundary conditions were calculated and compared herein.

As shown in Table 6.5, the side Duxseal is not modelled, however, the absorbing boundaries are simulated by applying quiet boundaries in Case 4. Therefore, Case 4 simulates an ideal circumstance due to that the initial K_0 condition is satisfied and reflected waves from the side walls are absorbed by the quiet boundaries. Case 1 replicates the centrifuge model with side Duxseal. Therefore, the dynamic model response is mainly affected by the soil stiffness changing and secondly part of the reflected waves due to part of the waves being absorbed by Duxseal. Case 3 models the centrifuge tests without the side Duxseal. Therefore, the initial K_0 condition is satisfied, however, reflected waves from the side walls can affect the dynamic model behaviour in Case 3. The effects of the soil stiffness changing and the reflected waves on the centrifuge measurements can be found by looking at the RMS distances of Case 1 and Case 4 (D_{RMS} of 1&4) and the RMS distances of Case 3 and Case 4 (D_{RMS} of 3&4). D_{RMS} of 1&4 and D_{RMS} of 3&4 are shown in Table 6.8.

It can be seen that D_{RMS} of 1&4 at PCV is about 3 times the D_{RMS} of 3&4. This indicates the soil stiffness changing has a larger effect on the pile behaviour compared to reflected waves. In terms of the soil response, D_{RMS} of 1&4 is larger

than D_{RMS} of 3&4 at some locations, such as VPNP1, VPDP3 and VPDP1. To the contrary, D_{RMS} of 1&4 is smaller than D_{RMS} of 3&4 at the other locations, VPNP3, VPNP2 and VPDP2. One feature observed is the D_{RMS} differences are similar at most locations. This suggests the effects of soil stiffness changing on the dynamic soil behaviour are similar to the effects of reflected waves.

TABLE 6.8: RMS distances of the FRFs used to evaluate the boundary effects

Main effect	Case	PCV	VPNP3	VPNP2	VPNP1	VPDP3	VPDP2	VPDP1
Stiffness changing	1&4	0.0102	0.1830	0.2235	0.3749	0.2648	0.2417	0.8592
Reflected waves	3&4	0.0036	0.2536	0.2786	0.2186	0.2190	0.2761	0.5972

Based on the above analysis, it is suggested that side Duxseal should not be used to investigate the ground-borne vibration from the oscillation of a single pile. This is because the soil-pile interaction is the dominant factor which determines the vibrations in the soil. Therefore, the correct modelling of soil-pile interaction is more important. The effects of reflected waves can be reduced by using a larger model container because waves attenuate with distance and vibrations with smaller amplitudes will be reflected in a larger container, as indicated in Figure 5.41. However, the side Duxseal induced stress and stiffness changing can not be overcome.

6.6 Piezoelectric accelerometer effects

Another potential effect may come from the Piezos embedded in the soil. This is because the density and the stiffness of the Piezos are quite different from the soil. Given that the dynamic soil response is mass and stiffness dependent, the measured vibration level in the soil may be affected by the presence of Piezos. It is impossible to measure the vibration of soil without any sensors in the centrifuge. Therefore, the Piezos effects cannot be directly investigated by performing centrifuge tests. To examine the effects of Piezos on the centrifuge test results, a new FLAC3D model, as shown in Figure 6.20, was built based on the previous FLAC3D model FLAC3D-m2, see Figure 6.1. The only difference from the model FLAC3D-m2 is Piezos were not included in this model. The Piezos effects can be found by comparing the numerical modelling results from the model with Piezos and the model without Piezos.

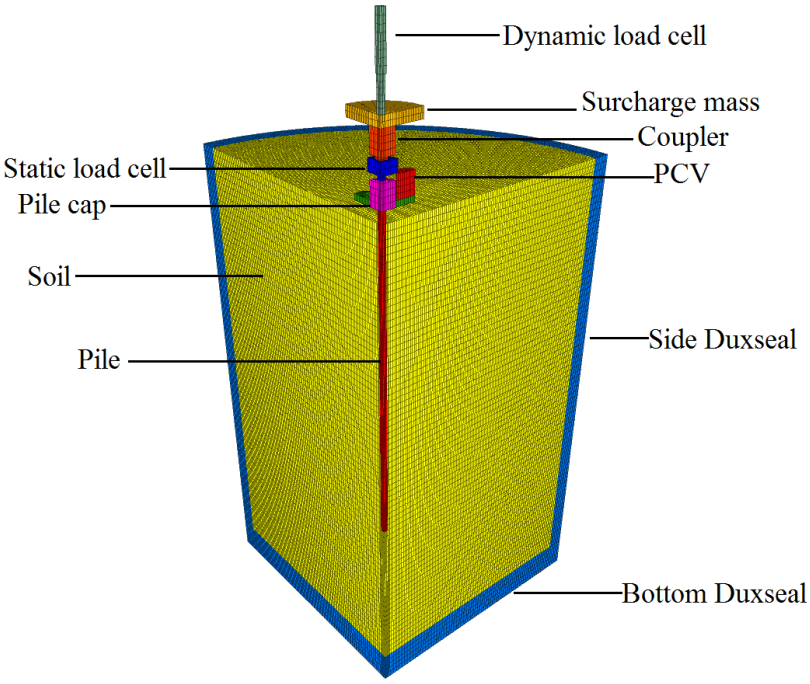


FIGURE 6.20: FLAC3D model used to simulate the centrifuge model without Piezos in the soil

The FRFs of the soil response in linear scale at all the locations are shown in Figure 6.21 and Figure 6.22. It can be observed that calculated results with and without the Piezos are close to each other at most frequencies. This indicates the embedded Piezos have a good coupling with the surrounding soil and vibrate together with the surrounding soil. However, at some frequencies, the FRFs obtained with Piezos are approximately twice the FRFs without Piezos, such as 40 Hz and 70 Hz for VPNP3; 80 Hz and 90 Hz for VPDP1. On the contrary, the FRFs obtained without Piezos are approximately twice the FRFs with Piezos at some other frequencies, such as 50 Hz and 60 Hz for VPNP1 and 30 Hz for VPDP1.

This implies the presence of Piezos can affect the soil response. This is probably due to two reasons. The first reason is the Piezos can change the local mass and stiffness at the observation points, thus affecting the soil response. The second is the existence of Piezos may generate reflected waves. These reflections can interfere with the propagating waves. At some frequencies, constructive interference of input waves and reflected waves occurs and this can increase the model responses. However, at some frequencies, destructive interference occurs which leads to the reduction in model response.

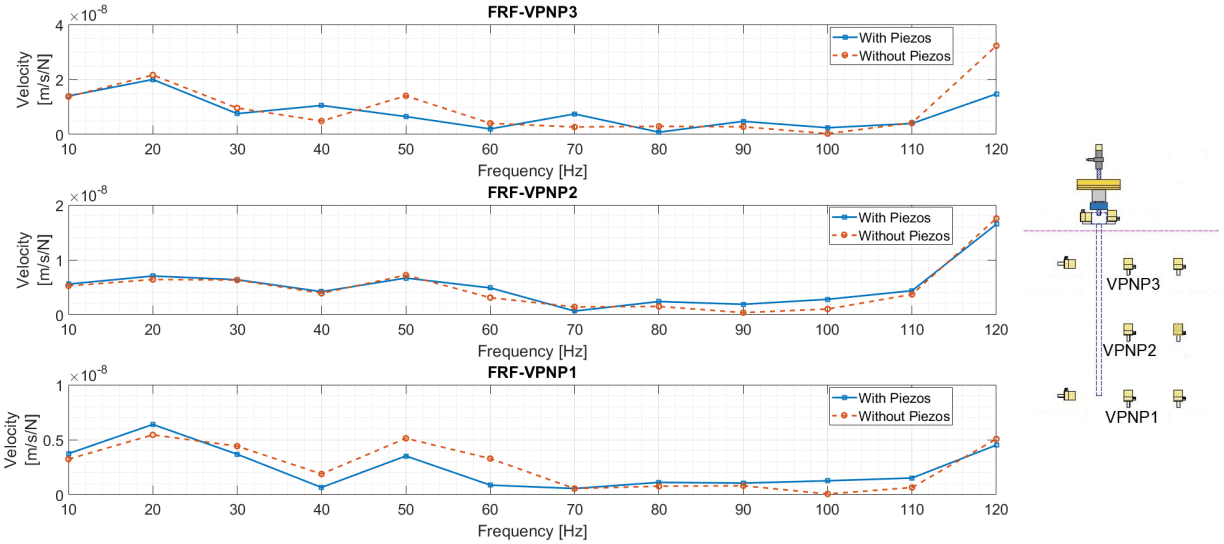


FIGURE 6.21: Comparison of numercal modelling results with and without Piezos in the soil (soil response near pile)

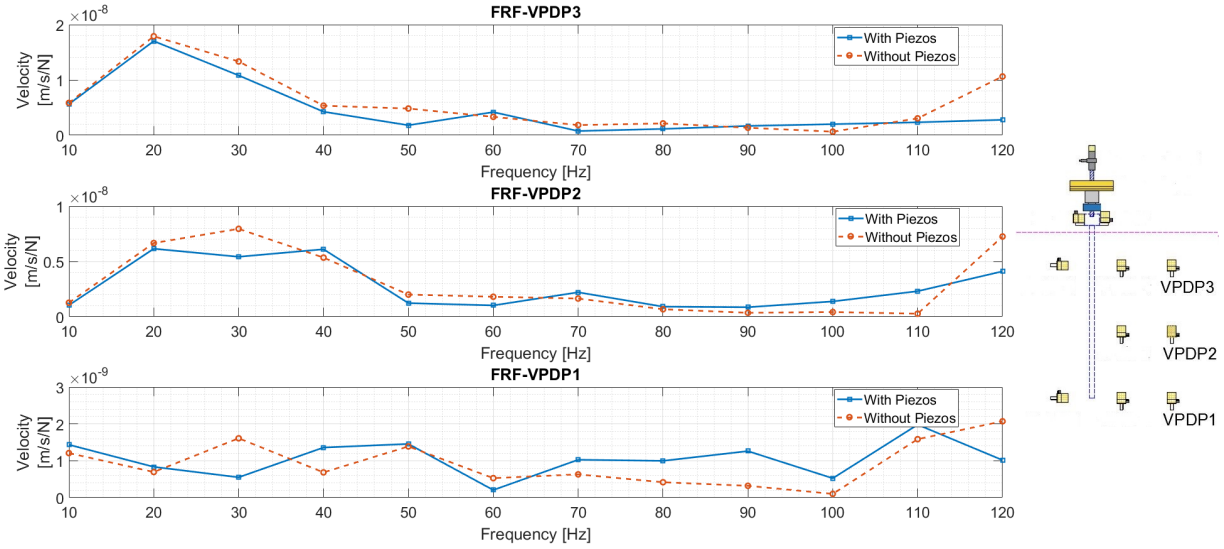


FIGURE 6.22: Comparison of numercal modelling results with and without Piezos in the soil (soil response distant to pile)

6.7 Chapter summary

Three-dimensional numerical models were built in FLAC3D to simulate the centrifuge tests and to provide further insights into the problem of ground-borne vibration from the oscillation of a single pile. The effects of Duxseal and Piezos on the centrifuge measurements were examined by the numerical models. The following is a summary of all the findings:

(1) The numerical models developed in FLAC3D were calibrated using results obtained from the physical modelling. Key challenges were the correct modelling of the 'spin-up' process (in other words: the soil property should be updated based on the confining stress from 1 g to 60 g in the centrifuge) and the determination of the elastic modulus of the Duxseal. Calibration results indicated that the numerical modelling procedure employed in this study can reasonably replicate the centrifuge tests. In addition, the comparison of the lateral earth pressure coefficients obtained from the experiments and the numerical models suggested Duxseal properties were stress dependent and the proposed equation can be used to predict the elastic modulus of the Duxseal.

(2) In order to obtain a better understanding of the Duxseal effects on the stress field in the soil, two numerical models, which only accounted for the soil and the Duxseal, were developed: one model with side Duxseal and one model without side Duxseal. It was found that the effects of Duxseal on the vertical stress was insignificant. Compared to the vertical stress, the presence of Duxseal can remarkably affect the lateral stress. It was found that without side Duxseal, the rigid boundary model can maintain the initial K_0 condition. With side Duxseal, K increased with depth, ranging from 0.15 to approximately 0.55. The soil within the radius of 144 mm above the depth of 310 mm moved towards the side Duxseal and the horizontal displacement decreased with depth. As a consequence, the lateral stress was reduced. K increased from 0.15 near the ground surface to 0.5 at the depth of 310 mm because the lateral earth pressure reduction is inversely proportional to the horizontal displacement amplitude. By contrast, the soil below the depth of 310 mm moved towards the fixed left boundary due to the lateral expansion of the side Duxseal under high vertical stress, thus leading to the increase in K (0.5-0.55). At some locations (such as the soil near the side Duxseal just below the ground surface), the side Duxseal expanded laterally under high vertical stress and this led to the increase in K (0.5 to 0.55).

(3) Four different cases (two models and each with two different boundary conditions) were modelled in FLAC3D to investigate the side Duxseal effects on the dynamic model behaviour. It was found that Duxseal was capable of absorbing part of the vibrations, however,

its presence can change the soil stiffness and affect the dynamic model behaviour.

Comparison of soil stiffness changing effects and reflected waves effects indicated the former had a larger effect on the pile behaviour and the effects of the former on the soil behaviour was similar to the latter. Therefore, it is suggested that side Duxseal should not be used to investigate the ground-borne vibration from the oscillation of a single pile. This is because the soil-pile interaction is the dominant factor which determines the vibrations in the soil. Therefore, the correct modelling of soil-pile interaction is more important. The effects of reflected waves can be reduced by using a larger model container due to waves attenuate with distance and vibrations with smaller amplitudes will be reflected in a larger container. However, the side Duxseal induced stress and stiffness changing can not be overcome and the Duxseal is not able to eliminate reflections.

(4) The soil Piezos effects were examined by comparing the results from two FLAC3D models: one with soil Piezos and one without soil Piezos. It was observed that calculated results with and without the soil Piezos were close to each other at most frequencies. This indicated the embedded Piezos had a good coupling with the surrounding soil and vibrated together with the soil. However, response differences at the observation points were approximately twice at some frequencies. This may be caused from the mass and stiffness changing of the observation points, as well as the reflected waves generated from the housing of the Piezos. Overall, the presence of Piezos would not significantly change the model responses.

Chapter 7

Conclusions and Recommendations for Future Work

This chapter summarises the main conclusions drawn from the work of previous chapters and some recommendations are made for future work.

7.1 Conclusions

The main aims of this study were to provide insights into the soil-pile interaction and ground-borne vibrations in sand from the vertical oscillation of a single pile and to examine the use of centrifuge modelling as a tool for investigating this problem. To achieve these aims, centrifuge tests were performed to simulate the ground-borne vibration by applying small vertical harmonic loads to the top of a single pile embedded in sand. The effects of vibration absorbing material used in the centrifuge tests, Duxseal, on the soil stress field and soil stiffness were investigated experimentally by measuring the shear wave velocity of the soil using centrifuge based air hammer tests and triaxial based bender elememt tests. A series of numerical models were developed in FLAC3D to further the understanding of soil-pile interaction under vertical harmonic loads and to examine the effects of Duxseal and Piezos on the centrifuge measurements.

7.1.1 Soil-pile interaction and ground-borne vibrations

The dynamic pile behaviour, the soil-pile interaction and ground-borne vibrations under the combined vertical static and dynamic loads were investigated experimentally (in the centrifuge) and numerically (in FLAC3D) in this study. The results were presented in Chapters 5 and 6, respectively. Three dead loads with a safety factor of approximately 8, 4 and 2 were employed in this study to investigate the effect of the static load amplitude on the dynamic pile and soil behaviour. Two different input dynamic forces were applied to the pile top under each dead load. It was found that consistent and reliable results were obtained from the two methods and centrifuge tests used to model the ground-borne vibration from a single pile were successfully conducted. The following is a summary of the findings from the two methods:

- It was found that both dynamic pile and soil behaviour were in the linear range due to the fact that the frequency response function (FRF= displacement/force) were insensitive to the dynamic load amplitude. This indicated the dead load would not affect the dynamic soil-pile interaction at least when the safety factor is greater than 2.
- The accumulated pile and soil displacements were examined and results indicated both the pile and the ground settled at almost the same rate. This indicated the soil and the pile experienced the same displacement at the interface and the dynamic load applied to the pile top would not result in accumulated pile displacement. This also suggested the soil-pile interface can be treated as a perfectly bonded interface under all the combined forces applied in this study. The settlement of the whole model (pile and soil) may be caused by the flexible Duxseal attached to the bottom of the container.
- Under three dead loads (safety factor>2), the pile top response amplitudes indicated that the overall trend was the pile top response decreased with the increasing dead load. Results from the FLAC3D models also proved that the larger the dead load, the smaller the pile top response.
- It was found that the pile was compressible and a simplified soil-pile mechanical model was employed to analyse the soil-pile interaction. This model was proposed based on two findings: the soil-pile interface was perfectly bonded and the displacement of the pile element was purely caused by the axial elastic deformation. This model indicated the axial load within the pile decreased with depth, thus resulting in

the decreasing axial elastic deformation of the pile and soil particle displacement along depth. The numerical modelling results confirmed that the deformation of the pile did decrease with depth.

- The damping ratio of soil along depth was calculated by the logarithmic decrement method using data measured by the accelerometers. It was found that the estimated damping ratios were approximately 1.0% at three depths (3.36 m, 10.0 m and 16.8 m in prototype scale). This indicated material damping may have a slight effect on the vibration attenuation at the three depths.

- It was found that the vibration level at the same horizontal distance from the pile center decreased almost linearly with depth. This suggested vertical vibrations generated at the soil-pile interface decreased with depth which agreed with the proposed model that the pile segment was moving less at depth. It also demonstrated the damping effect on vibration attenuation within the very small shear strain range was insignificant.

- The vibration attenuation along radial distance was evaluated by comparing the ratio of vibration responses measured by two accelerometers with the same embedded depth. It was found test that results agreed well with the theoretical estimation at most frequencies. The vibration amplitudes along radial distance at three depths (3.36 m, 10 m and 16.8 m) were calculated using the theoretical vibration attenuation equation. It was found that within 3 m to 15 m, the vibration attenuated very quickly. The curves tended to be flat when the radial distance from the pile was greater than 27 m.

7.1.2 Duxseal effects

Duxseal effects on the centrifuge model behaviour were examined experimentally, presented in Chapter 4, and numerically, presented in Chapter 6. The original purpose of the use of Duxseal was to absorb vibrations and reduce reflections from the rigid boundaries of the centrifuge container so that more accurate model responses can be measured in the centrifuge. However, it was found Duxseal can change the lateral stress in the soil and the soil stiffness due to soil behaviours being stress dependent.

First of all, it should be noted that the experimental and numerical results both indicated that without side Duxseal, the initial K_0 condition can be satisfied. This is because the rigid boundary model can maintain zero lateral strain condition. In

addition, results from the numerical models with and without the side Duxseal implied the vertical stress in the soil was slightly affected by the side Duxseal and can be neglected.

It was found from the centrifuge based air hammer tests with Duxseal attached to the sides of the model container that the lateral earth pressure coefficient K was reduced. Particularly, K was reduced to approximately 0.3 at shallow depths. Consequently, the soil stiffness near the ground surface was about 14% smaller than that without side Duxseal. The Duxseal effects were also examined by numerical models, presented in Chapter 6. Numerical modelling results indicated that Duxseal can absorb part of the incident waves. On the other hand, it was found that the side Duxseal provided a flexible boundary and it can lead to the lateral deformation of soil, thus significantly changing the lateral stress field and soil stiffness throughout the model. Overall, the soil above 2/3 of the model depth moved towards the side Duxseal and the horizontal displacement decreased with depth. As a consequence, the lateral stress was reduced and K ranged from 0.15 near the ground surface to 0.5 at 2/3 of the model depth. By contrast, the soil below 2/3 of the model depth moved towards the fixed left boundary due to the lateral expansion of the side Duxseal under high vertical stress, thus leading to the increase in K (0.5-0.55). Moreover, the dynamic pile and soil behaviours were affected due to the change in stress and soil stiffness, in particular, the pile behaviour.

Therefore, it is suggested that side Duxseal should not be used to investigate the ground-borne vibration from the oscillation of a single pile. This is because the soil-pile interaction is the dominant factor which determines the vibrations in the soil. Therefore, the correct modelling of soil-pile interaction is more important. The effects of reflected waves can be reduced by using a larger model container because waves attenuate with distance and vibrations with smaller amplitudes will be reflected in a larger container. However, the side Duxseal induced stress and stiffness changes can not be overcome and the Duxseal is not able to eliminate reflections.

7.1.3 Piezoelectric accelerometer effects

The Piezos embedded in the soil may affect the measured soil responses at the observation points due to that the density and the stiffness of the Piezos are quite different from the soil. The soil Piezos effects were examined in Chapter 6 by comparing the results from two FLAC3D models: one with soil Piezos and one without soil Piezos. It was observed that calculated results with and without the soil Piezos were close to each other at most frequencies. This indicated the

embedded Piezos had a good coupling with the surrounding soil and vibrated together with the soil. However, response differences at the observation points were approximately twice at some frequencies. This may be resulted from the mass and stiffness changing of the observation points, as well as the reflected waves generated from the housing of the Piezos. Overall, the presence of Piezos did not significantly change the model response.

7.2 Recommendations for future work

Research work presented in this thesis constitutes a small part of the comprehensive subject. Building on the results and analysis, some areas where more research could be undertaken experimentally and numerically are listed as follows:

- Comparing the ball dropping system with the electromagnetic shaker:

  In this study, the electromagnetic shaker was used to excite the pile. To apply harmonic loads, the shaker had to be connected to the pile top with a bolt, referred to as shaker attachment. It was found the shaker attachment may affect the pile behaviour in the centrifuge tests. In order to examine the shaker attachment effects on the pile response, the ball dropping system, an excitation method which does not suffer from the above issue, can be used in future tests to make a comparison with the electromagnetic shaker.

- Reducing the boundary effects in the centrifuge:

  Based on the research results, it is suggested that side Duxseal should not be used in the dynamic centrifuge tests due to the change in the lateral stress field and soil stiffness throughout the model. Therefore, more work should be carried out to find a better approach to maintain the zero lateral strain condition and absorb waves at the same time. A better method would not significantly alter the lateral stress in the soil, however, it would be capable of absorbing part of the waves to reduce boundary effects. An alternative method to achieve this aim is using a larger rigid container. By doing this, the zero lateral strain condition is maintained and smaller amplitude waves are reflected.

- Testing sand with different densities or different type of soils:

  In this research, only one type of dry sand (HST95 Congleton sand) with a certain relative density (85%) was used. In the future, the same sand with different densities and more complicated soils, such as clay or real material in the field, should be tested.

- Testing pile groups under vertical harmonic loads:

  A single pile is the fundamental unit for understanding the dynamic response of piled foundations. This research project investigated the dynamic behaviour of a single pile and the resulting ground-borne vibrations. Future work should focus on the behaviour of a pile group and study the ground-borne vibration level and vibration propagation characteristics generated from the vertical oscillation of a pile group.

- Pile material effects:

  It was found that the elastic deformation of the pile determines the vertical vibration in the soil. In this study, the pile was made of aluminium to simplify the tests. It is believed that under the same vertical dynamic load, piles made of different materials undergo different deformations due to the stiffness being different. Therefore, the ground-borne vibration level is affected by the material stiffness of the pile and piles made of different materials should be tested.

- Dynamic response of soil-pile interaction under larger dead loads:

  The dead load applied to the pile top in this study was up to just below half of the ultimate bearing capacity of the pile. In other words, the smallest safety factor was about 2. The dynamic behaviour of the pile was found to be in the linear range when the safety factor was larger than 2. Future work should investigate the dynamic behaviour of the pile and the soil-pile interaction using smaller safety factors.

- Vibrations from a pile to nearby buildings:

  This study focused on the ground-borne vibrations in sand from a single pile. Only the soil and a pile were involved in the centrifuge model. In the future, a building with different forms of foundations adjacent to the pile should be modelled to study how much of the vibrations could propagate into it and to determine an appropriate distance between the pile and the building.

- Extending the numerical model to account for more structures:

  Numerical models were developed in FLAC3D to simulate the centrifuge models in this study. It was found that the centrifuge model results were reasonably close to the numerical results. Similar to the centrifuge model, only the soil and a pile were modelled and the structures above the pile top was simplified. The numerical model can be extended to account for more structures, such as nearby buildings, piers and beams, to provide a more realistic model of the problem.

– Modelling dry sand with discrete element modelling software:

  The soil used in this study was a dry silica sand, a granular material best described as a discontinuous medium. However, the numerical modelling software FLAC3D used in this research is not able to realistically model the behaviour of discontinuous media, i.e. particle-to-particle contact in sand. Therefore, future work should use discrete element modelling to more correctly simulate dry sand and to investigate the wave transmission in dry sand, thus providing more accurate numerical results.

References

Ai, Z. Y. and Liu, C. L. (2015). Vertical vibration of a pile in transversely isotropic multilayered soils. *Journal of Sound and Vibration*, 357:145 – 155.

Aiello, V., Boiero, D., D'Apuzzo, M., Socco, L. V., and Silvestri, F. (2008). Experimental and numerical analysis of vibrations induced by underground trains in an urban environment. *Structural Control and Health Monitoring*, 15(3):315–348.

Akgüner, C. and Kirkit, M. (2012). Axial bearing capacity of socketed single cast-in-place piles. *Soils and Foundations*, 52(1):59–68.

Al-Defae, A. H. H. (2013). *Seismic performance of pile-reinforced slopes*. PhD thesis.

Andersen, L. and Jones, C. (2006). Coupled boundary and finite element analysis of vibration from railway tunnels—a comparison of two- and three-dimensional models. *Journal of Sound and Vibration*, 293(3):611 – 625. Proceedings of the Eigth International Workshop on Railway Noise.

Arulnathan, R. (2018). New Tool for Shear Wave Velocity Measurements in Model Tests. pages 444–453.

Asano, G. and Kumagai, K. (1978). Model test for propagation of ground vibration above tunnel. Technical report.

Avitabile, P. (2001). Experimental Modal Analysis. *Sound and Vibration*, (January):1–11.

Bartake, P. P. and Singh, D. N. (2007). Studies on the determination of shear wave velocity in sands. *Geomechanics and Geoengineering*, 2(1):41–49.

Bolton, M. D. (1986). The strength and dilatancy of sands. *Géotechnique*, 36(1):65–78.

Bolton, M. D., Gui, M. W., Garnier, J., Corte, J. F., Bagge, G., Laue, J., and Renzi, R. (1999). Centrifuge cone penetration tests in sand. *Géotechnique*, 49(4):543–552.

Bolton, M. D. and Wilson, J. M. R. (1990). *Soil stiffness and damping*. Cambridge Univ., Engineering Department.

Brandenberg, S. J., Choi, S., Kutter, B. L., Wilson, D. W., and Santamarina, J. C. (2006). A bender element system for measuring shear wave velocities in centrifuge models.

Brigham, E. O. (1974). *The fast Fourier transform / E. Oran Brigham*. Englewood Cliffs, N.J. ; London.

BS (1992). Noise Control on Construction and Open Sites Part 4: Code of Practice for Noise and Vibration Control Applicable to Piling Operations.

BS (2005). Mechanical vibration — Ground-borne noise and vibration arising from rail systems — Part 1: General guidance. BS ISO 148:54.

Cai, Y., Ding, G., and Xu, C. (2009). Amplitude reduction of elastic waves by a row of piles in poroelastic soil. *Computers and Geotechnics*, 36(3):463–473.

Camacho-Tauta, J., Jimenez Alvarez, J. D., and Reyez-Ortiz, O. J. (2012). A procedure to calibrate and perform the bender element test. *Dyna*, 79(176):10–18.

Cheney, J. A., Brown, R. K., Dhat, N. R., and Hor, O. Y. (1990). Modeling free-field conditions in centrifuge models. *Journal of Geotechnical Engineering*, 116(9):1347–1367.

Chiang, K.-H. and Lee, C.-J. (2007). Responses of single piles to tunneling-induced soil movements in sandy ground. *Canadian Geotechnical Journal*, 44(10):1224–1241.

Cilingir, U. (2009). *Seismic Response of Tunnels*. PhD thesis.

Cleary, J. C. and Steward, E. J. (2016). Analysis of ground vibrations induced by pile driving and a comparison of vibration prediction methods. *DFI Journal - The Journal of the Deep Foundations Institute*, 10(3):125–134.

Connolly, D. P., Alves Costa, P., Kouroussis, G., Galvin, P., Woodward, P. K., and Laghrouche, O. (2015). Large scale international testing of railway ground vibrations across Europe. *Soil Dynamics and Earthquake Engineering*, 71:1–12.

Connolly, D. P., Kouroussis, G., Woodward, P. K., Costa, P. A., Verlinden, O., and Forde, M. C. (2014). Field testing and analysis of high speed rail vibrations. *Soil Dynamics and Earthquake Engineering*, 67:102–118.

Coyle, H. M. and Reese, L. C. (1966). Load transfer for axially loaded piles in clay. *J. Soil Mech. and Found. Div.*, 92:1.

De Silva, C. W. (2007). *Vibration : fundamentals and practice / Clarence W. De Silva*. Boca Raton, Fla. : CRC/Taylor & Francis, Boca Raton, Fla.

Dietz, M. S. (2000). *Developing an holistic understanding of interface friction using sand with direct shear apparatus*. PhD thesis.

Dobry, R. and Vucetic, M. (1987). Dynamic properties and seismic response of soft clay deposits.

El-Sekelly, W., Mercado, V., Abdoun, T., Zeghal, M., and El-Ganainy, H. (2013). Bender elements and system identification for estimation of Vs. *International Journal of Physical Modelling in Geotechnics*, 13(4):111–121.

El-Sekelly, W., Tessari, A., and Abdoun, T. (2014). Shear Wave Velocity Measurement in the Centrifuge Using Bender Elements.

Ewins, D. J. (2000). *Modal testing : theory, practice, and application / D. J. Ewins*. Baldock, 2nd ed. edition.

Fioravante, V. (2002). On the shaft friction modelling of non-displacement piles in sand. *SOILS AND FOUNDATIONS*, 42(2):23–33.

Fleming, K., Weltman, A., Randolph, M., and Elson, K. (2008). *Piling Engineering*. Taylor Francis, New York, NY 10016, USA.

Forrest, J. and Hunt, H. (2006a). Ground vibration generated by trains in underground tunnels. *Journal of Sound and Vibration*, 294(4):706 – 736.

Forrest, J. and Hunt, H. (2006b). A three-dimensional tunnel model for calculation of train-induced ground vibration. *Journal of Sound and Vibration*, 294(4):678 – 705.

Fu, L., Zeng, X., and Figueroa, J. L. (2004). Shear wave velocity measurement in centrifuge using bender elements. *International Journal of Physical Modelling in Geotechnics*, 4(2):01–11.

Garnier, J. (1998). Scale effects in piles and nails loading tests in sand. *Centrifuge '98*, pages 205–210.

Ghosh, B ; Madabhushi, S. P. G. (2002). An efficient tool for measuring shear wave velocity in the centrifuge. In *Proceedings of the international conference on physical modelling in geotechnics*, pages 119–124. AA Balkema.

Giraldo, J. and Rayhani, M. (2013). Influence of fiber-reinforced polymers on pile–soil interface strength in clays. *Advances in Civil Engineering Materials*, 2:20120043.

Gupta, S. and Degrande, G. (2005). Analysis of a beam on elastic foundation. Technical report, Catholic University of Lenuven.

Gupta, S., Hussein, M., Degrande, G., Hunt, H., and Clouteau, D. (2007). A comparison of two numerical models for the prediction of vibrations from underground railway traffic. *Soil Dynamics and Earthquake Engineering*, 27(7):608 – 624.

Ha, I.-S., Olson, S. M., Seo, M.-W., and Kim, M.-M. (2011). Evaluation of reliquefaction resistance using shaking table tests. *Soil Dynamics and Earthquake Engineering*, 31(4):682 – 691.

Hajialilue-Bonab, M., Chazelas, J., and Levacher, D. (2007). Procedures used for dynamically laterally loaded pile tests in a centrifuge. *Geotechnical Testing Journal*, 30(1):1–9.

Hardin, B. (1965). Dynamic versus static shear modulus for dry sand. *Materials Research and Standards*, 5:232–235.

Hardin, B. O. and Drnevich, V. P. (1972). Shear Modulus and Damping in Soils: Design Equations and Curves. *Journal of Soil Mechanics and Foundation Engineering Division*, 98(SM7):667–692.

Hardin, B. O. and Richart, J. F. E. (1963). Elastic wave velocities in granular soils. *ASCE – Proceedings – Journal of the Soil Mechanics and Foundations Division*, 89(SM1, Part 1):33–65.

Heckl, M., Hauck, G., and Wettschureck, R. (1996). Structure-borne sound and vibration from rail traffic. *Journal of Sound and Vibration*, 193(1):175 – 184.

Himanshu, M ; Dipal, P. (2016). Experimental determination of structural damping of different materials. *Procedia Engineering*, 144:110 – 115. International Conference on Vibration Problems 2015.

Holmquist, D. V. and Matlock, H. V. (1976). Resistance-Displacement Relationships For Axially-Loaded Piles In Soft Clay. In *Proceedings of the Annual Offshore Technology Conference*, pages 553–570.

Hunt, H. E. M. (2001). Measures for reducing ground vibration generated by trains in tunnels. In Krylov, V. V., editor, *Noise and vibration from high-speed trains*. Thomas Telford, London.

Hussein, M. and Hunt, H. (2007). A numerical model for calculating vibration from a railway tunnel embedded in a full-space. *Journal of Sound and Vibration*, 305(3):401 – 431.

Hussein, M., Hunt, H., Kuo, K., Costa, P., and Barbosa, J. (2013). A numerical model for calculating vibration in a building with pile foundation from underground railway trains.

Hussein, M. F. M. and Hunt, H. E. M. (2006). Modelling of floating-slab tracks with continuous slabs under oscillating moving loads. *Journal of Sound and Vibration*, 297(1?2):37–54.

Iai, S., Tobita, T., and Nakahara, T. (2005). Generalised scaling relations for dynamic centrifuge tests. *Géotechnique*, 55(5):355–362.

Ishihara, K. (1996). *Soil behaviour in earthquake geotechnics*. Clarendon Press; Oxford University Press.

Itasca (2008). *FLAC3D: Fast Lagrangian Analysis of Continua in Three Dimensions, User Manuals*. Itasca Consulting Group.

Itoh, K., Koda, M., I, L. K., and Kusakabe, O. (2002). centrifugal simulation of wave propagation using a multiple ball dropping system. *International Journal of Physical Modelling in Geotechnics*, 2:33–51.

Itoh, K., Zeng, X., Koda, M., Murata, O., and Kusakabe, O. (2005). Centrifuge simulation of wave propagation due to vertical vibration on shallow foundations and vibration attenuation countermeasures. *Modal Analysis*, 11(6):781–800.

Jaky, J. (1944). The Coefficient of Earth Pressure at Rest. *Journal for Society of Hungarian Architects and Engineers*, (October):355–358.

Jian-hua, L., Man-qing, X., Bin, X., and Ming-fu, F. (2012). The vibration of pile groups embedded in a layered poroelastic half space subjected to harmonic axial loads by using integral equations method. *Procedia Engineering*, 28:8 – 11. 2012 International Conference on Modern Hydraulic Engineering.

Jin, Q., Thompson, D. J., Lurcock, D. E., Toward, M. G., and Ntotsios, E. (2018). A 2.5d finite element and boundary element model for the ground vibration from trains in tunnels and validation using measurement data. *Journal of Sound and Vibration*, 422:373 – 389.

Jones, C. J. C. and Block, J. R. (1996). Prediction of ground vibration from freight trains. *Journal of Sound and Vibration*, 193(1):205–213.

Jones, C. J. C., Thompson, D. J., and Petyt, M. (2002). A model for ground vibration from railway tunnels. *Proceedings of the Institution of Civil Engineers - Transport*, 153(2):121–129.

Jones, S., Kuo, K., Hussein, M., and Hunt, H. (2012). Prediction uncertainties and inaccuracies resulting from common assumptions in modelling vibration from underground railways. *Proceedings of the Institution of Mechanical Engineers, Part F: Journal of Rail and Rapid Transit*, 226(5):501–512.

Ju, S. (2007). Finite element analysis of structure-borne vibration from high-speed train. *Soil Dynamics and Earthquake Engineering*, 27(3):259 – 273.

Karl, L. (2005). *Dynamic soil properties out of SCPT and bender element tests with emphasis on material damping*. PhD thesis.

Kim, D.-S. and Lee, J.-S. (2000). Propagation and attenuation characteristics of various ground vibrations. *Soil Dynamics and Earthquake Engineering*, 19(2):115–126.

Kim, M. K., Lee, J. S., and Kim, M. K. (2004). Vertical vibration analysis of soil-pile interaction systems considering the soil-pile interface behavior. *KSCE Journal of Civil Engineering*, 8(2):221–226.

Kim, N. R. and Kim, D. S. (2010). Development of VS tomography testing system for geotechnical centrifuge experiments. *7th Physical modeling in geotechnics, 7th ICPMG, Springman*, 50(1):349–354.

Kouroussis, G., Connolly, D. P., and Verlinden, O. (2014). Railway-induced ground vibrations-a review of vehicle effects. *International Journal of Rail Transportation*, 2(2):69.

Krylov, V. (1995). Low-frequency ground vibrations from underground trains. *Journal of Low Frequency Noise, Vibration and Active Control*, 14(1):55–60.

Kumar, J. and Madhusudhan, B. (2010). Effect of relative density and confining pressure on poisson ratio from bender and extender elements tests. *Géotechnique*, 60(7):561–567.

Kuo, K. A. (2010). *Vibration from Underground Railways: Considering Piled Foundations and Twin Tunnels*. PhD thesis.

Lauder, K. (2010). *The performance of pipeline ploughs*. PhD thesis.

Lee, C.-J., Hung, W.-Y., Tsai, C.-H., Chen, T., Tu, Y., and Huang, C.-C. (2014). Shear wave velocity measurements and soil–pile system identifications in dynamic centrifuge tests. *Bulletin of earthquake engineering*, 12(2):717–734.

Lee, C.-J., Wang, C.-R., Wei, Y.-C., and Hung, W.-Y. (2012). Evolution of the shear wave velocity during shaking modeled in centrifuge shaking table tests. *Bulletin of earthquake engineering*, 10(2):401–420.

Lee, J.-s. and Santamarina, J. C. (2005). Bender Elements: Performance and Signal Interpretation. (September):1063–1070.

Lehane, B. M., Gaudin, C., and Schneider, J. A. (2005). Scale effects on tension capacity for rough piles buried in dense sand. *Geotechnique*, 55(10):709–719.

Lehane, B. M. and White, D. J. (2005). Lateral stress changes and shaft friction for model displacement piles in sand. *Canadian Geotechnical Journal*, 42(4):1039–1052.

Liu, G. (2009). *Verification of shear wave velocity based liquefaction criteria using centrifuge model*. PhD thesis.

Liu, J., Xiao, H., Tang, J., and Li, Q. (2004). Analysis of load-transfer of single pile in layered soil. *Computers and Geotechnics*, 31(2):127 – 135.

Lo Presti, D. C. F., Jamiolkowski, M., Pallara, O., Cavallaro, A., and Pedroni, S. (1997). Shear modulus and damping of soils. *Geotechnique*, 47(3):603–617.

Lombaert, G., Degrande, G., François, S., and Thompson, D. J. (2015). Ground-Borne Vibration due to Railway Traffic: A Review of Excitation Mechanisms, Prediction Methods and Mitigation Measures. In Nielsen, C. O. J., Anderson, D., Gautier, P.-E., Iida, M., Nelson, T. J., Thompson, D., Tielkes, T., Towers, A. D., and de Vos, P., editors, *Noise and Vibration Mitigation for Rail Transportation Systems: Proceedings of the 11th International Workshop on Railway Noise, Uddevalla, Sweden, 9–13 September 2013*, pages 253–287. Springer Berlin Heidelberg, Berlin, Heidelberg.

Luong, P. M. (1994). Centrifuge simulation of Rayleigh waves in soils using a drop-ball arrangement. pages 385–399, San Francisco, CA, USA. ASTM.

Madabhushi, G. (1991). *Response of tower structures to earthquake perturbations*. PhD thesis.

Maeso, O., Aznárez, J. J., and Garcıa, F. (2005). Dynamic impedances of piles and groups of piles in saturated soils. *Computers Structures*, 83(10):769 – 782. Boundary Element Methods.

Metrikine, A. and Vrouwenvelder, A. (2000). Surface ground vibration due to a moving train in a tunnel: Two-dimensional model. *Journal of Sound and Vibration*, 234(1):43 – 66.

Mitaritonna, G., Amorosi, A., and Cotecchia, F. (2010). Multidirectional bender element measurements in the triaxial cell : equipment set-up and signal interpretation.

Muravskii, G. (1997). Green functions for a compressible linearly non homogeneous half-space. *Archive of Applied Mechanics*, 67(8):521–534.

Nanda, S ; Patra, N. R. (2014). Theoretical Load-Transfer Curves along Piles Considering Soil Nonlinearity. *Journal of Geotechnical and Geoenvironmental Engineering*, 140(1):91–101.

Nejati, H. R., Ahmadi, M., and Hashemolhosseini, H. (2012). Numerical analysis of ground surface vibration induced by underground train movement. *Tunnelling and Underground Space Technology*, 29:1 – 9.

Nugent, R. E., Village, W., and Zapfe, J. A. (2012). Designing Vibration-Sensitive Facilities Near Rail Lines. *Sound and Vibration*, (November):13–16.

Owen, J. (2003). Monitoring the degradation of reinforced concrete beams under cyclic loading. In *Damage Assessment of Structures V*, volume 245 of *Key Engineering Materials*, pages 307–314. Trans Tech Publications Ltd.

Pak, R. Y. S. and Guzina, B. B. (1995). Dynamic characterization of vertically loaded foundations on granular soils. *Journal of geotechnical engineering*, 121(3):274–286.

Poulos, H. G. (1981). Cyclic Axial Response of Single File. *Journal of the Geotechncial Engineering Division*, 107:41–58.

Poulos, H. G. and Davis, E. H. (1968). Settlement Behaviour of Single Axially Loaded Incompressible Piles And Piers. *Geotechnique*, 18(3):351–371.

Rabiner, L. R. and Gold, B. (1975). Theory and application of digital signal processing. *Englewood Cliffs, NJ, Prentice-Hall, Inc., 1975. 777 p.*, 1.

Rankine, W. (1857). *On stability of Loose Earth.* Philosophic Transactions of Royal Society, London.

Rayhani, M. H. T. and El Naggar, M. H. (2007). Centrifuge modeling of seismic response of layered soft clay. *Bulletin of Earthquake Engineering*, 5(4):571.

Reddy, E. S. B. (1996). *An investigation into the response of piles in sand under vertical cyclic tensile loads.* PhD thesis.

Rees, J. and Gomez-Agustina, L. (2018). Assessment of ground-borne vibration from underground trains on a proposed residential development. In *11th European Congress and Exposition on Noise Control Engineering*.

Reese, Lymon C., . (2006). *Analysis and design of shallow and deep foundations / Lymon C. Reese, William M. Isenhower, Shin-Tower Wang*. Hoboken, N.J.

Rikse, L., Hunt, H., Hussein, M., Degrande, G., and Gupta, S. (2007). A model for calculating vibration from a railway tunnel buried in a full-space including rigid bedrock.

Rollins, K. M., Evans, M. D., Diehl, N. B., and Daily III, W. D. (1998). Shear modulus and damping relationships for gravels. *Journal of Geotechnical and Geoenvironmental Engineering*, 124(5):396–405.

Ronald, J. E., Vincent, P. D., and Bruce, L. K. (1994). Dynamic Geotechnical Testing II.

Schofield, A. N. (1980). Cambridge geotechnical centrifuge operations. *Géotechnique*, 30(3):227–268.

Seed, H. B., Wong, R. T., Idriss, I. M., and Tokimatsu, K. (1986). Moduli and Damping Factors for Dynamic Analyses of Cohesionless Soils. *Journal of geotechnical engineering*, 112(11):1016–1032.

Shantz, B. R. W. J. T. D. T. (2012). Guidelines for Estimation of Shear Wave Velocity Profiles. Technical report.

Sheng, X., Jones, C., and Petyt, M. (1999a). Ground vibration generated by a load moving along a railway track. *Journal of Sound and Vibration*, 228(1):129 – 156.

Sheng, X., Jones, C., and Thompson, D. (2006). Prediction of ground vibration from trains using the wavenumber finite and boundary element methods. *Journal of Sound and Vibration*, 293(3):575 – 586. Proceedings of the Eigth International Workshop on Railway Noise.

Sheng, X., Jones, C. J. C., and Petyt, M. (1999b). Ground vibration generated by a harmonic load acting on a railway track. *Journal of Sound and Vibration*, 225(1):3–28.

Steedman, R. S., Madabhushi, S. P. G., and of Cambridge. Engineering Department, U. (1990). *Wave Propagation in Sand Medium*. CUED/D - soils TR. University of Cambridge, Department of Engineering.

Stokoe, K., Lee, S., and Knox, D. (1985). Shear moduli measurements under true triaxial stresses. In *Advances in the art of testing soils under cyclic conditions*, pages 166–185. ASCE.

Tamura, C., Moriti, S., and Nakamura, Y. (1975). Experimental research for subway-induced vibration on the tunnel formulation and ground.

Taylor, R. N. (1995). *Geotechnical Centrifuge Technology*. Blackie Academic and Professional, London.

Thompson, D. D. (2009). *Railway noise and vibration : mechanisms, modelling and means of control / David Thompson with contributions from Chris Jones and Pierre-Etienne Gautier*. Oxford : Elsevier, Oxford.

Thusyanthan, N. I. and Madabhushi, S. P. G. (2003). Experimental study of vibrations in underground structures. *Proceedings of the Institution of Civil Engineers: Geotechnical Engineering*, 156(2):75–81.

Tsuno, K., Morimoto, W., Itoh, K., Murata, O., and Kusakabe, O. (2005). Centrifugal modelling of subway-induced vibration. *International Journal of Physical Modelling in Geotechnics*, 5(4):15–26.

Viggiani, C. (2012). *Piles and pile foundations / Carlo Viggiani, Alessandro Mandolini and Gianpiero Russo*. London : Spon Press, London.

Wang, G., Ge, W., Pan, X., and Wang, Z. (2008). Torsional vibrations of single piles embedded in saturated medium. 35:11–21.

Wang, J., Zhou, X., and Lu, J. (2003). Dynamic response of pile groups embedded in a poroelastic medium. *Soil Dynamics and Earthquake Engineering*, 23(3):53 – 60.

White, D. J. and Bolton, M. D. (2004). Displacement and strain paths during plane-strain model pile installation in sand. *Géotechnique*, 54(6):375–397.

Wilson, G., Saurenman, H., and Nelson, J. (1983). Control of ground-borne noise and vibration. *Journal of Sound and Vibration*, 87(2):339 – 350.

Wiss, J. F. (1981). Construction vibrations: State-of-the-art. volume 107, pages 167–181.

Wolf, J. P. (1994). *Foundation vibration analysis using simple physical models*. Prentice-Hall, Englewood Cliffs, NJ United States.

Wolf, S. (2003). Potential low frequency ground vibration (¡6.3hz) impacts from underground lrt operations. *Journal of Sound and Vibration*, 267(3):651 – 661. Proceedings of the Seventh International Workshop on Railway Noise.

Wu, H.-N., Shen, S.-L., Chai, J.-C., Zhang, D.-M., and Xu, Y.-S. (2015). Evaluation of train-load-induced settlement in metro tunnels. *Proceedings of the Institution of Civil Engineers - Geotechnical Engineering*, 168(5):396–406.

Wu, Y.-S. and Yang, Y.-B. (2004). A semi-analytical approach for analyzing ground vibrations caused by trains moving over elevated bridges. *Soil Dynamics and Earthquake Engineering*, 24(12):949 – 962.

Xu, F., Zhang, Q., Li, L., He, P., Wang, B., and Zhang, Y. (2018). A simplified approach for settlement analysis of single pile considering pile end settlement induced by skin friction in multilayered soils. *European Journal of Environmental and Civil Engineering*, 22(11):1325–1340.

Xu, K. J. and Poulos, H. G. (2001). 3-D elastic analysis of vertical piles subjected to "passive" loadings. *Computers and Geotechnics*, 28(5):349–375.

Yang, W. (2011). Physical and numerical modelling of railway induced ground-borne vibration Wenbo Yang BEng , MSc. (August).

Yang, W. (2012). *Physical and numerical modelling of railway induced ground-borne vibration*. PhD thesis.

Yang, W., Cui, G., Xu, Z., Yan, Q., He, C., and Zhang, Y. (2018). An experimental study of ground-borne vibration from shield tunnels. *Tunnelling and Underground Space Technology*, 71:244 – 252.

Yuan, Z., Xu, C., Cai, Y., and Cao, Z. (2015). Dynamic response of a tunnel buried in a saturated poroelastic soil layer to a moving point load. *Soil Dynamics and Earthquake Engineering*, 77:348 – 359.

Zeng, X. and Schofield, A. N. (1996). Design and performance of an equivalent-shear-beam container for earthquake centrifuge modelling. *Géotechnique*, 46(1):83–102.

Zhang, J., Andrus, R. D., and Juang, C. H. (2005). Normalized shear modulus and material damping ratio relationships. *Journal of Geotechnical and Geoenvironmental Engineering*, 131(4):453–464.

Zhang, Q., Zhang, Z., and He, J. (2010). A simplified approach for settlement analysis of single pile and pile groups considering interaction between identical piles in multilayered soils. *Computers and Geotechnics*, 37(7):969 – 976.

Zhang, T., Cui, Y., Lamas-Lopez, F., Calon, N., and D'Aguiar, S. C. (2016). Modelling stress distribution in substructure of french conventional railway tracks. *Construction and Building Materials*, 116:326 – 334.

Zhou, X.-l., Wang, J.-h., Jiang, L.-f., and Xu, B. (2009). Transient dynamic response of pile to vertical load in saturated soil. *Mechanics Research Communications*, 36(5):618–624.

Appendix: material, equipment and transducer specifications

Introduction

This chapter illustrates the specification data sheets of the electromagnetic shaker, Duxseal, the piezoelectric accelerometer, the dynamic load cell, the static load cell, the MEMS accelerometer, and two LVDTs (LVDT-G and LVDT-P, as shown in Figure 3.5).

Shaker specification data sheet-page 1

PRODUCT DATA

LDS V101, V102, V201 and V203 Shakers
Imperial

Performance Parameters and Characteristics*

Shaker	V101/2	V201/3
Standard LDS Amplifier	PA25E	
Sine Force (peak) – forced air cooled	–	6 lbf
Sine Force (peak) – naturally cooled	2 lbf	4 lbf
Armature Resonance (f_n)	12 kHz	13 kHz
Useful Frequency Range	5 Hz – 12 kHz	5 Hz – 13 kHz
Effective Mass of Moving Element	0.0143 lb	0.044 lb
Velocity (sine peak)	51.6 in/s	72 in/s
Maximum Acceleration (sine peak) – naturally cooled	140 g	91 g
Maximum Acceleration (sine peak) – forced air cooled	–	136 g
Amplifier Rating	0.048 kVA	0.048 kVA
Displacement (pk–pk) – continuous	0.1 in	0.2 in
Suspension Axial Stiffness	18 lbf/in	16 lbf/in
Aux. Suspension Axial Stiffness	–	70 lbf/in
Shaker Body Mass – base mounted	2 lb	4 lb
Shaker Body Mass – trunnion mounted	–	7 lb
Impedance at 500 Hz	3.0 Ω	2.0 Ω
Cooling Air Flow	–	2.1 ft^3/min
Armature Diameter	Central spigot	
Armature Insert Pattern: Centre Insert	1	1

This range of permanent magnetic shakers is ideal for vibration testing of components, small assemblies or modal and structural analysis. The shakers' efficient armature design enables them to deliver impressive peak forces and accelerations over a wide frequency range.

The V100 and V200 series are miniature units designed to reproduce a vibration environment under laboratory conditions. They are also suitable as non-seismic pick-ups and are widely used in educational and research establishments to investigate the dynamic behaviour of structures and materials.

Features

- Wide frequency band combined with high peak forces
- Low mass, high performance armature construction
- Base or trunnion mounted
- Powered by compact, quiet and energy efficient amplifiers
- Robust, lightweight suspension system provides excellent torsional and traverse stiffness with minimal impact on system acceleration

Industry Applications

- Modal and structural analysis
- Electronic assembly testing
- Laboratory experiments and various medical purposes
- Fatigue and resonance testing
- Use as velocity transducer or high speed actuator



* Shaker ratings are those which can be achieved with a larger amplifier than that supplied as standard.

Brüel & Kjær

Shaker specification data sheet-page 2

Some of the features listed are available as standard, others as options. Please contact Brüel & Kjær for advice on the optimum specification to meet your system needs.

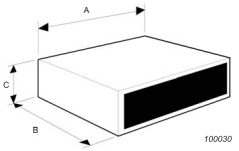
System Characteristics

Shaker + PA25E Amplifier	**V101/2**	**V201/3**
System Maximum ½-sine Shock Force*	2 lbf	4 lbf
Acoustic Noise at 3.3 ft Distance:†		
Shaker‡	<70 dBA	75 dBA
Amplifier	silent	silent
Total Heat Dissipation:		
Shaker – heat rejected to air	9.5 W	48 W
Amplifier	0.067 kW	0.067 kW
Amplfier Electrical Requirement	0.09 kVA	0.13 kVA
Max. Working Ambient Temperature:		
Shaker	86° F	86° F
Amplifier	95° F	95° F
Health and Safety:		

Complies with the following EU directives:
- Machinery: 2006/42/EC
- Low Voltage: 2006/95/EC
- EMC: 2004/108/EC
- CE

Designed in accordance with EN 61010 – 1:2001

PA25E Amplifier Data



Dimensions:	
Dim. A (in)	19.2
Dim. B (in)	13.3
Dim. C (in)	3.6
Weight (lb)	20
Protection:	
Fast acting current limit	

Characteristics:	
Rated Sinusoidal Power Output – matched resistive load	48 W (5R3)
Signal-to-noise Ratio	>75 dB
Total Harmonic Distortion – at rated output (10 Hz – 10 kHZ)	Typically 0.3%
Input Sensitivity for Maximum Output (400 Hz)	1.0 V rms
Amplifier Efficiency	59%
Voltage Regulation	1%
Maximum Continuous Sinusoidal VA Output (0.5 pf)	48 VA
Frequency Range – at rated power	10 Hz – 10 kHz
Output Current – at rated VA	2.7 A rms
Random Output Current	5.9 A pk
Maximum Output Current	3 A rms
Maximum Output Voltage	16 V rms
Maximum No Load Voltage	24 V rms
Overcurrent Trip Level	4.2 A rms

Shaker Options

Armature Insert Selection:	
M 4	◆
6/32″ UNC (with V102)	◆
10/32″ UNC (with V203)	◆
Mounting Selection:	
Base Mounting	◆
Support Trunnion (with V201/3)	●
Other Options:	
Auxiliary Suspension (with V201/3)	●

Key:
◆ Standard – Available on shortest delivery
● Option – Stocked item, available on short delivery

Make Our Experience Your Advantage

From application engineering, installation and training through to maintenance, spares and repairs, Brüel & Kjær offers a total service approach to keep your system operating efficiently and reliably. All LDS systems (standards and specials) are designed and manufactured to ISO 9001 standard. Brüel & Kjær offers a comprehensive range of vibration, measurement and analysis equipment. Please consult our website for details.

* ½-sine shock force is calculated with the standard payload, 2 ms pulse width, 10% pre/post pulse
† Measured at a height of 63 in above floor level in enclosed cell
‡ Maximum noise when running at full level

© Brüel & Kjær. All rights reserved.

Brüel & Kjær reserves the right to change specifications and accessories without notice.

2012-02
BP 2418 – 11

HEADQUARTERS: Brüel & Kjær Sound & Vibration Measurement A/S · DK-2850 Nærum · Denmark
Telephone: +45 7741 2000 · Fax: +45 4580 1405 · www.bksv.com · info@bksv.com

Local representatives and service organisations worldwide

Brüel & Kjær

Duxseal specification data sheet-page 1

May 2014

INDUSTRIES 3R

MATERIAL SAFETY DATA SHEET

IDENTITY

Part Number:	**DUXSEAL**
Identity:	Rubber Compound
Description:	Caulking Compound

SUPPLIER

Industries 3R inc.
55, route 116 Ouest
Danville (Québec) J0A 1A0
Tel: 819-839-2793
Fax: 819-839-2797

COMPOSITION/INFORMATION ON INGREDIENTS

INGREDIENT NAME	***# CAS***	***% WT or % VOL***
Talc	14807-96-6	25-40
Chlorinated Paraffin	63449-39-8	20-30
Mineral Wool	None Assigned	17-21
Diatomite	61790-53-2	5-8
Non-fibrous Amphiboles	None Assigned	3-5
Dolomite	16389-88-1	2-4
Butyl Rubber	None Assigned	2-4
Quartz	14808-60-7	1-2

Trace Impurities: None Identified

	OSHA PEL		**ACGIH TLV**		**NIOSH REL**		**NIOSH**
Ingredient	**TWA**	**STEL**	**TWA**	**STEL**	**TWA**	**STEL**	**IDLH**
Talc	2 mg/m^3 Respirable Dust	none estab.	2 mg/m^3 Respirable Dust	None estab.	none estab.	none estab.	none estab.
Chlorinated Paraffin.	None estab.	None estab.	None estab.	None estab.	None estab.	None estab.	None estab
Mineral Wool	5 mg/m^3 Respirable Dust 15 mg/m^3 Total Dust	None estab.	10 mg/m^3 Total Dust	None estab.	None estab.	None estab.	None estab.
Diatomite	None estab.	None estab.	10 mg/m^3 Total Dust	None estab.	None estab.	None estab.	None estab
. **Non-Fibrous Amphiboles**	None estab.	None estab.	None estab.	None estab.	None estab.	None estab.	None estab.
Dolomite	None estab.	None estab.	None estab.	None estab.	None estab.	None estab.	None estab.

Duxseal specification data sheet-page 2

Butyl rubber	None estab.	None estab.	None estab.	None estab.	None estab.	None estab.	None estab.
Quartz	0.1 mg/m^3 Respirable Dust	None estab.	0.1 mg/m^3 Respirable Dust	None estab.	None estab.	None estab.	None estab

Toxicity Data:	Talc	LD_{50}: Not Determined	LC_{50}: Not Determined
	Chlorinated Paraffin	LD_{50}: Not Determined	LC_{50}: Not Determined
	Mineral Wool	LD_{50}: Not Determined	LC_{50}: Not Determined
	Diatomite	LD_{50}: Not Determined	LC_{50}: Not Determined
	Non-Fibrous Amphiboles	LD_{50}: Not Determined	LC_{50}: Not Determined
	Dolomite	LD_{50}: Not Determined	LC_{50}: Not Determined
	Butyl Rubber	LD_{50}: Not Determined	LC_{50}: Not Determined
	Quartz	LD_{50}: Not Determined	LC_{50}: Not Determined

PHYSICAL AND CHEMICAL PROPERTIES

Physical State:	Solid (Putty like consistency)
Appearance and Odor:	Brown to Gray-Green Putty –Slight Rubber Odor
Odor Threshold:	Not Available
Vapor Pressure:	Not Available
Vapor Density (Air=1):	Not Available
Formula Weight:	Not Applicable
Density:	14.3 lb/gal
Specific Gravity (H_2O=1, at 4°C):	1.71
pH:	Neutral
Water Solubility:	Negligible
Other Solubilities:	Not Available
Boiling Point:	Not Determined
Freezing/Melting Point:	Not Determined
Viscosity:	Not Determined
Refractive Index:	Not Available
Surface Tension:	Not Available
% Volatile:	<1 %
Evaporation Rate:	Nil
Coefficient Water/Oil:	Not Applicable

FIRE-FIGHTING MEASURES

Flash Point: >200°F
Flash Point Method: Not Available
Burning Rate: Not Available
Autoignition Temperature: Not Determined
LEL: Not Determined
UEL: Not Determined
Flammability Classification: Not Determined
Extinguishing Media: Foam, Dry Chemical, Carbon Dioxide, Water Spray
Unusual Fire or Explosion Hazards: Smoke contains hydrogen chloride gas. Wear a self-contained breathing apparatus and full protective gear.
Hazardous Combustion Products: Hydrogen chloride, carbon monoxide, carbon dioxide and other partially oxidized hydrocarbons may form during a fire.
Fire-Fighting Instructions: Material is fire retardant and self-extinguishing, but will burn in a large fire. This material can produce acrid smoke in a large fire.

Duxseal specification data sheet-page 3

Fire-Fighting Equipment: Because fire may produce toxic thermal decomposition products, wear a self-contained breathing apparatus (SCBA) with a full facepiece operated in pressure-demand or positive-pressure mode and full protective gear.

STABILITY AND REACTIVITY
Stability: This product is stable.

Polymerization: Hazardous polymerization cannot occur.

Chemical Incompatibilities: Avoid exposure to strong oxidizing agents.

Conditions to Avoid: Temperatures above 400°F.

Hazardous Decomposition Products: Hydrogen chloride

Substances evolved during Curing: Not applicable. Material does not cure under normal conditions of use.

EXPOSURE CONTROLS/PERSONAL PROTECTION
Engineering Controls: Not normally required
Ventilation: Not normally required.
Administrative Controls: Not normally required.
Respiratory Protection: Not normally required.
Protective Clothing/Equipment: Gloves and protective eyeglasses with side shields are recommended.
Safety Stations: Not normally required.
Contaminated Equipment: Not applicable
Comments: Never eat, drink, or smoke in work areas. Practice good personal hygiene after using this material, especially before eating, drinking, smoking, using the toilet, or applying cosmetics.

SPILL, LEAK AN DISPOSAL PROCEDURES
Spill /Leak Procedures: Pick up or sweep up waste.
Small Spills: Pick up or sweep up waste.
Large Spills: Pick up or sweep up waste.
Containment: Not Applicable.
Cleanup: No special personal protective equipment required.
Regulatory Requirements: Comply with Federal, State, Provincial and Local regulations.
Disposal: In manufactured form, not a RCRA regulated waste. Comply with Federal, state, provincial and local regulations. Recycle when possible. Preferred method of disposal – landfill
Disposal Regulatory Requirements: None known
Container Cleaning and Disposal: No known regulations.
Ecological Information: Not Available
TSCA: Not Regulated
EPA Regulations:
RCRA Hazardous Waste Number: Not applicable
RCRA Hazardous Waste Classification: Not applicable
CERCLA Hazardous Substance: Not applicable
CERCLA Reportable Quantity (RQ): Not applicable
SARA 311/312 Codes: Not applicable
SARA Toxic Chemical (40 CFR 372.65): Not applicable
SARA EHS (Extremely Hazardous Substance) (40 CFR 355): Not listed,
Threshold Planning Quantity (TPQ): Not applicable
Clean Water Act: This material is not considered an oil under Section 313 of the CWA

Duxseal specification data sheet-page 4

OSHA Regulations:
Air Contaminant (29 CFR 1910.1000, Table Z-1, Z-1-A): See *Section Composition/information on Ingredients*
OSHA Specifically Regulated Substance (29CFR 1910): See *Section Composition/information on Ingredients*
State Regulations: None Known

HEALTH HAZARDS INFORMATION

Potential Health Effects

Primary Entry Routes: Eye and Skin Contact, Inhalation
Target Organs: Eyes, Skin and Upper Respiratory System.
Acute Effects: There are no anticipated acute health hazards when this material is handled within the normal range of usage. The talc, mineral wool, diatomite and quartz in this mixture pose a health hazard in the form of dust. These four compounds are bound within the putty and no respiratory hazards are expected.
Inhalation: May cause slight respiratory tract irritation.
Eye: Mechanical Irritant.
Skin: May cause slight transitory irritation to sensitive skin.
Ingestion: May cause slight discomfort.
Carcinogenicity: This product contains mineral wool which is considered a possible human carcinogen by IARC based on animal inhalation studies.
Synergistic Effects: None Known
Reproductive Toxin: No
Teratogen: No
Mutagen: No
Medical Conditions Aggravated by Long-Term Exposure: None known
Chronic Effects: There are no anticipated chronic health effects when this material is handled within the normal range of usage. Talc dust can produce fibrotic lung changes. Mineral wool dust has caused peribronchial sclerosis in animal experiments. Diatomaceous earth dust may cause fibrosis of the lungs. Prolonged inhalation of quartz may cause silicosis. However, there are no dusts associated with this product. IARC has classified man-made vitreous fibers (MMVF) as a possible human carcinogen based on animal inhalation studies using ceramic fibers and fiberglass. Several research studies using animals have shown that breathing air borne MMVF does not cause any lung cancer or other lung disease. Industry studies of mineral manufacturing workers are being expanded to investigate what effects other occupational exposures and lifestyle had on these workers. For example, smoking by these workers was found to contribute to the higher incidence of lung cancer.

Emergency and First Aid Procedures

Inhalation: Not considered a hazard under normal conditions of use.
Eye Contact: Flush eyes with clean running water for at least 15 minutes. If irritation persists, consult a physician.
Skin Contact: Wash affected areas with mild soap and warm water.
Ingestion: Drink water and seek emergency medical attention. DO NOT induce vomiting.
Note to Physicians: Not Available
Special Precautions/Procedures: None Known

SPECIAL PRECAUTIONS AND COMMENTS

Handling Precautions: None known
Storage Requirements: Store trendy tightly closed containers.

ADDITIONAL INFORMATION

The information, details, dimensions and values indicated are to our best knowledge. We recommend testing according to local conditions. The specifications are subject to change without notice.

Piezoelectric accelerometers specification data sheet-page 1

DJB Instruments
SENSING ENGINEERING INNOVATION

A/120/V Piezo-Tronic IEPE Accelerometer

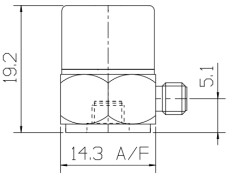
10mV/g up to 1V/g ±10% 12.5gm Std temp 125°C



The A/120 range of general purpose Konic shear IEPE vibration transducers offer a wide range of mounting, connectors and sensitivities all using DJB's unique and technically superior Konic shear design of piezoelectric ceramic sensor. Offering anything from 10mV/g up to 1V/g output within the same size accelerometer body it is perfectly suited to applications from vibration shaker control and delicate testing through to industrial machine monitoring.

Using a wide range of IEPE signal conditioning levels the A/120 can interface directly to a wide range of commercially available vibration spectrum analyzers and data acquisition systems as well as in our own VV/04, V3/04, V4/04 and CV9 signal conditioners which offer a range of normalizing and amplification options.

A/120/V

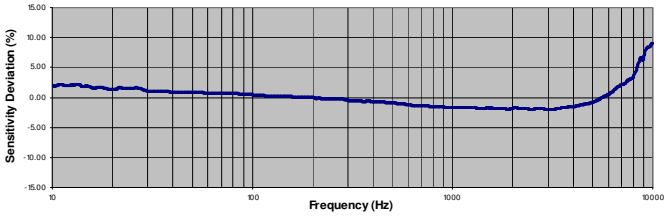


Note:
Voltage sensitivities shown are standard. We offer a wide range of sensitivities on request and recommend that applications are evaluated to determine the requisite sensitivity.

Options:
Cable assemblies available to any length and with any terminating connector.

A/120/CR – Side entry
A/120/V – Side entry
A/120/VI – Side entry
A/120/VT – Top entry
A/120/VTC – Top entry
A/120/VTI – Top entry

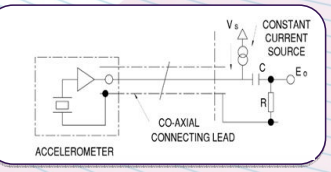
Typical Frequency Response



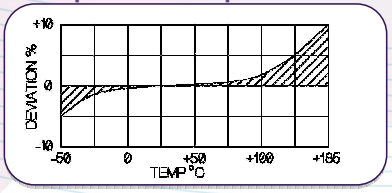
Typical Spectral Noise (100mV/g)

1Hz	732 µg/√Hz
10Hz	28.7 µg/√Hz
100Hz	8.9 µg/√Hz
1kHz	4.75 µg/√Hz
10kHz	3.99 µg/√Hz

Accelerometer Connection



Temperature Response



Please note: For information and reference only. Data should not be used as pass / fail criteria for calibration purposes

DJB Instruments (UK) Ltd
Finchley Avenue,
Mildenhall, Suffolk IP28 7BG

Tel +44 (0)1638 712 288
Email sales@djbinstruments.com
Web www.djbinstruments.com

A UK company with UK-based manufacturing, assembly and calibration in-house.

DJB Iss.4.2018

bsi. ISO 9001 Quality Management
FM11310

Piezoelectric accelerometers specification data sheet-page 2

DJB Instruments
SENSING ENGINEERING INNOVATION

A/120/V Piezo-Tronic IEPE Accelerometer

10mV/g up to 1V/g ±10% 12.5gm Std temp 125°C



	Metric			Imperial		
Voltage Sensitivity ±10%	1.0mV/(m/s²)	10.2mV/(m/s²)	50.98mV/(m/s²)	10mV/g	100mV/g	500mV/g
Resonant frequency	28 kHz					
Typical Frequency ±5% Response ±10%	1Hz – 8kHz 0.7Hz – 9kHz					
Cross Axis error/Transverse Sensitivity	≤5%					
Temperature Range	-50/+125°C			-58/+257°F		
Voltage sensitivity deviation (20°C/68°F)	-5% @ -50°C +5% @ +125°C			-5% @ -58°F +5% @ +257°F		
Supply voltage	15/35 V DC					
Supply current	2/20mA					
Bias voltage	10 - 14 V DC					
Settling time to 90% final val.	<2 secs					
Max continuous accn. g sine	9807m/s²			1000g		
Measurement Range	±4903m/s²	±490m/s²	±98m/s²	±500g	±50g	±10g
Base Strain Sensitivity	≤ 5%			≤ 5%		
Discharge Time Coef.	1 to 3 Seconds					
Non-linearity (%FS)	≤1%					
Broadband Resolution (1Hz to 10kHz – Typical)	0.0025grms					
Case material	Titanium Grade 2					
Mounting	Base tapped hole, 10-32 UNF x 4mm deep			Base tapped hole, 10-32 UNF x 0.16 deep		
Weight	12.5g			0.44oz		
Case seal	Welded hermetic connector			Welded hermetic connector		
Connector	10-32 UNF Microdot, TNC					
Size	14.3 (A/F) x 19.2mm			0.562" (A/F) x 0.75"		

Please note: For information and reference only. Data should not be used as pass / fail criteria for calibration purposes

DJB Instruments (UK) Ltd
Finchley Avenue,
Mildenhall, Suffolk IP28 7BG

Tel +44 (0)1638 712 288
Email sales@djbinstruments.com
Web www.djbinstruments.com

A UK company with UK-based manufacturing, assembly and calibration in-house.

DJB Iss.6 2019

bsi. ISO 9001 Quality Management
FM11310

Dynamic load cell specification data sheet

Model Number	ICP® FORCE SENSOR	Revision: H
221B02		ECN #: 30732

Performance	ENGLISH	SI	
Sensitivity(± 15 %)	50 mV/lb	11,241 mV/kN	
Measurement Range(Compression)	100 lb	0.4448 kN	
Measurement Range(Tension)	100 lb	0.4448 kN	
Maximum Static Force(Compression)	600 lb	2.669 kN	
Maximum Static Force(Tension)	500 lb	2.224 kN	
Broadband Resolution(1 to 10,000 Hz)	0.002 lb-rms	0.008896 N-rms	[1]
Low Frequency Response(-5 %)	0.006 Hz	0.006 Hz	[2]
Upper Frequency Limit	15 kHz	15 kHz	[3]
Non-Linearity	≤ 1 % FS	≤ 1 % FS	[4]
Environmental			
Temperature Range	-65 to +250 °F	-54 to +121 °C	
Temperature Coefficient of Sensitivity	≤ 0.03 %/°F	≤ 0.054 %/°C	
Electrical			
Discharge Time Constant(at room temp)	≥ 120 sec	≥ 120 sec	
Excitation Voltage	20 to 30 VDC	20 to 30 VDC	
Constant Current Excitation	2 to 20 mA	2 to 20 mA	
Output Impedance	≤ 100 ohm	≤ 100 ohm	
Output Bias Voltage	8 to 14 VDC	8 to 14 VDC	
Output Polarity(Compression)	Positive	Positive	
Physical			
Stiffness	2 lb/µin	0.35 kN/µm	[1]
Size (Diameter x Height)	0.65 in x 1.25 in	16.51 mm x 31.75 mm	
Weight	1.1 oz	31 gm	
Housing Material	Stainless Steel	Stainless Steel	
Sealing	Hermetic	Hermetic	
Electrical Connector	10-32 Coaxial Jack	10-32 Coaxial Jack	
Electrical Connection Position	Side	Side	
Mounting Thread	1/4-28 Female	1/4-28 Female	

CE [5]

All specifications are at room temperature unless otherwise specified.
In the interest of constant product improvement, we reserve the right to change specifications without notice.

ICP® is a registered trademark of PCB Group, Inc.

OPTIONAL VERSIONS

Optional versions have identical specifications and accessories as listed for the standard model except where noted below. More than one option may be used.

J - Ground Isolated		
M - Metric Mount		
Mounting Thread		M6 x 0.75 Female
N - Negative Output Polarity		
Output Polarity(Compression)	Negative	Negative
W - Water Resistant Cable		
Electrical Connector	Sealed Cable	Sealed Cable
Electrical Connection Position	Side	Side

NOTES:
[1] Typical.
[2] Calculated from discharge time constant.
[3] Estimated using rigid body dynamics calculations.
[4] Zero-based, least-squares, straight line method.
[5] See PCB Declaration of Conformance PS023 for details.

OPTIONAL ACCESSORIES:
Model 081A06 Mounting stud, 1/4-28 to 1/4-28 x .37 in. long, BeCu, no shoulder (1)

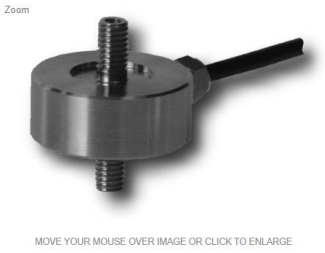
Entered: RLS	Engineer: APB	Sales: KW	Approved: EB	Spec Number:
Date: 5/26/09	Date: 5/26/09	Date: 5/26/09	Date: 5/26/09	1242

PCB PIEZOTRONICS
FORCE / TORQUE DIVISION
3425 Walden Avenue, Depew, NY 14043

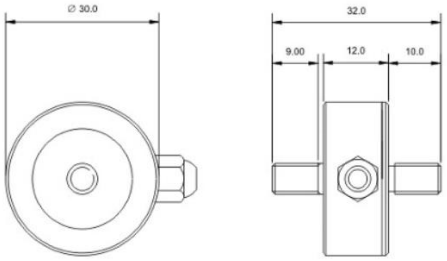
Phone: 716-684-0001
Fax: 716-684-8877
E-Mail: force@pcb.com

Static load cell specification data sheet

Miniature In Line Load Cell - Richmond Industries



Miniature In Line Load Cell up to 1kN (100kg)



(all in mm)

Product Description

The 210 Series is a smaller version of the 200 Series with M6x1 threads each end. The 210 Series is a range of miniature In-line mounting Load Cells which can be used to measure tensile or compressive forces and are used across a wide range of research and industrial applications. Typical applications include electro-mechanical test rigs and cable tension monitoring/testing.

Now Available with In-line conditioning modules. PC-USB, 0-5V, 0-10V, +/-10V, 4-20mA.

Specification: (Standard Output)

Standard Ranges	0 to 100N, 200N, 500N, 1kN
Excitation Voltage	10V (normal), 15V (max) DC*
Sensitivity	1.5 mV/V (Nominal) - (100N 1.3mV/V nominal)*
Non-Linearity	0.29% of F.R.O or Better
Hysteresis	0.29% of F.R.O or Better
Zero Balance	0.5% of F.R.O or Better
Bridge Resistance	350 Ohm (4 Gauge Bridge)
Over Load Characteristics	125% Safe Overload 150% Ultimate Overload
Insulation Resistance	> 2000M Ohm
Storage Temp	-40 to +70 Degrees C
Operating Temp	-20 to +70 Degrees C
Compensated Temp	+20 to +70 Degrees C
Electrical Connections	Integral Screened Cable
Thermal Sensitivity	0.025% of F.R.O/Degrees C

MEMS accelerometers (ADXL001-70) specification data sheet-page 1

ANALOG DEVICES

High Performance, Wide Bandwidth Accelerometer

ADXL001

FEATURES

High performance accelerometer
±70 *g*, ±250 *g*, and ±500 *g* wideband ranges available
22 kHz resonant frequency structure
High linearity: 0.2% of full scale
Low noise: 4 mg/√Hz
Sensitive axis in the plane of the chip
Frequency response down to dc
Full differential signal processing
High resistance to EMI/RFI
Complete electromechanical self-test
Output ratiometric to supply
Velocity preservation during acceleration input overload
Low power consumption: 2.5 mA typical
8-terminal, hermetic ceramic, LCC package

APPLICATIONS

Vibration monitoring
Shock detection
Sports diagnostic equipment
Medical instrumentation
Industrial monitoring

GENERAL DESCRIPTION

The ADXL001 is a major advance over previous generations of accelerometers providing high performance and wide bandwidth. This part is ideal for industrial, medical, and military applications where wide bandwidth, small size, low power, and robust performance are essential.

Using the Analog Devices, Inc. proprietary fifth-generation *i*MEMs® process enables the ADXL001 to provide the desired dynamic range that extends from ±70 *g* to ±500 *g* in combination with 22 kHz of bandwidth. The accelerometer output channel passes through a wide bandwidth differential-to-single-ended converter, which allows access to the full mechanical performance of the sensor.

The part can operate on voltage supplies from 3.3 V to 5 V.

The ADXL001 also has a self-test (ST) pin that can be asserted to verify the full electromechanical signal chain for the accelerometer channel.

The ADXL001 is available in the industry-standard 8-terminal LCC and is rated to work over the extended industrial temperature range (−40°C to +125°C).

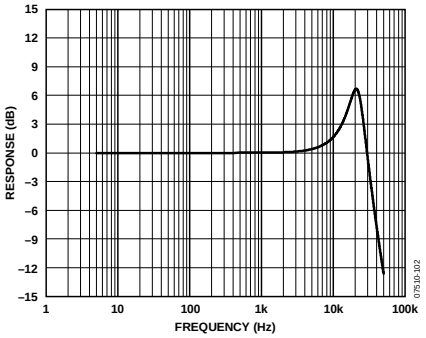


Figure 1. Sensor Frequency Response

FUNCTIONAL BLOCK DIAGRAM

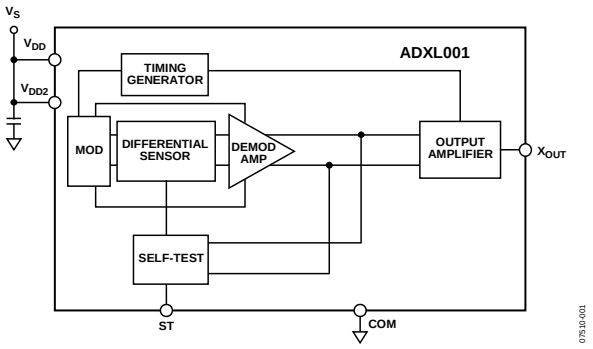


Figure 2.

Rev. A
Information furnished by Analog Devices is believed to be accurate and reliable. However, no responsibility is assumed by Analog Devices for its use, nor for any infringements of patents or other rights of third parties that may result from its use. Specifications subject to change without notice. No license is granted by implication or otherwise under any patent or patent rights of Analog Devices. Trademarks and registered trademarks are the property of their respective owners.

One Technology Way, P.O. Box 9106, Norwood, MA 02062-9106, U.S.A.
Tel: 781.329.4700 www.analog.com
Fax: 781.461.3113 ©2010 Analog Devices, Inc. All rights reserved.

MEMS accelerometers (ADXL001-70) specification data sheet-page 2

SPECIFICATIONS

SPECIFICATIONS FOR 3.3 V OPERATION

T_A = −40°C to +125°C, V_S = 3.3 V ± 5% dc, acceleration = 0 *g*, unless otherwise noted.

Table 1.

		ADXL001-70			ADXL001-250			ADXL001-500			
Parameter	**Conditions**	**Min**	**Typ**	**Max**	**Min**	**Typ**	**Max**	**Min**	**Typ**	**Max**	**Unit**
SENSOR											
Nonlinearity			0.2	2		0.2	2		0.2	2	%
Cross-Axis Sensitivity	Includes package alignment		2			2			2		%
Resonant Frequency			22			22			22		kHz
Quality Factor			2.5			2.5			2.5		
SENSITIVITY											
Full-Scale Range	I_{OUT} ≤ ±100 µA	−70		+70	−250		+250	−500		+500	*g*
Sensitivity	100 Hz		16.0			4.4			2.2		mV/*g*
OFFSET	Ratiometric										
Zero-*g* Output		1.35	1.65	1.95	1.35	1.65	1.95	1.35	1.65	1.95	V
NOISE											
Noise	10 Hz to 400 Hz		85			95			105		m*g* rms
Noise Density	10 Hz to 400 Hz		3.3			3.65			4.25		m*g*/√Hz
FREQUENCY RESPONSE											
−3 dB Frequency			32			32			32		kHz
−3 dB Frequency Drift Over Temperature			2			2			2		%
SELF-TEST											
Output Voltage Change			400			125			62		mV
Logic Input High		2.1			2.1			2.1			V
Logic Input Low				0.66			0.66			0.66	V
Input Resistance	To ground	30	50		30	50		30	50		kΩ
OUTPUT AMPLIFIER											
Output Swing	I_{OUT} = ±100 µA	0.2		V_S − 0.2	0.2		V_S − 0.2	0.2		V_S − 0.2	V
Capacitive Load		1000			1000			1000			pF
PSRR (CFSR)	DC to 1 MHz		0.9			0.9			0.9		V/V
POWER SUPPLY (V_S)											
Functional Range		3.135		6	3.135		6	3.135		6	V
I_{SUPPLY}			2.5	5		2.5	5		2.5	5	mA
Turn-On Time			10			10			10		ms

MEMS accelerometers (ADXL001-70) specification data sheet-page 3

ADXL001

SPECIFICATIONS FOR 5 V OPERATION

T_A = -40°C to +125°C, V_S = 5 V ± 5% dc, acceleration = 0 *g*, unless otherwise noted.

Table 2.

		ADXL001-70			ADXL001-250			ADXL001-500			
Parameter	**Conditions**	**Min**	**Typ**	**Max**	**Min**	**Typ**	**Max**	**Min**	**Typ**	**Max**	**Unit**
SENSOR											
Nonlinearity			0.2	2		0.2	2		0.2	2	%
Cross-Axis Sensitivity	Includes package alignment		2			2			2		%
Resonant Frequency			22			22			22		kHz
Quality Factor			2.5			2.5			2.5		
SENSITIVITY											
Full-Scale Range	$I_{OUT} \leq \pm 100$ µA	−70		+70	−250		+250	−500		+500	*g*
Sensitivity	100 Hz		24.2			6.7			3.3		mV/*g*
OFFSET	Ratiometric										
Zero-*g* Output		2.00	2.5	3.00	2.00	2.5	3.00	2.00	2.5	3.00	V
NOISE											
Noise	10 Hz to 400 Hz		55			60			70		m*g* rms
Noise Density	10 Hz to 400 Hz		2.15			2.35			2.76		m*g*/√Hz
FREQUENCY RESPONSE											
−3 dB Frequency			32			32			32		kHz
−3 dB Frequency Drift Over Temperature			2			2			2		%
SELF-TEST											
Output Voltage Change			1435			445			217		mV
Logic Input High		3.3			3.3			3.3			V
Logic Input Low				0.66			0.66			0.66	V
Input Resistance	To ground	30	50		30	50		30	50		kΩ
OUTPUT AMPLIFIER											
Output Swing	$I_{OUT} = \pm 100$ µA	0.2		$V_S - 0.2$	0.2		$V_S - 0.2$	0.2		$V_S - 0.2$	V
Capacitive Load		1000			1000			1000			pF
PSRR (CFSR)	DC to 1 MHz		0.9			0.9			0.9		V/V
POWER SUPPLY (V_S)											
Functional Range		3.135		6	3.135		6	3.135		6	V
I_{SUPPLY}			4.5	9		4.5	9		4.5	9	mA
Turn-On Time			10			10			10		ms

LVDT-G (S015.0) specification data sheet-page 1

AMETEK®
ULTRA PRECISION TECHNOLOGIES

Solartron Metrology
Precision Driven

Technical Specification

Generic Product Types

LVDT	S002.5	S005.0	S007.5	S010.0	S015.0	S025.0	S050.0	S075.0	S100.0	S150.0
Voltage Output (±DC Bipolar)	V002.5	V005.0	V007.5	V010.0	V015.0	V025.0	V050.0	V075.0	V100.0	V150.0
Voltage Output (DC Unipolar)	V005.0	V010.0	V015.0	V020.0	V030.0	V050.0	V100.0	V150.0	V200.0	V300.0
Current Output (4-20mA)	I005.0	I010.0	I015.0	I020.0	I030.0	I050.0	I100.0	I150.0	I200.0	I250.0
Digital Output (Orbit)	SD005	SD010	SD015	SD020	SD030	SD050	SD100	SD150	SD200	SD250

Measurement

Measurement Range (LVDT/±DC) (mm)	±2.5	±5	±7.5	±10	±15	±25	±50	±75	±100	±150
Measurement Range (4-20mA/DC/ORBIT) (mm)	5	10	15	20	30	50	100	150	200	300
Linearity (% FSO)	<0.20	<0.20	<0.20	<0.20	<0.20	<0.20	<0.20	<0.20	<0.20	<0.25
Resolution µm (Note 1)	<0.1	<0.1	<0.1	<0.2	<0.2	<0.3	<0.5	<0.7	<1.0	<2.0
Pre-travel ±0.5 mm (Guided Versions only)	2.0	3.0	1.6	3.1	6.7	6.9	4.9	5.0	8.8	16.2
Post Travel ±0.5 mm (Guided Versions only)	4.3	5.3	3.9	5.6	9.0	9.3	7.3	7.4	11.1	18.6
Temperature Coefficients (%FSO/°C) LVDT	<0.02	<0.01	<0.01	<0.01	<0.01	<0.01	<0.01	<0.015	<0.01	<0.01
Temperature Coefficients (%FSO/°C) DC/4-20mA	<0.03	<0.02	<0.02	<0.02	<0.02	<0.02	<0.02	<0.03	<0.02	<0.02
Tip Force ±20% (Horizontal at middle of range) N	1.1	1.0	1.0	1.1	1.2	1.5	2.1	1.9	2.3	2.6

Mechanical

Nominal Mass (g) LVDT	58	66	67	80	92	110	153	167	243	344
Nominal Mass (g) (4-20mA/DC)	72	80	81	94	106	124	167	181	257	358
Nominal Mass of Core (g)	2.6	5.0	5.8	7.2	6.4	6.6	9.0	9.0	9.0	9.0
Body diameter (mm)	19 (+0.0, -0.2)									
Case material	300 Series Stainless Steel									
Core material	Nickel Iron									
Cable Standard Type/Length (m)	F.E.P./3									

Electrical Interface (LVDT)

Energising Voltage (Vrms) at 5 kHz	1-10									
Energising Current at 5kHz (mA/V)	1.00	2.60	2.20	0.70	1.50	0.50	0.60	2.50	1.65	1.83
Sensitivity at 5kHz ±5% mV/V/mm	144.0	178.0	121.0	76.0	60.0	21.5	15.0	10.5	6.9	3.9

Electrical Interface (4-20mA & DC)

Input	10 to 30 V @ 30mA (Typ) or 4-20mA loop powered
Noise (DC Output) measured in 500Hz	<0.2 % FSO
Output Change with Power Supply Variation	<0.5 mV
Bandwidth (-3dB)	500Hz

Electrical Interface (ORBIT)

Bandwidth	Up to 460 Hz (selectable)
Output	Solartron Orbit
Power (VDC)	5±0.25 @ 0.06A
Sealing (Orbit Module)	IP43

Note 1: Resolution specification is only applicable to Orbit® digital transducers.
The resolution of LVDT transducers is effectively infinite and is only limited by the conditioning electronics

LVDT-G (S015.0) specification data sheet-page 2

AMETEK®
ULTRA PRECISION TECHNOLOGIES

Solartron Metrology
Precision Driven

Technical Specification

Environment

Temperature (Standard LVDT)	-40 to +120 °C
Temperature (HT LVDT)	-40 to +200 °C
Operating/Storage Temperature (4-20mA/DC)	0 to +65 / -20 to 85 °C
Sealing	IP65 or IP67
Vibration Sinusoidal	1 to 10g rms linear 10 to 50 Hz & 10g rms 50Hz to 1kHz
Vibration Random	DO160F Curve D
Shock	Drop test from 1m onto hard surface

S Series Options

Standard Output Options
LVDT
±5V DC
±10V DC
0-5V DC
5-0V DC
0-10V DC
10-0V DC
4-20 mA
20-4 mA
Solartron Orbit (Digital)
TTL

Mechanical Options
Free Core
Free Core/Carrier
Guided Core
Tip
Spring Push
Universal Joints

Connection Options
Cable (wire ends)
Cable + Connector
Axial Connector
Orbit Module

For non standard products contact your local Sales Office or Distributor

Solartron can provide a range of LVDT Conditioning Modules and Readouts for use with the LVDT versions of the S Series. Please see the LVDT Conditioning Data Sheet

LVDT-P (DFg5) specification data sheet-page 1

AMETEK®
ULTRA PRECISION TECHNOLOGIES

Solartron Metrology
Precision Driven

Technical Specification

Product Type	SM Type		MD Type					DF Type		
LVDT with Free Core	SM1	SM3	M6D1	MD1	MD2.5	MD5	MD10			
Half Bridge (HB) with Free Core			M6DH1	MD1H	MD2.5H	MD5H	MD10H			
DC Output with Free Core								DF1	DF2.5	DF5
DC Output with Guided Core								DFg1	DFg2.5	DFg5

Measurement										
Measurement Range (mm)	±1	±3	±1	±1	±2.5	±5	±10	±1	±2.5	±5
Linearity (% FSO)	0.25							0.50		
Linearity (% Reading)			0.5							
Resolution µm (Note 1)	<0.1		<0.1				<0.2	See Note 1		
Temperature Coefficients (%FSO/°C)	<0.03%		<0.01%					<0.025%		

Mechanical										
Body diameter (mm)	9.52		Φ6h6	Φ8h6				19.0		
Case Material	400 Stainless Steel									
Cable Type	PVC		PU							
Standard cable Length (m)	0.5		2					3		
Standard cable Style (Note 2)	A		B							
Nominal Mass (g)	6.0	8.0	2.6	5.0	7.6	8.5	13.0	26.0	26.0	30.0
Nominal Mass of Moving Parts (g)	0.5	1.5	0.1	0.2	0.2	0.3	0.7	1.0	1.0	1.2

Environment			
Operating Temperature	-40 to +85	-10 to + 80	-5 to +70
Storage Temperature	-40 to +100	-40 to +105	-10 to + 80
Sealing	Splash Proof		

Electrical Interface										
Energising Voltage	1-10 (Vrms)		1-10 (Vrms)					10-24 (VDC)		
Energising (LVDT) Current at 5kHz (mA/V)	3.8	1.8	3.0	1.8	2.0	1.0	0.6			
Energising Current (HB) at 10kHz (mA/V)			1.2	1.0		1.2				
Energising Current DC at 10V (mA)								10	13	
Frequency Response (-3db) Hz	Depends on Conditioning Electronics							50	75	
Sensitivity at 10VDC ±10% mV/mm								750	540	
Sensitivity at 5kHz ±5% mV/V/mm	142	136	269	210	150	105	33			
Sensitivity (HB) at 5kHz ±5% mV/V/mm			88	83	82	51	33			

Note 1: Resolution specification is only applicable to ORBIT digital transducers.
The resolution of LVDT transducers is effectively infinite and is only limited by the conditioning electronics

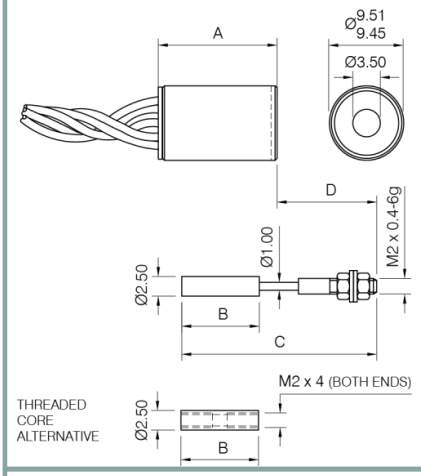
Note 2: Cable Style A comprises of individual twisted cores , Style B comprises a sheathed and screened cable

LVDT-P (DFg5) specification data sheet-page 2

AMETEK® ULTRA PRECISION TECHNOLOGIES

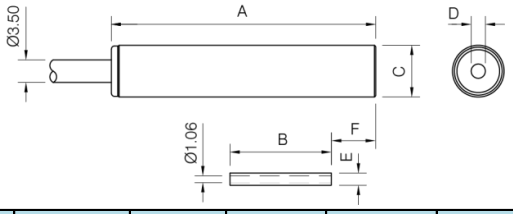
Solartron Metrology
Precision Driven

Dimensions



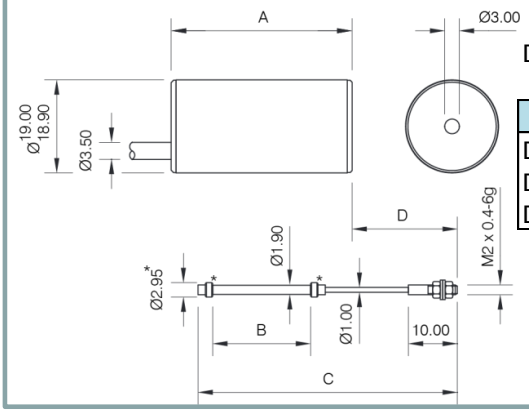
SM Series

Type	A	B	C	D (at Null)
SM1	15.20	9.90	24.90	12.70
SM3	35.00	20.60	42.60	15.30



MD Series

Type	A	B LVDT	B H/B	C	D	E	F(at null)
M6D1 / M6D1H	28.00	11.00	10.30	Ø6h6	Ø1.95	Ø1.60	2.00
MD1 / MD1H	28.00	11.00	8.85	Ø8h6	Ø2.20	Ø1.90	3.00
MD2.5 / MD2.5H	41.00	15.70	15.00	Ø8h6	Ø2.20	Ø1.90	6.90
MD5 / MD5H	49.00	21.20	18.40	Ø8h6	Ø2.20	Ø1.90	8.40
MD10 / MD10H	68.00	24.40	29.00	Ø8h6	Ø2.20	Ø1.90	16.40



DF SERIES

Type	A	B	C	D
DF1 / DFg1	37.0	20.0	53.0	21.5
DF2.5 / DFg2.5	37.0	20.0	53.0	21.5
DF5 / DFg5	43.0	24.3	57.3	20.5